An Adaptively Controlled MEMS Triaxial Angular Rate Sensor

James D. John

(Doctor of Philosophy)

March 2006

RMIT University

An Adaptively Controlled MEMS Triaxial Angular Rate Sensor

A thesis submitted in fulfilment of the requirements for

the degree of Doctor of Philosophy

James D. John

Bachelor of Engineering with Honours (Mechatronics)

School of Electrical and Computer Engineering

Science, Engineering and Technology Portfolio

RMIT University

March 2006

Declaration

I certify that except where due acknowledgement has been made, the work is that of the author alone; the work has not been submitted previously, in whole or in part, to qualify for any other academic award; the content of the thesis is the result of work which has been carried out since the official commencement date of the approved research program; and, any editorial work, paid or unpaid, carried out by a third party is acknowledged.

James D. John

March 2006

Acknowledgements

This thesis would not have been possible without: Dr Thurai Vinay, Dr Conrad Jakob, Dr Jason Chaffey and Dr Liang Qin whose supervision and guidance were invaluable throughout my candidature, my fellow researchers in the now extinct Dungeon and building 55 for your companionship, my loving family for their ever-present love, support and encouragement and finally my friends for taking care of the non-academic aspects of my life.

Abstract

Prohibitive cost and large size of conventional angular rate sensors have limited their use to large scale aeronautical applications. However, the emergence of MEMS technology in the last two decades has enabled angular rate sensors to be fabricated that are orders of magnitude smaller in size and in cost. The reduction in size and cost has subsequently encouraged new applications to emerge, but the accuracy and resolution of MEMS angular rate sensors will have to be greatly improved before they can be successfully utilised for such high end applications as inertial navigation.

MEMS angular rate sensors consist of a vibratory structure with two main resonant modes and high Q factors. By means of an external excitation, the device is driven into a constant amplitude sinusoidal vibration in the first mode, normally at resonance. When the device is subject to an angular rate input, Coriolis acceleration causes a transfer of energy between the two modes and results in a sinusoidal motion in the second mode, whose amplitude is a measure of the input angular rate. Ideally the only coupling between the two modes is the Coriolis acceleration, however fabrication imperfections always result in some cross stiffness and cross damping effects between the two modes. Much of the previous research work has focussed on improving the physical structure through advanced fabrication techniques and structural design; however attention has been directed in recent years to the use of control strategies to compensate for these structural imperfections. The performance of the MEMS angular rate sensors is also hindered by the effects of time varying parameter values as well as noise sources such as thermal-mechanical noise and sensing circuitry noise.

In this thesis, MEMS angular rate sensing literature is first reviewed to show the evolution of MEMS angular rate sensing from the basic principles of open-loop operation to the use of complex control strategies designed to compensate for any fabrication imperfections and time-

varying effects. Building on existing knowledge, a novel adaptively controlled MEMS triaxial angular rate sensor that uses a single vibrating mass is then presented. Ability to sense all three components of the angular rate vector with a single vibrating mass has advantages such as less energy usage, smaller wafer footprint, avoidance of any mechanical interference between multiple resonating masses and removal of the need for precise alignment of three separate devices.

The adaptive controller makes real-time estimates of the triaxial angular rates as well as the device cross stiffness and cross damping terms. These estimates are then used to compensate for their effects on the vibrating mass, resulting in the mass being controlled to follow a predefined reference model trajectory. The estimates are updated using the error between the reference model trajectory and the mass's real trajectory. The reference model trajectory is designed to provide excitation to the system that is sufficiently rich to enable all parameter estimates to converge to their true values. Avenues for controller simplification and optimisation are investigated through system simulations. The triaxial controller is analysed for stability, averaged convergence rate and resolution. The convergence rate analysis is further utilised to determine the ideal adaptation gains for the system that minimises the unwanted oscillatory behaviour of the parameter estimates.

A physical structure for the triaxial device along with the sensing and actuation means is synthesised. The device is realisable using MEMS fabrication techniques due to its planar nature and the use of conventional MEMS sensing and actuation elements. Independent actuation and sensing is achieved using a novel checkerboard electrode arrangement. The physical structure is refined using a design automation process which utilises finite element analysis (FEA) and design optimisation tools that adjust the design variables until suitable design requirements are met.

Finally, processing steps are outlined for the fabrication of the device using a modified, commercially available polysilicon MEMS process.

Contents

List of Figures

List of Tables

Abbreviations and Acronyms

APCVD	Atmospheric Pressure Chemical Vapor Deposition
DOF	Degree Of Freedom
FBAR	Film Bulk Acoustic Resonator
FEA	Finite Element Analysis
FEM	Finite Element Model
FOG	Fibre Optic Gyroscope
HF	Hydrofluoric Acid
IMU	Inertial Measurement Unit
LPCVD	Low Pressure Chemical Vapor Deposition
LQG	Linear Quadratic Gaussian
MBE	Molecular Beam Epitaxy
MEMS	Micro Electro Mechanical Systems
MRAC	Model Reference Adaptive Control
MUAV	Micro Unmanned Arial Vehicles
PolyMUMPs	Polysilicon Multi User MEMS Process
PACVD	Plasma Assisted Chemical Vapor Deposition
PECVD	Plasma Enhanced Chemical Vapor Deposition
PID	Proportional Integral Derivative
POCl3	Phosphoroxidchloride
PSD	Power Spectral Density
PSG	Phosphosilcate Glass

PVD	Physical Vapour Deposition
PVDF	PolyVinylidine DiFluoride
PZT	Lead Zirconate Titanate
RIE	Reactive Ion Etching
RLG	Ring Laser Gyroscope
RPM	Revolutions Per Minute
SAW	Surface Acoustic Wave
SOG	Silicon-On-Glass
STR	Self-Tuning Resonator
UV	Ultra Violet
VLSI	Very Large Scale Integration

Chapter 1

Introduction

From military to marketing, angular rate sensors have uses in a wide variety of applications. With the cost reduction and miniaturisation that Micro Electro Mechanical Systems (MEMS) enable, we are sure to see countless other uses emerge.

The following is a brief but varied list of applications that either rely on, or could make use of angular rate information.

- Active stabilisation in cars that compensates for body roll during cornering.
- Flight control systems in aeroplanes and helicopters that keep them from falling out of our skies.
- Navigation systems that help drivers reach their destination.
- Correcting for hand shake in hand-held cameras.
- Guiding Micro Unmanned Arial Vehicles (MUAV).
- Guiding shoppers through an indoor shopping complex.
- Location based information, services and marketing.
- Human-computer and gaming interfaces
- Head mounted display systems
- Satellite position control
- Space navigation and motion control

In its most simple definition an angular rate sensor measures the velocity at which it is rotating in inertial space. In the past this has been achieved using a gimballed spinning mass gyroscope whose angular momentum maintains its orientation with respect to inertial space. These devices are inherently large in size and are prone to mechanical failure. Laser ring gyroscopes also measure angular rate, they use the interference pattern created by two lasers traveling in opposite directions around a polished glass ring. They are very accurate however are again large in size and very expensive. MEMS utilise alternative angular rate sensing techniques that measure the effect of Coriolis forces on vibrating mass, ring, plate or finger elements. These Coriolis forces are proportional to angular rate. MEMS angular rate sensor performance still lags behind that of their macro-sized counterparts due to the Coriolis forces being very small, but they overcome the cost and size limitations of conventional devices. Their performance is hindered by resolution limiting noise sources and error causing fabrication imperfections.

Making the perfect MEMS angular rate sensor has been seen as the "Holy Grail" of MEMS problems. The performance of angular rate sensors is continually improving. In the eight years prior to 1998, reported device performances improved by an order of magnitude every two years [83]. The adoption of MEMS technology for fabricating angular rate sensors has allowed the fabrication of smaller, cheaper and much more energy efficient devices than conventional macro-sized devices [83]. This in turn has enabled and encouraged new mainstream applications to emerge.

Much of the previous research into MEMS angular rate sensors has been aimed at developing a device structure without fabrication imperfections or a structure that is more resilient to fabrication imperfections [34, 37, 48]. Recent research work however has adopted an alternative strategy. It accepts that fabrication imperfections will be present in the MEMS structure and works to estimate and compensate for them in real-time using various control techniques, this in effect makes the imperfect device behave more like a perfect one [28, 41, 42, 51, 56, 61, 70]. This approach also allows for fabrication tolerances to be relaxed, which can lead to higher production yield and therefore cheaper cost.

The majority of angular rate applications require triaxial angular rate information: pitch, roll and yaw. For example a basic Inertial Measurement Unit (IMU) consists of x, y and z axis angular rate sensors to track orientation, x, y and z axis accelerometers for locating gravity and linear motion and often x, y and z magnetometers for resolving magnetic north to correct for any

long term drift in the angular rate sensors. Together they can resolve orientation information and be used to keep track of motion. A major focus of this thesis is the development of a triaxial angular rate sensor that uses a single vibrating mass instead of a separate one for each of the three axes. This offers further advantages including size, power and also allows some of the sensing circuitry to be used by all three axes.

1.1 Original Contributions

This thesis presents a number of original contributions to the field of MEMS angular rate sensing and optimising the transient response of model reference adaptive control (MRAC) systems.

A single mass triaxial angular rate sensor concept. It is beneficial for a device to provide triaxial angular rate information given that few application require only single axis angular rate information. This is usually achieved by mounting three single axis devices together or fabricating all three on the same substrate. Having multiple resonant elements can lead to mechanical interference. This is avoided in the proposed device by using a single vibrating mass to measure angular rate in all three axes. This system also has inherent size and cost advantages due to a reduced substrate footprint.

An adaptive controller for the triaxial angular rate sensor. The adaptive controller makes real-time estimates of triaxial angular rate as well as the device stiffness error and damping. These estimates are then used to compensate for their effects on the vibrating mass; resulting in the mass being controlled along a predefined reference model trajectory. The estimates are updated using the error between the reference model trajectory and the mass's real trajectory. This approach removes the need for any additional driving control and output demodulation stages.

Performance analysis including bandwidth and resolution. The adaptive controller is analysed using standard adaptive control techniques to prove system stability, estimate device bandwidth and ultimate achievable resolution.

Simplified adaptive controller gain selection. The guesswork is taken out of choosing the adaptive controller gains using a novel approach of matching all the parameter estimate

convergence rates. This is shown to reduce the undesirable oscillations during parameter estimate transients. This approach is applicable to many other adaptively controlled applications.

A MEMS structural design for realisation of the triaxial angular rate sensor. A structure design suitable for implementing the single mass adaptively controlled triaxial angular rate sensor is presented. It is a planar structure that is suited to MEMS fabrication techniques and uses standard MEMS sensing and actuation elements. Independent actuation and sensing is achieved using a novel checkerboard electrode arrangement.

An automated design approach. An automated design approach which utilises optimisation tools is shown to result in a structure that meets predefined design requirements. This approach aims to reduce costly development time and again is not limited to the angular rate application.

A fabrication method for the triaxial angular rate sensor The proposed fabrication method is based on a commercially available set of fabrication steps that has been modified to better suit the proposed design. It can be used to fabricate the proposed angular rate sensor or could be adapted to implement a similar design topology for a triaxial accelerometer.

A phase differential angular rate sensor concept. [1] An alternative angular rate sensor design based on the phase differential demodulation scheme. The device removes the need for any drive amplitude control stages and gives an angular rate output that is independent of any scale factor variation in the sensing element scale factor.

1.1.1 Publications

Peer reviewed journal publications.

- J.D. John, C.F. Jakob, T. Vinay, and Lijiang Q. Phase differential angular rate sensor - concept and analysis. IEEE Sensors Journal Volume 4, Issue 4 , 2004, Pages 471-478 ISSN: 1530437.

- J.D. John and T. Vinay. Novel concept of a single mass adaptively controlled triaxial angular rate sensor. Sensors Journal, IEEE, Accepted for publication April, 2005.

Conference presentations and papers.

- J.D. John, C.F. Jakob, T. Vinay, and Lijiang Q. Phase differential angular rate sensor - concept and analysis. Device and Process Technologies for MEMS, Microelectronics, and Photonics III; Proceedings of SPIE - The International Society for Optical Engineering Volume 5276 , 2004, Pages 332-340 ISSN: 0277-786X.

1.2 Chapter Summary

Chapter 2 This chapter introduces Micro Electro Mechanical Systems (MEMS) and the inherent benefits that the technology offers, including size and the scaling effects on physical phenomenon, batch fabrication costs and integration with supporting electronic circuitry. The basic fabrication techniques used to make MEMS devices are outlined with particular emphasis on the techniques to fabricate the proposed device in Chapter 7. It is also intended to give the reader an appreciation of why thinking planar is so important in MEMS design. Sense and actuation elements commonly used for MEMS angular rate sensor devices are introduced, as is some basic information on software tools. These are available to aid in the MEMS development process, to reduce costly fabrication iterations.

Chapter 3 The current state of the art in angular rate sensing is reviewed. Included are conventional macro devices namely spinning mass and laser ring gyroscopes and MEMS angular rate and angular displacement sensors. The progression of MEMS angular rate sensing approaches are covered from basic open-loop operation and its inherent error sources, to complex control strategies that have been employed in order to overcome those error sources and enhance device performance. The move towards triaxial angular rate sensing is presented along with the advantages of attaining triaxial angular rate sensing with a single vibratory mass.

Chapter 4 This chapter presents the derivation a novel concept for an adaptively controlled triaxial angular rate sensor device that is able to detect rotation in three orthogonal axes, using a single vibrating mass. The physical system equations for the sensor are derived including asymmetric stiffness and damping terms. These equations are non-dimensionalised to simplify subsequent investigation. The adaptive controller performs various functions.

It updates estimates of all stiffness error, damping and input rotation parameters in real time, removing the need for any off-line calibration stages. The parameter estimates are used in feedforward control to cancel out the erroneous effects of any fabrication imperfections. The controller also drives the mass along a controlled oscillation trajectory, removing the need for additional drive control. Finally, the output of the device is simply an estimate of input rotation, removing the need for additional demodulation. To enable all unknown parameter estimates to converge to their true values, the necessary model trajectory is shown to be a three dimensional Lissajous pattern. This is created by having unmatched oscillatory frequencies in each of the three axes. The triaxial controller is investigated thoroughly in terms of is average convergence rate, optimum adaptive gain selection and resolution analysis.

Chapter 5 An initial device structure has been designed and modeled to prove realisation of the novel device is possible. In the design process many considerations were made. These include the design being of a planar nature, the suitability of the design for existing MEMS fabrication techniques, ensuring the displacements in the x, y and z axes were independently measurable and that conventional drive and sense elements are used. The possibility of using shared drive and sense electronic circuitry is also explored. A finite element modal analysis of the structural design is presented. It shows a MEMS realisable design having modal shapes and frequencies suitable for implementing the adaptive controller presented in Chapter 4. The controller requires that the first three resonant modes are slightly unmatched. Additionally the fourth and subsequent unwanted-twisting modes are made as far away as possible from the first three. This results in the 6 DOF system behaving like a 3 DOF system within the range of operating frequencies.

Chapter 6 A design automation process is presented that utilises the ANSYS design optimisation tools. It aims to find device dimensions that will meet the required design goals within the defined design space. Two sets of design automation results are presented. In both, the resonant frequencies of each axis and the maximum stress intensity were made state variables that need to be maintained within defined limits. The design objective of the first was to maximise the frequency of the unwanted fourth mode. In the second the design objective was changed to minimising the unwanted distortion of the electrostatic

comb elements. Both designs have all structural elements sharing the same height, this is an improvement on the initial structure design presented in Chapter 5, since it reduces the number of fabrication steps. This is beneficial because additional fabrication complexity generally results in more fabrication imperfections. Both designs are feasible in that they meet the application requirements however the second has an improved suspension beam design that reduces the amount of twisting experienced by the moving comb elements.

Chapter 7 A fabrication proposal for the triaxial angular rate sensor is presented. It consists of three structural polysilicon layers, two sacrificial oxide layers and an electrical isolation layer. The process is based on a commercially available fabrication process, that has been modified to better suit the triaxial angular rate sensor.

Chapters 8 and 9 Presented are the conclusions of this work and the resulting avenues for future research.

Appendix A-F The finite element analysis code for the automated design work is presented along with the results.

Appendix G Earlier research on a novel differential phase angular rate sensor concept is presented as an appendix. It uses a vibrating beam mass structure that traces an elliptical path when subject to rotation due to Coriolis force. Two sensing elements are strategically located to sense a combination of drive and Coriolis vibration to create a phase differential representative of the input rotation rate. A general model is developed describing the device operation. The main advantages of the phase detection scheme are explored, including removing the need to maintain constant drive amplitude, independence of sensing element gain factor and advantageous response shapes. A ratio of device parameters is defined and shown to dictate the device response shape. This ratio can be varied to give an optimally linear phase difference output over a set input range, a high sensitivity around zero input rate or a response shape not seen before, that can give maximum sensitivity around an offset from the zero-rate input. A worked example shows how the developed equations can be used as design tools to achieve a desired response with low sensitivity to variation in device parameters. This concept was found to have some advantageous characteristics, however it is unable to overcome cross stiffness and damping errors and its bandwidth is limited to that of an angular rate sensor operating in open loop mode.

Chapter 2

MEMS Background Information

2.1 Background

Micro Electro Mechanical Systems (MEMS) is a technology that has spawned from the semiconductor industry. MEMS devices are fabricated using much of the same equipment and technology however MEMS specific techniques such as bulk micromachining have also emerged. MEMS devices are characterised by their size. Their features are readily measured in micrometres (μm). Many of their advantages stem from their size. Being small means that MEMS devices can be incorporated into more applications, hand held devices for example. Their small size means very low power consumption and also contributes to their cheap fabrication. Being planar in nature, it takes the same fabrication steps to make a single MEMS device as it does to make hundreds of devices on the same wafer. Therefore the fabrication costs can be split between many devices. Making multiple devices using one set of fabrication steps is referred to as batch fabrication. The number of devices made in each batch is limited by how many devices can fit on the wafer footprint therefore the smaller the device the lower the cost per unit can become.

There are other advantages to being small that may not be immediately apparent. The relative influence of various physical phenomenon on the device behaviour could be quite different in the micro world in comparison with the macro world, depending on how they scale with a change in length. For example material density does not scale with length whereas volume scales by length cubed. Therefore mass moment of inertia ($density \times volume \times length^2$) scales by $length^5$. This means that as the size of a device decreases, the mass moment of inertia diminishes rapidly. This is advantageous for micro motors which are able to reach their top

speed very quickly and micro relays which are able to switch much faster than conventional relays. However this effect also hinders a spinning wheel based micro gyroscope which relies on the momentum of a spinning mass. Additionally friction becomes very significant in the micro world making bearings for the spinning mass, difficult to realise. These examples show that scaled phenomena can be advantageous or disadvantageous depending on the application. It also demonstrates why MEMS angular rate sensors utilise different phenomenon than their macro counterparts.

The cost reduction that batch fabrication offers allows functionality to be added to applications that would have been too costly in the past. For example, modern cars are fitted with many air bags as standard, these are triggered by MEMS accelerometers. It also makes disposable devices feasible, this is beneficial for many biomedical application such as bedside blood analysis devices.

The fact that MEMS devices are fabricated using much of the same processes and technology as integrated circuits leads to an inherent feature of MEMS technology, in that supporting electronic circuits can often be fabricated on the same substrate. This makes them cheaper because they require less fabrication and fewer, if any assembly steps and often result in better performance due to shorter and therefore less noisy interconnections. The basic fabrication techniques used to make MEMS devices are covered in the following section.

2.2 Fabrication Basics

This section gives a very basic overview of the steps involved in MEMS fabrication with particular emphasis on the techniques used in Chapter 7 for the proposed triaxial device design. It covers a basic subset of the tools and techniques available to MEMS fabrication. It should also give an appreciation of why planar design is important. An excellent resource for further MEMS fabrication information is Madou's "Fundamentals of Microfabrication" [50].

2.2.1 Bulk Micromachining

Bulk micromachining is the removal of material from the bulk of the substrate to leave structures such as suspended masses, beams, membranes, trenches and vias to other layers. The material is removed by creating a patterned etch mask layer using photolithography (Section 2.2.5) followed

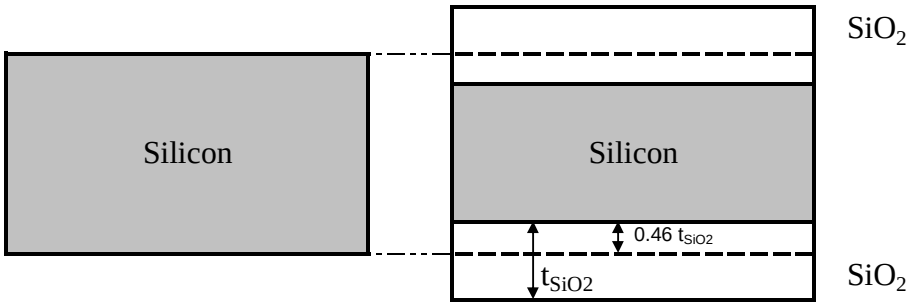

Figure 2.1: Reduction in thickness of the silicon substrate due to the oxidation process, is 0.46 times the thickness of the grown silicon dioxide layer t_{SiO_2}.

by wet etching.

2.2.2 Surface Micromachining

Surface micromachining is the building of structures on a substrate's surface. This is done using a series of deposition, photolithography and etching steps. By depositing structural layers and etching sacrificial areas, free standing structures are achievable.

2.2.3 Deposition

MEMS devices are generally made up of multiple layers of material that are deposited on to a substrate. Areas that are to be etched away are referred to as sacrificial and the areas that remain are referred to as structural. Deposition of material onto a substrate can be achieved in various ways.

Thermal Growth - Silicon Oxidation

Silicon dioxide SiO_2 can be grown by heating a silicon wafer to between $750°C$ and $1200°C$ in dry or wet oxygen/nitrogen mixtures [9].

Growth rates increase with temperature and the additional humidity of wet oxidation yields faster rates than dry oxidation [66]. Other factors can influence growth rates such as crystal orientation, impurities in the oxidizing gas and its pressure and dopant concentrations in the silicon. Growth rates can be further accelerated with the use of a plasma or photon flux during oxidation [50].

The resulting thickness of the silicon substrate is reduced by 46% of the grown SiO_2 thickness due to the silicon substrate's involvement in the reaction [50]. This can be seen in

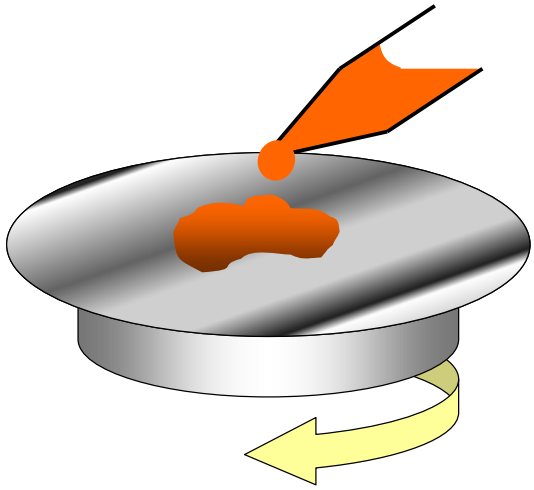

Figure 2.2: Spin coating for deposition of photoresist layers

Figure 2.2.3 adapted from [50].

Spin Coating

Spin coating is normally used to deposit thin $< 2\mu m$ layers of photoresist prior to the lithography process. However layers with orders of magnitude greater thickness are possible depending on the type of photoresist being used.

The substrate sits on a rotating vacuum chuck where the photoresist resin fluid is applied to its surface. This can be seen in Figure 2.2. It is then spun at around $500RPM$ for centrifugal forces to spread the resin before accelerating to between 1500 and $8000RPM$ for between 10 seconds and several minutes to achieve the desired resist thickness [18].

Physical Vapour Deposition (PVD)

The distinguishing feature of PVD is that materials are deposited in a line of sight fashion. This inhibits its ability to achieve a continuous covering over stepped features on the substrate, called shadowing. A good comparison between the two main types, thermal evaporation and sputtering, can be found in Table 2.1. Evaporation involves boiling off the molten source material in a vacuum chamber where the material then condenses on the substrate. Sputtering involves the bombardment of the target (material to be deposited) with argon ions. The collision releases target ions that are attracted to the substrate mounted on the anode of a large power supply of which the target is the cathode.

Property	Evaporation	Sputtering
Rate	Thousands of atomic layers per second (e.g., $0.5\mu m/min$ for Al)	One atomic layer per second
Choice of material	Limited	Almost unlimited
Purity	Better (No gas inclusions, very high vacuum)	Possibility of incorporating impurities (low to medium vacuum range)
Substrate heating	Very low	Unless magnetron enhancement is used, substrate heating can be substantial
Surface damage	Very low; with e-beam evaporation	Ionic bombardment damage
In situ cleaning	Not an option	Easily done with a sputter etch
Alloy compositions, stoichiometry	Little or no control	Alloy composition can be tightly controller
X-ray damage	Only with e-beam evaporation	Radiation and particle damage is possible
Changes in source material	Easy	Expensive
Decomposition of material	High	Low
Scaling-up	Difficult	Good
Uniformity	Difficult	Easy over large areas
Capital equipment	Low cost	More Expensive
Number of depositions	Only one deposition per charge	Many depositions can be carried out per target
Thickness control	Not easy to control	Several controls possible
Adhesion	Often poor	Excellent
Shadowing effects	Large	Small
Film properties (E.g., grain size and step coverage)	Difficult to control	Control by bias, pressure, substrate heat

Table 2.1: Comparison of evaporation and sputtering technologies. (Reproduced from [50].)

Layer	Gases	Temperature ($^{\circ}C$)
Polysilicon	SiH_4	550-700
Silicon nitride	$SiH_2Cl_2 + NH_3$	750-900
	$SiH_4 + NH_3$	700-800
Silicon dioxide undoped	$SiH_4 + O_2$	400-500
PSG (phosphorus doped)	$SiH_4 + O_2 + PH_3$	400-500
BSG (boron doped)	$SiH_4 + O_2 + BCl_3$	400-500
BPSG (phosphorus/boros doped)	$SiH_4 + O_2 + PH_3 + BCl_3$	400-500

Table 2.2: Commonly used gases and temperature ranges for CVD systems. (Taken from [66].)

Chemical Vapour Deposition (CVD)

CVD is used to form thin films on a surface and can achieve very good step coverage. It can be carried out in atmospheric pressure (APCVD) or low pressure (LPCVD). LPCVD gives good deposition coverage over non uniform features, referred to as conformal step coverage.

A volatile vapor/gas precursor reacts chemically, leaving a solid film of material on the surface and byproduct gases that are discarded. Many different films can be deposited. Some common ones are presented in Table 2.2. Plasma discharges are used to enhance the breakdown of gases in plasma-assisted (enhanced) chemical vapor deposition (PACVD, PECVD).

Epitaxal Growth

Epitaxal growth involves deposition of material in which the atoms arrange in a single crystal fashion on another crystalline substrate which acts as a seed layer. This can be achieved with CVD epitaxy or PVD epitaxy also called molecular beam epitaxy (MBE).

2.2.4 Doping

The electrical properties of silicon can be changed by introducing impurity atoms into the silicon crystal lattice. This is called doping. The element providing the impurities is referred to as the dopant. Dopants have either one valence electron more or less than silicon which has four, creating *n-type* or *p-type* doped silicon respectively. The most common dopants are boron (-1), phosphorus (+1), arsenic (+1) and antinomy (+1) [50].

Doping can be achieved in one of the following three ways:

Ion Implantation

Ion implantation is used for doping up to $2\mu m$ depths. It involves firing high energy dopant ions directly into the silicon surface. It has the advantage of being able to fire each ion to a desired depth in the silicon. The ion momentum is absorbed through nuclear collisions which cause crystal damage that reduces the resulting conductivity. This can be repaired by annealing at between $700°C$ and $1000°C$ [50]. Annealing also moves the dopant atoms to sites in place of silicon atoms where they become electrically active [9].

Diffusion

Diffusion is used for doping up to $\sim 10\mu m$ depths. It involves subjecting silicon to an atmosphere containing the desired dopant at temperatures between $800°C$ and $1200°C$ [9].

Epitaxal Growth

The only way to get doped depths larger than $\sim 10\mu m$ is by depositing doped material. This is referred to as "in situ doping".

2.2.5 Photolithography

Photolithography is the transfer of a pattern from a patterned mask to a photoresist layer using light projection and development. This patterned photoresist can then be used as a masking layer for selectively etching material layers beneath it, as a sacrificial layer to eventually leave a space between the layer beneath and the next material to be deposited or left as a structural layer. It can also be used to selectively remove areas of the next layer to be deposited in a technique called Lift-Off [53].

There are other lithography techniques besides photolithography such as X-ray, electron-beam and ion-beam lithography, details of which can be found in [50].

The steps involved in the photolithographic process are wafer cleaning, barrier layer formation, photoresist application, soft baking, mask alignment, exposure and development, and hard-baking [17].

Wafer Cleaning

Wafer cleaning is not a trivial step in the fabrication process. Surface contaminants include particulate matter and organic, ionic, and metallic impurities. They can form on the surface of a wafer during wafer transportation, from humans, from electrostatic charge build up, processing equipment etc. There are many cleaning procedures, the most prevalent being RCA1[1] wet cleaning procedure which removes organic dirt and RCA2[1] wet cleaning procedure which removes metal ions [50].

Barrier Layer Formation

If a patterned silicon dioxide mask is required for doping or etching of the silicon substrate then a thin layer of SiO_2 is thermally grown at this stage as described in Section 2.2.3.

Photoresist Application

A layer of photoresist is applied to the surface of the substrate using the spin coating deposition technique described in Section 2.2.3. There are two groups of photoresist, positive and negative. Positive photoresists are weakened by exposure to Ultra Violet (UV) light and subsequently are removed during the developing stage. Negative photoresists are strengthened by exposure to UV light and subsequently the unexposed areas are removed during the development stage. Sensitisers in the photoresist control the chemical reaction when exposed to UV light.

Soft Baking

After spin coating the wafer is soft baked for $\sim$10 minutes at between $75-100^{\circ}C$ to remove any trace of solvent from the photoresist, improve the adhesion to the wafer and remove any internal stresses [50]. Over soft-baking can destroy the sensitiser in the photoresist and under soft-baking will inhibit the UV light from reaching the sensitiser in the photoresist [17].

Mask Alignment and Exposure

A mask can be thought of as a stencil for UV light. They are usually made of glass or quartz and patterned with chromium. A mask aligner is used to align the patterned mask with the

[1] RCA is the name of the company that developed the cleaning procedures.

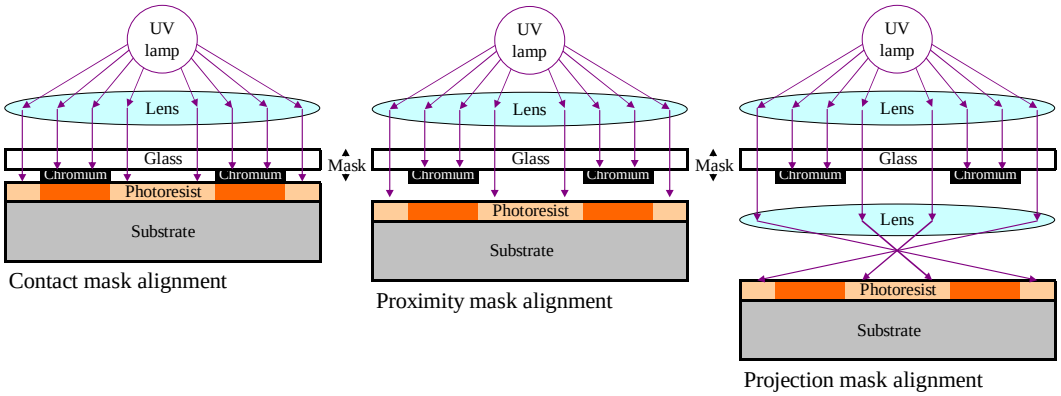

Figure 2.3: Contact, proximity and projection mask alignment systems.

wafer. It is aligned with either a straight edge of the wafer or to existing alignment marks on the wafer surface from previous photolithographic processing. The mask can be in direct contact with the photoresist layer in close proximity or aligned further from the photoresist layer with the pattern being transferred using a series of lenses. These three mask alignment systems can be seen in Figure 2.3.

Once the mask is aligned it is exposed to UV light for a calculated period of time. This duration is based on the intensity of the light source in the exposure system being used and the dose of light energy required by the photoresist.

Development

The exposed (positive photoresist) or unexposed (negative photoresist) is removed from the wafer during the development process. The two main techniques are immersion and spray developing. Immersion developing involves immersing the wafers in a developer and agitating. Spray developing involves spraying fresh developer over the surface using a fan-type sprayer [50].

Hard-Baking

Hard-baking is the final step in the photolithographic process. This step is necessary in order to harden the photoresist making it more resistant to further etching steps and to improve adhesion of the photoresist to the wafer surface.

2.2.6 Etching

Dry Etching

Dry etching uses a combination of physical and chemical processes. It is performed in a weakly ionised plasma at low pressure. The physical etching is a result of the ion bombardment which is anisotropic in nature and the chemical etching is isotropic in nature and has better etch rate selectivity among materials. This means that it will etch the masking layer more slowly than the material intending to be etched. The physical process is less selective. Generally surface micromachining uses dry etching techniques.

Wet Etching

Wet etching uses liquid etchants to remove material. The etchant can be anisotropic, where the etch rates are dependant on the orientation of the crystal planes being etched, or it can be isotropic, where the etch rate is independent of crystal planes. Most anisotropic etching is based on silicon substrates given that its etching behaviour is well known, it is mechanically stable and is suitable for making electronic components such as piezoresistive elements and transistors by selective doping (See Section 2.3.1).

Careful mask design is necessary in anisotropic etching, giving consideration to crystal lattice orientation and crystal plane etch rates. This is especially important around corner features where corner compensation patterns on the mask are required to minimise the difference between the desired structure shape and what is etched. Generally convex corners will be over-etched and concave corners will become under-etched. There has been much work done on convex corner compensation mask patterns [84] [46], in which additional mask areas are included around the corners and whose shapes are calculated so that they etch away to the desired corner just at the end of the etching period. Convex corners however are more difficult. Work by [39] uses clever mask patterns that utilise the different crystal plane etch rates to introduce delays before the etching begins deep in the corner. This greatly reduces the residual flanges

2.3 Sensing and Actuation Elements

There are some physical phenomena that are relatively negligible in the macro world that become significant in the micro world. This is due to the effects of scaling length dependent parameters.

These phenomena are often utilised for sensing and actuation elements. Conversely there are sensing and actuation mechanisms that exist in the macro world that do not translate well into the micro world due the effects of scaling. They may also be inherently complex and beyond the physical limitations of MEMS technology.

The sensing and actuation elements covered in this section are those that are used most often in MEMS inertial sensor applications.

2.3.1 Sensing Elements

Piezoresistive

Piezoresistivity refers to a change in electrical resistance with an applied pressure. All materials have some piezoresistivity however it is more prevalent in materials such as monocrystalline silicon. Piezoresistivity in semiconductor materials is a result of reduced mass and mobility of charge carriers due to the applied stress [50].

Piezoresistor elements are usually situated on areas of the device structure that experience high stress when the phenomenon to be measured occurs. This may be on the surface of a mass beam support of an inertial sensor or on the outer edge of a pressure senor diaphragm.

The change in resistivity can be expressed as

$$\frac{\Delta R}{R} = \sigma_l \pi_l + \sigma_t \pi_t \tag{2.1}$$

where σ_l and σ_t are the stresses and π_l and π_t are the piezoresistance coefficients in the respective longitudinal and transverse directions with respect to the current flow. This is taken from [50], where typical values for piezoresistance coefficients can be found.

Although piezoresistive sensors have a high sensitivity to strain variation, they are also highly sensitive to variations in temperature. Additional circuitry is required to compensate for this. One solution is to use a reference temperature sensor consisting of an always unstressed piezoresistive element.

Piezoresistive sensing also has a low sensitivity to wiring parasitics, which can be a major problem with capacitive sensing schemes. Therefore piezoresistive sensing is suitable for applications where the sensing element is physically separate from the sensing circuitry.

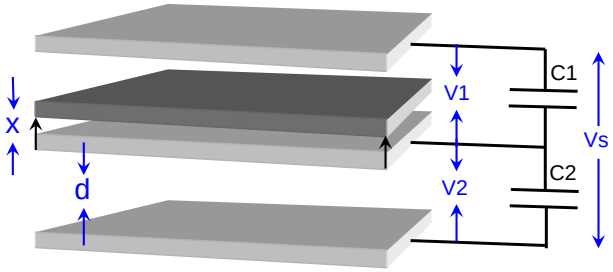

Figure 2.4: Differential capacitive sensing. (Adapted from [9])

Capacitive

Capacitive sensing uses either a change in area or a change in capacitive gap to vary the measured capacitance between parallel electrodes. Most capacitive sensing configurations vary the gap d however it is also possible to change the area $l \times w$ using a comb or sliding plate type setup. These configurations have been shown to be an order of magnitude less sensitive than ones that vary d [60]. Generally horizontal parallel plates are used to measure motion out of the substrate (z axis) plane while vertical parallel fingers are used to measure motion in the substrate plane (x, y axes).

Ignoring fringing effects, the capacitance between two parallel plates or fingers is given by

$$C = \varepsilon_0 \varepsilon_r \frac{lw}{d} \tag{2.2}$$

Where ε_0 is the permittivity of free space, ε_r is the relative permittivity of the material between the electrodes, lw is the overlapping area between the electrodes and d is the gap between them.

Equation (2.2) shows that the relationship between C and d is nonlinear. To linearise the output, a differential sensing arrangement can be used. This can be seen in Figure 2.4 where the capacitance is increased between the common and the top electrode and decreased between the common and the bottom electrode. Now the output of the device has a linear relationship with displacement

$$(V_2 - V_1) = V_s \left(\frac{x}{d_0} \right) \tag{2.3}$$

Where x is the displacement and d_0 is the nominal gap [9].

Capacitive sensing is very sensitive to parasitic capacitances caused by the substrate itself and also by interconnect wiring to the capacitive sensing circuitry. These can be reduced by incorporating shielding layers for the substrate and by integrating the capacitive sensing circuitry

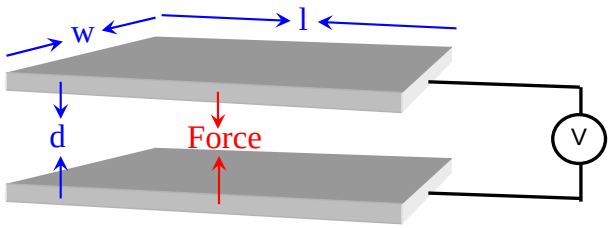

Figure 2.5: A simple parallel plate electrostatic actuator. (Adapted from [9])

in close proximity to the capacitive elements preferably fabricated on the same substrate.

Normally two synchronised oscillating signals are fed to the top and bottom electrode and the output signal is taken from the centre, moving electrode. This signal is then fed to an sensing circuit that can be configured to measure either displacement or velocity. Section 5.2.2 describes an alternative approach that uses a common signal applied to the centre electrode where the top and bottom electrodes are connected to the input of a differential amplifier. This is more convenient for devices that require motion to be sensed in more than one axis.

2.3.2 Actuation Elements

Electrostatic

Electrostatic actuation is based on the attractive force that two electrodes with opposite charges have on each other. Looking at Figure 2.5 the capacitive energy W stored in the system is equal to

$$W = \frac{1}{2}CV^2 = \frac{\varepsilon_0 \varepsilon_r lwV^2}{2d} \tag{2.4}$$

Where l is the length and w is the width of the electrostatic electrode area and the symbols are consistent with section 2.3.1. Therefore the attractive force becomes the capacitive energy differentiated with respect to the gap as

$$F = \frac{\partial W}{\partial d} = \frac{\varepsilon_0 \varepsilon_r lwV^2}{2d^2} \tag{2.5}$$

This shows that the resulting force has a non-linear relationship with both the applied voltage and also the size of the gap. Having two stationary electrodes, one above and one below the common moving electrode, helps to reduce this nonlinearity.

Electrostatic combs, however, provide a constant force displacement relationship. In

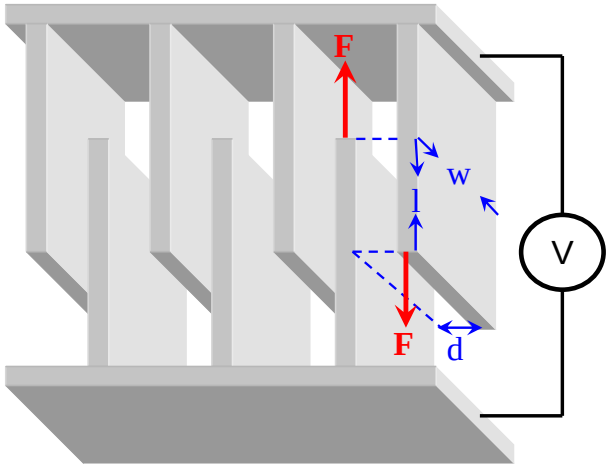

Figure 2.6: An electrostatic comb actuator.

this case the capacitive energy is differentiated with respect to the length of the electrostatic electrode surface.

$$F = \frac{\partial W}{\partial l} = \frac{\varepsilon_0 \varepsilon_r w V^2}{2d} \tag{2.6}$$

This shows that the F is independent of l. The above equation describes the force created by each gap and needs to be multiplied by the number of gaps in the comb actuator element.

Piezoelectric

Some classes of crystal produce an electric charge when they experience an applied stress. In these materials the opposite is also true; they deform in response to an applied electric field. This effect is reliant on the asymmetric charge in the crystal structure [9]. Silicon has a symmetric crystal structure and as such is not a piezoelectric material. However quartz, zinc oxide, polyvinylidine difluoride (PVDF), lead zirconate titanate (PZT) and lithium niobate are all piezoelectric materials and are commonly used in MEMS. Depending on the material they can be deposited onto silicon using spin coating, sputtering, screen-printing, and sol-gel [79] deposition techniques.

Piezoelectric actuators require relatively large voltages to achieve micron range displacements and therefore are generally utilised for sub-nanometre applications such as surface acoustic wave (SAW) devices. The structure can be made to have greater displacement through mechanical amplification. As an example if PZT was used as a surface layer along the length of a cantilever beam, then a small change in the surface length will create a significant displacement

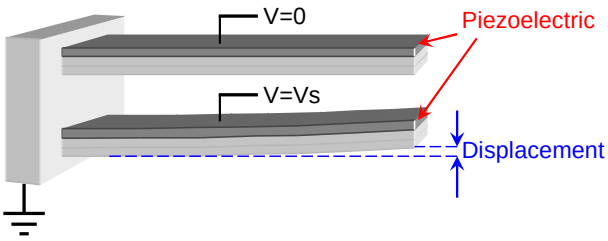

Figure 2.7: A simple cantilever beam with a surface layer of piezoelectric material showing how mechanical amplification can increase displacements.

of the cantilever beam end. This can be seen in Figure 2.7.

Using piezoelectric as an actuation (or sensing) element sets a limitation on operating temperature, since it loses its piezoelectric properties if it is heated above the Curie point. As an example the Curie point of PZT is $195°C$.

2.4 Application of Control to MEMS

Control refers to forcing a system to behave in a desired manner. The integration of control systems and MEMS is becoming more common. This is not surprising given that very large scale integration (VLSI) logic circuits can be fabricated on the same substrate as the mechanical elements and the range of benefits that this integration can offer. The roles that control plays in MEMS is varied, some of these include:

- providing precise control over MEMS actuation elements such as electrostatic plates.
- improving response time and device input range and accuracy through force-feedback schemes.
- provide real-time estimates of the unknown parameters of a system.
- compensation for the effects of fabrication imperfections.
- compensation for time varying effects such as the effect of temperature on resonant frequencies.

Various control approaches exist; the following gives an overview of the main approaches and examples of how they have been utilised for MEMS applications.

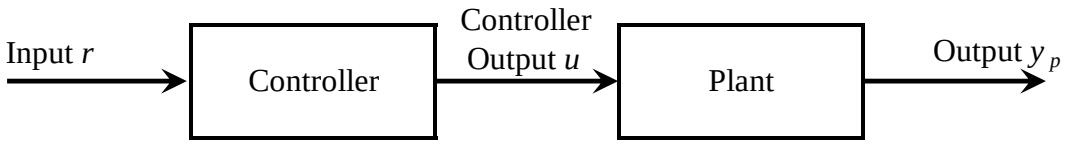

Figure 2.8: Open-loop control system

2.4.1 Open-loop Control

An open-loop controller controls a process directly to produce a desired output. It employs no feedback mechanism therefore the system output has no effect on the input. It requires an accurate knowledge of the plant dynamics to produce the correct control output u to achieve a desirable plant output y_p.

Systems that operate in open-loop mode are not robust to changes in the device dynamics and often have small bandwidths due to the increased time required for the physical phenomena to reach steady state. These devices may also require calibration steps to compensate for variations from one device to the next.

Many MEMS devices are controlled in open-loop mode such as the frequency-tunable film bulk acoustic resonator (FBAR) device presented by Pan *et al* [57] and the resonant suspension beam filter presented by Piekarski *et al* [63].

Passive sensor devices can also be considered as operating in open-loop with no control input. Two typical examples being a pressure sensor presented by Cho *et al* [16] whose output is simply a measure of a deflected capacitive diaphragm and a MEMS accelerometer presented by Selvakumar *et al* whose output is the capacitively sensed displacement of a proof mass caused by acceleration. Both devices employ no feedback mechanism.

2.4.2 Feedback Control

Feedback control creates a closed-loop from the measured plant output y_p back to the controller input. This feedback loop enables the controller to adjust its output until the desired plant output is achieved (when $r - y_p = 0$). A real-world example of this is thermostat temperature control which allows more heat into a system when the system temperature is below a set point and stops heat from reaching the system when the system temperature is above a set point.

A comparison of the performance and benefits between open and closed-loop control for electrostatic comb drives is given by Borovic [10], in which optical measurement of the displaced

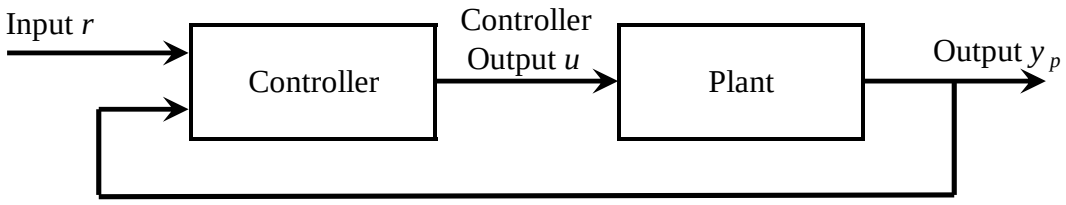

Figure 2.9: Feedback control system

comb drive was used in the feedback loop.

A force balanced pressure sensor presented by Gogoi *et al* [23] used capacitive sensing to measure the deflection of a MEMS pressure sensor diaphragm. This signal is then used in a simple feedback controller which uses an electrostatic actuator to null the diaphragms position, counteracting the effect of the external pressure force. The output of the device is taken at the feedback controller output. Similar MEMS pressure sensors presented by both Yeh *et al* [15] and Kenny *et al* [29] used a simple operational amplifier feedback circuit to control the distance between the pressure diaphragm and the tunneling tip using electrostatic actuation. This allowed the device to have sub-Å sensitivity and wide bandwidths.

2.4.3 Proportional Integral Derivative (PID) Control

The most common type of feedback controller is the PID controller. PID controllers have been used for many years to give good performance for a wide variety of process control applications, including motor speed control, precision positioning and temperature control. PID control has also been adopted for use in MEMS applications. Wang *et al* [78] has employed PID control to control the stroke length of MEMS resonator using optical measurement and electrostatic comb drive actuation. Song *et al* [73] and Cai *et al* [12] both used PID control for the tilt angle of their micro-mirrors for optical network switching.

The input to a PID controller is the error e between the measured system output y_p and a reference set-point value r. The output of a PID controller u consists of the sum of the error's proportional e, integral $\int edt$ and derivative $\frac{de}{dt}$ terms, each with an adjustable gain, K_p, K_i and K_d respectfully.

$$u = K_p e + K_i \int edt + K_d \frac{de}{dt} \tag{2.7}$$

In general PID controllers can be tuned to give more accurate and stable control than simpler control algorithms.

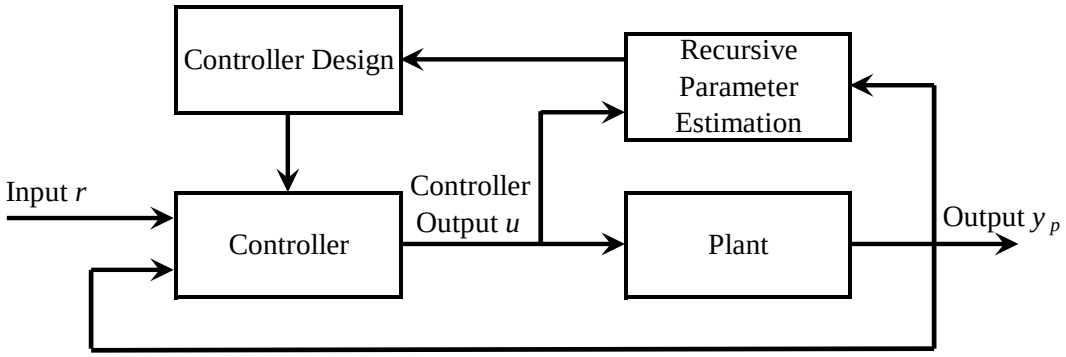

Figure 2.10: Self-tuning regulator (STR) system diagram

2.4.4 Adaptive Control

Adaptive control systems can be characterised by having the three following functions [14]:

1. Identification of unknown parameters or measurement of an index of performance.
2. Decision on the control strategy.
3. On-line modification of the parameters of the controller or the input signal.

There are two main categories of adaptive control: model reference adaptive control (MRAC) and self-tuning regulators (STR).

Self-Tuning Regulators

STR systems consist of a feedback controller whose parameters are adjusted by a recursive estimator via a control design algorithm. Any conventional feedback controller may be used such as a PID or dead-beat controller. Similarly any recursive estimator scheme may be used such as least squares or stochastic approximation.

Pantazi *et al* [58] used a STR with a linear quadratic gaussian (LQG) estimator for the precise positioning of a scanning probe for a polymer-based mass storage device and found its performance to be better, compared to a PID controller.

Model Reference Adaptive Control

MRAC systems use an ideal model of the plant which is subject to the same inputs as the real plant. The aim of a MRAC system is for error between the output of the unknown plant and that of the model reference to approach zero. The adaptation mechanism uses this error to modify

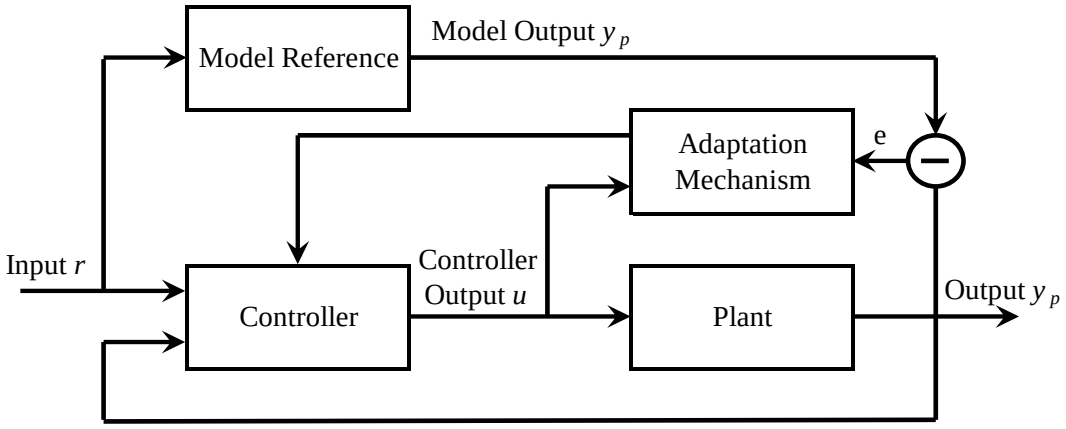

Figure 2.11: Model reference adaptive control (MRAC) system diagram

the controller parameters. If the controller parameters are modified directly then the system is referred to as direct whereas an indirect MRAC system uses the adaptation mechanism to update estimates of the plant parameters which are then used in the plant controller. Although direct and indirect MRAC systems give equivalent performance, the plant parameter estimates of an indirect system provide additional information about the plant.

The two common design approaches for MRAC systems are the MIT rule and the Lyapunov approach.

The MIT rule, first proposed for aircraft control, is based on minimising the integral of the squared error between the output of the reference model and the output of the plant. The adaptation mechanism updates the controller parameters based on the change in this error with respect to the change in the adjustable controller parameters. The MIT rule was popular because of its simplicity, however has been shown by Parks [62] to be unstable for certain types of input signals and higher-order systems are difficult to analyse.

The Lyapunov design approach is based on Lyapunov second method which shows that a system will reach a stable equilibrium point if a measure of the energy in the system is decreasing. This design method overcomes one disadvantages of the MIT rule in that it is inherently globally asymptotically stable. The Lyapunov approach involves finding a differential equation that describes the error between the output of the reference model and that of the plant. The objective then becomes finding the adaptation laws that will make this equation stable. To do so a positive-definite Lyapunov function for the error equation is formulated, and adaptation laws are selected so as to make the first derivative of this Lyapunov function

negative-definite.

2.4.5 Intelligent Control

Intelligent control covers techniques such as neural networks, machine learning and genetic algorithms. Although it is rarely used for control of MEMS, MEMS devices often form the sensory inputs to these types of control systems. Fuzzy logic controllers have been used for car stabilisation control, whose input comes from MEMS acceleromters and angular rate sensors as well as driver input such as throttle position. Pedestrian navigation applications have used Kalman filtering for fusion of GPS, magnetic compass and MEMS angular rate sensor data [38, 76]. These control approaches compensates for long term drift rates of MEMS angular rate sensors and the short tern inaccuracy of magnetic compass and GPS systems.

2.4.6 Averaging Analysis

The average behaviour of a systems containing both fast and slow (mixed) dynamics, can be analysed using averaging analysis. It can be used to analyse the stability of a system and is a powerful approximation tool for determining the averaged convergence rates of parameter estimates and system errors. Averaging analysis involves equating the real system equations with averaged ones. Section 4.8.1 gives a thorough treatment of averaging analysis and its application to the adaptively controlled triaxial angular rate sensor system. A good reference for averaging analysis techniques is by Sastry [67].

2.5 Design Tools

Batch fabricating MEMS devices is a relatively cheap exercise as it is possible to produce hundreds of devices on a single wafer using the same processing steps that would be needed to fabricate a single device. The converse is also true, fabricating one-off MEMS devices is an expensive exercise. For this reason it is desirable to keep the number of devices built during the prototyping phase to a minimum. Using simulation tools is crucial in achieving this. It allows design parameters to be varied and optimised prior to fabrication.

The batch fabrication aspect of MEMS can be utilised in the prototyping phase by fabricating a number of devices with slightly different dimensions on the substrate simultaneously.

However this step should still follow thorough system level and finite element modeling.

2.5.1 System Level

Also referred to as lumped parameter, reduced order or behavioural modeling. System level modeling uses differential and non-linear equations to represent a system in order to predict its behaviour. It can be used to simulate and analyse complex control systems and is useful for identifying how system parameters interact.

Matlab[2] is a powerful and widely used tool and can be used for simulating system level models. It's Simulink toolbox is a visual model implementation tool that uses functional blocks whose inputs and outputs are joined together to form a visual system block diagram that can be simulated in the time domain. The system outputs can be observed on virtual scopes or exported to the Matlab workspace for further processing.

2.5.2 Finite Element Analysis (FEA)

FEA is a very powerful numerical technique for boundary value problems that was originally developed for stress and displacement analysis for mechanical structures. However, FEA has been developed further, enabling it to also be used for modeling a system's mechanical, electrical, electrostatic, electromagnetic, thermal, fluidic and magnetic properties. FEA is most useful when hand calculations cannot provide accurate results. This is often the case for complex geometries or processes.

FEA involves building a geometric model of the system and breaking it into many finite parts called elements. Each element is joined to its neighbour via shared nodes. The collection of elements and nodes is called a mesh and forms the finite element model (FEM). The finer the mesh is, the more accurate the resulting numerical approximation will be. Boundary conditions such as displacement, force and voltage are then applied to parts of the model. Equations are then set up for each element resulting in a system of simultaneous equations that are solved using a combination of linear algebra or nonlinear numerical techniques.

The software package that was used for all the FEA for this work was ANSYS[3]. It is able to perform multi-physics simulation to couple together more than one of the above effects. For

[2] www.mathworks.com
[3] www.ansys.com

example two differently charged plates in close proximity will create an attractive force due to electrostatic effects. This force can then be coupled to the structure to measure the maximum mechanical stress and deflection it causes on the structure. ANSYS also contains a collection of design optimisation tools that have been utilised in Chapter 6.

Chapter 3

Angular Rate Sensors

Angular rate sensors measure the rotation of the device in inertial space in one, two or three perpendicular axes.

There are several important measures of performance for angular rate sensors including resolution, scale factor, drift, and zero-rate output (ZRO). In the absence of rotation, the output signal is a the sum of white noise and a slowly varying function. The white noise defines the resolution, also called angle random walk, and is expressed in terms of the standard deviation of equivalent rotation rate per square root of bandwidth of detection in $deg/s/\sqrt{Hz}$ or $deg/h/\sqrt{Hz}$ or simply $deg/\sqrt{h}$. The slowly varying function represents the long and short term drift measured in deg/s or deg/h. Scale factor is defined as the amount of change in the output signal per unit change of rotation rate and is expressed in V/deg/s. The ZRO measure represents the output of the device when it is subject to no rotation. [83]

Angular rate sensors can be categorised into three different grades based on their performance requirements: rate; tactical; and inertial. The performance measures of each are summarised in Table 3.1.

Parameter	Rate Grade	Tactical Grade	Inertial Grade
Angle Random Walk, $deg/\sqrt{h}$	> 0.5	0.5-0.05	< 0.001
Bias Drift, deg/h	10-1000	0.1-10	< 0.01
Scale Factor Accuracy, %	0.1-1	0.01-0.1	< 0.001
Full Scale Range, deg/s	$50 - 1000$	> 500	> 400
Max Shock in 1ms, g's	10^3	$10^3 - 10^4$	10^3
Bandwidth, Hz	> 70	~ 100	~ 100

Table 3.1: Performance requirements for different classes of angular rate sensors. [83]

3.1 Conventional (Macro) Angular Rate Sensors

Prior to the emergence of the MEMS angular rate sensors, the conventional devices for measuring angular rate were the spinning mass gyroscope, the ring laser gyroscope (RLG) and the fibre optic gyroscope (FOG).

3.1.1 Spinning Mass Gyroscopes

When a wheel is spun at high speed it tends to maintain its orientation with respect to inertial space. This is called the gyroscopic effect and it is caused by conservation of angular momentum. Spinning mass gyroscopes consist of a spinning mass, mounted on a gimballed platform that allows it freedom of motion. Sensors on the gimbal axes show the orientation of the spinning mass with respect to the device casing which, because of the gyroscopic effect, is representative of the rotation of the device with respect to inertial space. The mechanical coupling of the gimbal and the bearings create many errors causing the orientation of the spinning axis to drift. This problem lead to the axes being constrained by springs, with the tension in the springs now being proportional to the angular rate. These devices are called rate-gyroscopes.

Both gyroscopes and rate-gyroscopes have mechanical elements that introduce errors, such as the friction in the bearings and any imbalance in the mass. To compensate for these, feedback control strategies have been developed [11, 13, 54].

Spinning mass gyroscopes are large in size and because of the disadvantageous scaling of mass moment of inertia and friction, miniaturisation becomes problematic. The size and cost of spinning mass gyroscopes generally limits their uses to large scale air, sea and space applications.

3.1.2 Ring Laser Gyroscopes RLG and Fibre Optic Gyroscopes FOG

RLGs and FOGs measure angular rate by firing pulses of laser light in opposite directions along a polished glass ring, mirrored path or optical fibre. The induced rotation acts to shorten the path in one direction while lengthening it in the opposite direction, this results in an interference pattern, from which angular rate can be inferred [49]. This is called the Sagnac effect, first discovered by Frenchman G. Sagnac in 1913.

RLGs remain the most accurate angular rate sensors and have advantages over spinning mass gyroscopes given that they have no moving parts and do not physically resist rotation.

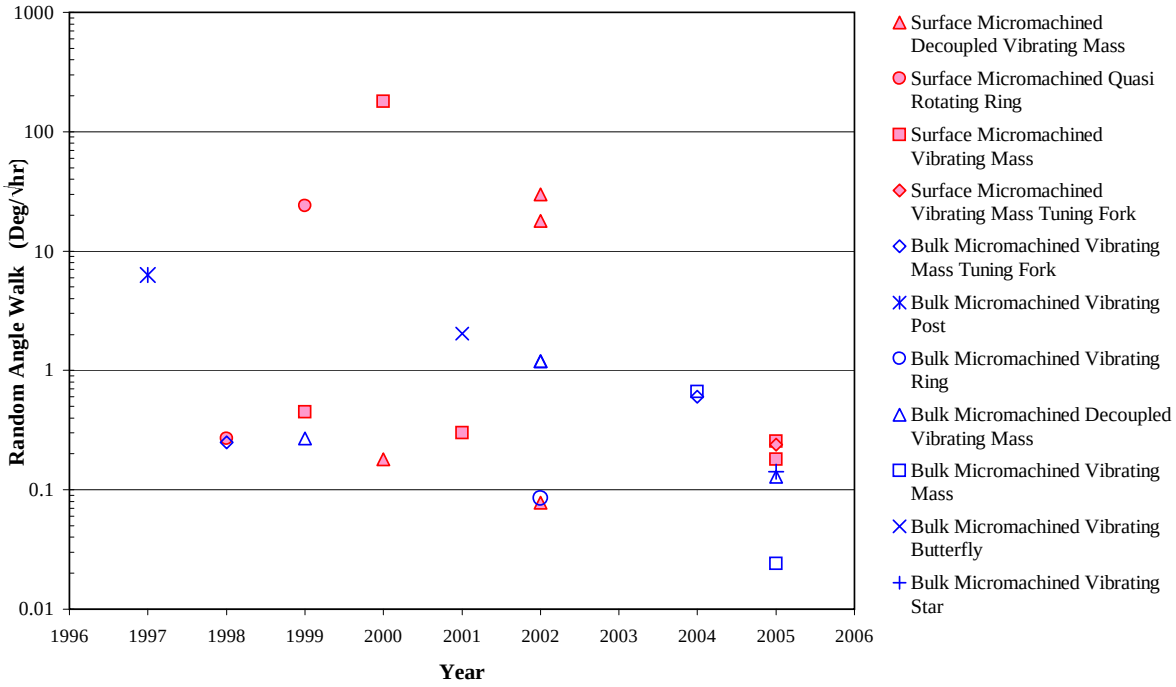

Figure 3.1: Recent performance of MEMS angular rate sensors in terms of random angle walk

However they are again too large and costly for many emerging applications.

3.2 MEMS Angular Rate Sensors

Since shortly after the realisation the first MEMS accelerometers in the late 1980's, much research effort has gone into MEMS angular rate sensing.

A thorough review of MEMS angular rate sensing up to 1998 is given by Yazdi, Ayazi and Najafi in [83] who found that bulk micromachined devices performed better than surface micromachined devices and that the performance of MEMS angular rate sensors had improved by an order of magnitude every two years. Reviewing MEMS angular rate sensing since 1998 has found continuing performance improvement however its rate has slowed. What is interesting is the closing of the previous gap in performance between that of surface and bulk micromachined devices and that no single sensing configuration is consistently outperforming the others. This can be seen in Figure 3.1, which shows the random angle walk performance of a sample of MEMS angular rate sensors. This figure forms a continuation of Figure 17 in [83].

While there are many different structural configurations that have been used for MEMS angular rate sensing including vibratory masses, rings, stars, tuning forks, posts, beams and

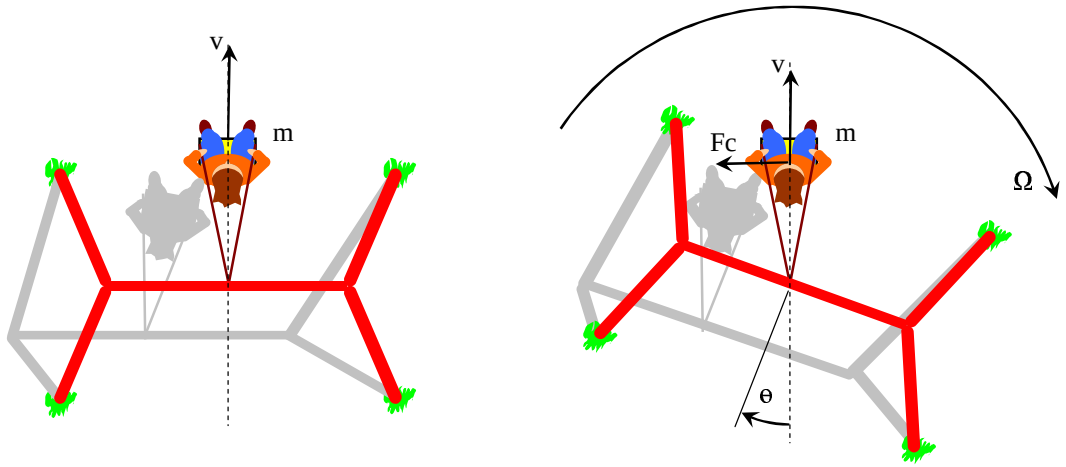

Figure 3.2: Coriolis effect shown on a playground swing set looking from above. This shows how angular displacement θ sensors operate. Note that F_c only appears with respect to the frame of reference of the rotating swing set.

butterflies, they all operate using the same basic principle. The structure is driven into oscillation in a primary mode of vibration and when the device is subjected to an angular rate, energy from the primary mode is transferred to a secondary mode causing it to oscillate. This transfer of energy to the secondary mode is due to the Coriolis effect and is indicative of the angular rate input.

3.2.1 The Coriolis Effect

All vibratory mass angular rate sensors utilise the Coriolis effect. Coriolis force is named after the French scientist and engineer G.G. de Coriolis (1792-1843) and can be explained with an everyday analogy. Imagine the child in Figure 3.2 swinging on a playground swing with velocity v. If the swing frame were to rotate around its base with a rotation rate of Ω, the child will continue to swing in the same path with respect to inertial space. However, with respect to the rotating swing set, the child's motion appears to shift as if being acted upon by force perpendicular to the child's motion. This apparent force is called Coriolis force F_C. Coriolis force appears in the rotating frame of reference, in this case the swing set frame of reference and is given by

$$F_C = -2m\Omega \times v \tag{3.1}$$

Where m is the mass of the body, Ω is the rotation rate that the mass is subject to and v is the velocity with which it is moving from the axis of rotation.

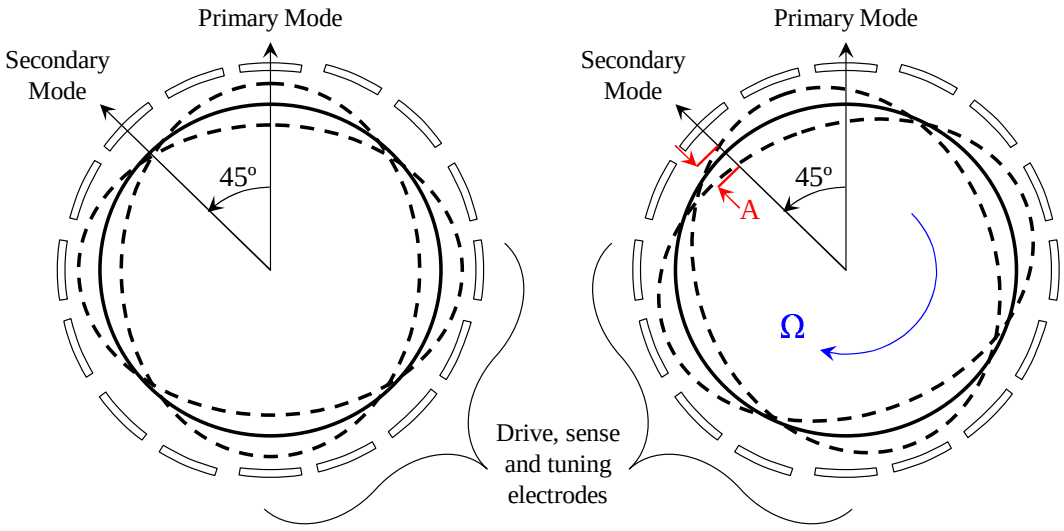

Figure 3.3: Vibratory ring angular rate sensor diagram showing the amplitude of vibration A in the second mode caused by a transfer of energy from the first mode through the applied angular rate Ω

The angular displacement θ can be inferred by measuring the angle of the child's oscillation axis with respect to the swing. This is the principle that Foucault's pendulum works on and all the devices covered in Section 3.4.7 utilise.

3.3 MEMS Vibrating Ring Angular Rate Sensors

This group of angular rate sensors operate using a method first proposed by Newton [54] in which a supported ring of material is driven into its primary mode of vibration causing the ring to form alternating perpendicular ellipses. When subject to a rotation, a transfer of energy occurs, through the Coriolis effect, from the primary mode to the secondary mode of oscillation which is aligned at 45° from the primary mode, as shown in Figure 3.3. The amplitude of vibration in the secondary mode is proportional to the angular rate the device is being subjected to.

Vibrating ring angular rate sensors are less sensitive to environmental vibrations than other sensor configurations and output errors only occur when there is an asymmetry in stiffness or mass. Being a symmetric device, the primary and secondary modes have equal resonant frequencies, varying only with fabrication imperfections. This leads to a device with sensitivity amplified by the quality factor of the device. The effects of temperature on both modes are equal and any mismatch in resonant frequencies between modes can be electronically compensated using the tuning electrodes located around the perimeter of the device. The small

ring mass and small sensing capacitances pose challenges for the vibratory ring devices [24] and temperature dependence issues have been reported due to the capacitive gap between the ring and the electrodes altering because of the different expansion rates between the electrode's substrate. [7]

In 1998, Ayazi and Najafi presented a micromachined vibrating ring angular rate sensor, which used bulk micromachining to fabricate a $35\mu m$ thick polysilicon ring supported by symmetric beams to the centre of the ring, surrounded by 16 electrostatic drive and sense electrodes. The resonant frequency was $\sim 36kHz$ and the projected resolution (random angle walk) was estimated at $0.05deg/\sqrt{hr}$ [6]. Later they fabricated a $80\mu m$ thick ring with electronic tuning to compensate for mismatched resonant frequencies between the two modes caused by fabrication imperfections [7]. The measured resolution was $60deg/\sqrt{hr}$ which is significantly worse than that proposed in [6], this was due to parasitic capacitances between the structure and the external sensing electronics. A silicon-on-glass (SOG) implementation by He and Najafi [24] reduced the parasitic capacitances significantly because of the insulating substrate and achieved a resolution of $10.4deg/\sqrt{hr}$.

Recently a novel device with a resonating star structure has been presented by Zaman, Sharma, Amini and Ayazi. Its shape is that of two merged squares at 45° to one another creating an eight pointed star and it operates in the same manner as the vibratory ring devices. The anisotropic nature of the single crystal silicon structure caused a 3.6kHz frequency mismatch between the resonant modes which was impossible to electrostatically tune. However higher order resonant modes were found to be within a 1kHz mismatch making electrostatic tuning feasible. The high Q factor of the device enabled a resolution of $0.14deg/\sqrt{hr}$ with a projected resolution of $0.017deg/\sqrt{hr}$ with future improvements.

3.4 Vibratory Mass Angular Rate Sensor

The simplest of vibratory angular rate sensors is shown in Figure 3.6. The physical structure consists of a two degree of freedom (DOF) spring mass damper system. The proof mass is driven into oscillation in one axis and the mass's displacement is sensed in a perpendicular axis [31]. This perpendicular vibration is caused by a transfer of energy from the primary to the secondary vibration mode, through rotation induced Coriolis force acting on the mass. The

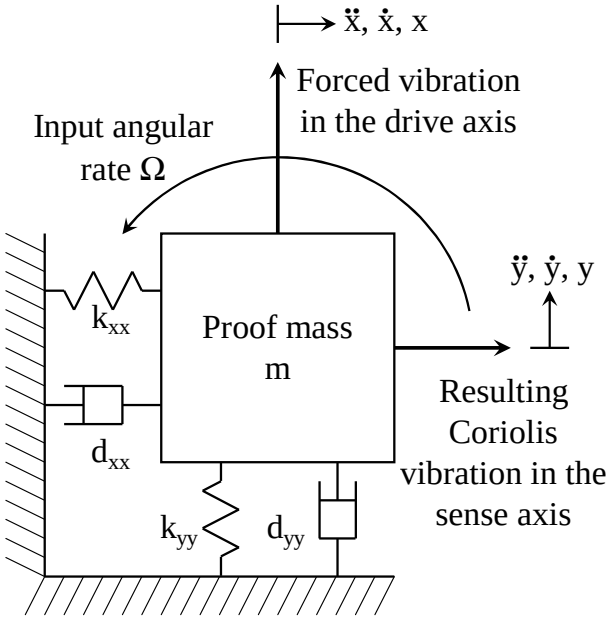

Figure 3.4: Basic angular rate sensor operation showing the two degree of freedom spring, mass, damper system

sensor operation is shown for a typical angular rate sensor in the series of plots in Figure 3.5(a). They show the drive axis displacement, the angular rate input and the resulting sensing axis motion. The combined drive and sense axis displacements are shown in Figure 3.5(b). Typically for MEMS devices the motion in the sense axis is orders of magnitude smaller than that of the drive axis.

3.4.1 Ideal Model

The drive (y) axis of this system can be represented as

$$F_d \sin(\omega t) = m\ddot{y} + d_{yy}\dot{y} + k_{yy}y + 2m\Omega_z\dot{x} \tag{3.2}$$

The Coriolis effect on the drive axis is negligible since the sense axis velocity is so small, therefore

$$F_d \sin(\omega t) = m\ddot{y} + d_{yy}\dot{y} + k_{yy}y \tag{3.3}$$

and the y axis displacement becomes

$$y = Y_0 \sin(\omega t - \phi_y) \tag{3.4}$$

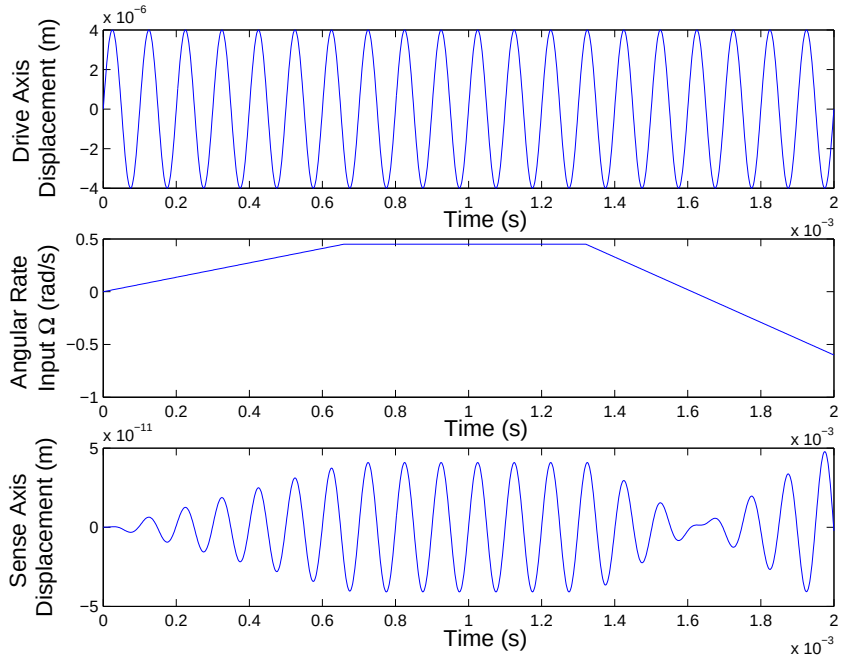

(a) Plot showing the mass's constant amplitude drive axis displacement, the time varying input rotation and the resulting amplitude modulated sense axis displacement.

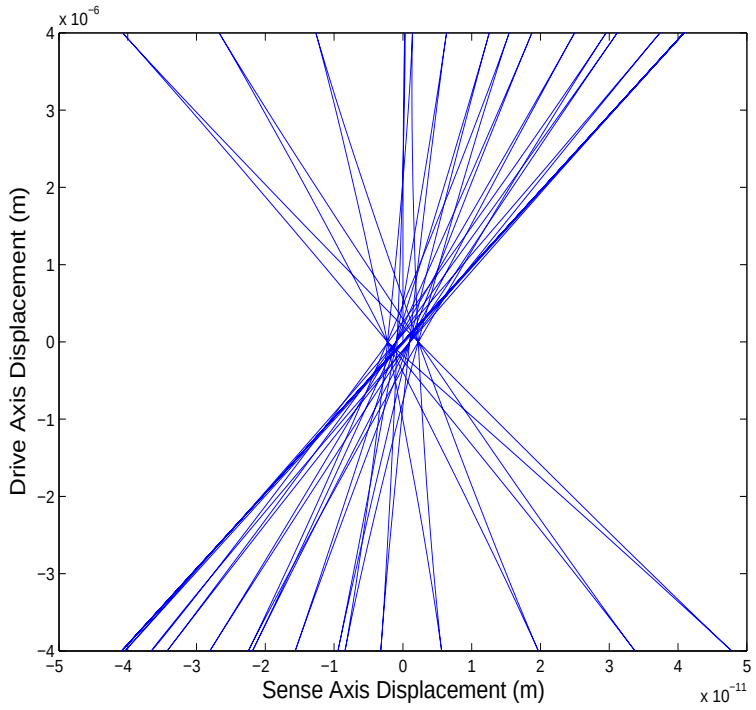

(b) Proof mass displacement trajectory corresponding to the angular rate input of Figure 3.5(a). The plot shows the orders of magnitude difference between the mass drive axis displacement and that of the sense axis caused by Coriolis force.

Figure 3.5: Open loop angular rate sensor operation for a typical sensor with matched resonant frequencies of 10kHz and drive amplitude of $4\mu m$.

with

$$Y_0 = \frac{F_d}{\sqrt{d_{yy}^2\omega + (m\omega^2 - k_{yy})}} \tag{3.5}$$

$$\phi_y = \arctan\left(\frac{m\omega^2 - k_{yy}}{d_{yy}\omega}\right) \tag{3.6}$$

This shows that the least amount of driving force is required when $\frac{Y_0}{F_d}$ is maximised, i.e. at resonance $\omega = \sqrt{\frac{k_{yy}}{m}}$ and when damping d_{yy} is very small.

The sense (x) axis can be expressed as

$$0 = m\ddot{x} + d_{xx}\dot{x} + k_{xx}x - 2m\Omega_z\dot{y} \tag{3.7}$$

Therefore the x axis displacement becomes

$$x = X_0 \sin(\omega t - \phi_x) \tag{3.8}$$

with

$$X_0 = \frac{2m\Omega\dot{y}}{\sqrt{d_{xx}^2\omega + (m\omega^2 - k_{xx})}} \tag{3.9}$$

$$\phi_x = \arctan\left(\frac{m\omega^2 - k_{xx}}{d_{xx}\omega}\right) \tag{3.10}$$

This shows that the amplitude of vibration in the sense axis X_0 is proportional to the input rotation Ω as long as the dynamics of the system don't change over time and the amplitude of $\dot{y}$ is constant. Once again $\frac{X_0}{\Omega_z}$ is maximised when $d_x x$ is very small and at resonance when $\omega = \sqrt{\frac{k_{xx}}{m}}$.

Since the sense axis vibration is a sine wave amplitude modulated by the Coriolis term, the system requires an amplitude demodulation and low pass filtering stage to extract the final angular rate signal.

The ideal single axis sensor dynamic system can be expressed in matrix form as

$$\begin{bmatrix} 0 \\ F \end{bmatrix} = m \begin{bmatrix} \ddot{x} \\ \ddot{y} \end{bmatrix} + \begin{bmatrix} d_{xx} & 0 \\ 0 & d_{yy} \end{bmatrix} \begin{bmatrix} \dot{x} \\ \dot{y} \end{bmatrix} + \begin{bmatrix} k_{xx} & 0 \\ 0 & k_{yy} \end{bmatrix} \begin{bmatrix} x \\ y \end{bmatrix} + 2m \begin{bmatrix} 0 & -\Omega_z \\ \Omega_z & 0 \end{bmatrix} \begin{bmatrix} \dot{x} \\ \dot{y} \end{bmatrix} \tag{3.11}$$

Notice in the ideal system model the only cross coupling between the x and y axes is through the Coriolis terms.

3.4.2 Error Sources

To understand the advantages and limitations of the various angular rate sensor approaches, it is necessary to look at the error sources that they aim to overcome.

Sensing Noise

As can be seen in Figure 3.5(b), the amplitude of vibration in the sense axis is orders of magnitude smaller than that of the drive axis, making it difficult to measure accurately. How well the vibrating mass's motion can be measured becomes a limiting factor on the device resolution. Noise can enter at various stages of the position and/or velocity sensing process: from the sensing element itself; any associated sensing circuits and wiring; and also the quantisation error associated with digitisation of the sensing element output [26]. These can be modeled as a noise source added to the sense axis signal in the ideal model of Equation (3.11), giving

$$\begin{aligned} \begin{bmatrix} 0 \\ F \end{bmatrix} &= m \begin{bmatrix} \ddot{x} \\ \ddot{y} \end{bmatrix} + \begin{bmatrix} d_{xx} & 0 \\ 0 & d_{yy} \end{bmatrix} \begin{bmatrix} \dot{x} \\ \dot{y} \end{bmatrix} + \begin{bmatrix} k_{xx} & 0 \\ 0 & k_{yy} \end{bmatrix} \begin{bmatrix} x \\ y \end{bmatrix} + 2m \begin{bmatrix} 0 & -\Omega_z \\ \Omega_z & 0 \end{bmatrix} \begin{bmatrix} \dot{x} \\ \dot{y} \end{bmatrix} \\ \breve{x} &= x + n_{Sensing} \end{aligned} \tag{3.12}$$

Here $n_{Sensing}$ is the sensing noise and $\breve{x}$ is the measured (noise affected) sense axis signal.

One of the most common noise sources reported in the literature is parasitic capacitances that form between capacitive sensing elements, the device substrate and in the interconnects to the sensing circuitry. Significant improvements have been found by using an insulating substrate such as glass. Sharma, Zaman Amini and Ayazi [69] showed a sensing noise floor of $0.02deg/h/\sqrt{Hz}$ which is well below the devices Brownian noise floor of $0.3deg/h/\sqrt{Hz}$.

One of the many advantages of MEMS devices is the ability to integrate sensing elements

and their associated circuitry on the same silicon substrate as the mechanical structure. This reduces the parasitic effects associated with wiring to external sensing circuitry [44].

The sensing element scale factor may also be time varying, including sensitivity to changes in operating environment, namely temperature. Capacitive sensing elements are generally less sensitive to temperature than piezoresistive or piezoelectric alternatives [80]. However it is also possible to incorporate temperature compensation circuits to counteract these issues. Phase differential sensing schemes have been shown to be robust against variations in sensing element scale factor [1,27,81]. An alternative tunneling-based sensing element has been employed to improve mass displacement sensitivity [37], however the use of tunneling is limited to angular rate sensors that operate in the force-to-rebalance mode described in section 3.4.5.

Thermal Mechanical (Brownian) Noise

Thermal mechanical noise appears as a white noise force acting on the vibrating proof mass wherever there is damping [20]. Adding thermal mechanical noise to the system model Equation (3.12) gives

$$\begin{aligned}\begin{bmatrix} 0 \\ F \end{bmatrix} &= m\begin{bmatrix} \ddot{x} \\ \ddot{y} \end{bmatrix}+\begin{bmatrix} d_{xx} & 0 \\ 0 & d_{yy} \end{bmatrix}\begin{bmatrix} \dot{x} \\ \dot{y} \end{bmatrix}+\begin{bmatrix} k_{xx} & 0 \\ 0 & k_{yy} \end{bmatrix}\begin{bmatrix} x \\ y \end{bmatrix}+2m\begin{bmatrix} 0 & -\Omega_z \\ \Omega_z & 0 \end{bmatrix}\begin{bmatrix} \dot{x} \\ \dot{y} \end{bmatrix}+\begin{bmatrix} d_{Bx} \\ d_{By} \end{bmatrix} \\ \breve{x} &= x + n_{Sensing}\end{aligned} \tag{3.13}$$

Here d_{Bx} and d_{By} are the thermal mechanical noise on the mass in the x and y axes respectively.

Thermal mechanical noise limits the ultimate achievable resolution of all vibratory angular rate sensors [26]. Using a larger proof mass or encasing the vibrating mass in a vacuum would decrease thermal mechanical noise [26], as would artificially decreasing the operating temperature around the proof mass, but this has not been encountered in the literature. However thermal mechanical noise cannot be eliminated completely.

The noise power of the output signal can be reduced using filtering techniques. Research by Qi and Stern has shown that using a practical correlation filter can greatly reduce thermal noise in gyroscope output signals compared to using a conventional low pass filter [65]. Another approach to de-noising gyroscope signals by Wang and Huang uses wavelet packet analysis [77].

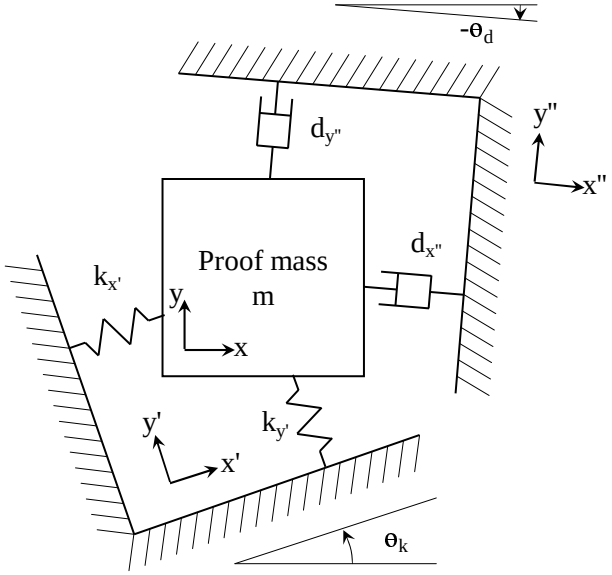

Figure 3.6: Asymmetric stiffness and damping in the angular rate sensor system

Asymmetric Stiffness and Damping

Most angular rate sensors such as that by Mochida *et al* [52] and Alper and Akin [5] employ symmetric structures to reduce any asymmetries in the device dynamics. However, due to the limitations of fabrication, it is unlikely that the principle stiffness axes (x', y') or damping axes (x'', y'') will be perfectly aligned with the geometric axes of device. Figure 3.6 shows a diagram of this where $k_{x'}$ and $k_{y'}$ are the principle stiffness and $d_{x''}$ and $d_{y''}$ are the principle damping terms. The following transforms the principle stiffness terms back to the x and y axes.

Consider a force vector caused by a displacement in the principle axes

$$\begin{bmatrix} F_{x'} \\ F_{y'} \end{bmatrix} = \underbrace{\begin{bmatrix} k_{x'} & 0 \\ 0 & k_{y'} \end{bmatrix}}_{\substack{\text{Principle stiffness} \\ \text{matrix will always} \\ \text{be diagonal}}} \begin{bmatrix} x' \\ y' \end{bmatrix} \tag{3.14}$$

and a force vector caused by a displacement in the device axes

$$\begin{bmatrix} F_x \\ F_y \end{bmatrix} = \begin{bmatrix} k_{xx} & k_{xy} \\ k_{yx} & k_{yy} \end{bmatrix} \begin{bmatrix} x \\ y \end{bmatrix} \tag{3.15}$$

The cross stiffness and cross damping terms can be thought of as causing a rotation of the respective stiffness and damping principle axes from their ideal alignment with the x and y axes.

Transforming the principle stiffness axes x' and y' to the x, and y axes is done with the rotation matrix

$$\begin{bmatrix} x \\ y \end{bmatrix} = \begin{bmatrix} \cos(\theta_k) & \sin(\theta_k) \\ -\sin(\theta_k) & \cos(\theta_k) \end{bmatrix} \begin{bmatrix} x' \\ y' \end{bmatrix} \tag{3.16}$$

Similarly the force in the principle axes can be transformed to a force in the device axes

$$\begin{bmatrix} F_x \\ F_y \end{bmatrix} = \begin{bmatrix} \cos(\theta_k) & \sin(\theta_k) \\ -\sin(\theta_k) & \cos(\theta_k) \end{bmatrix} \begin{bmatrix} F_{x'} \\ F_{y'} \end{bmatrix} \tag{3.17}$$

Therefore the relationship between the principle axes stiffness matrix and the device axes stiffness matrix can be shown to be

$$\begin{bmatrix} k_{xx} & k_{xy} \\ k_{xy} & k_{yy} \end{bmatrix} = \begin{bmatrix} \cos(\theta_k) & \sin(\theta_k) \\ -\sin(\theta_k) & \cos(\theta_k) \end{bmatrix}^{-1} \begin{bmatrix} k_{x'} & 0 \\ 0 & k_{y'} \end{bmatrix} \begin{bmatrix} \cos(\theta_k) & \sin(\theta_k) \\ -\sin(\theta_k) & \cos(\theta_k) \end{bmatrix} \tag{3.18}$$

$$\begin{bmatrix} k_{xx} & k_{xy} \\ k_{xy} & k_{yy} \end{bmatrix} = \begin{bmatrix} \cos(-\theta_k) & \sin(-\theta_k) \\ -\sin(-\theta_k) & \cos(-\theta_k) \end{bmatrix} \begin{bmatrix} k_{x'} & 0 \\ 0 & k_{y'} \end{bmatrix} \begin{bmatrix} \cos(\theta_k) & \sin(\theta_k) \\ -\sin(\theta_k) & \cos(\theta_k) \end{bmatrix} \tag{3.19}$$

Similarly the relationship between the principle axes damping matrix and the device axes damping matrix can be shown to be

$$\begin{bmatrix} d_{xx} & d_{xy} \\ d_{xy} & d_{yy} \end{bmatrix} = \begin{bmatrix} \cos(-\theta_d) & \sin(-\theta_d) \\ -\sin(-\theta_d) & \cos(-\theta_d) \end{bmatrix} \begin{bmatrix} d_{x''} & 0 \\ 0 & d_{y''} \end{bmatrix} \begin{bmatrix} \cos(\theta_k) & \sin(\theta_k) \\ -\sin(\theta_k) & \cos(\theta_k) \end{bmatrix} \tag{3.20}$$

Adding these asymmetric stiffness and damping terms to the model in Equation (3.13) gives us the final error model.

$$\begin{bmatrix} 0 \\ F \end{bmatrix} = m\begin{bmatrix} \ddot{x} \\ \ddot{y} \end{bmatrix} + \begin{bmatrix} d_{xx} & d_{xy} \\ d_{xy} & d_{yy} \end{bmatrix} \begin{bmatrix} \dot{x} \\ \dot{y} \end{bmatrix} + \begin{bmatrix} k_{xx} & k_{xy} \\ k_{xy} & k_{yy} \end{bmatrix} \begin{bmatrix} x \\ y \end{bmatrix} + 2m \begin{bmatrix} 0 & -\Omega_z \\ \Omega_z & 0 \end{bmatrix} \begin{bmatrix} \dot{x} \\ \dot{y} \end{bmatrix} + \begin{bmatrix} d_{Bx} \\ d_{By} \end{bmatrix}$$
$$\breve{x} = x + n_{Sensing} \tag{3.21}$$

The asymmetric stiffness terms (k_{xy}) may arise from such things as the centre of mass not coinciding perfectly with the geometric centre or the supporting spring having unequal stiffness. Asymmetric (or cross) stiffness causes unwanted forces that act on the mass, causing the proof mass to trace a circular path instead of a linear one. This results in a zero rate output (ZRO) called quadrature error [83]. ZRO is any erroneous signal that is output by the device when it is subject to zero angular rate input. The quadrature error forces are proportional to the mass's displacement and are therefore $\pm 90°$ out of phase (quadrature phase) with the Coriolis forces which are proportional to the mass's velocity. The quadrature phase makes asymmetric stiffness forces distinguishable from Coriolis forces. Asymmetric stiffness can be removed from the structure using focussed ion beam or laser ablation or its effects canceled by initial calibration and applying a tuning force as was done by Gallacher *et al* [22]. However given that asymmetric stiffness can be time varying, an improvement in performance can be achieved if it is estimated and compensated for using real-time control strategies [60]. Dong and Leland have proposed one such adaptive controller which estimates both the cross stiffness and input angular rate and compensates for their effects on the sense axis in a force-to-rebalance mode.

Like asymmetric stiffness, asymmetric (or cross) damping arises from fabrication imperfections. It is the misalignment of the principle damping axes from the geometric axes of the device. It also causes erroneous forces to act on the mass, however they are in phase with the Coriolis force since they are both proportional to the mass's velocity. By demodulating with respect to both a sine and a cosine signal the quadrature error can be distinguished from the combined Coriolis and asymmetric damping signals. However separating the Coriolis signal from the asymmetric damping signal is much more difficult. Only one approach encountered in the literature, that by Park [60], has shown to be able to distinguish from one another. He used a model reference adaptive control (MRAC) approach described in section 3.4.6. Usually the problem of asymmetric damping is reduced by minimising the total system damping by operating the device in a vacuum. Highly symmetrical structures can also reduce the size of asymmetric damping [5, 55].

3.4.3 Open-Loop Operation

An angular rate sensor that operates in open-loop mode employs no feedback control in either the drive or sense axes. Therefore they are highly reliant on the system dynamics remaining

unchanged and as such are helpless against any variation.

The sensitivity is increased if the drive and sense axes have matched resonant frequencies due to mechanical amplification in the Coriolis axis. Any mismatch in the resonant frequencies between the drive and sense axes can be tuned by applying a force offset to one of the axes. This has the effect of altering its stiffness. Alper and Akin [5] presented an open loop angular rate sensor with a symmetric structure that provided matched and decoupled resonant modes. It was fabricated using the MUMP's surface micromachining fabrication process. The device showed good sensitivity as expected due to the mechanical amplification however was found to have large parasitic capacitances. Later they fabricated a similar design on a glass substrate, achieving $0.25deg/\sqrt{h}$ resolution with a resonant frequency of $\sim 41kHz$ and a $10-15\mu m$ mass thickness. A very similar silicon-on-glass device was reported by Lee *et al* [40], which had a resonant frequency of $\sim 9.2kHz$, an $80-120\mu m$ mass thickness and a resolution of $0.024deg/\sqrt{h}$.

However, operating at resonance, the open loop approach suffers from a small bandwidth since the motion caused by the Coriolis force needs a relatively long time to reach a steady state. With matched resonant frequencies, the bandwidth of the open loop device is equal to $\frac{\omega_x}{2Q_x}$ [60], where $Q_x = \frac{\sqrt{mk_{xx}}}{d_{xx}}$ is the quality factor and $\omega_x = \sqrt{\frac{k}{m}}$ is the natural frequency in the sense axis. Also operating at resonance presents difficulties with high Q devices because a slight change in resonant frequency will cause a significant change in the mechanical amplification and therefore scale factor because of the sharp roll-off in the frequency response.

To overcome the reduction in bandwidth and scale factor instability, slightly unmatched modes in the drive and sense axes can be employed with the inherent tradeoff in sensitivity [31]. This approach also makes the device more resilient to changes in resonant frequency because it operates outside of the resonant peak where the response is flatter. Grétillat and Grétillat proposed an improved design of their bulk micromachined tuning fork angular rate sensor which aimed to reduce the ZRO of their previous device by employing mismatched modes to uncouple the two axes and better isolate the driving motion from the piezoresistive sensing elements. The other solution to increase bandwidth is to add a negative feedback loop to null the motion of the mass in the sense axis, as outlined in section 3.4.5.

Another approach by Acar, Eler and Shkel uses a mechanical solution to the problem by using two coupled masses each with two degrees of freedom and separate resonant peaks and operating the device in the flatter and wider operating region between the two peaks for more

robust performance [2]. This sort of approach was further developed by Acar and Shkel [3] in which eight interconnected vibrating masses in a ring arrangement are used, each with a slightly different resonant mode. Each is driven into oscillation resulting in a very wide bandwidth that is robust against temperature fluctuations and has small ZRO due to the decouplng nature of the multiple mismatched modes.

Differential phase demodulation has been shown to be insensitive to variations in drive amplitude [1, 27, 81], however its use is limited to open-loop operation.

3.4.4 Drive Axis Control

Typically MEMS devices are driven in their primary mode at resonance so that the vibration will be mechanically amplified. Generally MEMS devices have high Q factors that drop off sharply from resonance. The device's resonant frequencies are dependent on ambient temperature and pressure [68] and are therefore time varying. This can be problematic in maintaining the constant amplitude of vibration in the drive axis required to obtain a constant output scale factor. Commonly a phase locked loop (PLL) is used to maintain drive oscillation at resonance [42]. It is also possible to do the opposite and tune the resonant frequency to match a time invariant reference model [41].

Oboe and Antonello used drive axis control to maintain a constant drive axis velocity amplitude using a transresistance amplifier fed to a saturated amplifier. This gives a constant drive axis amplitude, however is not controlable. Amplitude control was achieved using a variable gain amplifier that is controlled by a discrete automatic gain controller.

The Jet Propulsion Laboratory cloverleaf vibrating post angular rate sensor [74] also used a variable gain amplifier controlled by an automatic gain controller. This device have very large structural mass ($7mm \times 7mm$) and low resonant frequency and gave a resolution of $6.3deg/\sqrt{h}$.

3.4.5 Force-to-Rebalance Closed Loop Feedback

In force-to-rebalance mode [59], instead of using the sense axis motion resulting from the Coriolis force as an output, it is used as an input to a negative feedback loop. This feedback loop acts to null the motion in the sense axis using the control signal τ, given in Equation (3.23) below. It results in a marked improvement in the bandwidth due to the mass remaining essentially

motionless in the sense axis. The demodulated feedback force then becomes the output of the device, since in an ideal system it is proportional to the angular rate input.

$$\begin{aligned}\begin{bmatrix} \tau \\ F \end{bmatrix} &= m\begin{bmatrix} \ddot{x} \\ \ddot{y} \end{bmatrix}+\begin{bmatrix} d_{xx} & d_{xy} \\ d_{xy} & d_{yy} \end{bmatrix}\begin{bmatrix} \dot{x} \\ \dot{y} \end{bmatrix}+\begin{bmatrix} k_{xx} & k_{xy} \\ k_{xy} & k_{yy} \end{bmatrix}\begin{bmatrix} x \\ y \end{bmatrix}+2m\begin{bmatrix} 0 & -\Omega_z \\ \Omega_z & 0 \end{bmatrix}\begin{bmatrix} \dot{x} \\ \dot{y} \end{bmatrix}+\begin{bmatrix} d_{Bx} \\ d_{By} \end{bmatrix} \\ \breve{x} &= x + n_{Sensing} \end{aligned} \tag{3.22}$$

Looking at Equation (3.22), since the sense axis signal is nulled, $\ddot{\breve{x}} = \dot{\breve{x}} = \breve{x} = 0$ and therefore the feedback force τ becomes

$$\tau = m(\ddot{\breve{x}} - \ddot{x}) + d_{xx}(\dot{\breve{x}} - \dot{x}) + k_{xx}(\breve{x} - x) + k_{xy}y + d_{xy}\dot{y} - 2m\Omega_z\dot{y} + d_{Brownian} \tag{3.23}$$

The feedback force consists of not only a counteractive force to the Coriolis force but also to the error between the measured sense axis acceleration, velocity and position, erroneous cross stiffness and damping forces and Brownian motion forces covered above. To overcome this, more complex control strategies are required to identify and compensate for the errors and the angular rate separately.

Force-to-rebalance mode is an integral part of the tunneling based angular rate sensor proposed by Kenuba *et al* [37] which uses force-to-rebalance mode to maintain the tunneling gap and therefore tunneling current.

3.4.6 Adaptive Control

Adaptively controlled systems can be characterised as those that can adapt to changes in the system dynamics over time.

Leland proposed an adaptive controller for an open loop device that tunes the frequency of vibration of the drive axis to match that of a fixed reference drive signal [41]. This offers advantages over using a PLL, which tunes the driving signal frequency to match the resonant frequency because the dynamics of the system are dictated by the time invariant reference model instead of the natural resonant frequency of the device, which may be time varying. Later work also added adaptive control to regulate the drive oscillation amplitude, cancel out quadrature error due to asymmetric stiffness and null the sense axis vibration in force-to-rebalance mode [42]. In this work the analysis assumed that the angular rate input was constant, recent work

incorporated time varying input rate in a lyapunov based adaptive controller which estimates and compensates for both input angular rate and cross stiffness terms [45]. Cross damping terms were not compensated for.

M'Closkey, Gibson and Hui at the Jet Propulsion Laboratory [51] used off-line lattice-filter based algorithms to estimate high-order linear multi-input multi-output (MIMO) models for their cloverleaf vibrating post angular rate sensor dynamics. Chirp signals were used to excite the dynamics for identification. All the stiffness terms were successfully identified, however it was concluded that it was impossible to identify the cross damping terms, as they are indistinguishable from the angular rate terms. Justification was given why the cross damping terms could be assumed to be small and it was proposed that devices be constructed with as little total damping as possible. The work indicated a feasibility of performing the identification and calibration in real-time. Later work on the same cloverleaf design proposed evolutionary optimisation computation to tune the mismatch in resonant modes in an off-line fashion [30].

A unique angular rate sensing approach presented by Park *et al.* [61] uses adaptive control laws to update stiffness, damping and angular rate estimates that are then used in a feedforward control to null their effects and control the motion of the mass along an ideal reference model Lissajous trajectory. This reference trajectory, shown in Figure 3.7, provides enough excitation richness for all parameter estimates to converge to their true values including estimates of cross damping, which are difficult to distinguish from angular rate.

3.4.7 Angular Displacement Measurement and Control

Angular displacement sensors differ from angular rate sensors in that their output is absolute angle as opposed to angular rate. They are often and possibly more accurately referred to as rate integral gyroscopes. These devices keep track of absolute angle mechanically. To get the same signal from an angular rate sensor requires the angular rate signal to be integrated which accumulates any error in the sensor output.

Early research by Friedland and Hutton [19] investigated the vibrating mass gyroscope concept consisting of a linearly vibrating mass, driven at a constant amplitude that is able to move in a $2D$ plane. The line of oscillation of the vibrating mass is allowed to precess in the plane through Coriolis force (See Figures 3.8(a) and 3.8(b)). The axis of oscillation indicates angular displacement rather than angular rate and can be calculated with Equation 3.24 from [70]. This

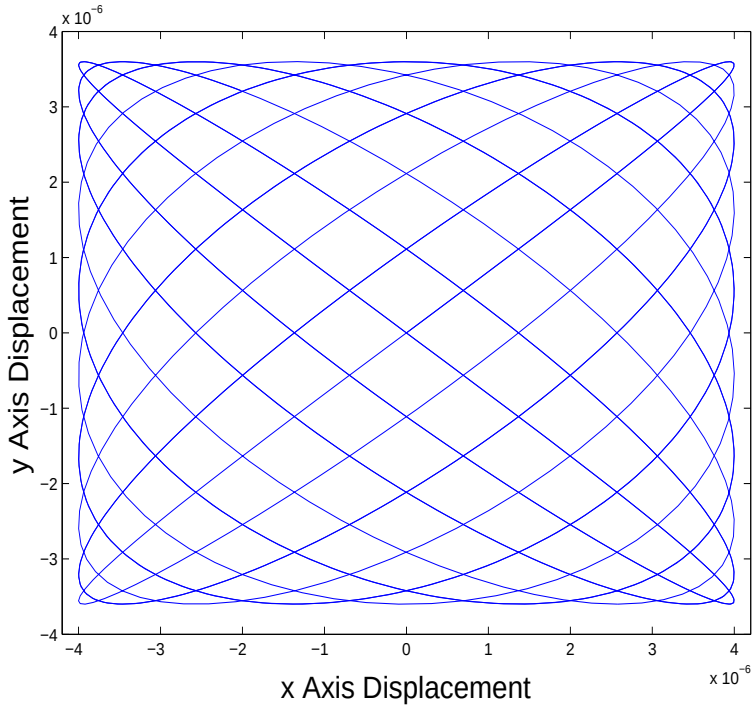

Figure 3.7: The frequency rich excitation of the Lissajous pattern created by having unmatched modes in the reference model trajectory allows all the parameter estimates to converge to their true values.

device approach lends itself well to enabling the identification of asymmetric stiffness errors and mismatched modes.

$$\tan 2\theta = \frac{2\left(\omega_n^2 xy + \dot{x}\dot{y}\right)}{\omega_n^2\left(x^2 - y^2\right) + \left(\dot{x}^2 - \dot{y}^2\right)} \tag{3.24}$$

It was concluded that in an ideal system, the vibrating mass would have constant energy so as to overcome damping dissipation forces and maintain the amplitude of oscillation and would also have zero angular momentum to maintain a straight line trajectory. To implement these control strategies, the device would require both sensing and actuation elements in two perpendicular axes and be constrained in the third.

A very similar approach was later presented by Shkel *et al* [70], in which a control to null angular momentum F_{quadr} was used to suppress the elliptical effects of asymmetric stiffness and an energy maintaining control F_{energy} to overcome the damping dissipation forces. Here γ_1 and γ_2 are positive gain matrices, S^T is a skew-symmetric matrix, E_0 is the nominal energy, ΔE is the energy error, P is the angular momentum and q and $\dot{q}$ are the mass's position and

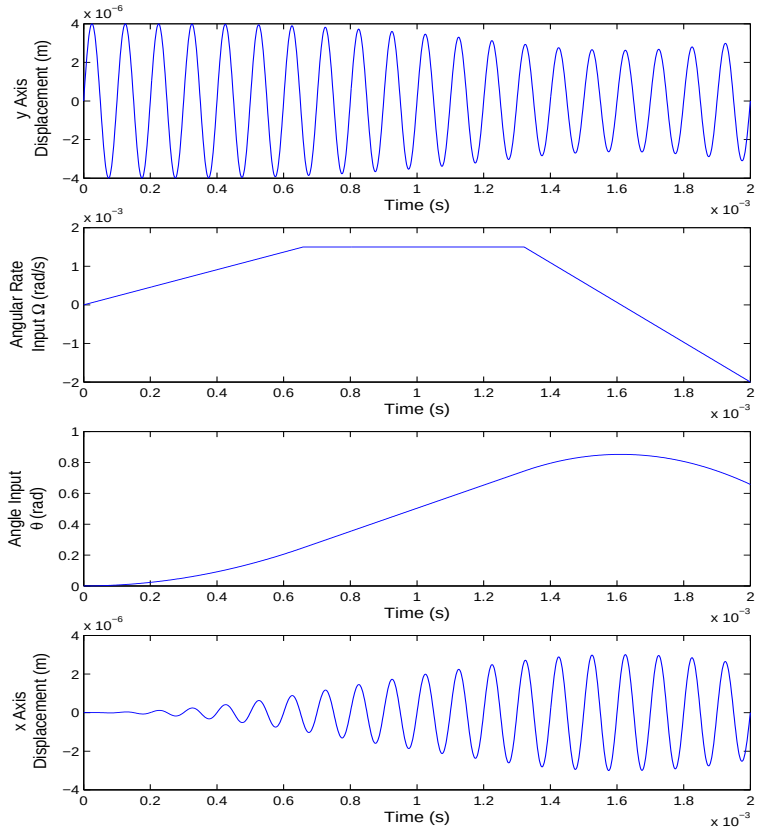

(a) Operation of the angular displacement devices in which the total energy of oscillation is kept constant and the output becomes the angle of the oscillation axis shown in Figure 3.8(b). Notice that both the x and y axis amplitudes vary.

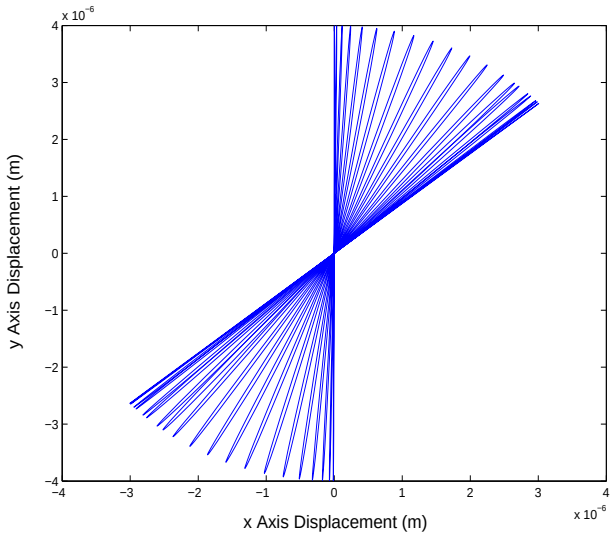

(b) Proof mass displacement trajectory for the angular displacement device corresponding to the angular rate input of Figure 3.8(a)

Figure 3.8: Angular displacement sensor operation for a typical sensor with matched resonant frequencies of 10kHz and drive amplitude of $4\mu m$

velocity vectors respectively.

$$\begin{aligned} F_{quadr} &= -\gamma_1 P S^T q \\ P &= = \pi \left(x\dot{y} - y\dot{x} \right) \end{aligned} \tag{3.25}$$

$$\begin{aligned} F_{energy} &= -\gamma_2 \Delta E \dot{q} \\ \Delta E &= = E_0 - \frac{\omega_n^2 \left(x^2 + y^2 \right) + \left(\dot{x}^2 - \dot{y}^2 \right)}{2} \end{aligned} \tag{3.26}$$

This control topology was found to not interfere with the Coriolis effects. An adaptive approach for estimating the stiffness and angular rate was also presented.

Another proposed angular displacement device [64] uses the same energy maintaining control and an alternative stiffness error control based on real-time estimations of stiffness, calculated by measuring the time interval of each oscillation half cycle. Additionally an adaptive observer was used to exploit the angular rate measurements to improve angular displacement output.

Using the same angular displacement concept as Friedland and Hutton [19], research by Painter and Shkel [56] concluded that estimating the asymmetric stiffness and compensating using feedforward control gave better results than simply using feedback control. Consequently they proposed a two stage process of estimating the asymmetric stiffness, compensating with a feedforward controller and finer feedback control for small perturbations. The asymmetric stiffness estimation is achieved by utilising results obtained in [71] and earlier in [19] in which mismatched and asymmetric stiffnesses were found to lead to free-vibration trajectories that trace rectangular-bounded Lissajous patterns, whose principle axes aligned to the principle stiffness axes. Lissajous patterns are described by perpendicular sinusoids with unmatched frequencies, Figure 3.7 shows an example. The stiffness estimates are extracted from these Lissajous patterns using principle component analysis of the frequency response in the x axis [56].

3.5 Single Vibrating Mass Triaxial Angular Rate Sensing

Many application that use angular rate require full pitch, roll and yaw information. Providing a triaxial angular rate sensor on one chip in a small package has been identified as a major impetus in inertial sensor technology trends [8].

Single chip triaxial angular rate sensors have been achieved where either three single axis devices or one biaxial and one single axis device have been fabricated on the same substrate. This can lead to mechanical interference. This is experienced when multiple vibrating masses are mounted together or share a substrate. The problem is amplified when the masses share similar resonant frequencies [47]. This effect can be eliminated by using a single vibrating mass to sense triaxial angular rate. This would also remove the need for precise alignment of three separate single axis angular rate sensors.

A review of the literature has uncovered one proposed method of resolving triaxial angular rate using a single vibrating mass [47]. It involves driving the mass in a circular trajectory in the x-y plane. The device uses an existing triaxial accelerometer [33]. It consists of a single cubic mass with three pairs of orthogonal displacement sensors assembled around it. The mass is then excited using additional electromagnetic actuation in two axes. This device however is quite large for a MEMS device ($3mm \times 3mm \times 3mm$, not including the electromagnetic actuation elements and electronics), requires assembly of the displacement sensors around the mass and is vulnerable to output errors caused by fabrication imperfections and time varying effects.

3.5.1 Problem Formulation

This review has shown the evolution of MEMS angular rate sensing. The most basic open loop vibrating mass device has a limited bandwidth due to the time needed to reach steady state. It does not compensate for fabrication errors and is sensitive to fluctuations in drive axis amplitude due to time varying resonant frequencies. Incorporating a simple feedback loop to null the mass's motion in the sense axis improves the bandwidth significantly, however does not compensate for cross stiffness and damping errors and fluctuations in resonant frequencies. Adaptive controllers have been designed to compensate for time varying resonant frequencies and cross stiffness errors and one has shown to be able to estimate and compensate for cross damping errors for a single axis device using a frequency rich reference model trajectory.

This dissertation aims develop a triaxial angular rate sensor that uses a single vibrating mass. The system will adopt a model reference adaptive control (MRAC) approach that aims to be able to estimate and compensate for all stiffness error and damping terms including the cross terms as well as angular rate in real-time.

This approach promises to reduce energy consumption given only one mass is driven

into vibration instead of three separate ones. It also promises to reduce wafer footprint. This increases production yield and subsequently decreases unit costs. These advantages suit the requirements of many emerging applications that require triaxial angular rate sensing as part of their inertial measurement.

Chapter 4

Novel Single Mass Adaptively Controlled Triaxial Angular Rate Sensor

This chapter presents a novel controller for an adaptive MEMS triaxial angular rate sensor device that is able to detect rotation in three orthogonal axes, using a single vibrating mass.

The adaptive controller performs various functions. It updates estimates of all stiffness error, damping and input rotation parameters in real time, removing the need for any offline calibration stages. The parameter estimates are used in feedforward control to cancel out their otherwise erroneous effects, including Zero Rate Output (ZRO). The controller also drives the mass along a controlled oscillation trajectory, removing the need for additional drive control. Finally, the output of the device is simply an estimate of input rotation, removing the need for additional demodulation normally used for vibratory mass angular rate sensors. To enable all unknown parameter estimates to converge to their true values, the necessary model trajectory is shown to be a three dimensional Lissajous pattern. Simulation results are presented to verify the operation of the adaptive controller.

4.1 Asymmetric Stiffness and Damping Effects

In order to measure triaxial angular rate using a single mass, the mass must have at least three degrees of freedom, namely each orthogonal axis. Each axis has inherent stiffness and

damping as can be seen in the simplified lumped model system in Figures 4.1 and 4.2. Ideally the principle stiffness and damping axes would be aligned perfectly with the device x, y and z axes. However any real device will have asymmetric stiffness and damping as a result of slight fabrication imperfections that will cause misalignment. There are many sources of error in a conventional angular rate sensor that contribute to the non-ideal K and D matrices. Some of these effects can be time varying, such as those affected by temperature or pressure.

The following transforms the principle stiffness terms back to the x, y and z axes for the triaxial device. The analysis is similar to that presented in section 3.4.2 for a single axis angular rate sensor. Consider a force vector caused by a displacement in the principle axes

$$\begin{bmatrix} F_{x'} \\ F_{y'} \\ F_{z'} \end{bmatrix} = \underbrace{\begin{bmatrix} k_{x'} & 0 & 0 \\ 0 & k_{y'} & 0 \\ 0 & 0 & k_{z'} \end{bmatrix}}_{\substack{\text{Principle stiffness} \\ \text{matrix will always} \\ \text{be diagonal}}} \begin{bmatrix} x' \\ y' \\ z' \end{bmatrix} \tag{4.1}$$

and a force vector caused by a displacement in the device axes

$$\begin{bmatrix} F_x \\ F_y \\ F_z \end{bmatrix} = \begin{bmatrix} k_{xx} & k_{xy} & k_{xz} \\ k_{yx} & k_{yy} & k_{yz} \\ k_{zx} & k_{zy} & k_{zz} \end{bmatrix} \begin{bmatrix} x \\ y \\ z \end{bmatrix} \tag{4.2}$$

The cross stiffness and cross damping terms can be thought of as causing a rotation of the respective stiffness and damping principle axes in three dimensional space from their ideal alignment with the x, y and z axes.

Transforming the three principle stiffness axes x', y' and z' to the x, y and z axes can always be done with combined rotations θ_x, θ_y and θ_z around the x, y and z device axes respectively. This can be represented as

$$\begin{bmatrix} x \\ y \\ z \end{bmatrix} = R_K \begin{bmatrix} x' \\ y' \\ z' \end{bmatrix} \tag{4.3}$$

where

$$R_K = \begin{bmatrix} 1 & 0 & 0 \\ 0 & \cos(\theta_x) & \sin(\theta_x) \\ 0 & -\sin(\theta_x) & \cos(\theta_x) \end{bmatrix} \begin{bmatrix} \cos(\theta_y) & 0 & \sin(\theta_y) \\ 0 & 1 & 0 \\ -\sin(\theta_y) & 0 & \cos(\theta_y) \end{bmatrix} \begin{bmatrix} \cos(\theta_z) & \sin(\theta_z) & 0 \\ -\sin(\theta_z) & \cos(\theta_z) & 0 \\ 0 & 0 & 1 \end{bmatrix} \tag{4.4}$$

Similarly the force in the principle axes can be transformed to a force in the device axes using the same rotation transformation R_K

$$\begin{bmatrix} F_x \\ F_y \\ F_z \end{bmatrix} = R_K \begin{bmatrix} F_{x'} \\ F_{y'} \\ F_{z'} \end{bmatrix} \tag{4.5}$$

Therefore the relationship between the principle axes stiffness matrix and the device axes stiffness matrix can be shown to be

$$K = \begin{bmatrix} k_{xx} & k_{xy} & k_{xz} \\ k_{xy} & k_{yy} & k_{yz} \\ k_{xz} & k_{yz} & k_{zz} \end{bmatrix} = R_K^{-1} \begin{bmatrix} k_{x'} & 0 & 0 \\ 0 & k_{y'} & 0 \\ 0 & 0 & k_{z'} \end{bmatrix} R_K \tag{4.6}$$

where R^{-1} can be expressed as

$$R_K^{-1} = \begin{bmatrix} \cos(-\theta_z) & \sin(-\theta_z) & 0 \\ -\sin(-\theta_z) & \cos(-\theta_z) & 0 \\ 0 & 0 & 1 \end{bmatrix} \begin{bmatrix} \cos(-\theta_y) & 0 & \sin(-\theta_y) \\ 0 & 1 & 0 \\ -\sin(-\theta_y) & 0 & \cos(-\theta_y) \end{bmatrix} \begin{bmatrix} 1 & 0 & 0 \\ 0 & \cos(-\theta_x) & \sin(-\theta_x) \\ 0 & -\sin(-\theta_x) & \cos(-\theta_x) \end{bmatrix} \tag{4.7}$$

Similarly the relationship between the principle axes damping matrix and the device axes damping matrix can be shown to be

$$D = \begin{bmatrix} d_{xx} & d_{xy} & d_{xz} \\ d_{xy} & d_{yy} & d_{yz} \\ d_{xz} & d_{yz} & d_{zz} \end{bmatrix} = R_D^{-1} \begin{bmatrix} d_{x'} & 0 & 0 \\ 0 & d_{y'} & 0 \\ 0 & 0 & d_{z'} \end{bmatrix} R_D \tag{4.8}$$

Note that R_D uses the same equation as R_K, however, because the principle stiffness axes and the principle damping axes may not coincide, the rotation transformation angles θ_x, θ_y and θ_z

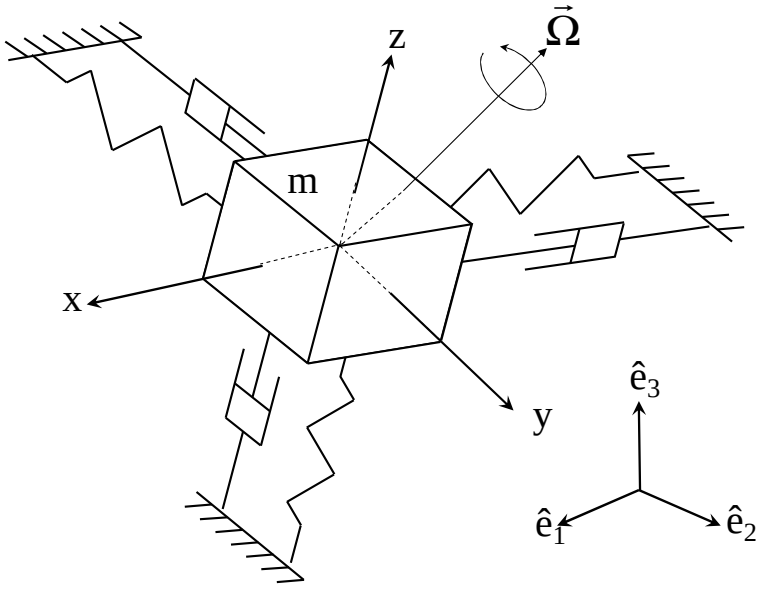

Figure 4.1: Triaxial angular rate sensor showing the sensor reference frame x, y and z and the inertial reference frame $\hat{e}_x$, $\hat{e}_y$ and $\hat{e}_z$

may be different for the stiffness and the damping. Also the stiffness matrix K and the damping matrix D are always symmetric [4], this agrees with Maxwell's Reciprocity Theorem, which states that the displacement at one point A on a linear system due to a force at another point B is equal to the displacement at point B due to the same force applied at point A [75]. This leads to $K_{ij} = K_{ji}$ and $D_{ij} = D_{ji}$.

4.2 Governing Equations

Figure 4.1 shows the angular rate sensor with it's own frame of reference x, y and z, in relation to the inertial frame of reference $\hat{e}_1$, $\hat{e}_2$ and $\hat{e}_3$.

Let $\vec{R}$ be the displacement vector of the origin of the sensor reference frame from the origin of the inertial reference frame, $\vec{r}$ be the displacement vector of the mass from the origin of the sensor reference frame and using the notation ${}^{a}\dot{\vec{b}}$ to denote the time derivative of vector $\vec{b}$ in the frame of reference a, where a can take either e for the inertial reference frame or s for the sensor reference frame.

We can write an expression for the forces acting on the proof mass as

$$\vec{\tau} = D\,{}^{s}\dot{\vec{r}} + K\vec{r} + m\left[{}^{e}\ddot{\vec{R}} + {}^{s}\ddot{\vec{r}} + 2\vec{\Omega} \times {}^{s}\dot{\vec{r}} + {}^{e}\dot{\vec{\Omega}} \times \vec{r} + \vec{\Omega} \times \left(\vec{\Omega} \times \vec{r}\right)\right] \tag{4.9}$$

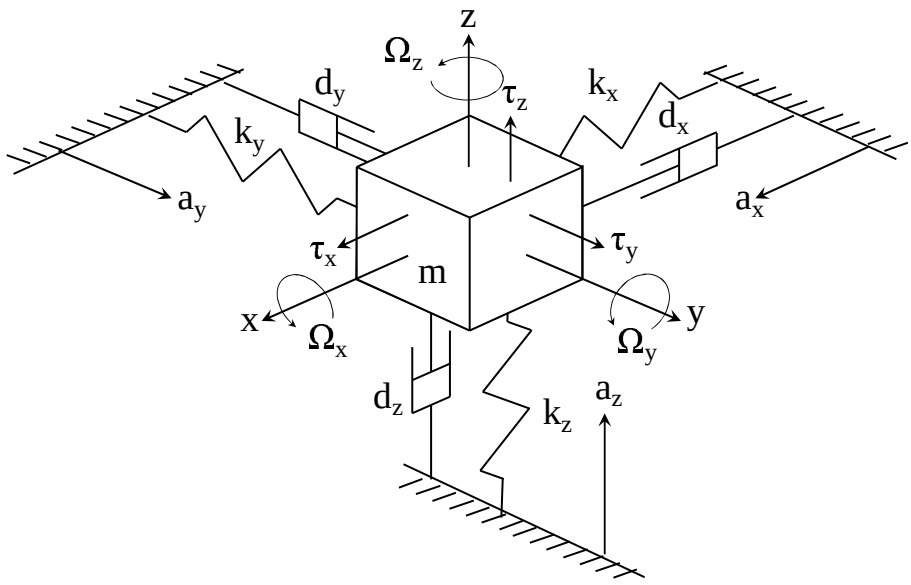

Figure 4.2: Simplified triaxial spring mass damper system with respect to the sensor reference frame.

where $\vec{\tau}$ is any applied control force vector, m is the mass of the proof mass, D is the sensor damping matrix and K is the sensor stiffness matrix, defined in Section (4.1).

The terms in the square brackets from left to right respectively are the lateral acceleration of the sensor casing with respect to the inertial reference frame, the lateral acceleration of the proof mass with respect to the sensor reference frame, the Coriolis acceleration that appears with respect to the sensor reference frame (note that by its very nature there is no Coriolis term with respect to the inertial reference frame), lateral acceleration caused by a change in the angular rate and finally centrifugal acceleration.

The vector expression Equation (4.9) can be expressed as a set of three equations describing each of the sensor reference frame's x, y and z axes. Figure 4.2 shows this diagramatically,

with cross terms omitted.

$$\begin{aligned}
\tau_x =& d_{xx}\dot{x} + d_{xy}\dot{y} + d_{xz}\dot{z} + k_{xx}x + k_{xy}y + k_{xz}z \\
&+ m\left[a_x + \ddot{x} + \left(\Omega_x\left(\Omega_y + \Omega_z\right) - \left(\Omega_y^2 + \Omega_z^2\right)\right)x + \left(\dot{\Omega}_y^2 z - \dot{\Omega}_z^2 y\right) + 2\left(\Omega_y\dot{z} - \Omega_z\dot{y}\right)\right] \\
\tau_y =& d_{xy}\dot{x} + d_{yy}\dot{y} + d_{yz}\dot{z} + k_{xy}x + k_{yy}y + k_{yz}z \\
&+ m\left[a_y + \ddot{y} + \left(\Omega_y\left(\Omega_x + \Omega_z\right) - \left(\Omega_x^2 + \Omega_z^2\right)\right)y + \left(\dot{\Omega}_z^2 x - \dot{\Omega}_x^2 z\right) + 2\left(\Omega_z\dot{x} - \Omega_x\dot{z}\right)\right] \\
\tau_z =& d_{xz}\dot{x} + d_{yz}\dot{y} + d_{zz}\dot{z} + k_{xz}x + k_{yz}y + k_{zz}z \\
&+ m\left[a_z + \ddot{z} + \left(\Omega_z\left(\Omega_x + \Omega_y\right) - \left(\Omega_x^2 + \Omega_y^2\right)\right)z + \left(\dot{\Omega}_x^2 y - \dot{\Omega}_y^2 x\right) + 2\left(\Omega_x\dot{y} - \Omega_y\dot{x}\right)\right]
\end{aligned} \tag{4.10}$$

The components of external acceleration on each axis are represented as a_x, a_y and a_z, the components of angular rate in each axis are Ω_x, Ω_y and Ω_z and linear proof mass displacements are x, y and z. Dot notation has been used to denote time derivatives.

Equation (4.10) can be further simplified. The angular rate is assumed to be steady over a long enough time period therefore the $\dot{\Omega}$ terms can be assumed to be zero. Since angular rate sensors operate near or at their relatively high resonant frequencies, external lateral accelerations a_x, a_y and a_z are likely to be at much lower frequencies that will not be mechanically amplified. They will also generally be cancelled out by control forces and can therefore also be assumed to be zero. The small magnitude of the Ω_x, Ω_y and Ω_z terms leads to $\Omega_x^2 \approx \Omega_y^2 \approx \Omega_z^2 \approx \Omega_x\Omega_y \approx \Omega_y\Omega_z \approx \Omega_x\Omega_z \approx 0$.

This leaves us with the simplified angular rate sensor dynamics

$$\begin{aligned}
\tau_x &= m\ddot{x} + d_{xx}\dot{x} + d_{xy}\dot{y} + d_{xz}\dot{z} + k_{xx}x + k_{xy}y + k_{xz}z + 2m\left(\Omega_y\dot{z} - \Omega_z\dot{y}\right) \\
\tau_y &= m\ddot{y} + d_{xy}\dot{x} + d_{yy}\dot{y} + d_{yz}\dot{z} + k_{xy}x + k_{yy}y + k_{yz}z + 2m\left(\Omega_z\dot{x} - \Omega_x\dot{z}\right) \\
\tau_z &= m\ddot{z} + d_{xz}\dot{x} + d_{yz}\dot{y} + d_{zz}\dot{z} + k_{xz}x + k_{yz}y + k_{zz}z + 2m\left(\Omega_x\dot{y} - \Omega_y\dot{x}\right)
\end{aligned} \tag{4.11}$$

This can be expressed more elegantly in matrix form as

$$\tau = M\ddot{q} + D\dot{q} + Kq + 2M\Omega\dot{q} \tag{4.12}$$

where

$$\tau = \begin{bmatrix} \tau_x \\ \tau_y \\ \tau_z \end{bmatrix} \qquad q = \begin{bmatrix} x \\ y \\ z \end{bmatrix} \qquad M = \begin{bmatrix} m & 0 & 0 \\ 0 & m & 0 \\ 0 & 0 & m \end{bmatrix}$$

$$D = \begin{bmatrix} d_{xx} & d_{xy} & d_{xz} \\ d_{xy} & d_{yy} & d_{yz} \\ d_{xz} & d_{yz} & d_{zz} \end{bmatrix} \quad K = \begin{bmatrix} k_{xx} & k_{xy} & k_{xz} \\ k_{xy} & k_{yy} & k_{yz} \\ k_{xz} & k_{yz} & k_{zz} \end{bmatrix} \quad \Omega = \begin{bmatrix} 0 & -\Omega_z & \Omega_y \\ \Omega_z & 0 & -\Omega_x \\ -\Omega_y & \Omega_x & 0 \end{bmatrix} \tag{4.13}$$

Looking at Equation (4.11), ideally the only dynamic coupling between each of the three axes would be through the Coriolis terms. This is true for a geometrically perfect device, however any real device will have some fabrication imperfections that cause dynamic coupling between the three axes through asymmetric stiffness terms k_{xy}, k_{xz}, k_{yz} and damping terms d_{xy}, d_{xz}, d_{yz}. The effects of these coupling terms on the system dynamics is similar to the effect of angular rate and contributes to erroneous signals on the device output.

4.3 Non-Dimensionalising

Non-dimensionalising the governing equations often results in fewer variables which simplifies investigation and leads to a better understanding of the model and also more efficient numerical computation .

It is based on making the model independent of the way things are measured which in turn allows subsequent results to be dimensionalised to any number of devices. This technique of non-dimensionalising is consistent with that of [60] and [61], as follows.

Starting with the angular rate sensor dynamic equation from Equation (4.12)

$$M\ddot{q} + D\dot{q} + Kq = \tau - 2M\Omega\dot{q} \tag{4.14}$$

non-dimensionalising takes the following steps. First dividing by a reference mass m, normally chosen as the proof mass, gives

$$\ddot{q} + \frac{D}{m}\dot{q} + \frac{K}{m}q = \frac{\tau}{m} - 2\Omega\dot{q} \tag{4.15}$$

Next, dividing by a reference length q_0, normally chosen as $1\mu m$ for MEMS devices gives

$$\frac{\ddot{q}}{q_0} + \frac{D}{m}\frac{\dot{q}}{q_0} + \frac{K}{m}\frac{q}{q_o} = \frac{\tau}{mq_0} - 2\Omega\frac{\dot{q}}{q_0} \tag{4.16}$$

Non-dimensional time $\tilde{t}$ is defined as $t\omega_0$ where ω_0 is a reference frequency, normally chosen as one of the axes natural frequencies, therefore the non-dimensional time derivatives are

$$\frac{d}{dt}(.) = \omega_0\frac{d}{d\tilde{t}}(.) \qquad \text{and} \qquad \frac{d^2}{dt^2}(.) = \omega_0^2\frac{d^2}{d\tilde{t}^2}(.) \tag{4.17}$$

which gives

$$\omega_0^2\frac{d^2}{d\tilde{t}^2}\left(\frac{q}{q_0}\right) + \omega_0\frac{D}{m}\frac{d}{d\tilde{t}}\left(\frac{q}{q_0}\right) + \frac{K}{m}\frac{q}{q_o} = \frac{\tau}{mq_0} - 2\omega_0\Omega\frac{d}{d\tilde{t}}\left(\frac{q}{q_0}\right) \tag{4.18}$$

Finally, dividing by ω_0^2 gives

$$\frac{d^2}{d\tilde{t}^2}\left(\frac{q}{q_0}\right) + \frac{D}{m\omega_0}\frac{d}{d\tilde{t}}\left(\frac{q}{q_0}\right) + \frac{K}{m\omega_0^2}\frac{q}{q_o} = \frac{\tau}{m\omega_0^2 q_0} - 2\frac{\Omega}{\omega_0}\frac{d}{d\tilde{t}}\left(\frac{q}{q_0}\right) \tag{4.19}$$

For convenience the following notation will be used,

$$\frac{d^2}{d\tilde{t}^2}\left(\frac{q}{q_0}\right) \to \ddot{q}, \qquad \frac{d}{d\tilde{t}}\left(\frac{q}{q_0}\right) \to \dot{q}, \qquad \frac{q}{q_o} \to q,$$

$$\frac{D}{m\omega_0} \to D, \qquad \frac{K}{m\omega_0^2} \to K, \qquad \frac{\tau}{m\omega_0^2 q_0} \to \tau \qquad \frac{\Omega}{\omega_0} \to \Omega \tag{4.20}$$

allowing the final non-dimensional equation to be expressed as

$$\ddot{q} + D\dot{q} + Kq = \tau - 2\Omega\dot{q} \tag{4.21}$$

4.4 Adaptive Controller Development

The following triaxial adaptive controller derivation has been adopted from that of the single axis system in [60] and [61]and can be seen as an extension of the single axis angular rate sensor approach into a triaxial system. Notation conventions have also been kept consistent where possible.

Ideal triaxial angular rate sensor dynamics can be expressed in matrix form as

$$\ddot{q} + K_{ideal} q = -2\Omega\dot{q} \tag{4.22}$$

where

$$K_{ideal} = \begin{bmatrix} \omega_x^2 & 0 & 0 \\ 0 & \omega_y^2 & 0 \\ 0 & 0 & \omega_z^2 \end{bmatrix} \tag{4.23}$$

$$\Omega = \begin{bmatrix} 0 & -\Omega_z & \Omega_y \\ \Omega_z & 0 & -\Omega_x \\ -\Omega_y & \Omega_x & 0 \end{bmatrix} \tag{4.24}$$

$$q = \begin{bmatrix} x \\ y \\ z \end{bmatrix} \tag{4.25}$$

Equation (4.22) is of the form of a perfect oscillator. Given that there are no damping terms in the ideal case, there is no energy lost in the system, only a transfer of energy between axes through the Coriolis term $-2\Omega\dot{q}$. The principle stiffness terms ω_x^2, ω_y^2 and ω_z^2 correspond to the squared non-dimensional resonant frequencies of each axis.

A practical angular rate sensor has a similar dynamic form to Equation (4.22) however it has a nonzero damping matrix D. The stiffness matrix K and damping matrix D also have unwanted cross coupling terms between each of the three axes as was shown in Section 4.1 and the stiffness in the x, y and z axes may not be as designed.

The dynamic equation for a real angular rate sensor is given in Equation (4.21) as

$$\ddot{q} + D\dot{q} + Kq = \tau - 2\Omega\dot{q} \tag{4.26}$$

This corresponds to the "Physical Device" block in the system block diagram of Figure 4.3,

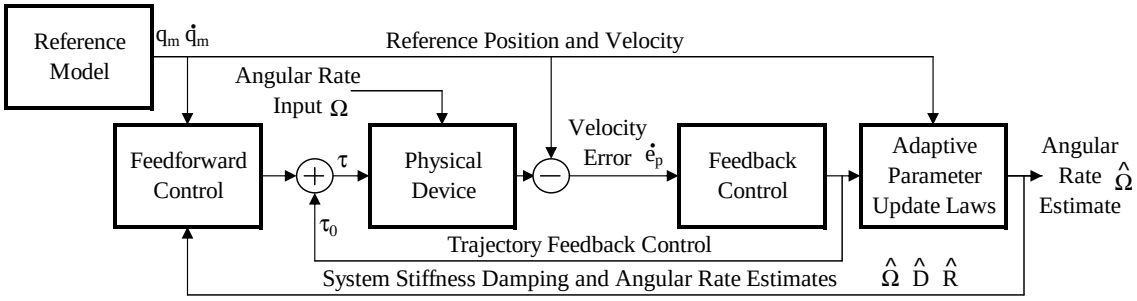

Figure 4.3: Proposed adaptive control system diagram.

where

$$K = \begin{bmatrix} k_{xx} & k_{xy} & k_{xz} \\ k_{xy} & k_{yy} & k_{yz} \\ k_{xz} & k_{yz} & k_{zz} \end{bmatrix} \tag{4.27}$$

$$D = \begin{bmatrix} d_{xx} & d_{xy} & d_{xz} \\ d_{xy} & d_{yy} & d_{yz} \\ d_{xz} & d_{yz} & d_{zz} \end{bmatrix} \tag{4.28}$$

and τ is the sum of the feedforward and feedback control forces. It is subsequently defined in Equation (4.30).

The reference model shown in Figure 4.3, is similar to the dynamic equation of the ideal angular rate sensor in Equation (4.22). However since the input rotation Ω is one of the unknown parameters, the Coriolis term is removed from the reference model and added to the feed forward control law τ so that it can be estimated and compensated in a similar manner to the stiffness and damping errors. Therefore the reference model becomes

$$\ddot{q}_m + K_m q_m = 0 \tag{4.29}$$

where K_m is identical to K_{ideal} in Equation (4.24) with the constraint $\omega_x \neq \omega_y \neq \omega_z$ given in Section 4.7. The m subscripts denote parameters belonging to the reference model.

The estimated parameters are the input rotation estimate $\hat{\Omega}$, the estimate of the damping matrix of the real system $\hat{D}$ and the estimate of the difference between the actual stiffness matrix and that of the reference model $\hat{R} = \hat{K} - K_m$. These system parameters are continuously estimated and their effects compensated using feedforward control.

The control law τ is defined as

$$\tau = \hat{D}\dot{q}_m + \hat{R}q_m + 2\hat{\Omega}\dot{q}_m + \tau_0 \tag{4.30}$$

The first three terms form the feedforward control. There is an additional feedback control term τ_0 defined as

$$\tau_0 = -\gamma\dot{e}_p \tag{4.31}$$

with the positive definite gain matrix

$$\gamma = \begin{bmatrix} \gamma_x & 0 & 0 \\ 0 & \gamma_y & 0 \\ 0 & 0 & \gamma_z \end{bmatrix} \tag{4.32}$$

and

$$e_p = q - q_m \tag{4.33}$$

The τ_0 term serves to correct the mass's trajectory due to any inaccurate estimates and is subsequently used to correct the estimates in the adaptation laws Equations (4.36)-(4.38). It also stabilises the system given that the damping matrix D could in theory be zero ($D \geq 0$). This is explained further following Equation (4.40).

Two good resources for the following Lyapunov-based adaptive controller design are [36] and [67]. The method is based on the existence of a Lyapunov function, which is an energylike function, zero at equilibrium and positive definite everywhere else. For the system to be deemed stable, the derivative of the Lyapunov function must be made negative semi-definite. This is done with careful selection of the adaptation laws.

Considering the positive definite Lyapunov function candidate V as presented for the single axis device in [60]

$$V = \frac{1}{2}\left(\dot{e}_p^T\gamma\dot{e}_p + e_p^T\gamma K e_p + tr\{\gamma_R^{-1}\tilde{R}\tilde{R}^T + \gamma_D^{-1}\tilde{D}\tilde{D}^T + \gamma_\Omega^{-1}\tilde{\Omega}\tilde{\Omega}^T\}\right) \tag{4.34}$$

Note that for any practical device the K matrix in the Lyapunov function will be positive definite; although structural imperfections will cause cross stiffness terms k_{xy}, k_{yz} and k_{xz} to

appear, with good structural design such as using mirrored symmetry in each axis, they will be small compared to the main diagonal terms k_{xx}, k_{yy} and k_{zz}. Therefore $K = K^T$ is positive definite.

Taking the time derivative of the above Lyapunov function Equation (4.34) along the error trajectory gives

$$\begin{aligned}\dot{V} &= -\dot{e}_p^T \gamma \left(\gamma + D + 2\Omega\right) \dot{e}_p \\ &\quad + tr\left\{\tilde{R}\left(\gamma_R^{-1}\dot{\hat{R}}^T - \frac{1}{2}\dot{q}_m\tau_0^T - \frac{1}{2}\tau_0\dot{q}_m^T\right)\right. \\ &\quad + \tilde{D}\left(\gamma_D^{-1}\dot{\hat{D}}^T - \frac{1}{2}q_m\tau_0^T - \frac{1}{2}\tau_0 q_m^T\right) \\ &\quad \left. + \tilde{\Omega}\left(\gamma_\Omega^{-1}\dot{\hat{\Omega}}^T - \dot{q}_m\tau_0^T + \tau_0\dot{q}_m^T\right)\right\} \end{aligned} \tag{4.35}$$

Given that $\dot{\hat{R}} = \dot{\hat{R}}^T$, $\dot{\hat{D}} = \dot{\hat{D}}^T$ and $\dot{\hat{\Omega}} = -\dot{\hat{\Omega}}^T$, in order to make Equation (4.35) negative semi-definite the adaptation laws are chosen as

$$\dot{\hat{R}} = \frac{1}{2}\gamma_R\left(\tau_0\dot{q}_m^T + \dot{q}_m\tau_0^T\right) \tag{4.36}$$

$$\dot{\hat{D}} = \frac{1}{2}\gamma_D\left(\tau_0\dot{q}_m^T + \dot{q}_m\tau_0^T\right) \tag{4.37}$$

$$\dot{\hat{\Omega}} = \gamma_\Omega\left(\tau_0\dot{q}_m^T - \dot{q}_m\tau_0^T\right) \tag{4.38}$$

This leaves

$$\dot{V} = -\dot{e}_p^T\gamma\left(\gamma + D + 2\Omega\right)\dot{e}_p \tag{4.39}$$

which, due to Ω being skew symmetric, leads to

$$\dot{V} = -\dot{e}_p^T\gamma\left(\gamma + D\right)\dot{e}_p \tag{4.40}$$

Given γ is positive definite and D is positive semi-definite then $\gamma + D$ will be positive definite and since $\dot{e}_p$ can be a zero vector, $\dot{V}$ is negative semi-definite and the Lyapunov stability criterion is satisfied. Since D can be a zero matrix, γ ensures that $\dot{V} \neq 0$ while $\dot{e}_p \neq 0$.

The outer parameter estimate loop is slow changing compared to the fast changing inner feedback control loop. In this respect the two loops can be considered as decoupled.

4.5 Operation

The operation of the adaptive controller for the triaxial angular rate sensor is outlined in Figure 4.3. The fast changing displacement and velocity variables of the vibrating mass are compared to those of an ideal reference model trajectory, which will be developed in Section 4.7. The error between the actual and model trajectories is used in a feedback control to maintain the mass's motion along the reference model three dimensional Lissajous trajectory, removing the need for additional drive control. This feedback signal is then used by the adaptation laws in Equations (4.36)-(4.38), to update the estimates of all the unknown, slow changing parameters, namely the damping D, stiffness error R and angular rate Ω. These parameter estimates are then used in a feed forward control to compensate for the effects of the undesirable imperfections and time varying effects (discussed in Section 4.1) as well as the input angular rate Ω. Estimation and control stages have been kept separate so that the output of the device can simply be taken from the parameter estimates of the input rotations $\hat{\Omega}_x$, $\hat{\Omega}_y$ and $\hat{\Omega}_z$. This removes the need for additional demodulation stages normally required by angular rate sensors [27].

4.6 Stability Analysis

It was shown above that the Lyapunov function is non-increasing and therefore the system is stable. This however is insufficient proof that the trajectory error e_p and its time derivatives $\dot{e}_p$ and $\ddot{e}_p$ approach zero.

It was shown that $\dot{V}$ is negative semi-definite therefore V is bounded and each element of V is also bounded, including e_p, $\dot{e}_p$, $\tilde{R}$, $\tilde{D}$ and $\tilde{\Omega}$.

Using Barbalat's lemma which states; If $f(t)$ is a uniformly continuous function such that $\lim_{x\to\infty} \int_0^t f(\tau)d\tau$ exists and is finite (i.e. bounded), then $f(t) \to 0$ as $t \to \infty$ [67]. Then since V is bounded $\dot{V} \to 0$ and from 4.40, leads to $\dot{e}_p \to 0$. Again using Barbalat's lemma, since $\dot{e}_p$ is bounded $\ddot{e}_p \to 0$. Lastly, to ensure that $e_p \to 0$, we need to show that $\int_0^\infty e_p dt$ is bounded as follows.

Substituting the control law Equation (4.30) into the system dynamics Equation (4.26) gives

$$\ddot{q} + (D + 2\Omega)\,\dot{q} + Kq = \hat{D}\dot{q}_m + \hat{R}q_m + 2\hat{\Omega}\dot{q}_m + \tau_0 \tag{4.41}$$

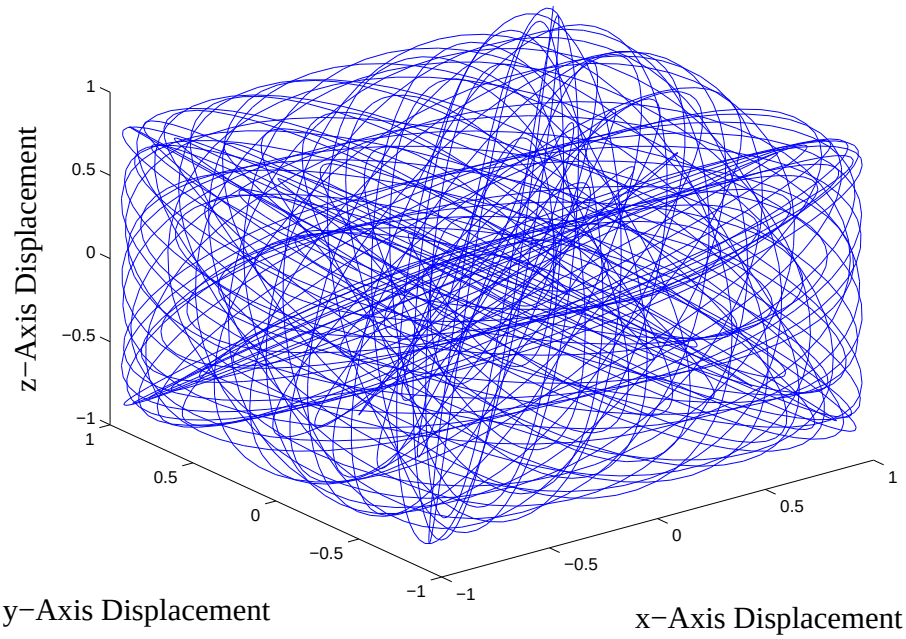

Figure 4.4: Three dimensional Lissajous reference model trajectory created by the unmatched frequencies modes in the x, y and z axes.

Expressing this in terms of the error vector e_p with Equation (4.31) gives the trajectory error dynamics

$$\ddot{e}_p + (\gamma + D + 2\Omega)\,\dot{e}_p + Ke_p = \tilde{D}\dot{q}_m + \tilde{R}q_m + 2\tilde{\Omega}\dot{q}_m \tag{4.42}$$

Rearranging and taking the integral of both sides

$$\int_0^\infty Ke_p dt = -\int_0^\infty \ddot{e}_p dt - \int_0^\infty (\gamma + D + 2\Omega)\dot{e}_p dt + \int_0^\infty \tilde{D}\dot{q}_m + \tilde{R}q_m + 2\tilde{\Omega}\dot{q}_m dt \tag{4.43}$$

Since $\ddot{e}_p \to 0$ and $\dot{e}_p \to 0$ the first two integrals are bounded. Also given that q_m and $\dot{q}_m$ are fast changing sinusoids (with zero averages) and the parameter estimate errors $\tilde{R}$, $\tilde{D}$ and $\tilde{\Omega}$ are slow changing and bounded, the last integral is also bounded. Therefore since $\int_0^\infty Ke_p dt$ is bounded, using Barbalat's lemma, $e_p \to 0$.

Revisiting Equation (4.42) shows that since the trajectory error and its derivatives approach zero $\ddot{e}_p, \dot{e}_p, e_p \to 0$ then $\tilde{D}\dot{q}_m + \tilde{R}q_m + 2\tilde{\Omega}\dot{q}_m \to 0$ and are therefore stable.

4.7 Persistence of Excitation

In order for all parameter estimates to converge to their true values, positive constants δ, α_1 and α_2 must exist so that the the persistence or excitation condition (Equation (4.44)) is met [67]. This ensures the excitation gives enough information about the estimated parameters.

$$\alpha_2 I \geq \int_t^{t+\delta} W\left(q_m, \dot{q}_m\right) W^T\left(q_m, \dot{q}_m\right) d\tau \geq \alpha_1 I \quad \forall t \geq t_0 \tag{4.44}$$

where I is an identity matrix and the triaxial error dynamics are expressed in regressor form as

$$W^T(q_m, \dot{q}_m)\tilde{\theta} = \tilde{D}\dot{q}_m + \tilde{K}q_m + 2\tilde{\Omega}\dot{q}_m \tag{4.45}$$

With the error vector $\tilde{\theta}$ and regressor $W(q_m, \dot{q}_m)$

$$\tilde{\theta} = \begin{bmatrix} \tilde{r}_{xx} \\ \tilde{r}_{yy} \\ \tilde{r}_{zz} \\ \tilde{r}_{xy} \\ \tilde{r}_{xz} \\ \tilde{r}_{yz} \\ \tilde{d}_{xx} \\ \tilde{d}_{yy} \\ \tilde{d}_{zz} \\ \tilde{d}_{xy} \\ \tilde{d}_{xz} \\ \tilde{d}_{yz} \\ \tilde{\Omega}_x \\ \tilde{\Omega}_y \\ \tilde{\Omega}_z \end{bmatrix}, \quad W(q_m, \dot{q}_m) = \begin{bmatrix} x_m & 0 & 0 \\ 0 & y_m & 0 \\ 0 & 0 & z_m \\ y_m & x_m & 0 \\ z_m & 0 & x_m \\ 0 & z_m & y_m \\ \dot{x}_m & 0 & 0 \\ 0 & \dot{y}_m & 0 \\ 0 & 0 & \dot{z}_m \\ \dot{y}_m & \dot{x}_m & 0 \\ \dot{z}_m & 0 & \dot{x}_m \\ 0 & \dot{z}_m & \dot{y}_m \\ 0 & -\dot{z}_m & 2\dot{y}_m \\ 2\dot{z}_m & 0 & -2\dot{x}_m \\ -2\dot{y}_m & 2\dot{x}_m & 0 \end{bmatrix} \tag{4.46}$$

where the displacement in each axis of the reference model trajectory is chosen to be sinusoidal.

$$\begin{aligned} x_m &= X_0 \sin(\omega_x t), & \dot{x}_m &= X_0 \omega_x \cos(\omega_x t) \\ y_m &= Y_0 \sin(\omega_y t), & \dot{y}_m &= Y_0 \omega_y \cos(\omega_y t) \\ z_m &= Z_0 \sin(\omega_z t), & \dot{z}_m &= Z_0 \omega_z \cos(\omega_z t) \end{aligned} \tag{4.47}$$

Here X_0, Y_0 and Z_0 are the amplitudes of vibration in the x, y and z axis respectively.

As stated in [60], the persistence of excitation condition can always be met for the single z axis angular rate sensor when the reference model's x and y axes resonant frequencies are unmatched ($\omega_x \neq \omega_y$). Extending this unmatched resonant frequencies condition to the triaxial case gives $\omega_x \neq \omega_y \neq \omega_z$. This creates a three dimensional Lissajous trajectory for the reference model as can be seen in Figure 4.4. Ideally the persistence of excitation condition (Equation (4.44)) with regressor $W^T(q_m, \dot{q}_m)$ (Equation (4.46)) could be shown analytically to hold for all cases. This requires showing the positive definiteness of a 15×15 matrix. By inspection it is at least semi-definite, however proof of positive definiteness was found to be intractable by hand and too computationally intense using the symbolic software package Maple. Numerical substitutions using realistic case values indicate the persistence of excitation condition can be met when all modes are unmatched and has also been found analytically to always fail when all the resonant frequencies are matched. Although three sine waves appears to be insufficient excitation to allow the estimation of 15 parameters, additional higher frequencies are developed as a result of the cross coupling effects that provides additional information. Clearly unmatched resonant frequencies are required for these higher frequencies to appear and integer multiples should also be avoided. The adaptive controller has been implemented in MATLAB for a thorough simulation study. All the simulations have shown that the mass's trajectory converges to the reference model trajectory and the parameter estimates all converge to the correct values when $\omega_x \neq \omega_y \neq \omega_z$. This behaviour is as expected for a system where the persistence of excitation condition is met.

4.8 Convergence Analysis

Analysing the convergence rate of the parameter estimates reveals important information about the adaptive control system including the bandwidth of the device. It reveals optimum operating

constraints on the reference model amplitudes and also gives insight into the selection of adaptive gains.

4.8.1 Averaging

Averaging is a method used to analyse the average behaviour of systems with both fast and slow (mixed) dynamics. It involves equating the system dynamics with a slow-varying averaged system.

In this section an overview of averaging in its simplest one-time scale form is given with an example taken from Sastry [67]. This is then extended to two-scale forms and the more general mixed-time scale form which is more often encountered in adaptive control. The mixed-time scale system undergoes a transformation to get it into the form of a two-time scale system that allows the averaging method to be used.

One-Time Scale Averaging

A system of the form

$$\dot{x} = \epsilon f(t, x) \tag{4.48}$$

can be equated with its *averaged* system

$$\dot{x}_{av} = \epsilon f_{av}(x_{av}) \tag{4.49}$$

where

$$f_{av} = \lim_{T \to \infty} \frac{1}{T} \int_{t_0}^{t_0+T} f(\tau, x) d\tau \tag{4.50}$$

assuming the limit exists and ϵ is sufficiently small. The small ϵ makes the system slow varying.

The following is a basic example showing the averaging method. A comparison of the averaged solution to the exact solution shows the accuracy of the averaged solution is inversely proportional to the size of ϵ.

Consider the differential equation

$$\dot{x} = -\epsilon \sin^2(t) x \qquad x(0) = x_0 \tag{4.51}$$

This is of the form of Equation (4.48). Using Equation (4.50)

$$\begin{aligned} f_{av} &= \lim_{T\to\infty}\frac{1}{T}\int_{t_0}^{t_0+T}\sin^2(\tau)xd\tau && (4.52)\\ &= \lim_{T\to\infty}\frac{1}{T}\int_{t_0}^{t_0+T}\frac{x}{2}-\frac{x}{2}\cos(2\tau)xd\tau && (4.53)\\ &= \frac{x}{2}-\lim_{T\to\infty}\frac{1}{T}\int_{t_0}^{t_0+T}\frac{x}{2}\cos(2\tau)xd\tau && (4.54)\\ &= \frac{x}{2} && (4.55)\end{aligned}$$

The limit here is zero since the average of a sinusoid wave is zero. Therefore the averaged system becomes simply

$$\dot{x}_{av} = \epsilon\frac{x_{av}}{2} \qquad x(0) = x_0 \tag{4.56}$$

The solution of which is

$$x_{av} = e^{\epsilon\frac{t}{2}}x_0 \tag{4.57}$$

Comparing this with the exact solution of Equation (4.51), which can be shown to be

$$x_t = e^{-\epsilon\frac{t}{2}+\frac{\epsilon}{4}\sin(2t)}x_0 \tag{4.58}$$

The difference between the solution, at some fixed time t is

$$|x(t) - x_{av}(t)| = e^{-\epsilon\frac{t}{2}}|e^{\frac{\epsilon}{4}\sin(2t)} - 1| \tag{4.59}$$

The error between the two solutions diminishes as $\epsilon \to 0$ and the system given in Equation (4.51) can be approximated by the averaged system given in Equation (4.56). As stated in [67] the original and averaged systems have identical convergence rates.

Two-Time Scale Averaging

Consider the following system

$$\begin{aligned} \dot{x} &= \epsilon f(t,x,y)\\ \dot{y} &= Ay + \epsilon g(t,x,y) && (4.60)\end{aligned}$$

with conditions

$$x(0) = x_0, \qquad x \in \Re^n, \qquad y(0) = y_0, \qquad y \in \Re^n \tag{4.61}$$

and assuming there is an equilibrium point at $x = 0, y = 0$, therefore

$$f(t, 0, 0) = 0 \qquad g(t, 0, 0) = 0, \qquad \forall t \geq 0 \tag{4.62}$$

Assuming that the matrix A of the fast dynamics is asymptotically stable. This system is called a two separated time scale system, since as $\epsilon \to 0$, the fast state y becomes independent of the slow state x. Therefore we can use the averaging method to relate the slow dynamics with the dynamics of the averaged system

$$\dot{x}_{av} = \epsilon f_{av}(t, x), \qquad x_{av}(0) = x_0 \tag{4.63}$$

where

$$f_{av}(x_{av}) = \lim_{T \to \infty} \frac{1}{T} \int_{t_0}^{t_0+T} f(\tau, x, 0) d\tau \tag{4.64}$$

Mixed-Time Scale Averaging

The more general class of systems encountered in adaptive control are mixed time scale systems of the form

$$\begin{aligned} \dot{x} &= \epsilon f' \left(t, x, y'\right) \\ \dot{y}' &= Ay' + h\left(t, x\right) + \epsilon g' \left(t, x, y'\right) \end{aligned} \tag{4.65}$$

In this case x is the slow state as before, since ϵ is sufficiently small, but y' has both fast (Ay) and slow ($h\left(t, x\right)$) components. (Notice that there is no ϵ in the $h\left(t, x\right)$ term.)

In order to use the averaging method on this type of system it must first be transformed into a two separated time scale systems. To do this we use the transformation

$$y = y' - \nu\left(t, x\right) \tag{4.66}$$

where $\nu(t,x)$ is defined as

$$\nu(t,x) = \int_0^t e^{A(t-\tau)} h(\tau,x)\, d\tau \tag{4.67}$$

which is the steady state solution to the second equation of 4.65

$$\dot{y}' = Ay' + h(t,x) + \epsilon g'\left(t,x,y'\right) \tag{4.68}$$

with x frozen and $\epsilon = 0$.

Applying the transformation Equation (4.66) to the mixed time scale system Equation (4.65) gives

$$\dot{x} = \epsilon f'(t,x,y+\nu(t,x)) \tag{4.69}$$

which is of the form $\epsilon f(t,x,y)$ as required and

$$\dot{y} + \dot{\nu} = A[y+\nu(t,x)] + h(t,x) + \epsilon g'(t,x,y+\nu(t,x)) \tag{4.70}$$

Since ν is a function of both x and t, it's time derivative can be found using the chain rule

$$\frac{d\nu}{dt} = \frac{\partial \nu}{\partial t} + \frac{\partial \nu}{\partial x}\frac{dx}{dt} \tag{4.71}$$

To find $\frac{\partial \nu}{\partial t}$ start with Equation (4.67) and add a small time differential to each t term

$$\nu(t+\delta t,x) = \int_0^{t+\delta t} e^{A(t+\delta t-\tau)} h(\tau,x)\, d\tau \tag{4.72}$$

Subtracting Equation (4.67) gives

$$\begin{aligned} \delta\nu &= \nu(t+\delta t,x) - \nu(t,x) && (4.73)\\ &= \int_0^{t+\delta t} e^{A(t+\delta t-\tau)} h(\tau,x)\, d\tau - \int_0^t e^{A(t-\tau)} h(\tau,x)\, d\tau && (4.74) \end{aligned}$$

The first integral can be split at time t giving

$$\delta\nu = \int_t^{t+\delta t} e^{A(t+\delta t-\tau)} h(\tau,x)\, d\tau + \int_0^t e^{A(t+\delta t-\tau)} h(\tau,x)\, d\tau - \int_0^t e^{A(t-\tau)} h(\tau,x)\, d\tau \tag{4.75}$$

This allows the grouping

$$\delta\nu = \int_t^{t+\delta t} e^{A(t+\delta t-\tau)} h\left(\tau, x\right) d\tau + \int_0^t \left[e^{A(t+\delta t-\tau)} - e^{A(t-\tau)}\right] h\left(\tau, x\right) d\tau \tag{4.76}$$

and further simplification to

$$\delta\nu = h\left(t, x\right) \delta t + \int_0^t \left[e^{A\delta t} - I\right] e^{A(t-\tau)} h\left(\tau, x\right) d\tau \tag{4.77}$$

Using the first two terms of the series expansion for $e^{A\delta t} = I + A\delta t + \frac{A\delta t}{2!} + \ldots$ gives

$$\delta\nu = h\left(t, x\right) \delta t + A\delta t \int_0^t e^{A(t-\tau)} h\left(\tau, x\right) d\tau \tag{4.78}$$

Substituting the definition of $\nu(t, x)$ from Equation (4.67)

$$\delta\nu = h\left(t, x\right) \delta t + A\nu(t, x)\delta t \tag{4.79}$$

Finally

$$\frac{\partial\nu}{\partial t} = h\left(\tau, x\right) + A\nu(t, x) \tag{4.80}$$

Substituting this and Equation (4.69) into the chain rule, Equation (4.71), then into Equation (4.70) gives

$$\dot{y} + h\left(\tau, x\right) + A\nu(x, t) + \frac{\partial\nu}{\partial x}\epsilon f'\left(t, x, y + \nu\left(t, x\right)\right) = A\left[y + \nu(t, x)\right] + h\left(t, x\right) + \epsilon g'\left(t, x, y + \nu(t, x)\right) \tag{4.81}$$

Rearranging gives

$$\dot{y} = Ay + \epsilon\left[-\frac{\partial\nu}{\partial x} f'\left(t, x, y + \nu\left(t, x\right)\right) + g'\left(t, x, y + \nu(t, x)\right)\right] \tag{4.82}$$

which is now in the required form

$$\dot{y} = Ay + \epsilon g\left(t, x, y\right) \tag{4.83}$$

where

$$g\left(t, x, y\right) = -\frac{\partial\nu}{\partial x} f'\left(t, x, y + \nu\left(t, x\right)\right) + g'\left(t, x, y + \nu(t, x)\right) \tag{4.84}$$

The average function, Equation (4.103), is also modified to

$$f_{av}(x_{av}) = \lim_{T\to\infty} \frac{1}{T} \int_{t_0}^{t_0+T} f'(\tau, x, \nu(\tau, x))d\tau \tag{4.85}$$

Application of Mixed-Time Scale Averaging to the Triaxial Angular Rate System

To use the transformed average function, the adaptive control dynamic equations must be arranged in the same form as Equation (4.65).

The error dynamics of the triaxial angular rate sensor are given in Equation (4.42) as

$$\ddot{e}_p + (\gamma + D + 2\Omega)\,\dot{e}_p + Ke_p = \tilde{D}\dot{q}_m + \tilde{R}q_m + 2\tilde{\Omega}\dot{q}_m$$

In order to use the averaging method it is assumed that $\gamma >> (D + 2\Omega)$ and therefore in the regressor form of Equation (4.45)

$$\ddot{e}_p + \gamma\dot{e}_p + K_m e_p = W^T(q_m, \dot{q}_m)\,\tilde{\theta} \tag{4.86}$$

$$\dot{\tilde{\theta}} = -\Gamma W(q_m, \dot{q}_m)\,\gamma\dot{e}_p \tag{4.87}$$

with Γ defined as

$$\Gamma = diag\{\gamma_R, \gamma_R, \gamma_R, \frac{1}{2}\gamma_R, \frac{1}{2}\gamma_R, \frac{1}{2}\gamma_R, \gamma_D, \gamma_D, \gamma_D, \frac{1}{2}\gamma_D, \frac{1}{2}\gamma_D, \frac{1}{2}\gamma_D, \frac{1}{2}\gamma_\Omega, \frac{1}{2}\gamma_\Omega, \frac{1}{2}\gamma_\Omega\} \tag{4.88}$$

Equation (4.86) can be expressed as

$$\ddot{e}_p = \begin{bmatrix} -K_m & -\gamma \end{bmatrix} \begin{bmatrix} e_p \\ \dot{e}_p \end{bmatrix} + W^T(q_m, \dot{q}_m)\,\tilde{\theta} \tag{4.89}$$

and introducing the notations $x = \tilde{\theta}$ and $y' = \begin{bmatrix} e_p \\ \dot{e}_p \end{bmatrix}$, Equation (4.86) becomes

$$\dot{y}' = \begin{bmatrix} 0 & I \\ -K_m & -\gamma \end{bmatrix} y' + \begin{bmatrix} 0 \\ W^T(q_m, \dot{q}_m) \end{bmatrix} x \tag{4.90}$$

$$= \begin{bmatrix} 0 & I \\ -K_m & -\gamma \end{bmatrix} y' + C^T W^T(q_m, \dot{q}_m)\, x \tag{4.91}$$

where C for the triaxial case is the $[3 \times 6]$ matrix

$$\begin{bmatrix} 0 & I \end{bmatrix} \tag{4.92}$$

Equating with Equation (4.65) gives

$$A = \begin{bmatrix} 0 & I \\ -K_m & -\gamma \end{bmatrix}, \qquad h(t,x) = C^T W^T(q_m, \dot{q}_m)\, x, \qquad g'\left(t, x, y'\right) = 0 \tag{4.93}$$

Using these substitutions in Equation (4.67) gives

$$\nu(t,x) = \int_0^t e^{A(t-\tau)} h(\tau, x)\, d\tau$$

$$= \int_0^t e^{A(t-\tau)} C^T W^T(q_m, \dot{q}_m)\, x d\tau \tag{4.94}$$

$$= \left[\int_0^t e^{A(t-\tau)} C^T W^T(q_m, \dot{q}_m)\, d\tau\right] x \tag{4.95}$$

$$= \nu(t) x \tag{4.96}$$

Equation (4.87) can also be expressed using the same notation as

$$\dot{x} = -\Gamma W(q_m, \dot{q}_m)\, \gamma C y' \tag{4.97}$$

Equating with Equation (4.65) gives

$$\epsilon = \Gamma, \qquad f'\left(t, x, y'\right) = W(q_m, \dot{q}_m)\, \gamma C y' \tag{4.98}$$

which leads to

$$f\left(t,x,y\right)=-W\left(q_m,\dot{q}_m\right)\gamma C(y+\nu(t)x) \tag{4.99}$$

Similarly using Equation (4.84),

$$\begin{aligned} g\left(t,x,y\right) &= -\frac{\partial\nu}{\partial x}f'\left(t,x,y+\nu\left(t,x\right)\right)+g'\left(t,x,y+\nu(t,x)\right) && (4.100)\\ &= \nu(t)W\left(q_m,\dot{q}_m\right)\gamma C(y+\nu(t)x) && (4.101)\end{aligned}$$

The averaged system is given by

$$\dot{x}_{av}=-\gamma f_{av}\left(x_{av}\right) \tag{4.102}$$

where

$$\begin{aligned} f_{av}(x_{av}) &= \lim_{T\to\infty}\frac{1}{T}\int_{t_0}^{t_0+T}f(\tau,x,\nu(\tau,x))d\tau && (4.103)\\ &= \lim_{T\to\infty}\frac{1}{T}\int_{t_0}^{t_0+T}W\left(q_m,\dot{q}_m\right)\gamma C\nu(t)dtx_{av} && (4.104)\\ &= \lim_{T\to\infty}\frac{1}{T}\int_{t_0}^{t_0+T}W\left(q_m,\dot{q}_m\right)\gamma C\int_0^t e^{A(t-\tau)}C^TW^T\left(q_m,\dot{q}_m\right)d\tau dtx_{av} && (4.105)\end{aligned}$$

This and Equations (4.99) and (4.100) are similar results to those in [60].

It can be shown that

$$x=\gamma C\int_0^t e^{A(t-\tau)}C^TW^T\left(q_m,\dot{q}_m\right)d\tau \tag{4.106}$$

is the solution to the system

$$\dot{x}(t)=Ax(t)+C^Tu(t) \tag{4.107}$$

$$y(t)=\gamma Cx(t) \tag{4.108}$$

with $x(0)=0$ and the input

$$u(t)=W^T\left(q_m,\dot{q}_m\right) \tag{4.109}$$

Taking the Laplace transform and rearranging gives the transfer function $\hat{M}$.

$$\hat{M}(s)=\gamma C\left[sI-A\right]^{-1}C^T \tag{4.110}$$

which equates to

$$\hat{M} = \begin{bmatrix} \frac{\gamma_x s}{s^2+\gamma_x s+\omega_x^2} & 0 & 0 \\ 0 & \frac{\gamma_y s}{s^2+\gamma_y s+\omega_y^2} & 0 \\ 0 & 0 & \frac{\gamma_z s}{s^2+\gamma_z s+\omega_z^2} \end{bmatrix} \tag{4.111}$$

The averaged system, Equation (4.102) can now be expressed as

$$\dot{\tilde{\theta}}_{av} = -\Gamma AVG\{W\left(q_m, \dot{q}_m\right)\hat{M}\left(W\left(q_m, \dot{q}_m\right)\right)\}\tilde{\theta}_{av} \tag{4.112}$$

Therefore the filtered steady-state response through $\hat{M}W\left(q_m, \dot{q}_m\right)$ is

$$\hat{M} \quad W^T\left(q_m, \dot{q}_m\right) \quad = \begin{bmatrix} X_0 sin(\omega_x t) & 0 & 0 \\ 0 & Y_0 sin(\omega_y t) & 0 \\ 0 & 0 & Z_0 sin(\omega_z t) \\ A_{xy} Y_0 sin(\omega_y t + \phi_{xy}) & A_{yx} X_0 sin(\omega_x t + \phi_{yx}) & 0 \\ A_{xz} Z_0 sin(\omega_z t + \phi_{xz}) & 0 & A_{zx} X_0 sin(\omega_x t + \phi_{zx}) \\ 0 & A_{yz} Z_0 sin(\omega_z t + \phi_{yz}) & A_{zy} Y_0 sin(\omega_y t + \phi_{zy}) \\ X_0 \omega_x cos(\omega_x t) & 0 & 0 \\ 0 & Y_0 \omega_y cos(\omega_y t) & 0 \\ 0 & 0 & Z_0 \omega_z cos(\omega_z t) \\ A_{xy} Y_0 \omega_y cos(\omega_y t + \phi_{xy}) & A_{yx} X_0 \omega_x cos(\omega_x t + \phi_{yx}) & 0 \\ A_{xz} Z_0 \omega_z cos(\omega_z t + \phi_{xz}) & 0 & A_{zx} X_0 \omega_x cos(\omega_x t + \phi_{zx}) \\ 0 & A_{yz} Z_0 \omega_z cos(\omega_z t + \phi_{yz}) & A_{zy} Y_0 \omega_y cos(\omega_y t + \phi_{zy}) \\ 0 & -2A_{yz} Z_0 \omega_z cos(\omega_z t + \phi_{yz}) & 2A_{zy} Y_0 \omega_y cos(\omega_y t + \phi_{zy}) \\ 2A_{xz} Z_0 \omega_z cos(\omega_z t + \phi_{xz}) & 0 & -2A_{zx} X_0 \omega_x cos(\omega_x t + \phi_{zx}) \\ -2A_{xy} Y_0 \omega_y cos(\omega_y t + \phi_{xy}) & 2A_{yx} X_0 \omega_x cos(\omega_x t + \phi_{yx}) & 0 \end{bmatrix}^T \tag{4.113}$$

where

$$A_{mn} = \frac{\gamma_m \omega_n}{\sqrt{\gamma_m^2 \omega_n^2 + \left(\omega_m^2 - \omega_n^2\right)^2}}, \quad \phi_{mn} = tan^{-1}\left(\frac{\omega_m^2 - \omega_n^2}{\gamma_m \omega_n}\right), \quad m, n = x, y, z \tag{4.114}$$

The transfer function matrix $\hat{M}$ is strictly positive real therefore $-90^\circ \leq \phi_{mn} \leq 90^\circ$ and

$$cos\left(\phi_{mn}\right) = A_{mn} \tag{4.115}$$

The products of two sinusoids with different frequencies have a zero averages as do the products

of a sine and cosine with the same frequencies. Using this and the trigonometric identities

$$sin(\omega t + \phi) = sin(\omega t)cos(\phi) + cos(\omega t)sin(\phi) \tag{4.116}$$

$$cos(\omega t + \phi) = cos(\omega t)cos(\phi) + sin(\omega t)sin(\phi) \tag{4.117}$$

the average equations of the parameter estimate errors, from Equation (4.112) are

$$\dot{\tilde{r}}_{xx_{av}} = -\frac{\gamma_R}{2} X_0^2 \tilde{r}_{xx_{av}} \tag{4.118}$$

$$\dot{\tilde{r}}_{yy_{av}} = -\frac{\gamma_R}{2} Y_0^2 \tilde{r}_{yy_{av}} \tag{4.119}$$

$$\dot{\tilde{r}}_{zz_{av}} = -\frac{\gamma_R}{2} Z_0^2 \tilde{r}_{zz_{av}} \tag{4.120}$$

$$\begin{aligned}
\dot{\tilde{r}}_{xy_{av}} = & -\frac{\gamma_R}{4}\left(\frac{\gamma_y^2 X_0^2 \omega_x^2}{\gamma_y^2\omega_x^2 + (\omega_x^2 - \omega_y^2)^2} + \frac{\gamma_x^2 Y_0^2 \omega_y^2}{\gamma_x^2\omega_y^2 + (\omega_y^2 - \omega_x^2)^2}\right)\tilde{r}_{xy_{av}} \\
& -\frac{\gamma_R}{4}\left(\frac{\gamma_y X_0^2 \omega_x^2 \left(\omega_y^2 - \omega_x^2\right)}{\gamma_y^2\omega_x^2 + (\omega_x^2 - \omega_y^2)^2} + \frac{\gamma_x Y_0^2 \omega_y^2 \left(\omega_x^2 - \omega_y^2\right)}{\gamma_x^2\omega_y^2 + (\omega_y^2 - \omega_x^2)^2}\right)\tilde{d}_{xy_{av}} \\
& -\frac{\gamma_R}{2}\left(\frac{\gamma_y X_0^2 \omega_x^2 \left(\omega_y^2 - \omega_x^2\right)}{\gamma_y^2\omega_x^2 + (\omega_x^2 - \omega_y^2)^2} - \frac{\gamma_x Y_0^2 \omega_y^2 \left(\omega_y^2 - \omega_x^2\right)}{\gamma_x^2\omega_y^2 + (\omega_y^2 - \omega_x^2)^2}\right)\tilde{\Omega}_{z_{av}}
\end{aligned} \tag{4.121}$$

$$\begin{aligned}
\dot{\tilde{r}}_{xz_{av}} = & -\frac{\gamma_R}{4}\left(\frac{\gamma_z^2 X_0^2 \omega_x^2}{\gamma_z^2\omega_x^2 + (\omega_x^2 - \omega_z^2)^2} + \frac{\gamma_x^2 Z_0^2 \omega_z^2}{\gamma_x^2\omega_z^2 + (\omega_z^2 - \omega_x^2)^2}\right)\tilde{r}_{xz_{av}} \\
& -\frac{\gamma_R}{4}\left(\frac{\gamma_z X_0^2 \omega_x^2 \left(\omega_z^2 - \omega_x^2\right)}{\gamma_z^2\omega_x^2 + (\omega_x^2 - \omega_z^2)^2} + \frac{\gamma_x Z_0^2 \omega_z^2 \left(\omega_x^2 - \omega_z^2\right)}{\gamma_x^2\omega_z^2 + (\omega_z^2 - \omega_x^2)^2}\right)\tilde{d}_{xz_{av}} \\
& -\frac{\gamma_R}{2}\left(\frac{\gamma_z X_0^2 \omega_x^2 \left(\omega_z^2 - \omega_x^2\right)}{\gamma_z^2\omega_x^2 + (\omega_x^2 - \omega_z^2)^2} - \frac{\gamma_x Z_0^2 \omega_z^2 \left(\omega_z^2 - \omega_x^2\right)}{\gamma_x^2\omega_z^2 + (\omega_z^2 - \omega_x^2)^2}\right)\tilde{\Omega}_{y_{av}}
\end{aligned} \tag{4.122}$$

$$\begin{aligned}
\dot{\tilde{r}}_{yz_{av}} = & -\frac{\gamma_R}{4}\left(\frac{\gamma_z^2 Y_0^2 \omega_y^2}{\gamma_z^2\omega_y^2 + (\omega_y^2 - \omega_z^2)^2} + \frac{\gamma_y^2 Z_0^2 \omega_z^2}{\gamma_y^2\omega_z^2 + (\omega_z^2 - \omega_y^2)^2}\right)\tilde{r}_{yz_{av}} \\
& -\frac{\gamma_R}{4}\left(\frac{\gamma_z Y_0^2 \omega_y^2 \left(\omega_z^2 - \omega_y^2\right)}{\gamma_z^2\omega_y^2 + (\omega_y^2 - \omega_z^2)^2} + \frac{\gamma_y Z_0^2 \omega_z^2 \left(\omega_y^2 - \omega_z^2\right)}{\gamma_y^2\omega_z^2 + (\omega_z^2 - \omega_y^2)^2}\right)\tilde{d}_{yz_{av}} \\
& -\frac{\gamma_R}{2}\left(\frac{\gamma_z Y_0^2 \omega_y^2 \left(\omega_z^2 - \omega_y^2\right)}{\gamma_z^2\omega_y^2 + (\omega_y^2 - \omega_z^2)^2} - \frac{\gamma_y Z_0^2 \omega_z^2 \left(\omega_z^2 - \omega_y^2\right)}{\gamma_y^2\omega_z^2 + (\omega_z^2 - \omega_y^2)^2}\right)\tilde{\Omega}_{x_{av}}
\end{aligned} \tag{4.123}$$

$$\dot{\tilde{d}}_{xx_{av}} = -\frac{\gamma_D}{2} X_0^2 \omega_x^2 \tilde{d}_{xx_{av}} \tag{4.124}$$

$$\dot{\tilde{d}}_{yy_{av}} = -\frac{\gamma_D}{2} Y_0^2 \omega_y^2 \tilde{d}_{yy_{av}} \tag{4.125}$$

$$\dot{\tilde{d}}_{zz_{av}} = -\frac{\gamma_D}{2} Z_0^2 \omega_z^2 \tilde{d}_{zz_{av}} \tag{4.126}$$

$$\begin{aligned}
\dot{\tilde{d}}_{xy_{av}} = & -\frac{\gamma_D}{4}\left(\frac{\gamma_y^2 X_0^2 \omega_x^4}{\gamma_y^2\omega_x^2 + (\omega_x^2-\omega_y^2)^2} + \frac{\gamma_x^2 Y_0^2 \omega_y^4}{\gamma_x^2\omega_y^2 + (\omega_y^2-\omega_x^2)^2}\right)\tilde{d}_{xy_{av}} \\
& + \frac{\gamma_D}{4}\left(\frac{\gamma_y^2 X_0^2 \omega_x^2\left(\omega_y^2-\omega_x^2\right)}{\gamma_y^2\omega_x^2 + (\omega_x^2-\omega_y^2)^2} + \frac{\gamma_x^2 Y_0^2 \omega_y^2\left(\omega_x^2-\omega_y^2\right)}{\gamma_x^2\omega_y^2 + (\omega_y^2-\omega_x^2)^2}\right)\tilde{r}_{xy_{av}} \\
& - \frac{\gamma_D}{2}\left(\frac{\gamma_y^2 X_0^2 \omega_x^4}{\gamma_y^2\omega_x^2 + (\omega_x^2-\omega_y^2)^2} - \frac{\gamma_x^2 Y_0^2 \omega_y^4}{\gamma_x^2\omega_y^2 + (\omega_y^2-\omega_x^2)^2}\right)\tilde{\Omega}_{z_{av}}
\end{aligned} \tag{4.127}$$

$$\begin{aligned}
\dot{\tilde{d}}_{xz_{av}} = & -\frac{\gamma_D}{4}\left(\frac{\gamma_z^2 X_0^2 \omega_x^4}{\gamma_z^2\omega_x^2 + (\omega_x^2-\omega_z^2)^2} + \frac{\gamma_x^2 Z_0^2 \omega_z^4}{\gamma_x^2\omega_z^2 + (\omega_z^2-\omega_x^2)^2}\right)\tilde{d}_{xz_{av}} \\
& + \frac{\gamma_D}{4}\left(\frac{\gamma_z^2 X_0^2 \omega_x^2\left(\omega_z^2-\omega_x^2\right)}{\gamma_z^2\omega_x^2 + (\omega_x^2-\omega_z^2)^2} + \frac{\gamma_x^2 Z_0^2 \omega_z^2\left(\omega_x^2-\omega_z^2\right)}{\gamma_x^2\omega_z^2 + (\omega_z^2-\omega_x^2)^2}\right)\tilde{r}_{xz_{av}} \\
& - \frac{\gamma_D}{2}\left(\frac{\gamma_z^2 X_0^2 \omega_x^4}{\gamma_z^2\omega_x^2 + (\omega_x^2-\omega_z^2)^2} - \frac{\gamma_x^2 Z_0^2 \omega_z^4}{\gamma_x^2\omega_z^2 + (\omega_z^2-\omega_x^2)^2}\right)\tilde{\Omega}_{y_{av}}
\end{aligned} \tag{4.128}$$

$$\begin{aligned}
\dot{\tilde{d}}_{yz_{av}} = & -\frac{\gamma_D}{4}\left(\frac{\gamma_z^2 Y_0^2 \omega_y^4}{\gamma_z^2\omega_y^2 + (\omega_y^2-\omega_z^2)^2} + \frac{\gamma_y^2 Z_0^2 \omega_z^4}{\gamma_y^2\omega_z^2 + (\omega_z^2-\omega_y^2)^2}\right)\tilde{d}_{yz_{av}} \\
& + \frac{\gamma_D}{4}\left(\frac{\gamma_z^2 Y_0^2 \omega_y^2\left(\omega_z^2-\omega_y^2\right)}{\gamma_z^2\omega_y^2 + (\omega_y^2-\omega_z^2)^2} + \frac{\gamma_y^2 Z_0^2 \omega_z^2\left(\omega_y^2-\omega_z^2\right)}{\gamma_y^2\omega_z^2 + (\omega_z^2-\omega_y^2)^2}\right)\tilde{r}_{yz_{av}} \\
& - \frac{\gamma_D}{2}\left(\frac{\gamma_z^2 Y_0^2 \omega_y^4}{\gamma_z^2\omega_y^2 + (\omega_y^2-\omega_z^2)^2} - \frac{\gamma_y^2 Z_0^2 \omega_z^4}{\gamma_y^2\omega_z^2 + (\omega_z^2-\omega_y^2)^2}\right)\tilde{\Omega}_{x_{av}}
\end{aligned} \tag{4.129}$$

$$\begin{aligned}
\dot{\tilde{\Omega}}_{x_{av}} &= -\gamma_\Omega \left(\frac{\gamma_z^2 Y_0^2 \omega_y^4}{\gamma_z^2 \omega_y^2 + (\omega_y^2 - \omega_z^2)^2} + \frac{\gamma_y^2 Z_0^2 \omega_z^4}{\gamma_y^2 \omega_z^2 + (\omega_z^2 - \omega_y^2)^2} \right) \tilde{\Omega}_{x_{av}} \\
&\quad -\frac{\gamma_\Omega}{2} \left(\frac{\gamma_z^2 Y_0^2 \omega_y^4}{\gamma_z^2 \omega_y^2 + (\omega_y^2 - \omega_z^2)^2} - \frac{\gamma_y^2 Z_0^2 \omega_z^4}{\gamma_y^2 \omega_z^2 + (\omega_z^2 - \omega_y^2)^2} \right) \tilde{d}_{yz_{av}} \\
&\quad -\frac{\gamma_\Omega}{2} \left(\frac{\gamma_z^2 Y_0^2 \omega_y^2 \left(\omega_z^2 - \omega_y^2\right)}{\gamma_z^2 \omega_y^2 + (\omega_y^2 - \omega_z^2)^2} + \frac{\gamma_y^2 Z_0^2 \omega_z^2 \left(\omega_z^2 - \omega_y^2\right)}{\gamma_y^2 \omega_z^2 + (\omega_z^2 - \omega_y^2)^2} \right) \tilde{r}_{yz_{av}}
\end{aligned} \tag{4.130}$$

$$\begin{aligned}
\dot{\tilde{\Omega}}_{y_{av}} &= -\gamma_\Omega \left(\frac{\gamma_z^2 X_0^2 \omega_x^4}{\gamma_z^2 \omega_x^2 + (\omega_x^2 - \omega_z^2)^2} + \frac{\gamma_x^2 Z_0^2 \omega_z^4}{\gamma_x^2 \omega_z^2 + (\omega_z^2 - \omega_x^2)^2} \right) \tilde{\Omega}_{y_{av}} \\
&\quad -\frac{\gamma_\Omega}{2} \left(\frac{\gamma_z^2 X_0^2 \omega_x^4}{\gamma_z^2 \omega_x^2 + (\omega_x^2 - \omega_z^2)^2} - \frac{\gamma_x^2 Z_0^2 \omega_z^4}{\gamma_x^2 \omega_z^2 + (\omega_z^2 - \omega_x^2)^2} \right) \tilde{d}_{xz_{av}} \\
&\quad -\frac{\gamma_\Omega}{2} \left(\frac{\gamma_z^2 X_0^2 \omega_x^2 \left(\omega_z^2 - \omega_x^2\right)}{\gamma_z^2 \omega_x^2 + (\omega_x^2 - \omega_z^2)^2} + \frac{\gamma_x^2 Z_0^2 \omega_z^2 \left(\omega_z^2 - \omega_x^2\right)}{\gamma_x^2 \omega_z^2 + (\omega_z^2 - \omega_x^2)^2} \right) \tilde{r}_{xz_{av}}
\end{aligned} \tag{4.131}$$

$$\begin{aligned}
\dot{\tilde{\Omega}}_{z_{av}} &= -\gamma_\Omega \left(\frac{\gamma_y^2 X_0^2 \omega_x^4}{\gamma_y^2 \omega_x^2 + (\omega_x^2 - \omega_y^2)^2} + \frac{\gamma_x^2 Y_0^2 \omega_y^4}{\gamma_x^2 \omega_y^2 + (\omega_y^2 - \omega_x^2)^2} \right) \tilde{\Omega}_{z_{av}} \\
&\quad -\frac{\gamma_\Omega}{2} \left(\frac{\gamma_y^2 X_0^2 \omega_x^4}{\gamma_y^2 \omega_x^2 + (\omega_x^2 - \omega_y^2)^2} - \frac{\gamma_x^2 Y_0^2 \omega_y^4}{\gamma_x^2 \omega_y^2 + (\omega_y^2 - \omega_x^2)^2} \right) \tilde{d}_{xy_{av}} \\
&\quad -\frac{\gamma_\Omega}{2} \left(\frac{\gamma_y^2 X_0^2 \omega_x^2 \left(\omega_y^2 - \omega_x^2\right)}{\gamma_y^2 \omega_x^2 + (\omega_x^2 - \omega_y^2)^2} + \frac{\gamma_x^2 Y_0^2 \omega_y^2 \left(\omega_y^2 - \omega_x^2\right)}{\gamma_x^2 \omega_y^2 + (\omega_y^2 - \omega_x^2)^2} \right) \tilde{r}_{xy_{av}}
\end{aligned} \tag{4.132}$$

It can be seen in the above equations that the terms that couple the averaged parameters estimates to other parameter estimates can be made very small with sufficiently large gains γ_x, γ_y and γ_z or with natural frequencies ω_x, ω_y and ω_z sufficiently close together. This is true apart from the coupling between $\dot{\tilde{\Omega}}_{x_{av}}$ and $\tilde{d}_{yz_{av}}$, $\dot{\tilde{\Omega}}_{y_{av}}$ and $\tilde{d}_{xz_{av}}$, and $\dot{\tilde{\Omega}}_{z_{av}}$ and $\tilde{d}_{xy_{av}}$. Their dynamics remain coupled through

$$\begin{bmatrix} \dot{\tilde{d}}_{xy_{av}} \\ \dot{\tilde{d}}_{xz_{av}} \\ \dot{\tilde{d}}_{yz_{av}} \\ \dot{\tilde{\Omega}}_{x_{av}} \\ \dot{\tilde{\Omega}}_{y_{av}} \\ \dot{\tilde{\Omega}}_{z_{av}} \end{bmatrix} \approx \begin{bmatrix} a_{11} & 0 & 0 & 0 & 0 & a_{16} \\ 0 & a_{22} & 0 & 0 & a_{25} & 0 \\ 0 & 0 & a_{33} & a_{34} & 0 & 0 \\ 0 & 0 & a_{43} & a_{44} & 0 & 0 \\ 0 & a_{52} & 0 & 0 & a_{25} & 0 \\ a_{61} & 0 & 0 & 0 & 0 & a_{66} \end{bmatrix} \begin{bmatrix} \tilde{d}_{xy_{av}} \\ \tilde{d}_{xz_{av}} \\ \tilde{d}_{yz_{av}} \\ \tilde{\Omega}_{x_{av}} \\ \tilde{\Omega}_{y_{av}} \\ \tilde{\Omega}_{z_{av}} \end{bmatrix} \tag{4.133}$$

where the elements of the bi-diagonal matrix are

$$\begin{aligned}
a_{11} &= -\tfrac{\gamma_D}{4}\left(X_0^2\omega_x^2 + Y_0^2\omega_y^2\right), \quad a_{16} = -\frac{\gamma_D}{2}\left(X_0^2\omega_x^2 - Y_0^2\omega_y^2\right) \\
a_{22} &= -\tfrac{\gamma_D}{4}\left(X_0^2\omega_x^2 + Z_0^2\omega_z^2\right), \quad a_{25} = -\frac{\gamma_D}{2}\left(X_0^2\omega_x^2 - Z_0^2\omega_z^2\right) \\
a_{33} &= -\tfrac{\gamma_D}{4}\left(Y_0^2\omega_y^2 + Z_0^2\omega_z^2\right), \quad a_{34} = -\frac{\gamma_D}{2}\left(Y_0^2\omega_y^2 - Z_0^2\omega_z^2\right) \\
a_{44} &= -\gamma_\Omega\left(Y_0^2\omega_y^2 + Z_0^2\omega_z^2\right), \quad a_{43} = -\frac{\gamma_\Omega}{2}\left(Y_0^2\omega_y^2 - Z_0^2\omega_z^2\right) \\
a_{55} &= -\gamma_\Omega\left(X_0^2\omega_x^2 + Z_0^2\omega_z^2\right), \quad a_{52} = -\frac{\gamma_\Omega}{2}\left(X_0^2\omega_x^2 - Z_0^2\omega_z^2\right) \\
a_{66} &= -\gamma_\Omega\left(X_0^2\omega_x^2 + Y_0^2\omega_y^2\right), \quad a_{61} = -\frac{\gamma_\Omega}{2}\left(X_0^2\omega_x^2 - Y_0^2\omega_y^2\right)
\end{aligned} \tag{4.134}$$

From this it can be seen that the coupling terms can be made to be zero if

$$X_0^2\omega_x^2 = Y_0^2\omega_y^2 = Z_0^2\omega_z^2 \tag{4.135}$$

which represents having equal energy in each of the three axes.

Using these decoupling conditions the average angular rate dynamics approximately become

$$\begin{aligned}
\dot{\tilde{\Omega}}_{x_{av}} &\approx -2\gamma_\Omega X_0^2\omega_x^2\tilde{\Omega}_{x_{av}} \\
\dot{\tilde{\Omega}}_{y_{av}} &\approx -2\gamma_\Omega Y_0^2\omega_y^2\tilde{\Omega}_{y_{av}} \\
\dot{\tilde{\Omega}}_{z_{av}} &\approx -2\gamma_\Omega Z_0^2\omega_z^2\tilde{\Omega}_{z_{av}}
\end{aligned} \tag{4.136}$$

Therefore an expression for bandwidth can be given as

$$BW \approx 2\gamma_\Omega X_0^2\omega_x^2 \tag{4.137}$$

This expression is valid for all axes if the equal energies decoupling condition, Equation (4.135) is satisfied.

Figure 4.8.1 shows an example of the convergence of the angular rate estimates compared to the predicted convergence rate of Equation 4.136 (blue dashed) for a stepped angular rate input (green dotted).

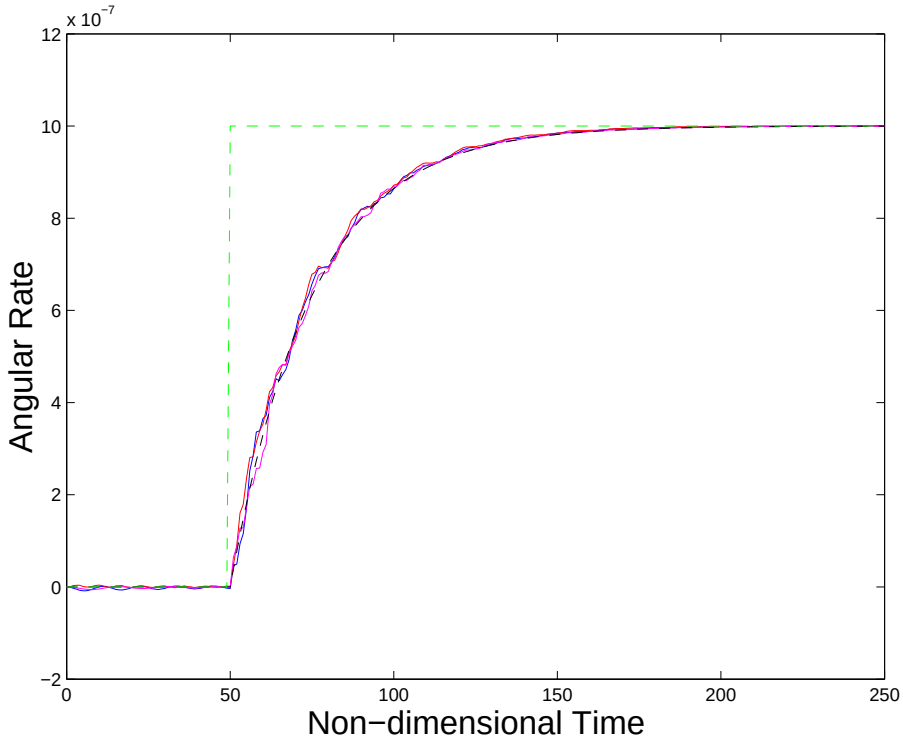

Figure 4.5: Example triaxial convergence rates compared to predicted convergence rate of Equation 4.136 (blue dashed) for a stepped angular rate input (green dotted)

4.9 Triaxial Adaptive Controller Design Simplification

4.9.1 Matching Controller Internal Damping

A bode plot of the filter elements of Equation (4.111) corresponds to the gain A_{mn} and phase ϕ_{mn} of Equation (4.114). Figure 4.6(a) shows a bode plot with feedback gains γ_x, γ_y γ_z all equal. It can be seen that the plots are slightly skewed. To preserve symmetry in the bode plots the damping of each of the filter elements should be equal.

Expressing Equation (4.111) in terms of a common damping ratio ζ gives

$$\hat{M} = \begin{bmatrix} \frac{\gamma_x s}{s^2+2\zeta\omega_x s+\omega_x^2} & 0 & 0 \\ 0 & \frac{\gamma_y s}{s^2+2\zeta\omega_y s+\omega_y^2} & 0 \\ 0 & 0 & \frac{\gamma_z s}{s^2+2\zeta\omega_z s+\omega_z^2} \end{bmatrix} \tag{4.138}$$

Equating this with Equation (4.111) leads to

$$2\zeta = \frac{\gamma_x}{\omega_x} = \frac{\gamma_y}{\omega_y} = \frac{\gamma_z}{\omega_z} \tag{4.139}$$

For design simplicity we can set $\frac{\omega_y}{\omega_x} = \frac{\omega_z}{\omega_y}$ giving the design guideline

$$\frac{\gamma_y}{\gamma_x} = \frac{\gamma_z}{\gamma_y} = \frac{\omega_y}{\omega_x} = \frac{\omega_z}{\omega_y} \tag{4.140}$$

Figure 4.6(b) shows a bode plot corresponding to this design guideline.

4.9.2 Matching Parameter Estimate Bandwidths

The bandwidth expression Equation 4.137 is in terms of the averaged convergence, however the actual system may have oscillatory behaviour around this averaged convergence. This oscillatory behaviour can be attributed to all the other parameter estimates not yet having converged to their true values. This is especially true if there are large differences between the estimates and the real values, such as when the system is initially turned on.

All parameter estimates will contain some oscillatory behaviour around their averaged convergence rate until all other parameters have converged sufficiently to their true values. It is a reasonable hypothesis then that to reduce, if not minimise, the unwanted oscillatory behaviour of any of the parameter estimates, that all parameter estimates must have the same convergence rates. In section 4.8.1 we found the averaged convergence rates, Equations (4.119) to (4.132). These expressions give the convergence rates of all the parameter estimate errors, ignoring the fast changing parts of their dynamics. It can be seen that the convergence rates of each is proportional to their respective adaptive gains, γ_R, γ_D and γ_{Omega}. Therefore we can match the convergence rates of all the parameter estimates through careful selection of these adaptive gains. We achieve this by equating all the convergence rates and expressing each adaptive gain in terms of a common bandwidth BW, taken from Equation (4.137). These can then be substituted into the adaptation laws Equations (4.36)-(4.38).

It was stated in section 4.8.1 that the coupling between parameter estimates can be made very small with sufficiently large gains γ_x, γ_y and γ_z or with natural frequencies ω_x, ω_y and ω_z sufficiently close together. This decoupling condition has also been used here to simplify the equating of convergence rates.

From Equation (4.136), all three angular rate estimate errors have the same convergence

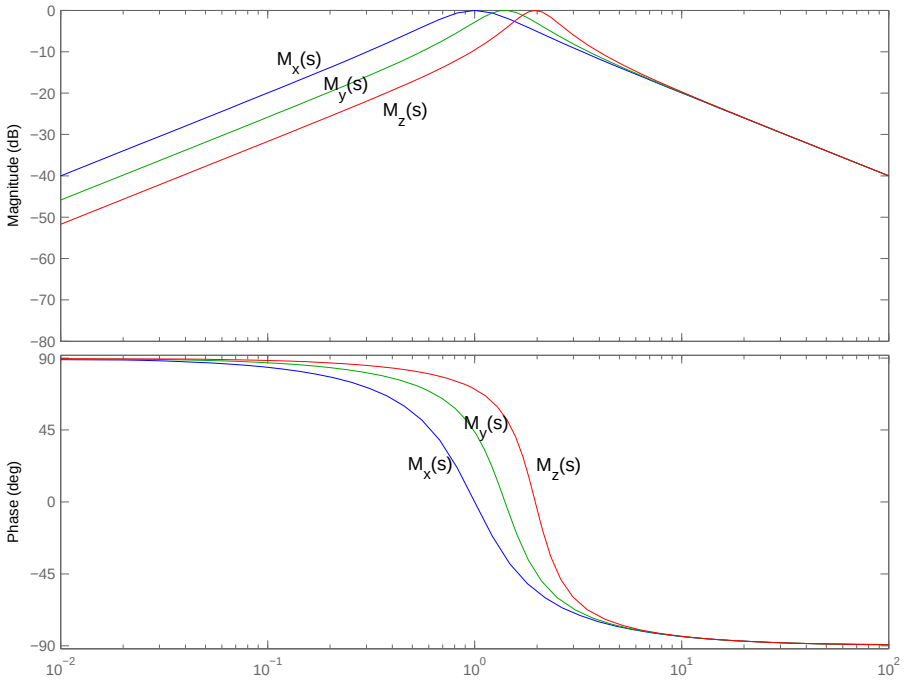

(a) $\hat{M}$ Filter bode plot with $\gamma_x = \gamma_y = \gamma_z$

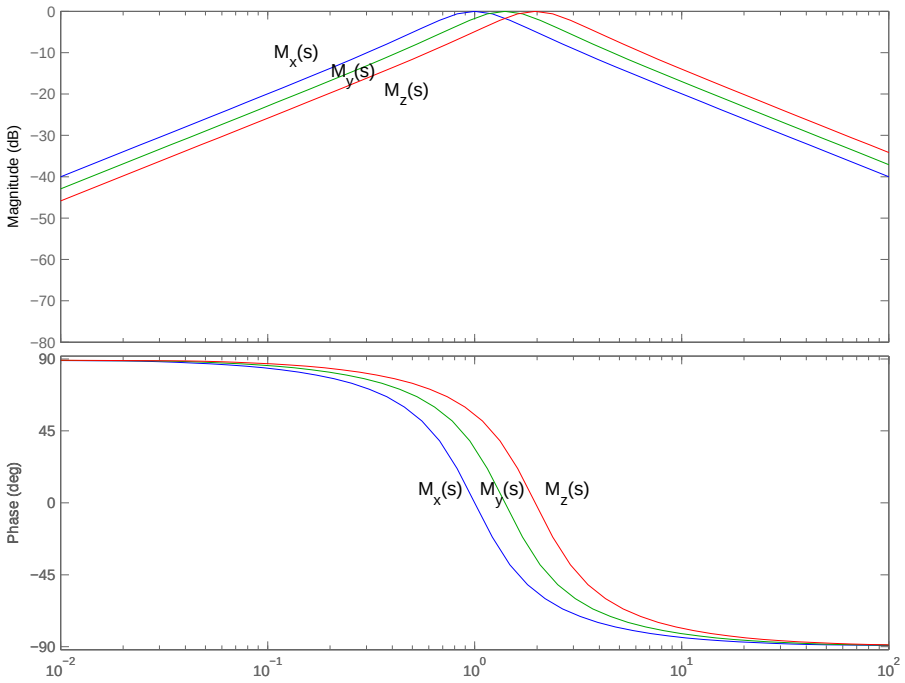

(b) $\hat{M}$ Filter bode plot with $\frac{\gamma_x}{\omega_x} = \frac{\gamma_y}{\omega_y} = \frac{\gamma_z}{\omega_z}$

Figure 4.6: Bode plots of $\hat{M}$ showing the symmetric frequency response when using the design guideline of control gains γ_x, γ_y and γ_z scaled by the resonant frequencies of their respective axes.

rate already. Therefore simply rearranging Equation (4.137) gives

$$\gamma_\Omega = \frac{BW}{2X_0^2\omega_x^2} \tag{4.141}$$

Equating the averaged convergence rate of the x axis damping estimate error to the averaged convergence rate of the x axis angular rate estimate error gives

$$\begin{aligned} -\frac{\gamma_D}{2}X_0^2\omega_x^2 &= -2\gamma_\Omega X_0^2\omega_x^2 \\ \gamma_D &= 4\gamma_\Omega \\ \gamma_D &= 2\frac{BW}{X_0^2\omega_x^2} \end{aligned} \tag{4.142}$$

Equation (4.142) holds true for all the averaged convergence rates of the damping estimate errors including the cross damping terms.

Equating the averaged convergence rate of the error in the x axis stiffness error estimate to the averaged convergence rate of the x axis angular rate estimate error gives

$$\begin{aligned} -\frac{\gamma_{R_{xx}}}{2}X_0^2 &= -2\gamma_\Omega X_0^2\omega_x^2 \\ \gamma_{R_{xx}} &= 4\gamma_\Omega\omega_x^2 \\ \gamma_{R_{xx}} &= 2\frac{BW}{X_0^2} \end{aligned} \tag{4.143}$$

Similarly for the y and z axis,

$$\gamma_{R_{yy}} = 2\frac{BW}{Y_0^2} \tag{4.144}$$

$$\gamma_{R_{zz}} = 2\frac{BW}{Z_0^2} \tag{4.145}$$

Doing the same for the cross stiffness terms

$$\begin{aligned} -\frac{\gamma_{R_{xy}}}{4}\left(X_0^2+Y_0^2\right) &= -2\gamma_\Omega X_0^2\omega_x^2 \\ -\frac{\gamma_{R_{xy}}}{4}\left(X_0^2+Y_0^2\right) &= -BW \\ \gamma_{R_{xy}} &= \frac{4BW}{X_0^2+Y_0^2} \qquad (4.146) \\ \gamma_{R_{xz}} &= \frac{4BW}{X_0^2+Z_0^2} \qquad (4.147) \\ \gamma_{R_{yz}} &= \frac{4BW}{Y_0^2+Z_0^2} \qquad (4.148) \end{aligned}$$

Therefore γ_R is changed from a scalar to a gain matrix

$$\gamma_R = 2BW\begin{bmatrix} \frac{1}{X_0^2} & \frac{2}{\left(X_0^2+Y_0^2\right)} & \frac{2}{\left(X_0^2+Z_0^2\right)} \\ \frac{2}{\left(X_0^2+Y_0^2\right)} & \frac{1}{Y_0^2} & \frac{2}{\left(Y_0^2+Z_0^2\right)} \\ \frac{2}{\left(X_0^2+Z_0^2\right)} & \frac{2}{\left(Y_0^2+Z_0^2\right)} & \frac{1}{Z_0^2} \end{bmatrix} \qquad (4.149)$$

which will then be dot multiplied in the adaptation laws, Equations (4.36)-(4.38).

$$\dot{\hat{R}} = 2BW\begin{bmatrix} \frac{1}{X_0^2} & \frac{2}{\left(X_0^2+Y_0^2\right)} & \frac{2}{\left(X_0^2+Z_0^2\right)} \\ \frac{2}{\left(X_0^2+Y_0^2\right)} & \frac{1}{Y_0^2} & \frac{2}{\left(Y_0^2+Z_0^2\right)} \\ \frac{2}{\left(X_0^2+Z_0^2\right)} & \frac{2}{\left(Y_0^2+Z_0^2\right)} & \frac{1}{Z_0^2} \end{bmatrix} \cdot \left(\tau_0\dot{q}_m^T + \dot{q}_m\tau_0^T\right) \qquad (4.150)$$

$$\dot{\hat{D}} = \frac{BW}{X_0^2\omega_x^2}\left(\tau_0\dot{q}_m^T + \dot{q}_m\tau_0^T\right) \qquad (4.151)$$

$$\dot{\hat{\Omega}} = \frac{BW}{2X_0^2\omega_x^2}\left(\tau_0\dot{q}_m^T - \dot{q}_m\tau_0^T\right) \qquad (4.152)$$

The following section presents simulation results that test the hypothesis that matched average convergence rates will give minimal unwanted oscillatory behaviour and therefore optimum convergence behaviour.

4.9.3 Simulation Results

To investigate whether the above adaptive laws give less oscillatory behaviour during their convergence, simulations where the adaptive gains are varied either side of their predicted optimum will be presented.

Simulation Variable	Non Dimensional Value
Frequency Ratio $\left(\frac{\omega_y}{\omega_x} = \frac{\omega_z}{\omega_y}\right)$	1.1
Quality Factor	10^4
x axis amplitude of vibration (X_0)	1
Internal controller damping ratio (ζ)	0.5
Bandwidth (BW)	0.04
Computation Period	10^{-3}

Table 4.1: Simulation variable values. Adaptive gains not being investigated are given values as per Equations (4.150)-(4.152).

Table 4.1 lists the other variable values that were used for the simulations in this section.

At time $t = 0$, all the parameters estimates were initialised to their true values except for the angular rate estimates which were each initialised to zero. This was done to replicate the state of the device during its operation, where all the parameters would have had ample time to converge prior to a change in input angular rate.

Damping

The set of simulation results in Figure 4.7 show the convergence of the angular rate estimates $\hat{\Omega}_x$, $\hat{\Omega}_y$ and $\hat{\Omega}_z$ for a step angular rate input of 10^{-9} at time $t = 0$.

Rearranging Equation 4.142 gives $\frac{\gamma_D X_0^2 \omega_x^2}{2BW} = 1$. This is the point at which the averaged averaged convergence rate of the damping estimate errors are equal to the averaged convergence rate of the angular rate estimate error. In the simulations, $\frac{\gamma_D X_0^2 \omega_x^2}{2BW}$ was varied between 0.1 and 10. It was expected that there would be less oscillatory behaviour around $\frac{\gamma_D X_0^2 \omega_x^2}{2BW} = 1$.

Settling time was chosen as a good measure for the amount of oscillatory behaviour on the angular rate estimates. Figure 4.7(d) shows the time taken for the angular rate estimates to settle to within 2% of the step input. The results show that the least time taken to settle is when $\frac{\gamma_D X_0^2 \omega_x^2}{2BW}$ is in the range of 1 to 4. The reason the minimum is not at 1 can be attributed to the assumptions made in the averaging analysis to simplify the convergence rate expressions. One of the simplifications was based on $\frac{\omega_y^2}{\omega_x^2} = \frac{\omega_z^2}{\omega_y^2} \approx 1$. If we move closer to this assumptions by making $\frac{\omega_y^2}{\omega_x^2} = \frac{\omega_z^2}{\omega_y^2} = 1.21$ from 1.4 previously. We can see in Figure 4.8 that the minimum settling time has moved much closer to the predicted optimum of $\frac{\gamma_D X_0^2 \omega_x^2}{2BW} = 1$. In terms of a design rule of thumb we can use $\frac{\gamma_D X_0^2 \omega_x^2}{2BW} = 1$.

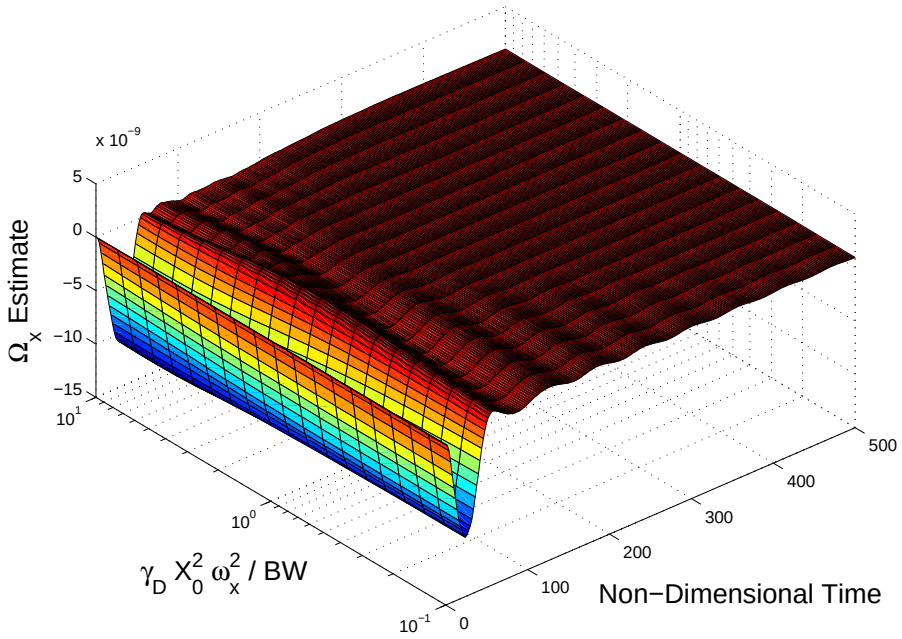

(a) x axis angular rate estimate $\hat{\Omega}_x$ simulations with $\frac{\gamma_D X_0^2 \omega_x^2}{BW}$ varied from 0.1 to 10

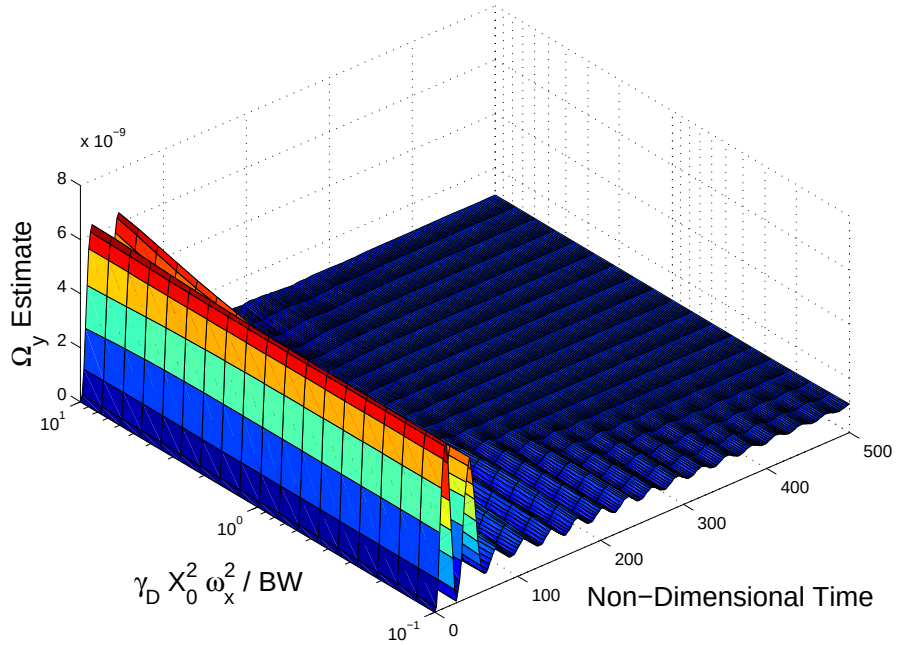

(b) y axis angular rate estimate $\hat{\Omega}_y$ simulations with $\frac{\gamma_D X_0^2 \omega_x^2}{BW}$ varied from 0.1 to 10

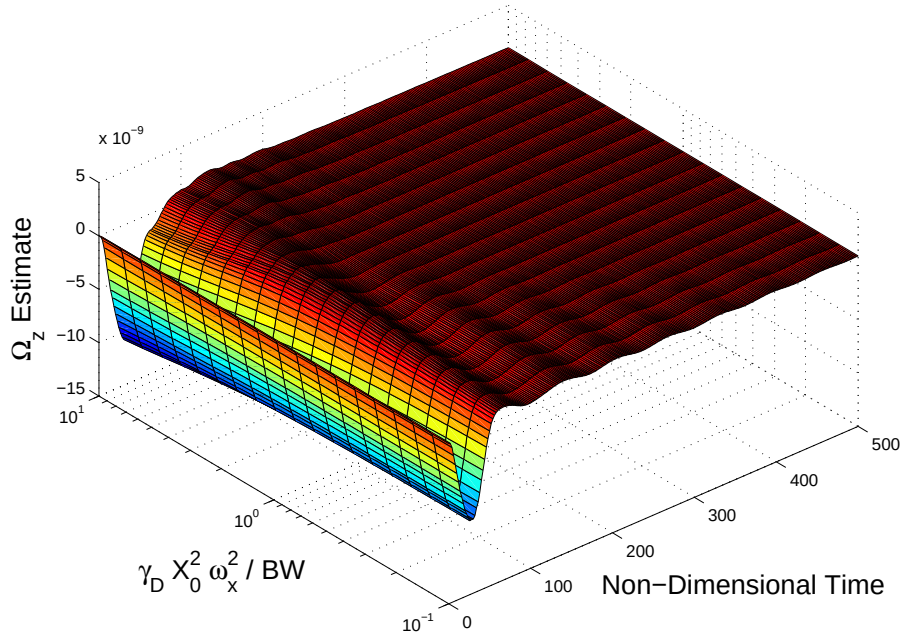

(c) z axis angular rate estimate $\hat{\Omega}_z$ simulations with $\frac{\gamma_D X_0^2 \omega_x^2}{BW}$ varied from 0.1 to 10

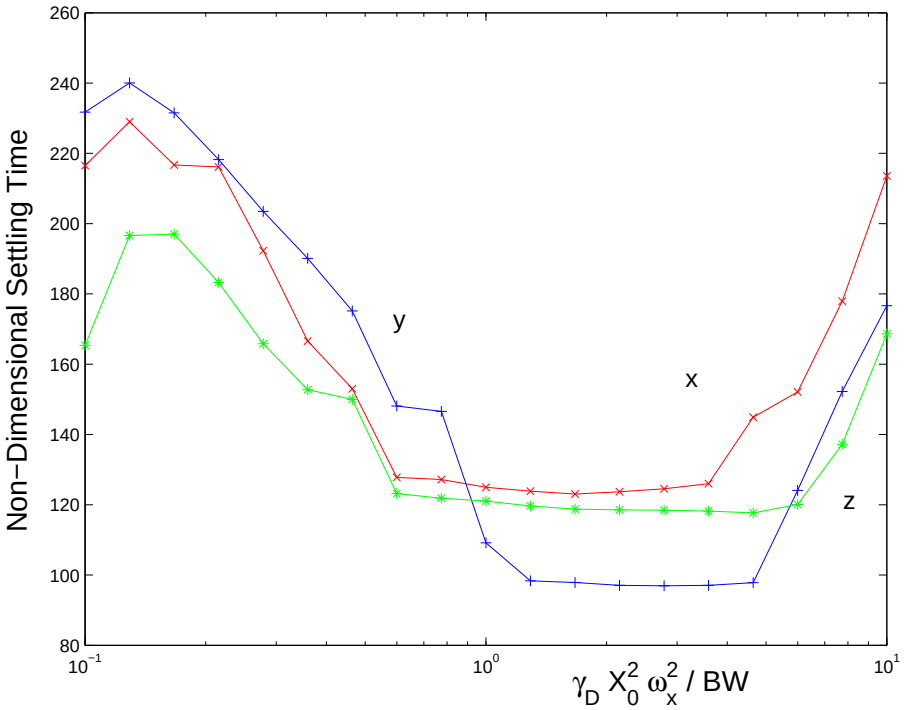

(d) Non-dimensional time taken for the x, y and z angular rate estimates to settle to within 2% of the input rotation with $\frac{\omega_y^2}{\omega_x^2} = \frac{\omega_z^2}{\omega_y^2} = 1.44$. This shows the minimum is higher than the estimated optimum of $\gamma_D = \frac{BW}{2X_0^2\omega_x^2}$.

Figure 4.7: Angular rate estimates showing the effect of a variation in γ_D.

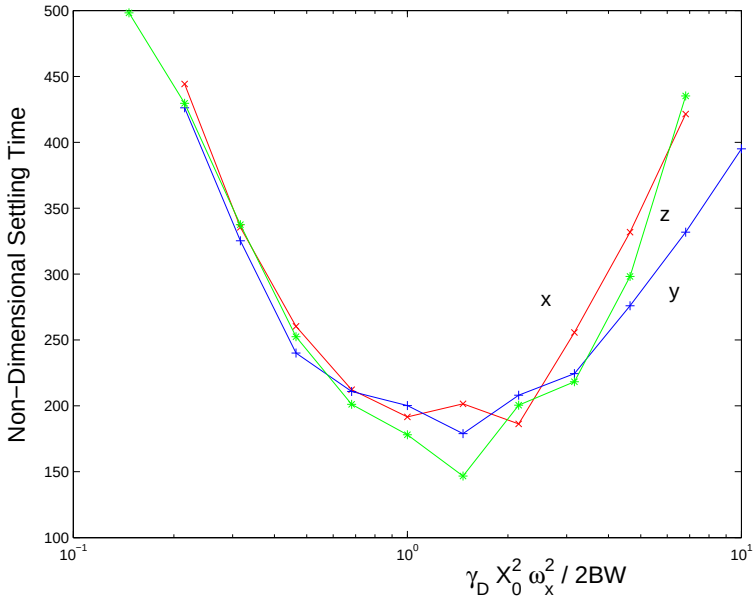

Figure 4.8: Non-dimensional time taken for the x, y and z angular rate estimates to settle to within 2% of the input rotation with $\frac{\omega_y^2}{\omega_x^2} = \frac{\omega_z^2}{\omega_y^2} = 1.21$. This shows the minimum has shifted much closer to $\gamma_D = \frac{BW}{2X_0^2\omega_x^2}$

Stiffness

The investigation of the stiffness gain has been split in two stages, with the first using scalar adaptive gains, Equations (4.143), (4.144) and (4.145) and second using the adaptive gain matrix of Equation (4.149).

In a similar manner as above, rearranging Equations 4.143, 4.143 and 4.143 gives $\frac{\gamma_R X_0^2}{2BW} = 1$, $\frac{\gamma_R Y_0^2}{2BW} = 1$ and $\frac{\gamma_R Z_0^2}{2BW} = 1$ respectively. These are the respective points at which the averaged convergence rates of the x, y and z axis stiffness error estimate errors are equal to the averaged convergence rate of the angular rate estimate error.

The set of simulation results in Figure 4.10 show angular rate estimates $\hat{\Omega}_x$, $\hat{\Omega}_y$ and $\hat{\Omega}_z$ for a step angular rate input of 10^{-9} at time $t = 0$ and with a variation of $\frac{\gamma_R X_0^2}{2BW}$ from 0.1 and 10. When $\frac{\gamma_R X_0^2}{2BW} = 1$, this is the point at which the averaged convergence rate of the x axis stiffness error estimate error is equal to the convergence rate of the angular rate estimate error. Again at time $t = 0$ all the parameters estimates were initialised to their true values except for the angular rate estimates which were each initialised to zero.

The results are summarised in Figure 4.10(a), which shows the time taken for the angular rate estimates to settle to within 2% of their true values. For similar reasons as given above,

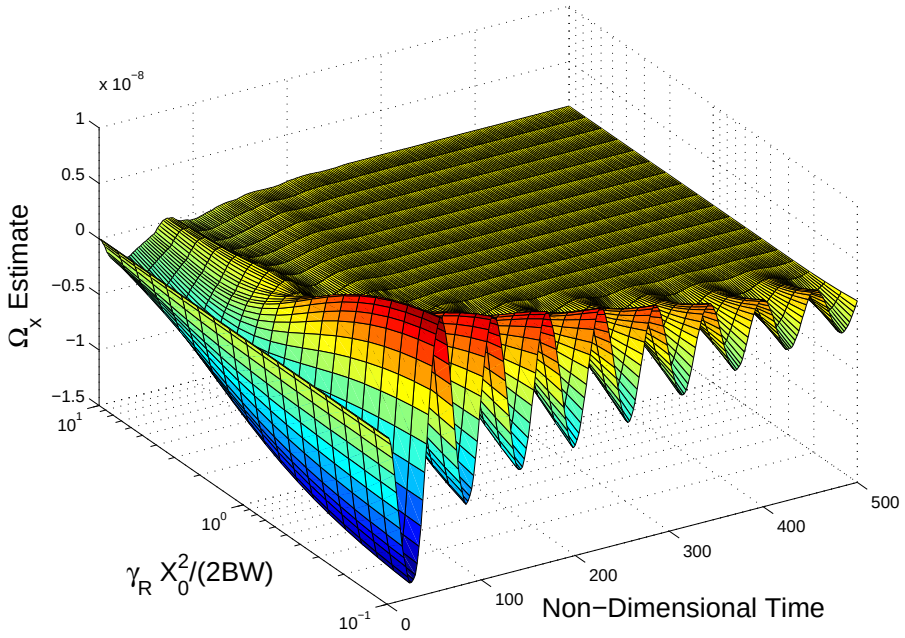

(a) x axis angular rate estimate $\hat{\Omega}_x$ simulations with $\frac{\gamma_R X_0^2}{2BW}$ varied from 0.1 to 10

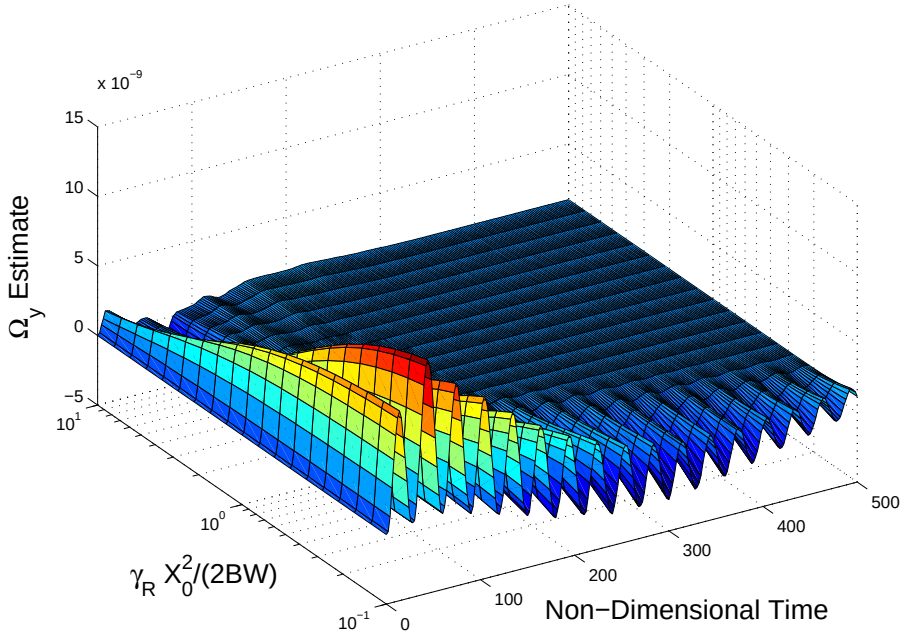

(b) y axis angular rate estimate $\hat{\Omega}_y$ simulations with $\frac{\gamma_R X_0^2}{2BW}$ varied from 0.1 to 10

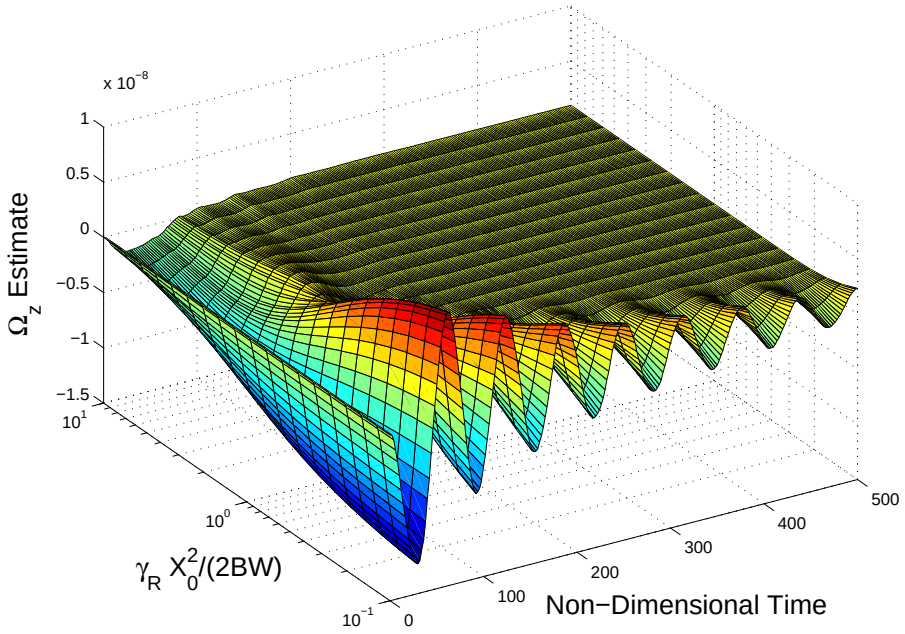

(c) z axis angular rate estimate $\hat{\Omega}_z$ simulations with $\frac{\gamma_R X_0^2}{2BW}$ varied from 0.1 to 10

Figure 4.9: Angular rate estimates showing the effect of a variation in γ_R.

it can be seen that the minimum settling time occurs when $\frac{\gamma_R X_0^2}{2BW}$ is between 1 and 2. These simulation were repeated using $\frac{\gamma_R Y_0^2}{2BW}$ and $\frac{\gamma_R Z_0^2}{2BW}$. The effect of which is the entire plot being shifted along the horizontal axis as one would expect. This can be seen in Figures 4.10(b) and 4.10(c).

Figure 4.11(a) shows the result of using the expression in Equation (4.149) multiplied by a gain variable from 0.1 to 10 to give the stiffness adaptive gain for each simulation run. The results show that there is slightly less oscillatory behaviour when the gain matrix is used and again the error disappears earliest when the gain variable ≈ 1. However compared to using a scalar gain, the gain matrix appears to give more consistent setting times between the $\hat{\Omega}_x$, $\hat{\Omega}_y$ and $\hat{\Omega}_z$.

The stiffness matrix gain adds a significant amount of computational complexity to the controller. Whether the increase in computational complexity translates into a significant increase in performance is questionable. Using the gain matrix, the results of which are shown in Figure 4.11(a), shows little improvement in settling time compared to using the scalar adaptive gain, the results of which are shown in Figures 4.10(a), 4.10(b) and 4.10(c). This indicates that the additional computational complexity involved in implementing the stiffness matrix would

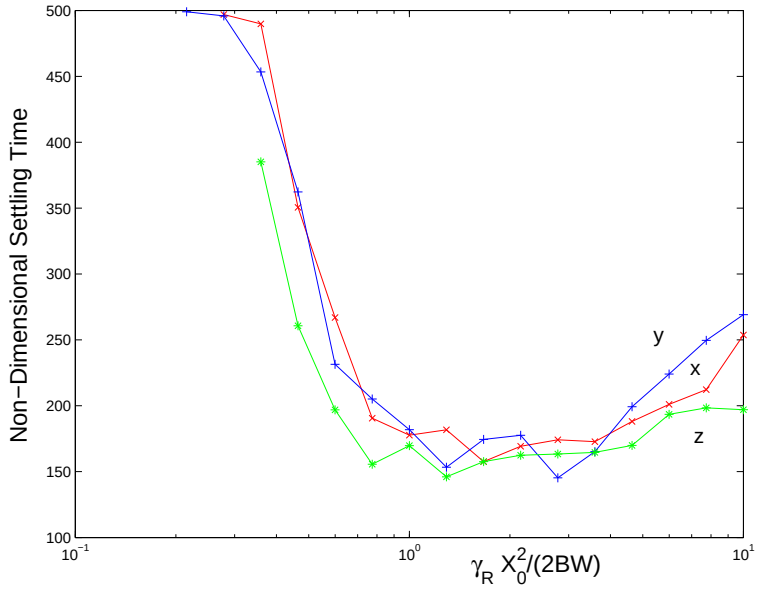

(a) $\frac{\gamma_R X_0^2}{2BW}$ varied from 0.1 to 10.

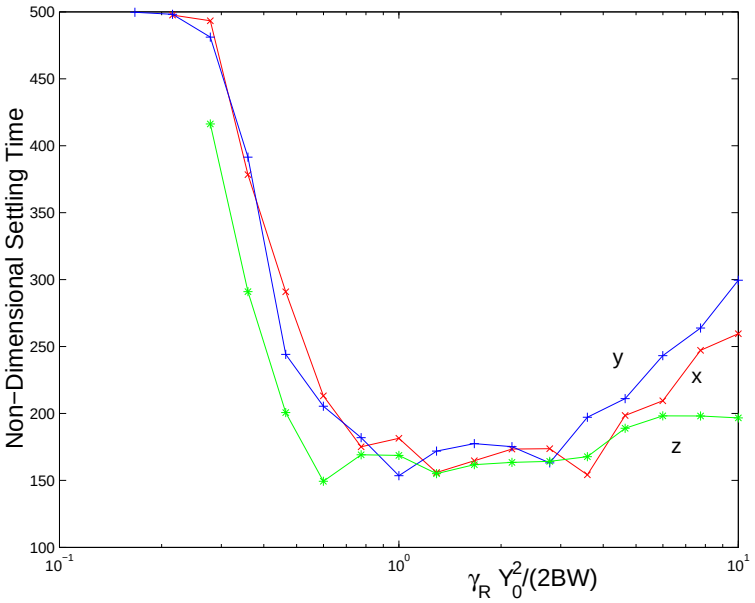

(b) $\frac{\gamma_R Y_0^2}{2BW}$ varied from 0.1 to 10.

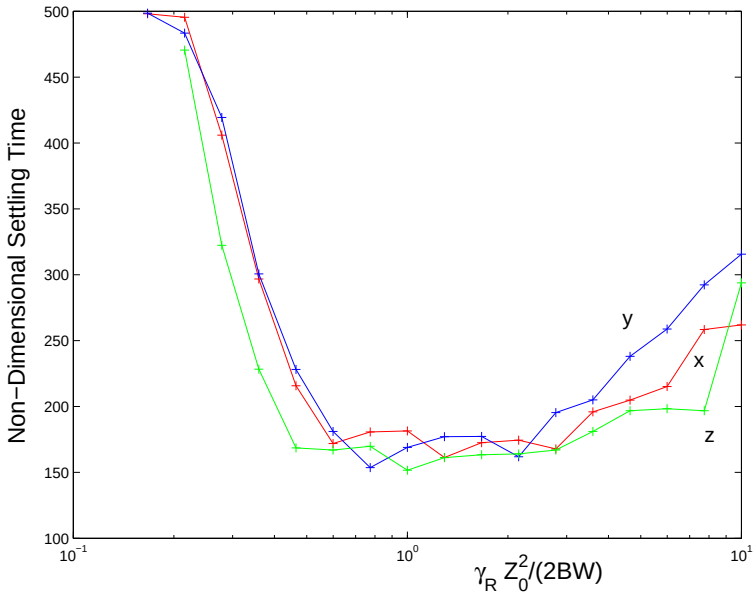

(c) $\frac{\gamma_R Z_0^2}{2BW}$ varied from 0.1 to 10.

Figure 4.10: Non-dimensional time taken for the x, y and z angular rate estimates to settle to within 2% of the input rotation with $\frac{\omega_y^2}{\omega_x^2} = \frac{\omega_z^2}{\omega_y^2} = 1.21$

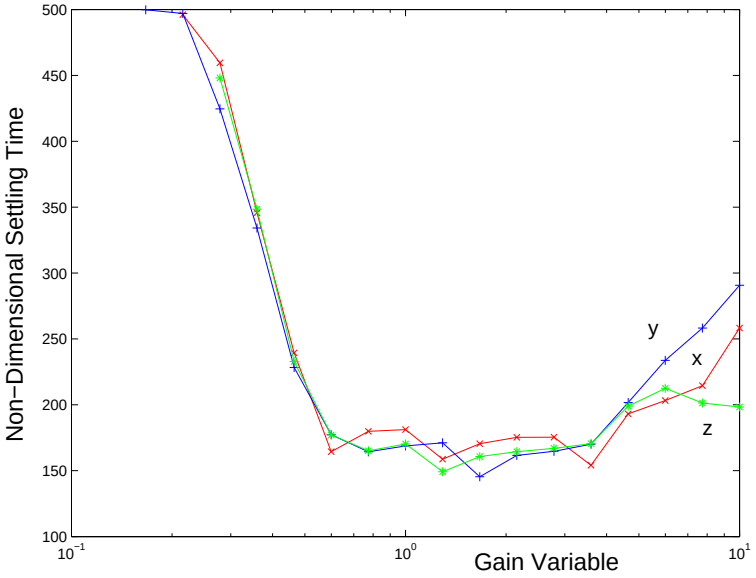

(a) Non-dimensional time taken for the x, y and z angular rate estimates to settle to within 2% of the input rotation with $\frac{\omega_y^2}{\omega_x^2} = \frac{\omega_z^2}{\omega_y^2} = 1.21$ and a gain variable varied from 0.1 to 10 multiplied by the gain matrix given in Equation 4.149

be difficult to justify in a real implementation and even more so as $\frac{\omega_y}{\omega_x} = \frac{\omega_z}{\omega_y} \rightarrow 1$.

4.10 Design Guidelines

The aim of this section is to define some design guidelines for choosing the many controller parameters such as resonant frequencies and gains. In the previous sections it was shown that all the adaptive gains could be expressed in terms of desired bandwidth to give matched averaged convergence rates. This not only reduced the unwanted oscillatory behaviour of the parameter estimates but also removes the guesswork from selection of the adaptation gains. Also, the feedback gain matrix γ is now defined in Equation (4.139) in terms of the damping ratio ζ of the transfer function matrix $M(s)$. Therefore the non-dimensionalised triaxial adaptive controller now has three variables that need to be selected that will dictate its performance: the desired bandwidth BW, the frequency ratio $\frac{\omega_y}{\omega_x} = \frac{\omega_z}{\omega_y}$, and the internal damping ratio ζ of the transfer function matrix $M(s)$. Selection of each of these has its tradeoffs.

As will be shown in Section 4.11, it is desirable to have a small γ, and hence ζ because a large value is detrimental to the resolution of the device. However a larger γ helps to decouple the parameter estimates.

There is also a trade-off in the selection of the frequency ratio $\frac{\omega_y}{\omega_x} = \frac{\omega_z}{\omega_y}$ because too small a ratio leads to less persistence of excitation and too large a value leads to greater coupling between parameter estimates and is also detrimental to the resolution of the device.

Although a large damping ratio and frequency ratio will have a negative affect on resolution, as will be shown here, they are a necessary evil in order to achieve larger bandwidths. If smaller bandwidths are tolerable, better resolution can be achieved by reducing the frequency ratio and damping ratio.

The series of plots in Figure 4.11 show the average non-dimensional time taken for the angular rate estimates to settle to within 2% of the stepped input value of $10e^{-6}$ for combinations of damping ratios and frequency ratios for a range of desired bandwidths. The settling times that exceeded 300 non-dimensional time units are not shown.

The results show that if the desired bandwidth is small then it allows the frequency ratio to be made closer to 1 and ζ to also be reduced. Both these contribute to a more desirable resolution. The opposite is true for larger bandwidth designs.

The Figure 4.11 plots show qualitatively the interaction amongst the design variables. Since non-dimensional values have been used, the plots also provide some quantitative value. However device's mechanical quality factor Q affects the achievable bandwidth for each damping and frequency ratio combination. Since it is difficult to estimate before a device has been built, it is likely that some tuning will be required. Zero mechanical damping was used in the simulations shown in Figure 4.11.

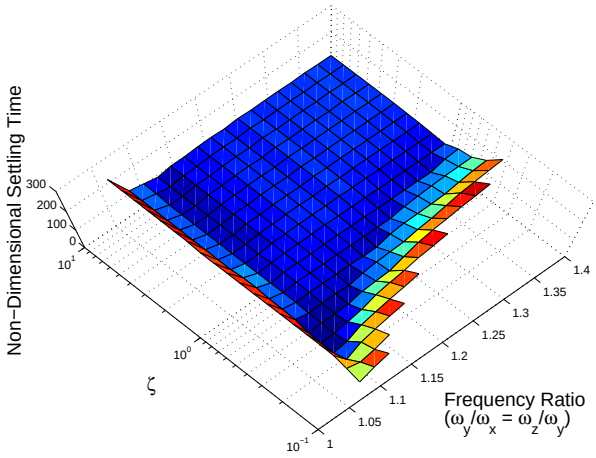

(b) Non-dimensional bandwidth of 0.0364

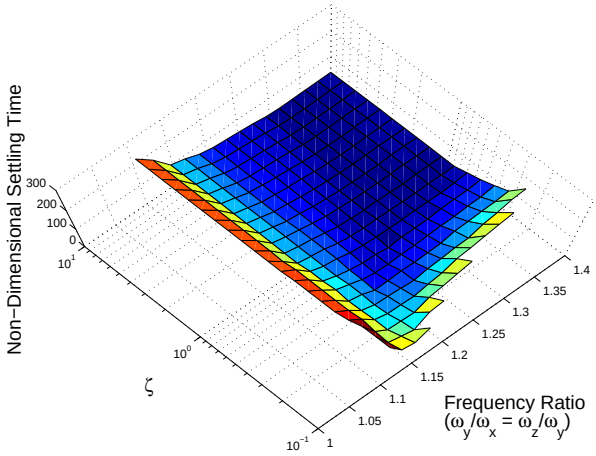

(c) Non-dimensional bandwidth of 0.1182

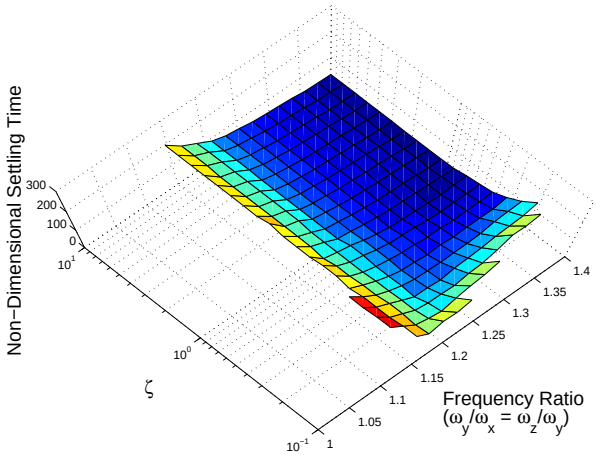

(d) Non-dimensional bandwidth of 0.2

Figure 4.11: Settling times for combinations of damping ratio ζ and frequency ratio for given non-dimensional bandwidths.

4.11 Resolution Analysis

The resolution of the triaxial angular rate sensor is limited by the thermal mechanical noise caused by the Brownian motion of the air molecules hitting the vibrating mass and also by the accuracy of the mass's position and velocity measurement.

The resolution of the device can be evaluated by adding the noise power intensities into the system dynamic equations and observing the steady state variance of the output.

Combining Equations (4.42) and (4.45) the controller error equations become

$$\begin{aligned} \ddot{e}_p + (\gamma + D + 2\Omega)\,\dot{e}_p + K e_p &= W^T(q_m, \dot{q}_m)\tilde{\theta} \\ \dot{\tilde{\theta}} &= -\Gamma W\,(q_m, \dot{q}_m)\,\gamma \dot{e}_p \end{aligned} \tag{4.153}$$

Adding the resolution limiting Brownian d, position n and velocity v noise sources to each of the acceleration, velocity and displacement terms gives

$$\begin{aligned} (\ddot{e}_p + d) + (\gamma + D + 2\Omega)\,(\dot{e}_p + v) + K\,(e_p + n) &= W^T(q_m, \dot{q}_m)\tilde{\theta} \\ \dot{\tilde{\theta}} &= -\Gamma W\,(q_m, \dot{q}_m)\,\gamma\,(\dot{e}_p + v) \end{aligned} \tag{4.154}$$

The feedforward controller uses the predefined reference model trajectory instead of the noise corrupted position and velocity measurement. Using this and the definition $R = K - K_m$ gives

$$\begin{aligned} (\ddot{e}_p + d) + \gamma\,(\dot{e}_p + v) + Km\,(e_p + n) &= W^T(q_m, \dot{q}_m)\tilde{\theta} \\ \dot{\tilde{\theta}} &= -\Gamma W\,(q_m, \dot{q}_m)\,\gamma\,(\dot{e}_p + v) \end{aligned} \tag{4.155}$$

Therefore there is no longer any position measurement noise. This can be expressed in the form

$$\dot{x} = A(t)x + G_r(t)w_r \tag{4.156}$$

where

$$x = \begin{bmatrix} \dot{e}_p \\ \ddot{e}_p \\ \tilde{\theta} \end{bmatrix}, \qquad A(t) = \begin{bmatrix} 0 & I & 0 \\ -K_m & -\gamma & W^T(q_m, \dot{q}_m) \\ 0 & -\Gamma W\left(q_m, \dot{q}_m\right)\gamma & 0 \end{bmatrix},$$

$$G_r(t) = \begin{bmatrix} 0 & 0 \\ I & -\gamma \\ 0 & -\Gamma W\left(q_m, \dot{q}_m\right)\gamma \end{bmatrix}, \qquad w_r = \begin{bmatrix} d \\ v \end{bmatrix} \tag{4.157}$$

The covariance matrix $P = E\left(x(t)x^T(t)\right)$ associated with the above system is given by

$$\dot{P} = A^T P + PA + G_r S_r G_r^T, \qquad P(0) = 0 \tag{4.158}$$

where $S_r = diag\{S_b, S_v\}$ are Brownian and velocity noise intensities. The steady state of Equation (4.158) represents the covariance of each of the estimated parameters. Of particular interest is the last three diagonal elements of the covariance matrix P, which represent the total variance of our angular rate estimates $\hat{\Omega}_x$, $\hat{\Omega}_y$ and $\hat{\Omega}_z$, the square root of which are representative of device resolution.

In order to evaluate the steady state of P, Equation (4.158) is simulated until $\dot{P} \approx 0$. The next section does does just that to study the effects of each parameter on the angular rate estimate resolution.

4.11.1 Parameter Effects on Resolution

This section investigates the effects of various device parameters on resolution. It is meant to be a qualitative investigation and as such values for thermal mechanical and velocity sensing noise have been taken from [60] as $S_b = 1.47 \times 10^{-26} N^2 sec$ and $S_v = 2.94 \times 10^{-12} msec^{-1}$. This also allows the comparison between the ultimate achievable resolution of the triaxial device in Section 4.11.2 with the single axis device of [60]. The other values used for non-dimensionalising noise and dimensionalising the results are given in Table 4.2, which also lists the values of the parameters used while they were not being investigated.

To investigate the effect each device parameter has on resolution, Equation (4.158) was simulated across a range of each variable.

Parameter	Value
mass	$5.095 \times 10^{-7} kg$
x-axis frequency	$4.17 kHz$
Quality factor	10^4
Brownian noise PSD	$1.47 \times 10^{-26} N^2 s$
Position noise PSD	$1.49 \times 10^{-27} m^2 s$
Velocity noise PSD	$2.94 \times 10^{-12} m s^{-1}$
Parameter	**Value when not being varied for investigation**
Frequency ratio	1.2
ζ	0.4
BW	0.04

Table 4.2: Parameters used for the resolution analysis simulations including the values used while other parameters are varied. Parameter values have been kept consistent with [60].

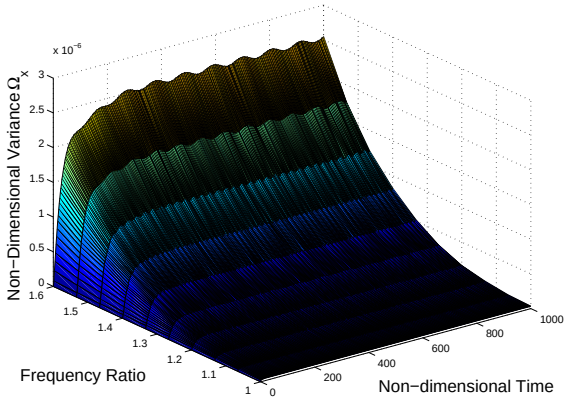

(a) Effect of the frequency ratio $\frac{\omega_y}{\omega_x} = \frac{\omega_z}{\omega_y}$ on $\hat{\Omega}_x$ variance.

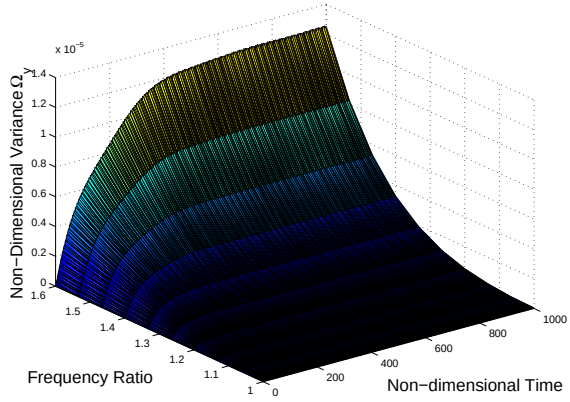

(b) Effect of the frequency ratio $\frac{\omega_y}{\omega_x} = \frac{\omega_z}{\omega_y}$ on $\hat{\Omega}_y$ variance.

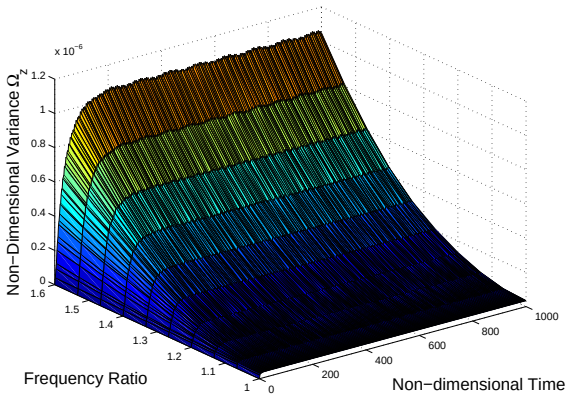

(c) Effect of the frequency ratio $\frac{\omega_y}{\omega_x} = \frac{\omega_z}{\omega_y}$ on $\hat{\Omega}_z$ variance.

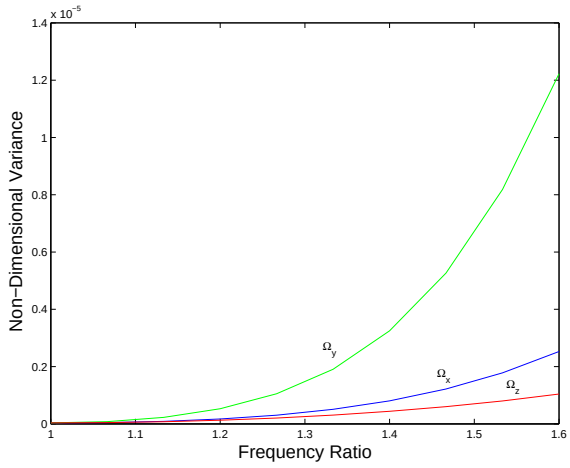

(d) Summary of steady state values of resolution simulations, Figures 4.12(a), 4.12(b) and 4.12(c), showing the effect of the frequency ratio $\frac{\omega_y}{\omega_x} = \frac{\omega_z}{\omega_y}$ on $\hat{\Omega}_x$, $\hat{\Omega}_y$ and $\hat{\Omega}_z$ variance.

Figure 4.12: Simulation results of Equation 4.158, showing the effect of the frequency ratio $\frac{\omega_y}{\omega_x} = \frac{\omega_z}{\omega_y}$ on angular rate estimate variance due to thermal mechanical and velocity noise. ($S_b = 1.47 \times 10^{-26} N^2 s$ and $S_v = 2.94 \times 10^{-12} m s^{-1}$)

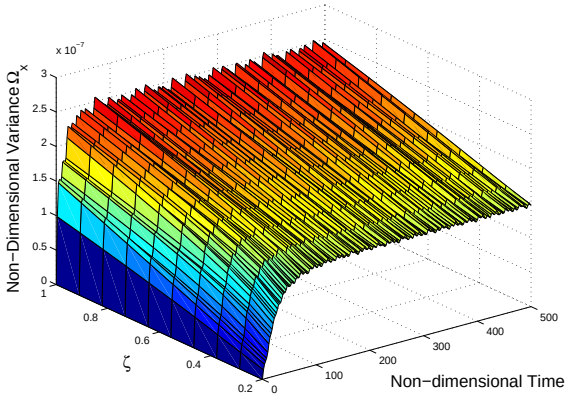

(a) Resolution simulations showing the effect of ζ on $\hat{\Omega}_x$ variance.

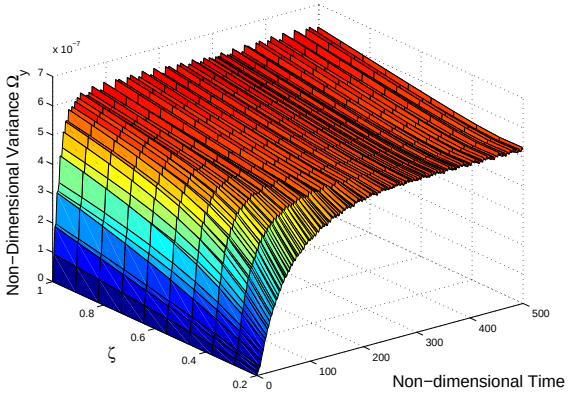

(b) Resolution simulations showing the effect of ζ on $\hat{\Omega}_y$ variance.

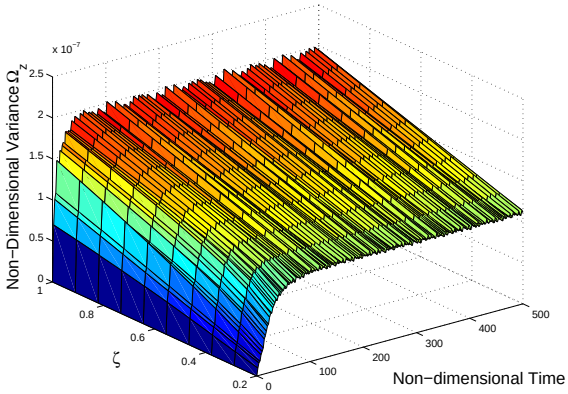

(c) Resolution simulations showing the effect of ζ on $\hat{\Omega}_z$ variance.

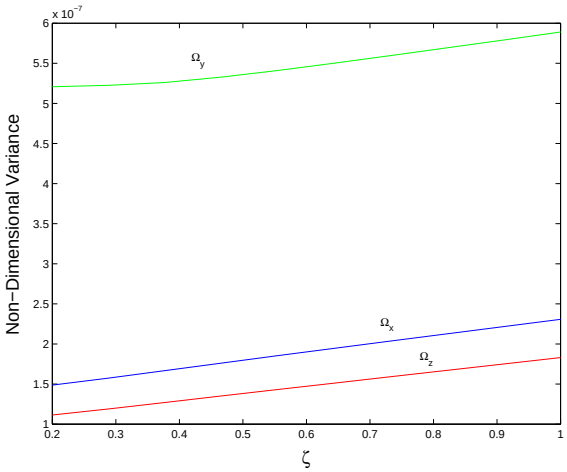

(d) Summary of steady state values of resolution simulations, Figures 4.13(a), 4.13(b) and 4.13(c), showing the effect of ζ on $\hat{\Omega}$ variance.

Figure 4.13: Simulation results of Equation 4.158, showing the effect of ζ on angular rate estimate variance due to thermal mechanical and velocity noise. ($S_b = 1.47 \times 10^{-26} N^2 s$ and $S_v = 2.94 \times 10^{-12} m s^{-1}$)

Figures 4.12(a), 4.12(b) and 4.12(c) are simulations of Equation (4.158) showing the $\hat{\Omega}_x$, $\hat{\Omega}_y$ and $\hat{\Omega}_z$ variance for a variation in frequency ratio $\frac{\omega_y}{\omega_x} = \frac{\omega_z}{\omega_y}$ from 1 to 1.6. Figure 4.12(d) gives the steady state information in a concise form. It indicates that the resolution improves significantly as the frequency ratio approaches 1. This result is intuitive because as $\frac{\omega_y}{\omega_x} \rightarrow 1$, any error caused by Coriolis acceleration will have greater mechanical amplification giving a better signal to noise ratio on the velocity sensor data. The tradeoff is the reduction in persistence of excitation which may cause unwanted oscillations in the estimates; these factors however are not picked up by this resolution analysis.

Figure 4.13 shows the simulations for a variation in the controllers internal damping

variable ζ defined in Equation (4.139). The ζ variable was changed from between 0.1 and 10. Figure 4.13(d) shows that resolution is improved as ζ (and therefore γ) is reduced. Again this is an intuitive result given that γ acts as a gain for the velocity error with its measurement noise which drives the parameter estimation. The tradeoff however is that the parameter estimates become increasingly coupled.

Figure 4.14 shows the simulations for a variation in the angular rate adaptation gain γ_Ω which is changed from 0.001 to 0.1. It shows the relationship between resolution and γ_Ω which was shown in Equation 4.137 to dictate the device bandwidth. The stiffness and damping adaptation gains have negligible effect on the resolution however in Section 4.9.2 it was shown that they should be chosen so as to synchronise the bandwidths of all the parameter estimates to minimise any unwanted oscillatory behaviour.

In all the above results it was seen that the variance on $\hat{\Omega}_y$ was greater than for $\hat{\Omega}_x$ and $\hat{\Omega}_z$. The reason for this is suspected to be because the resonant frequency of the y axis is between that of the x and the z axis frequencies, any x axis velocity sensing noise will not affect the z axis estimates as much as it will affect the y axis and vice versa due to the internal dynamics of the system. This can be understood more clearly using the bode plots in Figure 4.6(b) which are indicative of the internal dynamics of the system. This reasoning is supported by the results in Section 4.11.2 which shows that without the velocity sensing noise that the resolution results are equal for each of the three axes.

4.11.2 Ultimate Resolution

Given that thermal mechanical noise is unavoidable, the best possible resolution is that with perfect velocity sensing. Therefore we can evaluate the ultimate achievable resolution by letting $S_v = 0$ in Equation 4.158 and simulating in the time domain until $\dot{P} \approx 0$. These simulations can be seen in Figure 4.11.2. The results are interesting in that the three axes have equal ultimate resolutions. This supports the reasoning in the previous section that the larger variance in the y axis is caused by greater mechanical amplification of the velocity sensing noise on that axis compared to x and z.

The plots in Figure 4.11.2 show a linear relationship between the angular rate estimate resolution and the device bandwidth. The gradient of this graph is $0.65 deg/hr/\sqrt{Hz}$ which is equal to $0.01 deg/\sqrt{hr}$ and represents the resolution performance with zero velocity sensing

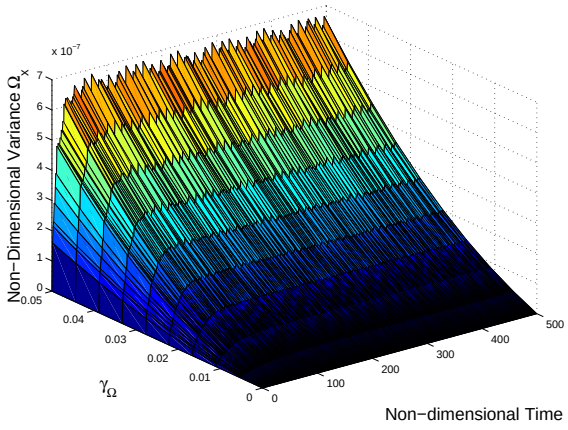

(a) Resolution simulations showing the effect of γ_Ω on $\hat{\Omega}_x$ variance.

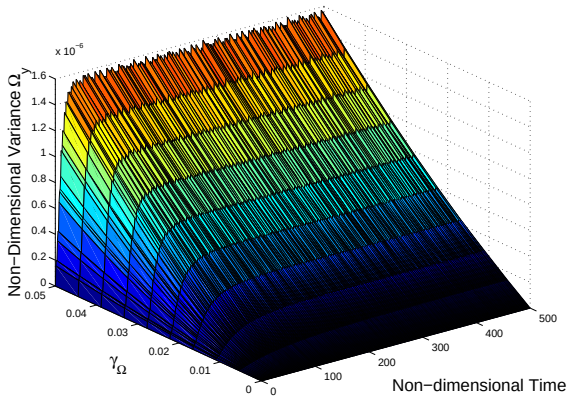

(b) Resolution simulations showing the effect of γ_Ω on $\hat{\Omega}_y$ variance.

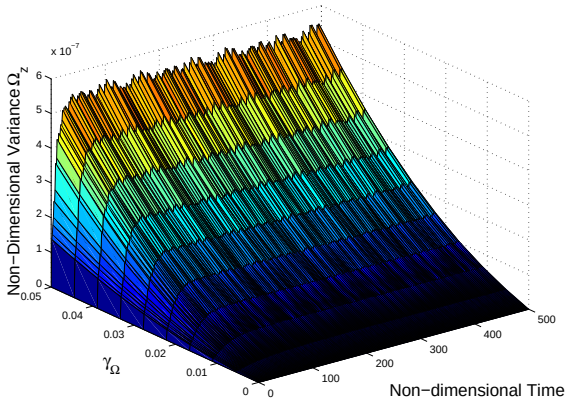

(c) Resolution simulations showing the effect of γ_Ω on $\hat{\Omega}_z$ variance.

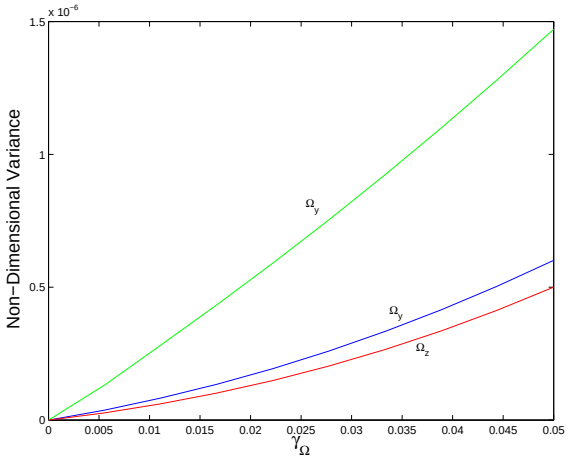

(d) Summary of steady state values of resolution simulations, Figures 4.14(a), 4.14(b) and 4.14(c), showing the effect of γ_Ω on $\hat{\Omega}$ variance.

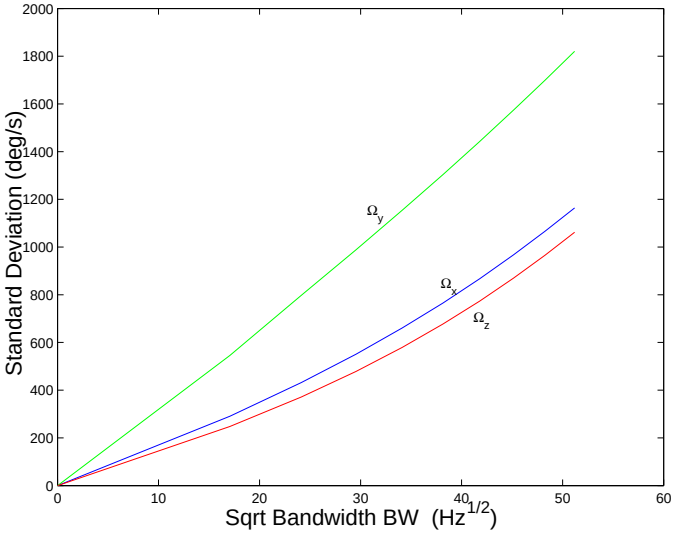

(e) Effect of bandwidth BW on the standard deviation of $\hat{\Omega}$ (Resolution).

Figure 4.14: Simulation results of Equation 4.158, showing the effect of γ_Ω and hence bandwidth BW on angular rate estimate variance due to thermal mechanical and velocity noise. ($S_b = 1.47 \times 10^{-26} N^2 s$ and $S_v = 2.94 \times 10^{-12} m s^{-1}$)

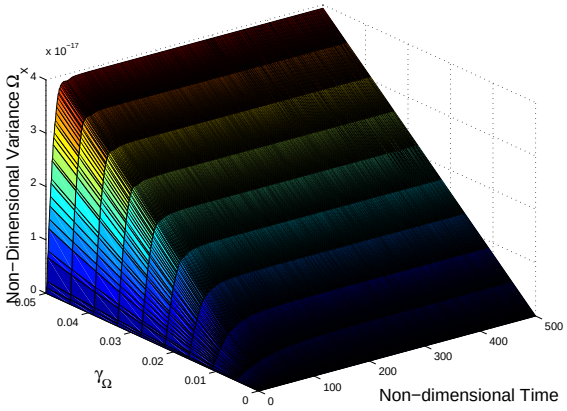

(a) Ultimate resolution simulations showing the effect of γ_Ω on $\hat{\Omega}_x$ variance.

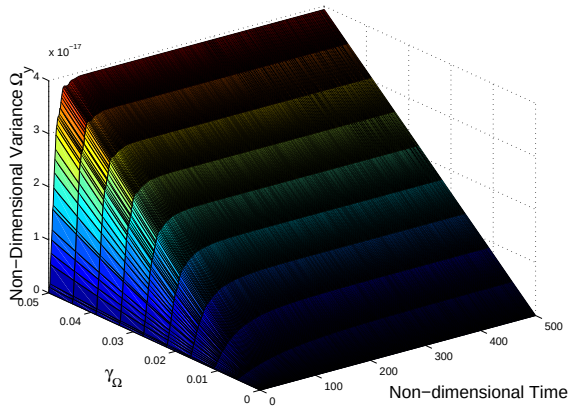

(b) Ultimate resolution simulations showing the effect of γ_Ω on $\hat{\Omega}_y$ variance.

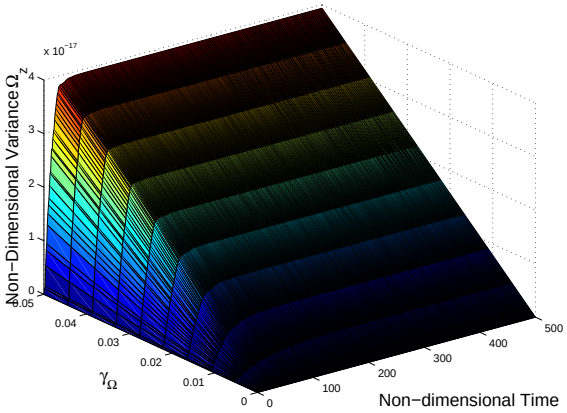

(c) Ultimate resolution simulations showing the effect of γ_Ω on $\hat{\Omega}_z$ variance.

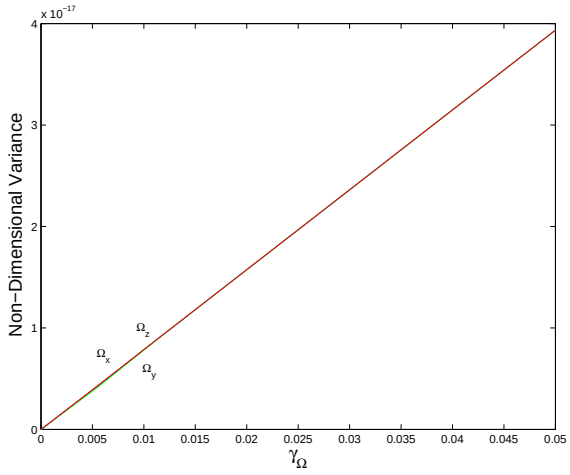

(d) Summary of steady state values of resolution simulations, Figures 4.15(a), 4.15(b) and 4.15(c), showing the effect of γ_Ω on $\hat{\Omega}$ variance.

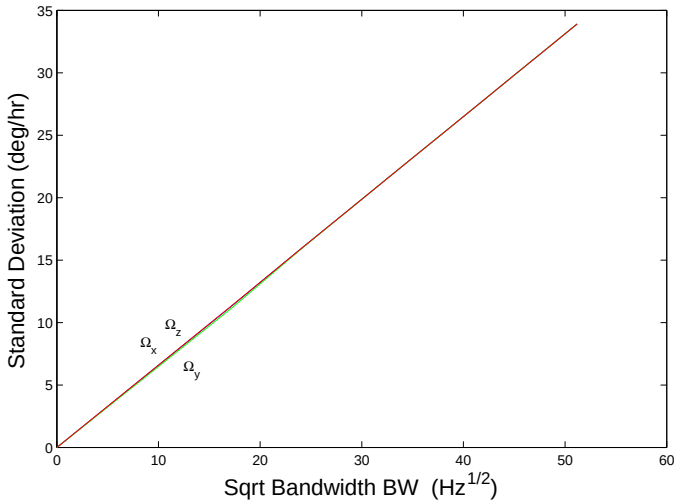

(e) Effect of bandwidth BW on the standard deviation of $\hat{\Omega}$ (Ultimate resolution).

Figure 4.15: Simulation results of Equation 4.158, showing the effect of γ_Ω and hence bandwidth BW on angular rate estimate variance due to thermal mechanical noise. ($S_b = 1.47 \times 10^{-26} N^2 s$ and $S_v = 0$)

noise. This figure is identical to that found for the single axis device in [60] from which the Brownian noise power was taken.

The ultimate achievable resolution is proportional to the thermal mechanical Brownian noise forces acting on the the mass in each axis. The size of these forces will vary depending on the chosen device structure and operating environment.

Chapter 5

Triaxial Angular Rate Sensor: Physical Structure

5.1 Introduction

In Chapter 4 an adaptive controller concept was developed for a triaxial angular rate sensor. It has been successfully modeled in software and simulation results verify that all unknown parameter estimates, including that for the triaxial angular rates, converge to their true values as required. It is also important however, to show that a suitable physical structure is realisable on which the controller may operate. This section addresses a major challenge of implementing the proposed MEMS device which lies in designing a structure that is suitable for fabrication using standard MEMS techniques. It develops a structure that has suitable modal properties, is planar in design and uses conventional MEMS actuation and sense element technologies. It is also desirable to use as few fabrication steps as possible, as every addition step not only adds cost but also contributes to structural imperfections. Attempts have been made to simplify and reduce the drive and sense circuitry by sharing between the three axes. Actuation elements have been designed that allow independent actuation of each axis.

5.2 Structure Design

Intuitively one would imagine a single mass triaxial angular rate sensor being identical in the three main axes, leading to a structure resembling a cube as proposed by Luinge [47] and Kooi

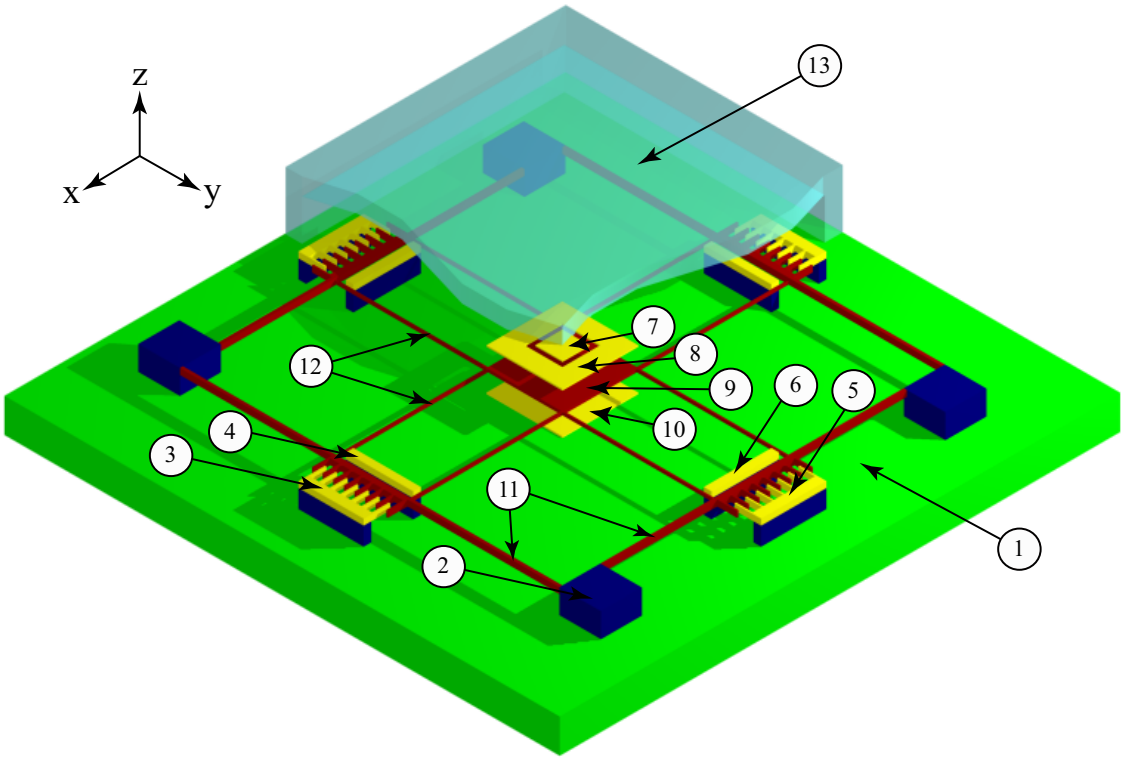

1. Substrate
2. Anchor points
3. X-axis stationary electrostatic comb drive
4. X-axis stationary capacitive sensing plate
5. Y-axis stationary electrostatic comb drive
6. Y-axis stationary capacitive sensing plate
7. Top z-axis stationary capacitive sensing plate
8. Top z axis stationary electrostatic drive plate
9. Vibrating proof mass
10. Bottom z-axis stationary electrostatic drive plate
11. Outer suspension support spring beams
12. Inner suspension support spring beams
13. Sealed enclosure with attached top electrodes

Figure 5.1: Conceptual drawing of the proposed device. It consists of a single suspended mass that is free to move in three dimensions, has actuation elements in three orthogonal axes and has sensing elements that are able to resolve the mass's instantaneous displacement and velocity in each axis with respect to the device casing. Ideally the sense and actuation elements should remain parallel when the mass is displaced

et al [33]. This approach however, does not translate well into the MEMS batch fabrication given that the design requires assembly steps due to its non-planar design. To keep fabrication costs to a minimum, it is necessary to use existing MEMS fabrication techniques and for the device to require no assembly steps prior to packaging. For this reason all parts of the structure have been kept planar in design.

The proposed adaptive controller requires a slight mismatch in natural frequencies between each of the x, y and z axes. This lends itself well to a design with some asymmetry between axes. This is beneficial because the planar nature of MEMS structures makes triaxial symmetry difficult without additional costly assembly steps.

An AutoCAD conceptual drawing of the basic device structure can be seen in Figure 5.1. It has been based on a symmetric single axis angular rate sensor [5]. This device was chosen from the literature because it provides parallel motion in the x and y axes sensing and actuation points using a structural mode decoupling design. This allows the mass's motion to be sensed and actuated in each axis independently of its perpendicular displacement. Being a single axis device, the mass's motion is constrained in the z axis. Therefore for the triaxial device the cross section shape of the inner spring elements needed to be modified to allow the mass to also vibrate in the z-axis. The beam lengths have been adjusted so that the x and y axes are unequal in length to create the mismatched modes required by the controller. The structure also incorporates the sensing and actuation elements. It is proposed that the x and y axes motion will be sensed using differential capacitive parallel fingers and driven using electrostatic combs. The z-axis motion will be sensed using capacitive plates and driven using electrostatic plates. This is covered in more detail in the following sections.

5.2.1 Actuation

The majority of MEMS angular rate sensors have utilised electrostatic actuation. This is due to compatibility with batch processing and materials, having little temperature dependence and providing a force that scales well to the micro dimensions. The use of comb fingers, as well as increasing the electrostatic actuation surface area, gives the actuator a desirable constant force to displacement relationship. Comb drives are easily implemented for the in-plane (x and y) axes using patterned masks, however are impractical for the out of plane (z) axis actuation. To keep the z axis as consistent as possible electrostatic actuation can still be used however plate

elements must replace the comb elements.

Since electrostatic actuation is only capable of providing an attractive force, a pair of electrostatic actuation elements are used to be able to move the mass in both directions in each axis.

The size of the control forces τ are highly dependent on the difference between the reference model and the actual stiffness of the device. If they are exactly the same, only the damping dissipation and Coriolis forces need be overcome, for the proposed device this is approximately $0.2nN$. However if they are very different larger control forces will be required conceivably up to the static deflection force which for the proposed device is approximately $20\mu N$. The voltages required to create these electrostatic forces vary with the comb drive dimensions however are in the range of 1-10's of Volts.

x and y axes electrostatic actuator design

Electrostatic comb actuation has been chosen for both the x and y axes. The advantage of using a comb actuator is that regardless of the comb's displacement the actuator will produce the same force for a given voltage. This is important since the actuation force in each axis should be independent of the mass' displacement in the other two. Electrostatic comb actuation maintains this independence in spite of any "pull-in" effect as described in section 5.2.3.

The length of the comb elements will be the same as the side length of the vibratory mass. Assuming this length is $228\mu m$, with a finger width and gap of $2\mu m$ gives 28 fingers plus an additional one on the stationary comb. The height of the comb will also share the height of the main structure which is assumed to be $5\mu m$. The length of each finger is chosen as $35\mu m$ to provide sufficient overlap between the two combs and room for the required displacements.

The force voltage relationship for each finger gap from Equation (2.6) becomes

$$F = \frac{\varepsilon_0 \varepsilon_r \times 5\mu m V^2}{2 \times 2\mu m} \tag{5.1}$$

$$= \frac{8.85 \times 10^{-12} F m^{-1} 5\mu m V^2}{4\mu m} \tag{5.2}$$

$$= 11.0625 \times 10^{-12} V^2 \tag{5.3}$$

This is multiplied by the number of gaps between fingers in the combs, which in this

case is 57 giving $F = 6.305625 \times 10^{-10}V^2$. Therefore, for example, a $100V$ driving signal will produce a $6.3\mu N$ force.

z axes electrostatic actuator design

Achieving electrostatic actuation in the z axis, whose force output is independent of the displacement of the mass, is a more complex task than that of the x a nd y axes, whose solution was to use comb actuators. For the device to maintain its planar design, comb actuators cannot be used. Instead this section describes a parallel plate electrostatic actuator whose shape achieves two things; firstly it maintains a constant overlapping area during any perpendicular displacements of the the mass between the stationary electrodes and the mass (the second electrostatic electrode). This achieves a driving force whose magnitude is independent of mass displacement. Secondly, the point at which the force acts always remains at the geometrical centre of the mass which avoids any unwanted torque acting on the mass.

The design consists of four square electrodes both above and below the vibrating mass. Having them both above and below the mass linearises the force. The four square stationary electrodes are arranged in a checkerboard pattern, with a square gap between them whose side length is equal to half the mass' side length. This checkerboard arrangement ensures that regardless of the mass' displacement, it will always have 50% of its area overlapping with the four electrodes. This can be seen in Figure 5.2. As will be shown in the following proof, the checkerboard pattern also makes the net force of the four electrodes always act through the geometric centre of the vibrating mass.

Referring to Figure 5.2. Assuming the side length of the square electrodes is a, then the mass will have a side length of $2a$. Assuming the mass is displaced by x in the x axis and y in the y axis, then the centroid of the four overlapping areas should be located at the mass' geometric centre. To show this only the location of the centroid in the x axis ($Centroid_x$) is calculated, as the y axis result will be identical.

$$Centroid_x = \frac{a\left(\frac{a}{2}-x\right)\left(\frac{a}{4}-\frac{x}{2}\right) + a\left(\frac{a}{2}-y\right)(a-x) + a\left(\frac{a}{2}+y\right)(a-x) + a\left(\frac{a}{2}-y\right)\left(\frac{7a}{4}-\frac{x}{2}\right)}{a\left(\frac{a}{2}-x\right) + a\left(\frac{a}{2}-y\right) + a\left(\frac{a}{2}+y\right) + a\left(\frac{a}{2}-y\right)} \quad (5.4)$$

$$= a \quad (5.5)$$

as required.

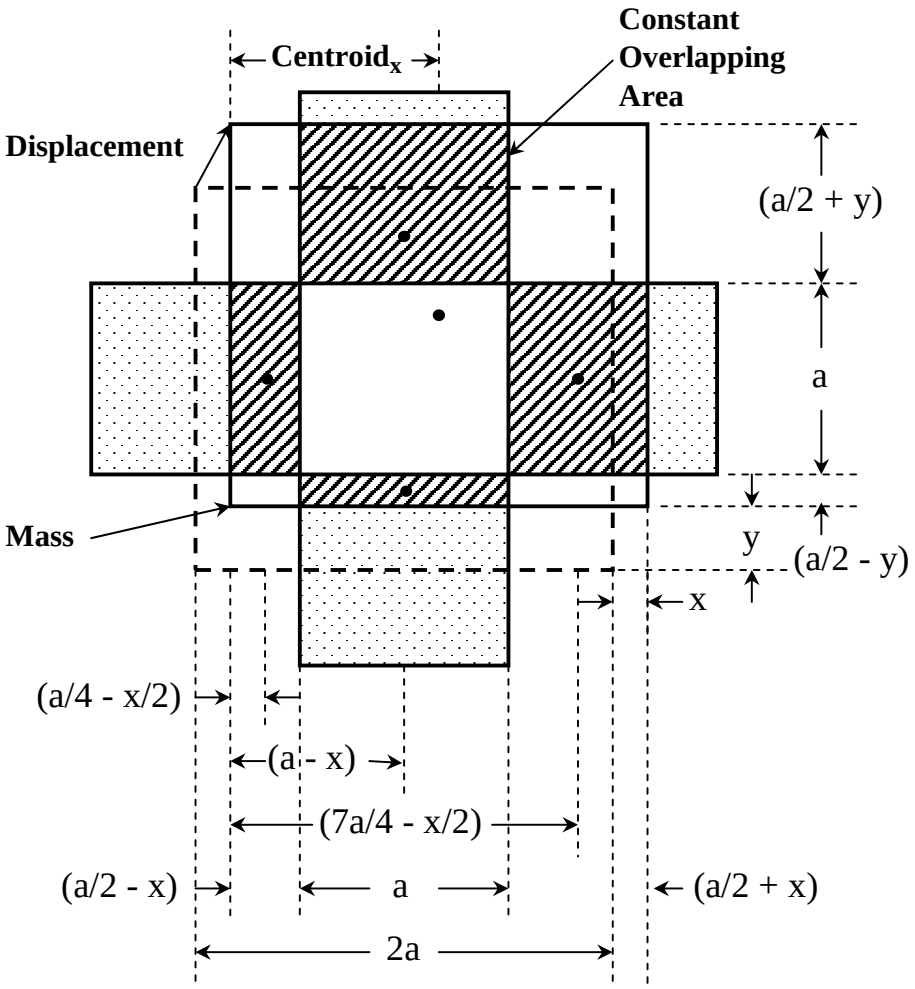

Figure 5.2: Electrostatic electrode design for the z axis actuation. The overlapping area (shaded) between the electrodes and the mass is independent of the mass displacement, as is the point at which the net actuation force acts.

To calculate the force voltage relationship, a mass side length of $228\mu m$ has been assumed and a nominal air gap of $5\mu m$. Given that the mass always has a 50% overlapping area with the checkerboard pattern electrodes, the force voltage equation becomes

$$F = \frac{\varepsilon_0 \varepsilon_r \times \frac{1}{2} (masslength)^2 V^2}{2d^2} \tag{5.6}$$

$$= \frac{8.85 \times 10^{-12} Fm^{-1} \frac{1}{2} (228\mu m)^2 V^2}{2 \times (5\mu m)^2} \tag{5.7}$$

$$= 4.60 \times 10^{-9} V^2 \tag{5.8}$$

Therefore, for example, a $100V$ driving signal will produce a $46.0\mu N$ force.

5.2.2 Sensing

Differential capacitive sensing has been chosen to sense the mass's position and velocity. Capacitive sensing can have high output sensitivity, has a low sensitivity to temperature variation and is compatible with CMOS processing which makes it suitable for integrating both the physical structure and micro electronics on a single substrate. If the structure was to be implemented on a separate substrate to the sensing electronics however, piezoresistivity or some other sensing technology may prove to be a more suitable option than capacitive sensing given that capacitive sensing is sensitive to parasitic capacitances at the electronic interface. Using a single substrate minimises these parasitic effects that are primarily caused by interconnects between multiple substrates. As was shown in section 2.3.1, using a differential sensing scheme makes the output of each axis have a linear relationship with displacement.

The capacitive sensing elements will consist of parallel plates in the z axis using the mass as the common electrode and using parallel sensing fingers in the x and y axes. Multiple rows of parallel fingers have the effect of increasing the sensing surface area in a similar manner to the multiple fingers in each electrostatic actuation comb. The size of the gap between the electrodes and therefore capacitance varies with the displacement in each of the axes. The nominal capacitance of the sensing elements is expected to be in the fF range, however this will be dependant on the dimensions and number of electrodes in the final design.

Shared Sensing Circuitry

Having a single vibrating mass that requires triaxial actuation and triaxial sensing allows some of the sensing circuitry to be shared between the three axes. This has the main advantage of reducing the device footprint even further.

Differential sensing is normally achieved by applying two synchronised sinusoidal signals of opposite phases to the outer electrodes and measuring the output from the common electrode, which normally is connected to or is the mass. The triaxial device would therefore require three common signals to come out of the common vibrating mass. This becomes problematic in that each of the three common signals would need to be isolated. This problem can be overcome using alternative sensing circuits.

One such differential capacitive sensing approach as been presented in [43] and a similar circuit in [72]; both are suitable for the triaxial device. Their single ended approach simplifies the sensing circuitry and the physical connections of the capacitive electrodes. This is made possible by using the mass as a common electrode where a single supply voltage is applied. The signals from each stationary outer electrode pair is then sent to a differential amplifier circuit.

The use of differential sensing also cancels out the pull in effect described in the following section.

In order to reduce the number of fabrication steps, ideally the entire vibrating structure will be electrically conductive therefore requiring no electrical isolation between the sense and actuation elements connected to the proof mass. To achieve this the shared sensing circuitry proposal already uses a common sinusoidal signal applied to the vibrating mass elements. This signal can also be used as the common signal for the actuation. This is achieved by adding the the same sensing sinusoidal signal to the desired actuation signal on each of the three axes. A overview of this system approach is shown in Figure 5.3. Note that the diode symbols indicate that the splitting of the actuation signal to each comb since electrostatics can only provide an attractive force.

x and y axes capacitive sensor design

The capacitive sensing for the x and y axes can be achieved with either parallel fingers whose gap varies with displacement or with combs whose overlapping areas vary with displacement. The comb arrangement has the advantage of giving a constant change in capacitance for a given

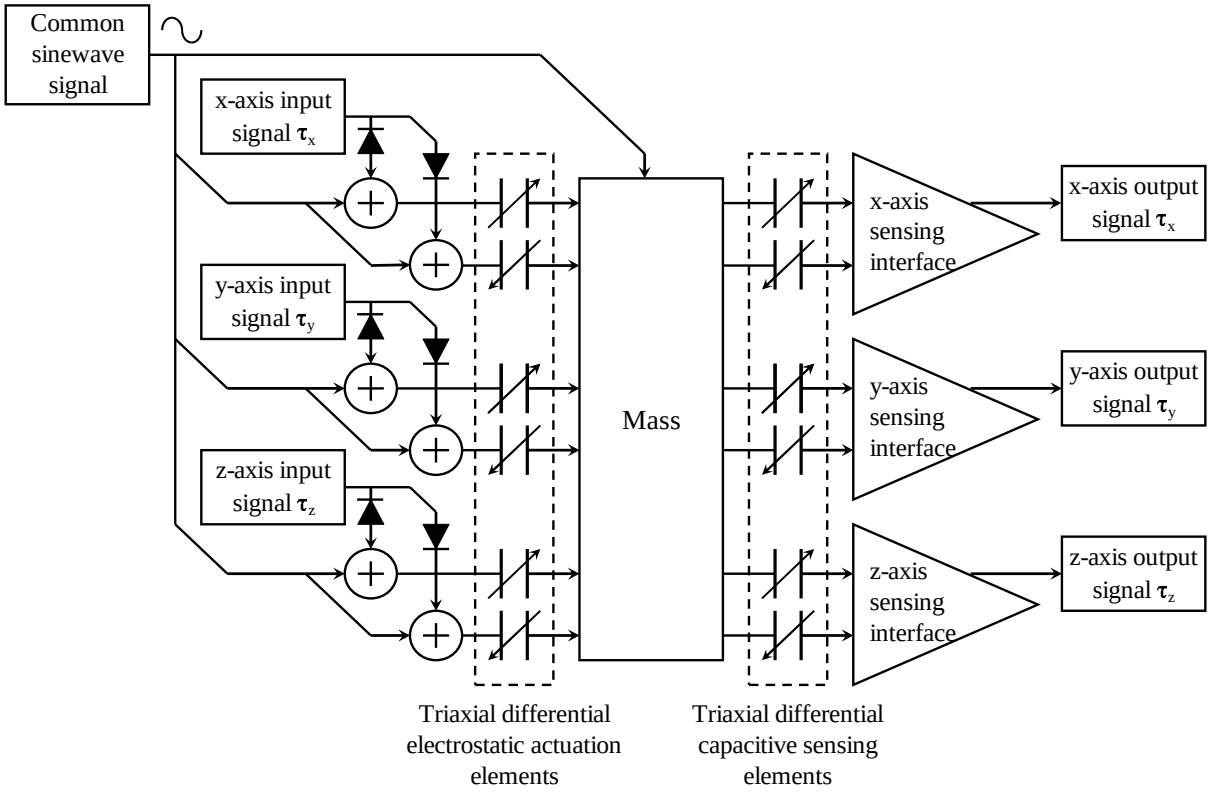

Figure 5.3: Actuation and sensing system that enables a common signal to be applied to the entire mass.

change in displacement given as

$$\frac{\partial C}{\partial x} = \frac{2\varepsilon_0 \varepsilon_r h N}{d} \tag{5.9}$$

However the output of a parallel finger arrangement can be linearised using differential sensing as was covered in section 2.3.2. The simplicity of a single parallel finger electrodes makes it convenient to incorporate in the triaxial design however if the nominal capacitance is found to be too small compared to noise on the signal, additional pairs of parallel fingers would need to be added to the structure. In this case the comb structure may prove to be simpler to incorporate.

The nominal capacitance for each of the x and y sensing electrodes with length of $220\mu m$, height of $5\mu m$ and nominal gap of $5\mu m$ is

$$C = \varepsilon_0 \varepsilon_r \frac{lw}{d} \tag{5.10}$$

$$= 8.85 \times 10^{-12} Fm^{-1} \frac{220\mu m \times 5\mu m}{5\mu m} \tag{5.11}$$

$$= 1.95fF \tag{5.12}$$

If capacitive combs such as those used for the x and y axis actuation are used as sensors, their nominal capacitance will be

$$C = \varepsilon_0 \varepsilon_r \frac{lhN}{d} \tag{5.13}$$

$$= 8.85 \times 10^{-12} Fm^{-1} \frac{30\mu m \times 5\mu m \times 57}{2\mu m} \tag{5.14}$$

$$= 37.83fF \tag{5.15}$$

The capacitive comb option has the advantage of being able to use a smaller capacitive gap because it does not need to allow space for the displacement.

z axis capacitive sensor design

The z axis capacitive sensing electrodes will be situated in the four corners between the actuator electrodes as well as in the central area. Again a set both above and below the vibrating mass will allow differential sensing to be used which linearises the output signal.

This arrangement, like the z axis actuators, maintains a constant overlapping area between the sensing electrodes and the mass, independent of any displacements of the mass.

Providing an interconnect to the central electrode could be done externally, however this will require additional fabrication steps. So it is proposed that a small corner of each actuator be omitted to provide enough room for small interconnecting tracks between the central and corner sensing electrodes. This can be seen in Figure 5.4.

The nominal capacitance for this z axis sensing arrangement, allowing a $2\mu m$ isolation gap between the sensing and actuation electrodes is

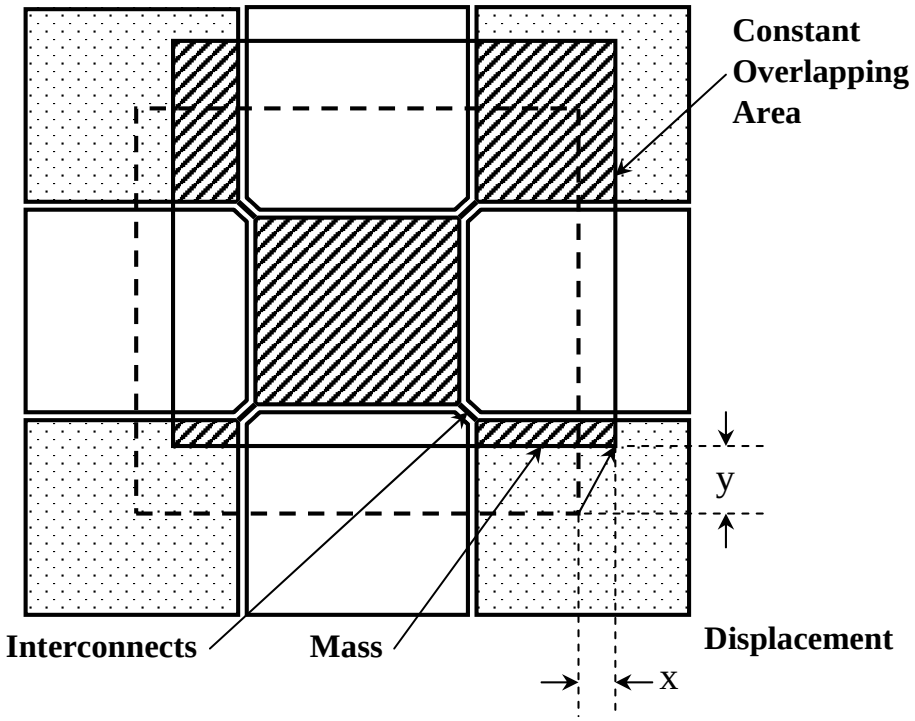

Figure 5.4: Capacitive electrode design for the z axis sensing. The overlapping area (shaded) between the electrodes and the mass is independent of the mass displacement.

$$C = \varepsilon_0 \varepsilon_r \frac{\sum lw}{d} \tag{5.16}$$

$$= 8.85 \times 10^{-12} Fm^{-1} \frac{110\mu m \times 110\mu m + 4 \times (55\mu m \times 55\mu m)}{5\mu m} \tag{5.17}$$

$$= 42.83 fF \tag{5.18}$$

Looking the magnitude of the nominal capacitance in the z axis to that in the x and y, it would be desirable for them to all have similar nominal capacitances. Therefore it may prove to be a better option to use a comb arrangement in the x and y axes, with the finger length extended to increase the nominal capacitance to that of the z axis.

5.2.3 Structural "Pull-In" and Common Mode Rejection

The proposed structure uses suspension beams that aim to isolate the x axis sensing electrodes from sensing any y and z axis motion and the y axis sensing electrodes from sensing any x and z axis motion. There is however, a slight "pull-in" that occurs as the mass moves perpendicular to either the x or y sensing electrodes. This "pull-in" motion can be seen in Figure 5.5. If

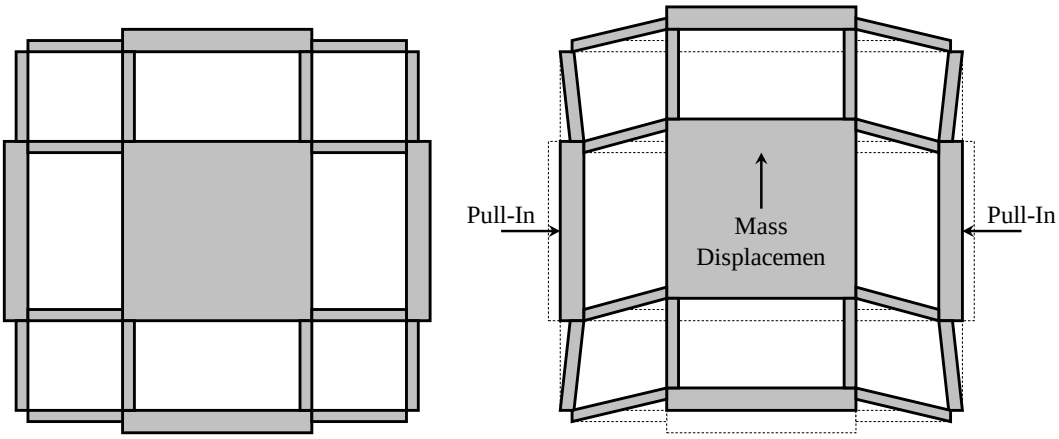

Figure 5.5: Pull in effect due to a perpendicular mass displacement

the length of the suspension beams is long compared to the magnitude of displacement then this "pull-in" effect will be minimal however it can be further reduced using a common mode rejection sensing scheme.

The "pull-in" effect causes both electrodes in each pair to pull in towards the mass. Therefore one electrode experiences a positive displacement while the other in the pair experiences a negative displacement. We can then add the two sensing element signal together so that the common "pull-in" error gets canceled. Additionally the signal that we want to measure gets doubled.

The differential sensing approach discussed in section 5.2.2 cancels out any unwanted "pull in" motion signals on the x and y axes sensing elements due to displacement in a perpendicular axis or unwanted twisting modes.

5.3 Alternative Sensing Considerations

Having a capacitive sensing plate both above and below the mass will allow differential sensing to be used which yields a linear relationship. However, the option of having a single electrostatic drive plate in the z-axis has been considered. This promises to considerably reduce the number of fabrication steps however has its own challenges. The scheme involves adding a DC offset to the electrostatic plate so that it is always creating an attractive force which can be increased or decreased to give a varying force.

Having a single z axis actuation plate creates a non-linear force/displacement relationship for the z axis actuator. This may be rectified by scaling the desired control force by $q^2_{m(z)}$,

the z axis reference model displacement. This unwraps the steady state force displacement relationship. The effect that this approach would have on the controller stability would need to be investigated, however has been left as further work.

It may also be possible to have piezoelectric or piezoresistive material along the top or bottom of the suspension beams for sensing displacement in the z axis. However is not an elegant solution since it is inconsistent with the x and y axes and it would therefore be unlikely to be able to share any sensing electronics. It may also introduce unnecessary asymmetric stiffness.

5.4 FEM Modal Analysis

Ideally the mass would remain parallel with respect to the device casing whilst vibrating laterally in the x, y and z axes, i.e. a 3 DOF system. However every realisable device also has unwanted twisting modes, given that they are inherently 6 DOF systems. The aim thus becomes to design a 6 DOF system that, in the operating frequency range of the device, behaves like a 3 DOF system. To achieve this the first three modes should have parallel lateral motion in the x, y and z axes, and the resonant frequency of the unwanted twisting modes should be sufficiently far away from the first three so as to not interfere with the operation of the device.

The proposed design has been modeled using the FEA software ANSYS (See section 2.5.2). It is more convenient to work with a system of units that is representative of the devices size. Therefore all units used in the ANSYS software were in the "μmks" system where μm was used everywhere in place of m (metre) meaning for example that N (Newtons $kg.ms^{-2}$) becomes μN ($kg.\mu ms^{-2}$) and P (Pascal pressure $kgm^{-1}s^{-2}$) becomes MPa ($kg\mu m^{-1}s^{-2}$). All input files used in the ANSYS modeling, including those in Appendix A,B,D and E, are written in this manner. The element used in the analysis, is the "SOLID92" element shown in Figure 5.6. It is defined by ten nodes having three degrees of freedom at each node: translations in the nodal x, y, and z directions. The element also has plasticity, creep, swelling, stress stiffening, large deflection, and large strain capabilities. (Taken from ANSYS help file)

Using the Block Lanczos mode extraction method built into ANSYS, the first six natural modal frequencies and their respective deformation shapes were found. After several design iterations a structure was found whose first three modes were at similar frequencies and whose deformations were lateral in each of the x, y and z axes. The following three modes are the unwanted twisting modes in the x, y and z axes. This design was then slightly modified by

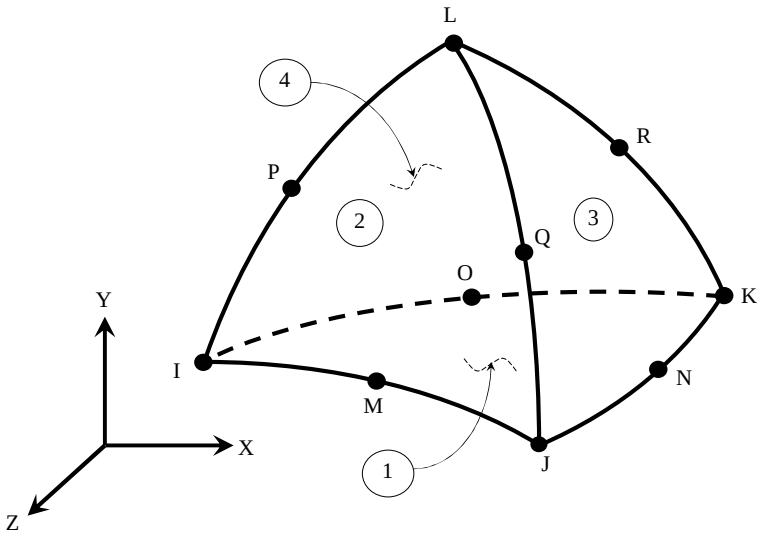

Figure 5.6: ANSYS SOLID92 element

shortening the length of the x axis outer spring element to create the slight mismatch in modal frequencies between the x, y and z axes needed by the adaptive controller. The modal shapes of the first six resonant modes and their respective frequencies are shown in Figure 5.7.

Initial modal analysis results have shown that a device made of silicon with feature dimensions achievable with standard silicon micromachining techniques can produce all three lateral vibration modes at similar but unmatched frequencies and the next mode, the first of the twisting modes, located at approximately 3-4 times the operating frequency region. Generally micro structures have high quality factors and these can be increased further by operating in a vacuum. Therefore due to the fast roll-off from the resonant peaks in the frequency response, the effect of the rotational modes around the operation frequencies should be negligible. The ratios between the x, y and z natural frequencies and the x axis frequency are 1, 1.15, 1.40 which are within the suitable range for the triaxial controller. The nominal resonant frequency of the x axis was $30kHz$ as this was similar to the device in [5] upon which the design was initially based.

The dimensions of the initial device is given in Table 5.1 with reference to the device diagram in Figure 5.1.

5.4.1 Discussion

The modal analysis has shown that the natural modal frequencies required for the triaxial adaptive controller are achievable with a planar silicon design. Looking at the final dimensions

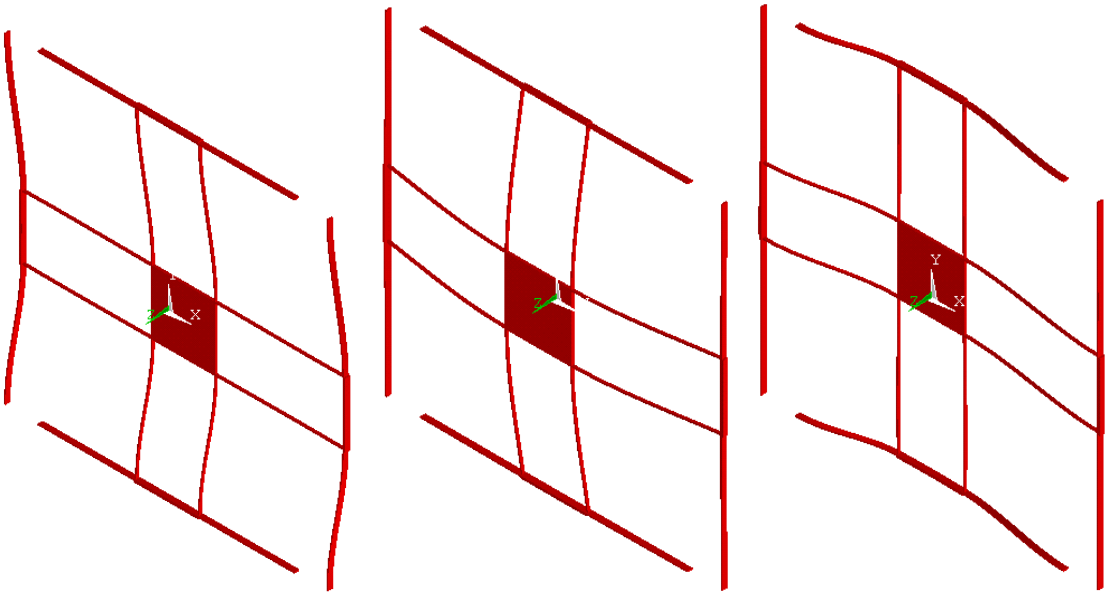

(a) x axis lateral, mode 1, 35.7kHz (b) z axis lateral, mode 2, 41.1kHz (c) y axis lateral, mode 3, 49.7kHz

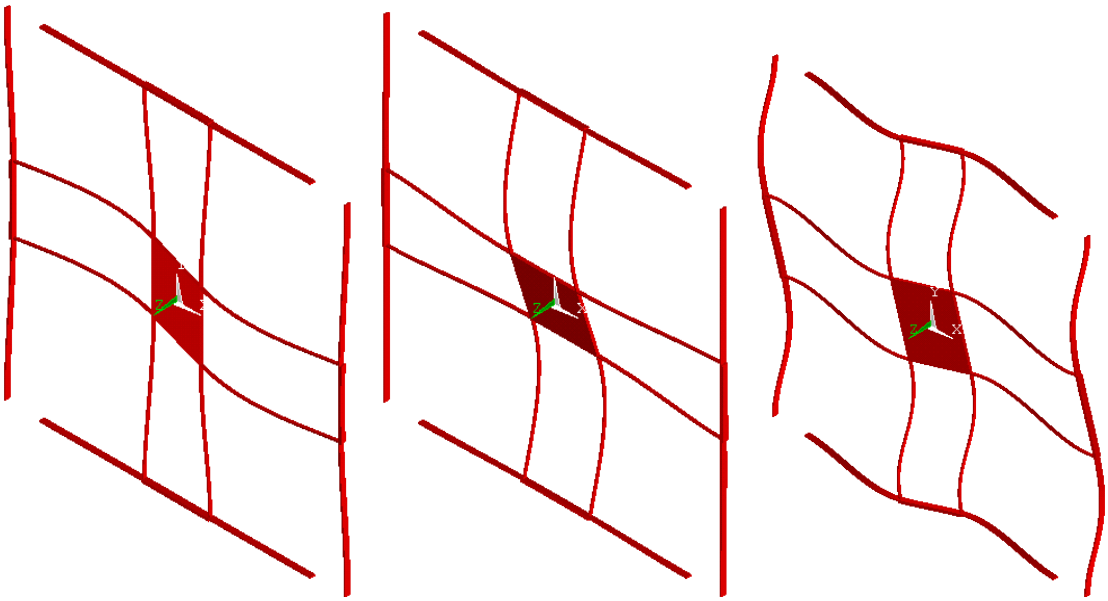

(d) y axis rotational, mode 4, 169.0kHz (e) x axis rotational, mode 5, 186.4kHz (f) z axis rotational, mode 6, 193.9kHz

Figure 5.7: The first six modal shapes and respective frequencies of the proposed device structure as found by ANSYS modal analysis.

Structural Dimension	Value (μm)
Mass length (x axis)	100
Mass length (y axis)	100
Mass height	4
Inner length (x axis)	200
Inner length (y axis)	200
Inner width	2
Inner height	4
Outer length (x axis)	150
Outer length (y axis)	200
Outer width	2
Outer height	8
Centre width	4
Centre height	4

Table 5.1: Device dimensions

in table 5.1 however shows an avenue for improvement. The inner beams and the mass share the same thickness, however the outer beams do not. This adds an additional level of complexity to the design that will introduce additional fabrication steps. This increases cost and is also likely to introduce additional fabrication imperfections.

The design that was modeled in this section was found using trial and error experimentation, getting a feel for the effect each design variable has on the design outputs. The next section aims to automate this design process using design optimisation tools that are available in the ANSYS FEA environment. This powerful approach allows an optimum design to be found within the allowable design space and also for the design space to evolve with the adoption of new technologies.

The proposed structure may also be designed with matched modes for implementation the triaxial device operation proposed by [47] *p.*78. It has advantages over their existing design including being a planar structure that is better suited to existing fabrication processes, it does not require any costly assembly steps prior to packaging and is significantly smaller in size.

Chapter 6

Structure Design Automation

There are many different structural designs that would be suitable for the triaxial angular rate sensor. Therefore this chapter focuses on a design automation approach that can then be applied to any structural design. It aims to achieve some predefined design output goals by fine tuning the specifications of a given structural topology within the allowable design space. If the goals cannot be achieved in the design space then the design topology may need to be altered or the design space redefined.

The design automation process for the triaxial angular rate sensor has three main objectives. The first is to find a suitable geometry for the proposed structural topology which has its first three resonant modes in the x, y and z axes whose frequencies match those required by the adaptive controller. This is important as ideally the device should operate as close to its natural frequency in each axis so that the size of the control forces required to drive the mass into its oscillation trajectory will be minimised. Secondly the mass should ideally remain parallel during its displacement in any axis, therefore any twisting of the mass should be avoided. This twisting behaviour is caused by the higher order resonant modes that have a rotational effect on the mass around each axis. The separation between the third and fourth modal frequency should therefore be maximised so that the twisting modes are sufficiently removed from the operating frequencies of the three axes. Another important design objective for any structure is to ensure that the maximum allowable stress of the material is not exceeded which will lead to mechanical failure.

For the second structure design automation, the area around the comb actuators was focused on, to minimise the twisting on this area. This is important so that the overlapping

area of the comb fingers does not change when the mass is displaced in the z axis.

6.1 ANSYS Optimisation Tools

The optimisation tools within the ANSYS environment have been used here for design automation. This approach is very powerful, especially when the relationship between design variables and simulation outputs are not immediately obvious. For example one of the objectives for the design is for the unwanted twisting modes to have frequencies as far from the operating frequency of the device as possible. It may be possible to intelligently guess how device variables influence the first three modes which have lateral deformation in the x, y and z axes, however their influence on modes beyond the third is much more difficult to predict without the aid of computer simulations.

ANSYS includes a series of design optimisation tools. Each of them works with three variable types; design variables, state variables and an objective variable.

Design variables Design variables are parameters of the model that can be changed by the design optimisation process. They are given an upper and lower limit which may be influenced by things such as fabrication capabilities.

State variables State variables are design requirements that need to be met. They are defined in terms of a tolerance band within which the design is deemed feasible.

Objective Variable The design objective that is to be minimised by the optimisation is called the objective variable. Although each optimisation can only have one objective variable, it can be the result of an objective function made up of many simulation outputs that are to be minimised.

The design optimisation tools vary the design variables within their allowable limits in a systematic manner to minimise the objective variable, while trying to maintain the state variables within their allowed range. If this can be achieved then the design is deemed feasible. ANSYS continues the optimisation process until the optimisation variable levels off to a predefined tolerance or after a predefined number of infeasible designs iterations.

While ANSYS provides powerful optimisation tools for the refinement of a structure to best achieve the design goals, it still requires the initial structural configuration or topology to be supplied by the designer. The process of optimisation does not replace this important innovative

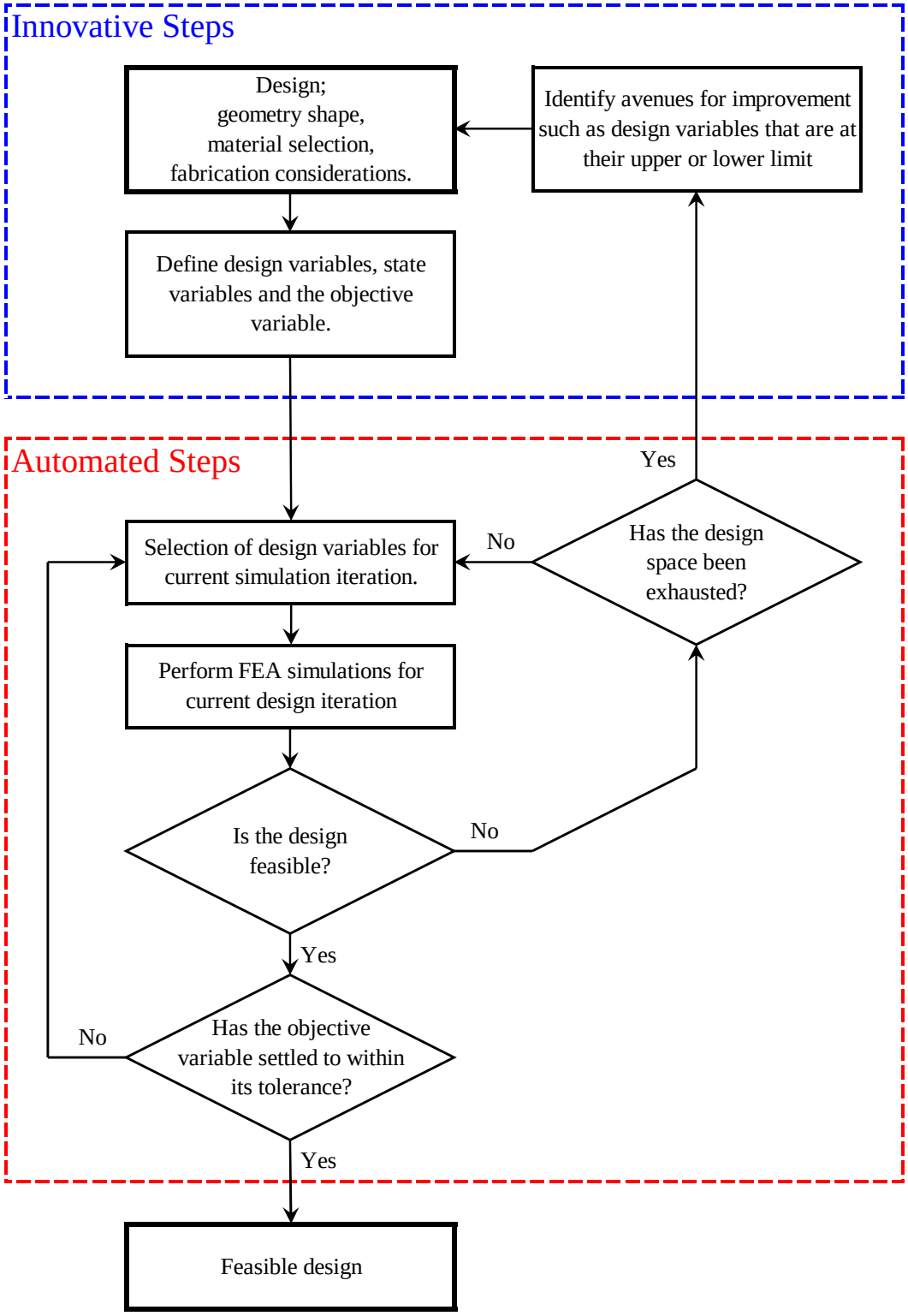

Figure 6.1: Design process diagram for finding a feasible design.

step. If a feasible design is not achievable within the design space, the structure configuration would need to be revisited, again requiring innovation from the designer. This process can be seen in the process diagram Figure 6.1. Chapter 4 covers the first block in Figure 6.1. It is possible to do more than one type of analysis during each design optimisation loop so that all design requirements can be met simultaneously.

Following the design optimisation, it should be checked whether any of the design variables are at their maximum or minimum limit. If so it may reveal an avenue for improved design.

6.2 First Structure: Design Automation

For the initial structure design optimisation two analyses were carried out in each optimisation iteration. The first was a modal analysis to determine the first four modal frequencies of the structure and their modal shapes. The second was a static analysis which involved displacing the centre of the proof mass by $10\mu m$ in the three axes simultaneously. This value is approximately twice as larger as the reference model's maximum displacement. The static analysis is designed to ensure that no part of the structure experiences a stress intensity larger than the yield stress of silicon. The quoted yield strength of silicon varies from $500MPa$ to $7GPa$ however for simulation purposes the more conservative $500MPa$ has been chosen.

Gravity loading was also considered however since the mass is so small and the stiffness of the system is so high, gravity will cause a very small force. This force will appear as a part of the stiffness error which will be estimated and compensated by the controller in real-time. Larger forces caused by environmental impacts have not been considered and remain as further work.

Since the research version of ANSYS has limitations on the number of finite elements that a model may contain, the meshes used were more coarse than ideal. Also, to reduce the number of elements in the FEM, the comb areas were simply represented by a bulk of mass four times as wide as the inner suspension beam widths. As such the precision of the design optimisation is somewhat compromised, however serve as a qualitative approach to future design automation.

The ANSYS batch files used for the first structure design optimisation are included in Appendix A and B.

The following naming conventions have been used.

- *HEIGHT* always refers to the z axis dimension of the component.
- *WIDTH* always refers to the smallest dimension of the component.
- *LENGTH* always refers to the longest dimension of the component.
- The X or Y descriptors refer to the axis with which the length of the component is aligned.
- *INNER* refers to the suspension beams connecting the mass to the centre beams. (Or centre to centre beams)
- *OUTER* refers to the suspension beams connecting the centre beams to the anchor supports.
- The *1* and *2* descriptors refer to the first or second row of suspension beams in the second design automation.

6.2.1 Design Variables

The design optimisation works better if the number of design variables are kept to a minimum. Therefore many of the structure dimensions are expressed in terms of other design variables. For example the length of the electrostatic comb area takes the same value as the mass width.

In order to improve on the initial device structure design, all the vibrating parts, the mass, the suspension beams and the comb elements were made the same thickness. This allows the device to be manufactured using fewer fabrication steps. Therefore the height (*HEIGHT*) was made a design variable. The largest polysilicon deposition thickness is approximately $5\mu m$ using LPCVD. This was used as the upper limit for the height of the structure.

The mass width (*MASS_WIDTH*) was made a design variable since it largely dictates the modal frequencies of the device. The x and y axis mass width were matched. This is partly to simplify the optimisation and also because the mass widths influence the width of the electrostatic comb areas which for simplicity of comb design should be equal in x and y.

The width of the inner (*INNER_WIDTH*) and outer (*OUTER_WIDTH*) suspension beams were made design variables as they were expected to largely influence the modal frequency ratio between the z axis and both the x and y axes.

The x axis inner suspension beam length ($INNER\_LENGTH\_X$) was made a design variable, as was the ratio of lengths between the y and x axis inner suspension beam lengths ($INN\_LENGTH\_Y\_INN\_LENGTH\_X$). It was more convenient to define the y axis inner suspension beam in terms of a ratio because it was expected that this ratio would correlate directly with the desired modal frequency ratios.

The final design variable was the ratio between the outer and inner suspension beam lengths ($OUTER\_INNER\_RATIO$). Here a ratio was used instead of a separate length variable for both the x and y axis since it reduced the number of design variables by one.

6.2.2 State Variables

The triaxial adaptive controller requires unmatched modes in the x, y and z axes to create the three dimensional Lissajous mass trajectory. Therefore the ratio between the first and second modes ($SV1$) and the second and third modes ($SV2$) were chosen as state variables. Their upper and lower limits were chosen as 1.09 and 1.11 respectfully.

The absolute modal frequency of the first mode ($MODE1VAR$) was also made a state variable and given upper and lower limits of 9kHz and 11kHz. This range of values was chosen over the $30kHz$ of the initial design in Chapter 5 so that the computation rate requirements of the adaptive controller would not be too large while the modal frequency would still be larger than external vibratory interference and have a reasonable device bandwidth.

Since the maximum stress experienced by any element ($STRS$) should not exceed the yield stress of silicon, this was also made a state variable with a lower limit of $0MPa$ and a conservative upper limit of $500MPa$.

6.2.3 Objective Variable

The frequency of the fourth resonant mode should be as far as possible from the third modal frequency, therefore it is desirable to try and maximise it. Since the objective variable gets minimised during the design automation process, the inverse of the fourth modal frequency was chosen as the objective variable ($OBJTVAR$).

6.2.4 Results

Plots of the design optimisation simulation iteration results can be found in Appendix C and the final structure dimensions are listed in Table 6.1

Structural Dimension	Value (μm)
HEIGHT	4.95
MASS_WIDTH	219.72
INNER_LENGTH_X	255.89
INNER_LENGTH_Y	289.13
INNER_WIDTH	1.76
OUTER_LENGTH_X	254.13
OUTER_LENGTH_Y	287.13
OUTER_WIDTH	2.61
CENTRE_WIDTH	7.02

Automation Result	Value
INN_LENGTH_Y_INN_LENGTH_X_RATIO	1.13
OBJTVAR	0.235E-04
OUTER_INNER_RATIO	0.99
STRS (MPa)	277.25
SV1 (y-x Freq. Ratio)	1.09
SV2 (z-y Freq. Ratio)	1.09
Mode 1 frequency (Hz)	11008
Mode 2 frequency (Hz)	12046
Mode 3 frequency (Hz)	13179
Mode 4 frequency (Hz)	42477

Table 6.1: First structure: design automation results

The primary goal of the exercise was to find a feasible design. This was achieved at the end of 45 iterations. This clearly demonstrates how this tool reduces costly fabrication, testing and design. However, it can be seen in Figure C.3(a) that in order to achieve a feasible design, little minimising the objective variable was achieved. In this design all the vibrating structure heights were made the same for simplification of the fabrication process. On the previous design the thicker outer beams not only helped to achieve the correct resonant modes but also served to stiffen the area around the electrostatic combs. This reduced unwanted twisting, as ideally the combs should remain perfectly parallel. This design however is more prone to this twisting. Therefore it is proposed that in the next design automation the objective variable be changed to a measure of this unwanted deformation at the comb areas.

6.3 Second Structure: Design Automation

The second structure differs from the first in that a second row of suspension beams has been added in order to reduce the unwanted twisting of the comb areas due to a displacement in the z axis. Also in the design automation, the objective variable has also been changed to a measure of this distortion of the comb areas, since ideally they will remain parallel.

6.3.1 Design Variables

All of the design variables from the first structure are used in the second, as well as additional ones to allow the variation of the additional row of suspension beams. These are the second inner length in the x and y axes (*INNER_LENGTH_X_2*, *INNER_LENGTH_Y_2*), the second inner and outer suspension beam widths (*INNER_WIDTH_2*, *OUTER_WIDTH_2*) as well as a

design variable (K) that determined the length of the second outer suspension beam where

$$\begin{aligned} OUTER\_LENGTH\_X\_2 &= 0.5INNER\_LENGTH\_X\_1 + \\ &\quad K(0.5INNER\_LENGTH\_X\_1 + INNER\_LENGTH\_X\_2) \\ OUTER\_LENGTH\_Y\_2 &= 0.5INNER\_LENGTH\_Y\_1 + \\ &\quad K(0.5INNER\_LENGTH\_Y\_1 + INNER\_LENGTH\_Y\_2) \end{aligned}$$

This enables the second outer suspension beams to take a large range of values while ensuring that none of the suspension beams overlap or cross.

6.3.2 State Variables

The state variables are identical to the first structure design automation.

6.3.3 Objective Variable

A concern with the chosen structure was whether there would be undesirable distortion on the comb areas particularly when the mass was displaced in the z axis. This is not a problem with x and y displacements since the outer suspension beams keep the comb area parallel. The magnitude that the top edge of the centre comb area displaces compared to the bottom edge was chosen as a measure of the distortion. The objective function ($OBJTVAR$) is the sum of the square of this measure in both the x and y axis. The optimisation aims to minimise this objective function and therefore minimise this unwanted distortion.

6.3.4 Results

A feasible design was achieved at the end of 61 iterations. Plots of the simulation results can be found in Appendix F and the final structure dimensions are listed in Table 6.2

The shape of the device needed to be modified to make up for the reduced outer beam thickness. An additional set of outer suspension beams was added. These can be seen in Figure F.5(a). The benefit of doing this was to reduce the amount of non-parallel motion that the electrostatic comb elements can experience.

Structural Dimension	Value (μm)
HEIGHT	4.54
MASS_WIDTH	228.45
INNER_LENGTH_X_1	258.51
INNER_LENGTH_Y_1	280.50
INNER_WIDTH_1	1.75
OUTER_LENGTH_X_1	250.07
OUTER_LENGTH_Y_1	271.35
OUTER_WIDTH_1	1.72
CENTRE_WIDTH_1	6.99
INNER_LENGTH_X_2	99.39
INNER_LENGTH_Y_2	97.95
INNER_WIDTH_2	1.76
OUTER_LENGTH_X_2	276.25
OUTER_LENGTH_Y_2	293.39
OUTER_WIDTH_2	2.79
CENTRE_WIDTH_2	6.99

Automation Result	Value
INN_LENGTH_Y_INN_LENGTH_X_RATIO	1.09
K	0.64
OBJTVAR	0.29E-01
OUTER_INNER_RATIO	0.97
STRS (MPa)	291.92
SV1 (y-x Freq. Ratio)	1.11
SV2 (z-y Freq. Ratio)	1.11
Mode 1 frequency (Hz)	10868
Mode 2 frequency (Hz)	12052
Mode 3 frequency (Hz)	13343
Mode 4 frequency (Hz)	38247

Table 6.2: Second design automation results

6.4 Discussion

The design process involving the optimisation capabilities of ANSYS forms the basis of an automated design process that enables incorporation of new design requirements, limitations and levels of detail. It can be applied to any number of engineering and design problems. It allows the structure to evolve with new and improved fabrication capabilities that may arise through acquisition of new equipment or processing technology.

Integrating a triaxial accelerometer and gyroscope on a single substrate as has been identified as significant focus of future inertial sensing research work. The proposed triaxial angular rate sensor design involves fabrication steps that would be able to be used to fabricate a similarly structured triaxial accelerometer. An accelerometer would be required to have a much lower resonant frequency than an angular rate sensor given the low bandwidth of accelerations to be sensed. This makes having a single vibrating mass for both the accelerometer and angular rate sensor extremely difficult as different device dimensions would be required to alter resonant frequencies. However a separate design for an accelerometer could be achieved by having different suspension beam stiffness or a different sized proof mass. The device dimensions for this application could be found using the design automation process with redefined design, state and objective variables.

Chapter 7

Fabrication Proposal

There are many fabrication processes available to the MEMS designer and no one set way of achieving any one design.

The fabrication proposal has been adapted from the PolyMUMPs process [32]. The PolyMUMPs process is a standardised three layer polysilicon fabrication process developed by MEMSCAP[1] for general purpose micromachining.

In the PolyMUMPs process, polysilicon is used as the structural layer, deposited oxide phosphosilicate glass (PSG) is used as the sacrificial layer and silicon nitride is used as electrical isolation between the polysilicon and the substrate.

The following fabrication process differs from that of the PolyMUMPs process in that many of the steps in the PolyMUMPs process are not required for the fabrication of this device. Also the layer thicknesses have been increased from those specified in the PolyMUMPs process to better suit the triaxial device, however remain within the limits achievable by the fabrication techniques involved.

7.1 Fabrication Process

Starting with a n-type (100) silicon wafer, seen in Figure 7.1(a), of 1-2 Ωcm resistivity. The wafer is heavily doped with phosphorus in a standard diffusion furnace using phosphoroxidchloride (POCl3) as the dopant source. This acts to reduce the charge feedthrough between any electrostatic or capacitive structures and the silicon substrate.

A $600nm$ layer of silicon nitride, seen in Figure 7.1(b), is deposited on the substrate

[1] www.memscap.com

using low pressure chemical vapor deposition (LPCVD). This is for electrical isolation of the structural elements from the silicon substrate.

Next a $500nm$ layer of polysilicon is deposited using LPCVD. A coating of photoresist is added, the photoresist is patterned using lithography and etching steps (Outlined in section 2.2.5). This patterned photoresist layer is used as an etch mask for the polysilicon layer, which is etched using reactive ion etching RIE. After the polysilicon etch, the remaining photoresist mask is stripped away to leave the first patterned polysilicon layer, seen in Figure 7.1(c). This polysilicon layer forms the lower electrostatic and capacitive elements, interconnects between the structural elements and to sense and actuation circuitry.

The first sacrificial layer, $5\mu m$ of phosphosilicate glass (PSG), is deposited using LPCVD and annealed for 1 hour at $1050°C$ in argon. Again a coating of photoresist is added and patterned and used as a etch mask for the RIE of the PSG layer. This creates the areas at which the structures will be anchored, seen in Figure 7.1(d), with the remaining photoresist mask stripped away. This sacrificial layer creates the air gap between the vibratory elements and the substrate and electrodes below.

Next the first structural layer, $5\mu m$ of polysilicon is deposited using LPCVD, as well as a thin $300\mu m$ layer of PSG. They are both annealed for 1 hour at $1050°C$. The annealing dopes the polysilicon with phosphorus from the PSG layer above and below it which makes the layer conductive and also reduces its internal stresses. A coating of photoresist is added and patterned using lithography and etching steps. This etch mask is used to pattern the PSG layer below. This creates a hard mask that is used in RIE to etch the polysilicon below. After the polysilicon is etched the remaining PSG mask and photoresist are stripped. The device at this stage can be seen in Figure 7.1(e).

Again using LPCVD, the second sacrificial layer, $5\mu m$ of PSG is deposited and annealed, then a coating of photoresist added. This layer is patterned to create holes where the upper electrodes will be anchored. This can be seen in Figure 7.1(f).

The same process of deposition, annealing and etching of the first structural layer is used for a second $5\mu m$ structural layer of polysilicon. This layer creates the the upper electrostatic and capacitive electrodes seen in Figure 7.1(g).

At this point the substrate would be diced into individual devices. Following this the sacrificial oxide is removed by immersing the device in a bath of 49% hydrofluoric acid (HF) for 2-5 minutes. This sacrificial etching is halted by immersing for several minutes in deionised

water, followed by alcohol to reduce stiction between the vibratory and stationary elements and at least 10 minutes in an oven at 110°. This leaves the final released structure shown in Figure 7.1(h)

7.2 Fabrication Challenges

While the presented fabrication process looks simple enough there will be many fabrication challenges that will need to be overcome. Some of these will be unforeseen challenges while others may be anticipated. Given that PolyMUMPS is a mature set of fabrication processes, one needs to question what issues any modification to the process may produce. Apart from the omission of unnecessary steps, the only modifications that have been made are to the thicknesses of the structural Polysilicon layers, from $2\mu m$ to $5\mu m$ and the thicknesses of the two sacrificial PSG layers from $1\mu m$ and $2\mu m$ to $5\mu m$ each. While this seems harmless enough it does raise some fabrication challenges.

7.2.1 Deposition of thick film Polysilicon

The structure of deposited Polysilicon is made up of small single crystal grains. The size of the grains increases as deposition layer thickness is increased and with it residual stress. This means that thick films such as those in the proposed fabrication, will have high internal stress at the bottom of the layer and low stress at the top. This will cause any suspended structures such as the mass to distort and will weaken the structure as well. The larger grain size at the top also causes the surface to be more rough than thin films. This increase in roughness can lead to higher stress concentration that can eventually lead to device failure, can make deposition of subsequent layers difficult [21] and can also reduce the resolution of the patterned structure.

A technique called epi-poly can be used to create thick films ($\approx 10\mu m$) that have near zero stress levels [82]. This technique also has deposition rates that are two orders of magnitude faster than LPCVD. It involves depositing a seed layer first using LPCVD and then CVD at high temperature ($\approx 1000°C$). This technique does however, leave high surface roughness with its previously mentioned disadvantages [82].

In another technique called MultiPoly, multiple thin films are deposited using LPCVD with each deposited layer alternating between compressive and tensile stress. In this way the resulting structure will have a near-zero stress. In 2000 research work showed a 10 layer beam

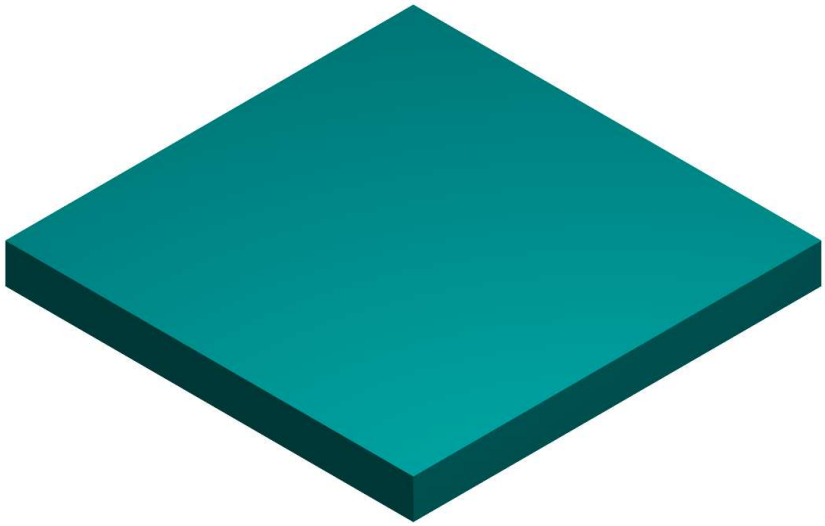

(a) N-type silicon wafer (Blue), heavily doped with phosphorous.

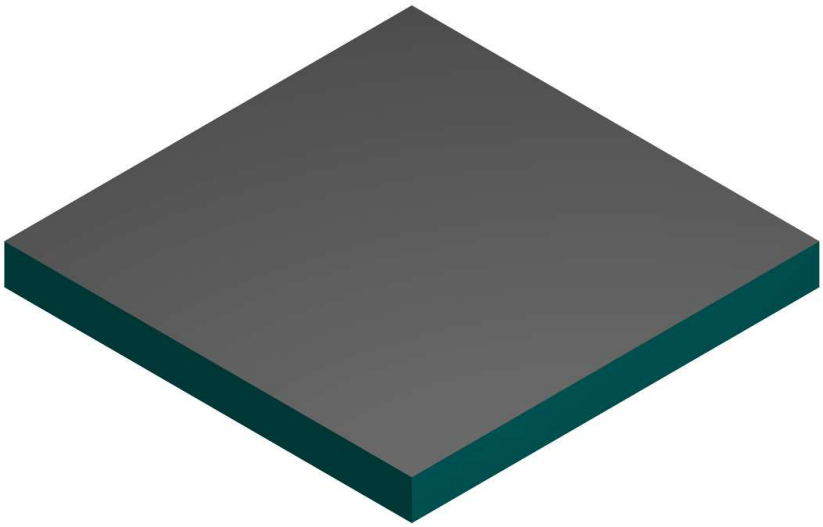

(b) 600nm blanket layer of low stress silicon nitride (Black) deposited.

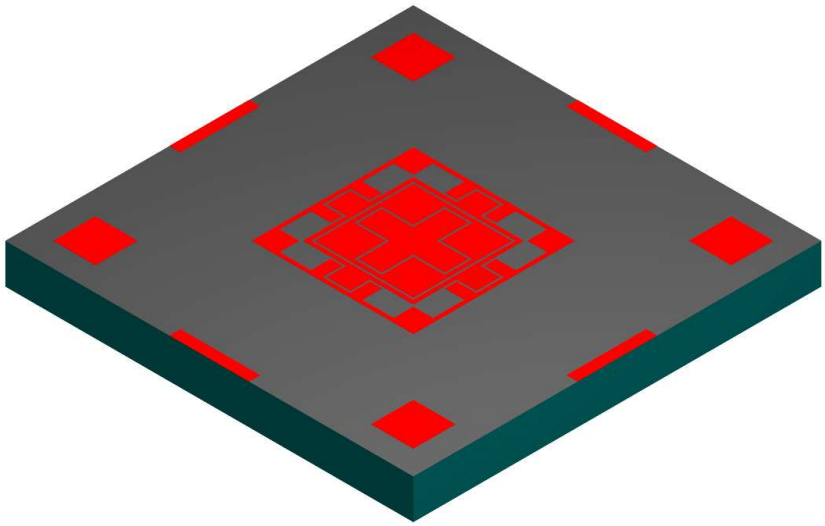

(c) $500nm$ layer of polysilicon (Red) deposited using low pressure chemical vapour deposition (LPCVD), followed by a layer of photoresist, patterned using lithography followed by reactive ion etching RIE to selectively etch the first polysilicon layer. The remaining photoresist mask is chemically stripped.

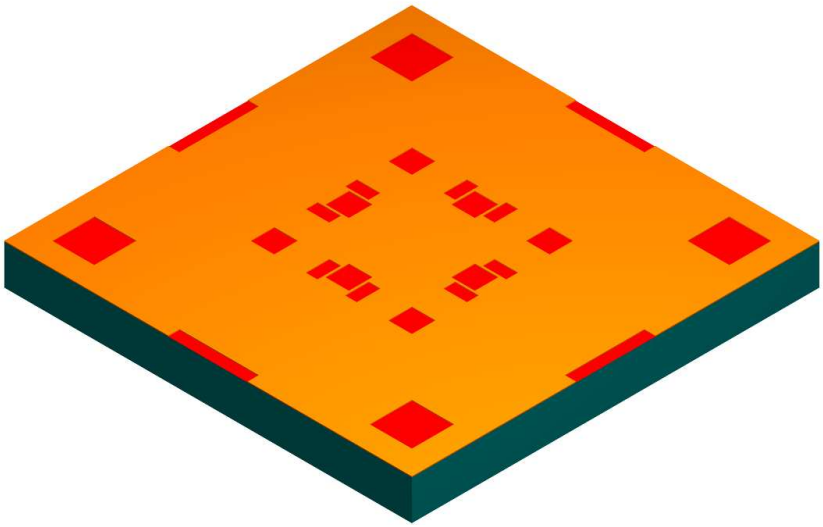

(d) $5\mu m$ Oxide layer of phosphosilcate glass (PSG) (Orange) deposited using LPCVD, forming the first sacrificial layer. This layer is patterned using the same lithography and RIE process as the polysilicon layer.

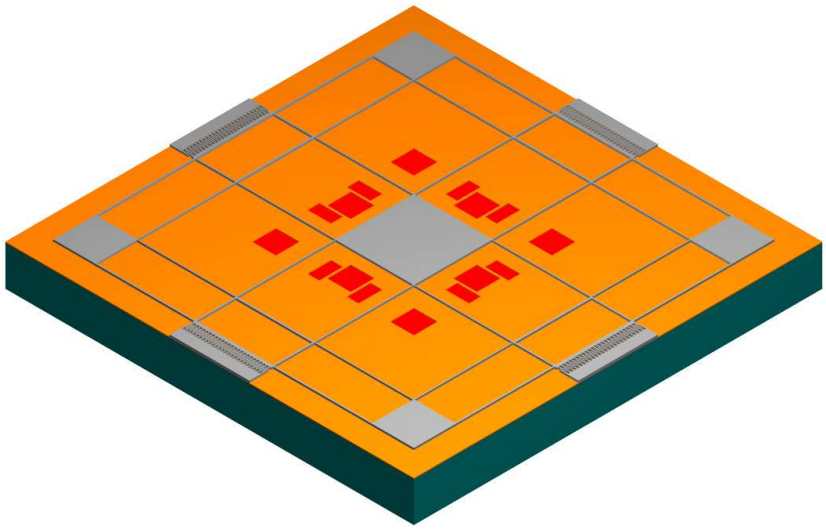

(e) $5\mu m$ layer of un-doped polysilicon (Grey) deposited using LPCVD, followed by a $300nm$ layer of PSG and a $1050°C/1$ hour anneal. A layer of photoresist is added, patterned using lithography and used as a mask for etching the PSG. The PSG is used as a mask for etching the polysilicon using RIE. Both masks are then stripped.

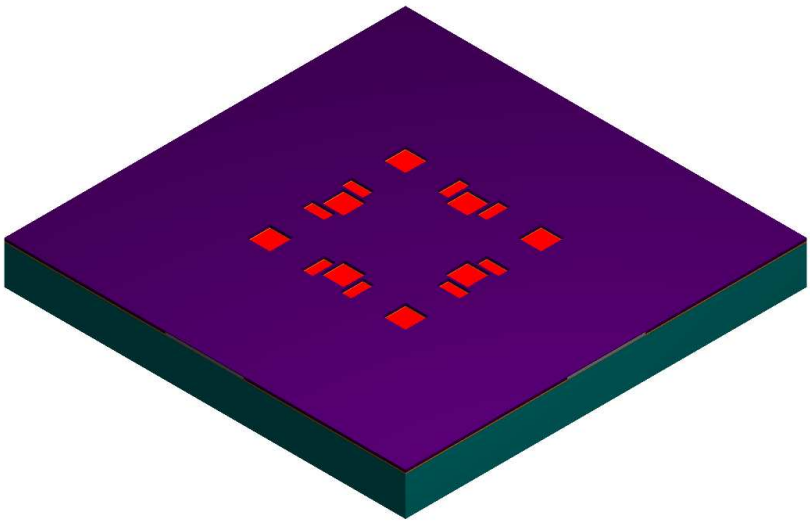

(f) Second $5\mu m$ Oxide layer of phosphosilcate glass (PSG) (Purple) deposited using LPCVD forming the second sacrificial layer. This is patterned, again using the lithography and RIE.

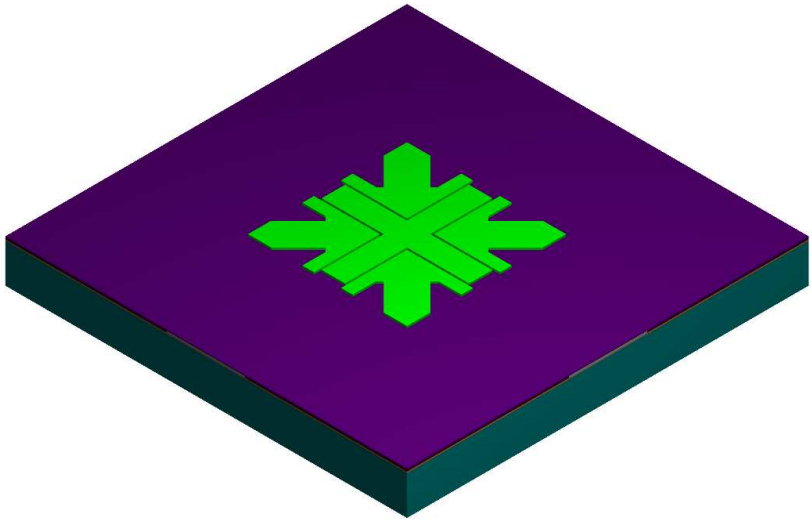

(g) Second $5\mu m$ layer of un-doped polysilicon deposited (Green) using LPCVD followed by a $300nm$ layer of PSG and a $1050^{\circ}/1$ hour anneal. This layer is patterned using the same process as the previous polysilicon layer.

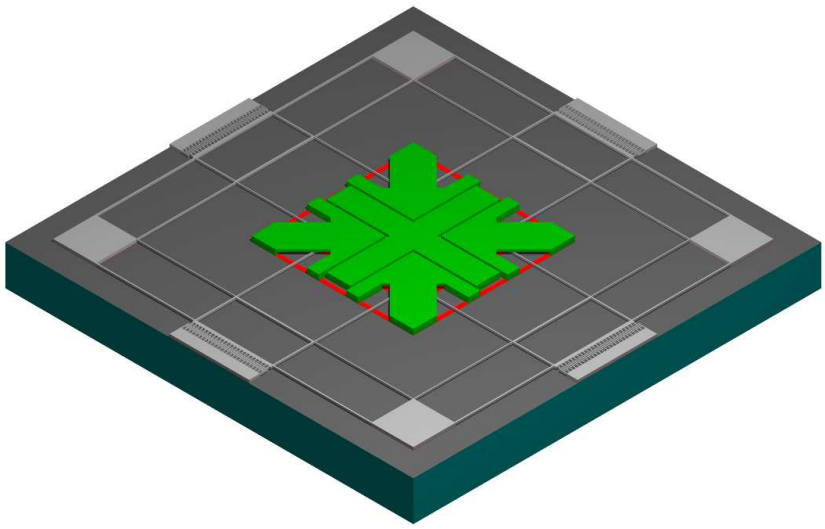

(h) Both sacrificial layers are removed by immersing in 49% hydrofluoric acid (HF), leaving the released structure.

Figure 7.1: Proposed fabrication process for the triaxial angular rate sensor structure. (See the text for a more detailed explanation of this process.)

structure $700\mu m$ long and $4.69\mu m$ thick with no measurable curvature indicating near-zero residual stress [82]. Also, with each layer being a thin film, the top surface of the last layer does not have the high surface roughness that is found with thick film deposition.

7.2.2 Deposition of thick film PSG

Thermal growth of SiO_2 on a Si substrate is a self-limiting process because its growth rate decreases as the SiO_2 thickness increases. LPCVD offers higher deposition rates for thick film PSG and also results in a lower density layer that is fast to etch in HF [21]. PSG also flows at high temperature, so annealing can produce a smooth surface topology. The deposition of thick PSG films does present some problems. Like thick film Polysilicon, it has issues with residual stress gradients through the thickness of the thick layer wich can cause warpage and cracking in the PSG layer. Breaking the deposition of the thick layer into multiple thin layers, with annealing steps after each layer, can reduce the overall stress due to densification of the film.

Crack free, low stress and very thick $< 20\mu m$ oxide layers have been demonstrated using Plasma Enhanced CVD (PECVD) with a tetraethylorthosilicate (TEOS) precursor, following a highly tensile silicon nitride (Si_3Ni_4) film [85]. This process works in the same manner as the MultiPoly process in that the initial tensile SiN layer compensates for the compressive stress in the deposited oxide film.

Chapter 8

Conclusions

This thesis has presented a solid basis for many aspects of a realisable MEMS single mass adaptively controlled angular rate sensor.

The developed adaptive control strategy is able to estimate in real-time all the device damping, stiffness error and angular rate terms. These are used in a feedforward control that compensates for their effect on the device trajectory. This makes a device with inevitable fabrication imperfections behave like an ideal device, that is one with no damping and perfect principle axis stiffness aligned to the geometric axes of the device. This is advantageous since they would otherwise corrupt the device output. Cross damping terms are generally very difficult to distinguish from angular rate since they are in phase with each other, however the proposed device is able to do so when the reference model trajectory is a three dimensional Lissajous trajectory.

The controller inherently drives the proof mass along a preset trajectory removing the need for additional drive control normally found on angular rate sensors and the output of the device is simply the angular rate parameter estimates therefore removing the need for any additional output demodulation stages. In fact it outputs triaxial angular rate estimates which actually means the adaptive controller replaces not one but three sets of drive controllers and output demodulation stages. Additionally the device achieves this with a single vibrating mass instead of three separate ones. The advantages of this are numerous including decreased wafer real estate, which leads to increased production yield as well as removing any mechanical interference caused when one resonating structure shares a substrate with another with a similar resonant frequency.

Design rules for the adaptive gain selection have been demonstrated. They are based on the hypothesis that no one parameter estimate can settle faster than any other since they are interdependent. This was shown to be true by matching the parameter estimate convergence rates found using averaging analysis. It resulted in significantly less unwanted oscillatory behaviour on the angular rate parameter estimates. This is a useful tool for not only the triaxial angular rate sensor but for any adaptively controlled system that uses parameter estimation and control.

The proposed structural topology design has drawn upon existing angular rate sensor designs. The result is a device that is suitable for MEMS fabrication and requires no additional assembly steps prior to packaging. This is important in keeping production costs to a minimum. The design utilises conventional MEMS sensing and actuation elements for the x and y axes and a unique checkerboard electrode arrangement that enables sensing and actuation in the z axis that is independent of perpendicular mass displacement. The actuation electrodes also have the feature of maintaining the point at which the net force acts at the geometrical centre of the mass. Non-conventional circuitry that allows sharing of the circuitry between all three axes has also been proposed. This also contributes to minimising the wafer footprint and allows the entire vibrating structure to be conductive removing any additional fabrication steps that may have been needed to create electrical isolation on the vibrating structure for each axis.

A design automation process has been developed in order to size a given device topology in order to achieve a feasible design. It utilises the design optimisation tools that are part of the FEA software package ANSYS. Two design automation iterations were presented, both of which resulted in feasible designs. The second design incorporated a second row of suspension beams that reduces the amount of unwanted distortion on the comb drive elements. Both designs also incorporated a common structure height for all the vibratory structures. This minimises the number of fabrication steps and also the number of fabrication imperfections, since as a rule, they become more numerous with each additional fabrication step.

A fabrication proposal based on the commercially available PolyMUMPs process has been presented. Modifications to the process have been made to better suit the triaxial angular rate sensor, namely the removal of the unnecessary steps and increasing the layer thicknesses. The proposed process has been presented for completeness and is one of many ways that the structure could be fabricated. As there are constant improvements in state of the art fabrication capabilities. The final processing steps used will depend largely on the available fabrication

resources and capabilities, as well as implementing techniques to overcome fabrication challenges that may arise due to increased layer thicknesses and any other unforeseen challenges. This may subsequently enable the design to be modified by for example making the structural layers thicker or the finer resolution comb fingers.

Chapter 9

Further Research

The real world implementation of the adaptive controller will be in the digital domain. Digital implementation of the controller will introduce discretisation errors that will be detrimental to the the device performance. It may be possible to reduce this discretisation errors through the use of an adaptive observer as was found in [60] or by implementing a trajectory switching algorithm proposed in [28]. The trajectory switching algorithm aims to significantly reduce the size of the stiffness error estimates by making the reference model stiffness match that of the imperfect device. This approach uses a result found in [60] in which the discretisation errors were shown to be dictated by the size of the parameter estimates being compensated for in the feedforward controller.

The controller design process has been simplified down to a relationship between desired bandwidth BW, internal damping ratio ζ and the ratio of natural frequencies in the three axes. There is an optimum combination of these parameters that is dependant on the quality factor of the physical device. Since the adaptive controller makes estimates of the system damping in real-time which are indicative of the quality factor, it may be possible fine tune this combination in real-time. This could be achieved by varying the internal damping ratio ζ from Equation (4.139). The basis for and effect of this additional feedback loop would need to be investigated.

If it is possible to estimate what the current bandwidth requirements are, then it may also be possible to change the damping ratio to suit. This would make the device more flexible for varying application requirements.

An interesting result of the convergence rate analysis was the beneficial effect of matching the averaged convergence rates of all parameter estimates. This is a design rule that can be

applied to all adaptive controllers with similar design architecture. It minimises the guesswork in selecting the adaptive gains and removes the unwanted oscillatory behaviour of all parameter estimates. A strong mathematical proof of this hypothesis would add greatly to the general adaptive control field.

It may be possible to combine the first and second design objectives into one objective function. This would aim to achieve both objectives simultaneously. This would lead to a highly nonlinear objective function. The effectiveness and efficiency of the optimisation tools under these conditions may be compromised and would need to be investigated. There may also be existing optimisation techniques that are better suited to having multiple design objectives.

While a basic fabrication process has been proposed, it also presents with it some fabrication challenges that need to be addressed. Most of these challenges stem from the use of thick films. Subsequently much research effort will be required to develop a mature fabrication process for the triaxial angular rate sensor.

Although this thesis has set the foundation for many aspects of the realisation of a single mass adaptive controlled angular rate sensor, fabrication of a prototype device will reveal many additional, unforeseen and exciting research questions for further research.

Appendix A

ANSYS code for the triaxial single suspension beam design analysis

```
! TriaxialCombinedAnalysis.txt
!
! This file builds the ANSYS FEM for the optimisation process. It is a
! triaxial vibrating mass supported by a parallel flexural beam structure.
! This file works in conjunction with TriaxialCombinedOpt.txt which
! controls the optimisation process.
!
! Some of the device geometries have been given fixed values while others
! are able to be varied by the optimisation process within their specified
! ranges.
!
! This file has been developed under ANSYS 8.1
!

/title, Triaxial Analysis
!/filename, TriaxialCombinedAnalysis.txt

/com, ***********  Define Constants  ************

/com, Defining - Units scaling factor constants
/prep7
youngs_unit   = 1e-6
force_unit    = 1e6
density_unit  = 1e-18
pressure_unit = 1e-6
velocity_unit = 1e6
acc_unit      = 1e6
stress_unit   = 1e-6
power_unit    = 1e12
conduct_unit  = 1e6
specheat_unit = 1e12

/com, Defining - Design geometric constants
```

```
! height always refers to the z axis dimension
! length refers to the longest of the x and y axis dimensions
! width refers to the smaller of the x and y axis dimensions
! mass refers to the vibrating mass element
height=5
mass_width=200

! inner_1 refers to the beams susspension beams connected to the mass
! the x and y subscript refers to the axis that their length runs along
inn_length_y_inn_length_x_ratio = 1.1
inner_width = 2.5
inner_length_x = 250
inner_length_y = inn_length_y_inn_length_x_ratio*inner_length_x

! outer refers to the suspension beams that support the centre comb area
! the x and y subscript refers to the axis that their length runs along
outer_inner_ratio = 1 ! This cannot be more than 1
outer_width=2.5
outer_length_x=outer_inner_ratio*inner_length_x
outer_length_y=outer_inner_ratio*inner_length_y

! Centre refers to the area that the combs would be located
centre_width = 4*inner_width


/com, ************  Define Element  *************
/prep7
ET,1,SOLID92

/com, ******  Define Material Properties  *******

/PREP7
!*
MAT,1,
! /INPUT,..\Material_Libraries\Si_blk_ln.SI_MPL
!
!ANSYS MEMS MATERIAL DATA BASE
!
!Silicon (Si), Bulk.
!Linear properties, temperture independent
!
!Reference: -CRC Materials Handbook
!  *Mechanics of Materials, 23(1996)
!  +Sensors & Actuators, Vol 20, #1&2,1989
!
!Notes:  -Coefficient of thermal expansion in units of: /K  At temp=300 K
!  *Young's Modulus in units of: MPa
!  -Solid Density in units of: Kg/um3
!  *Poisson's Ratio
!  -Specific heat in units of: pJ/Kg.C  At Temp=25 C.
!  +Thermal conductivity in units of: pW/um.K  At temp=300 K
!
/COM,ANSYS RELEASE  5.5.2                   14:36:43    07/22/1999
/NOP
/COM,Internal UNITS set at file creation time = SI   (uMKS)
```

```
TBDEL,ALL,_MATL
MPDEL,ALL,_MATL
MPTEMP,R5.0, 1, 1,  0.00000000    ,
MPDATA,R5.0, 1,EX  ,_MATL   , 1,  165.000000e3,
MPTEMP,R5.0, 1, 1,  0.00000000    ,
MPDATA,R5.0, 1,NUXY,_MATL   , 1,  0.22000000,
MPTEMP,R5.0, 1, 1,  0.00000000    ,
MPDATA,R5.0, 1,DENS,_MATL   , 1,  2330.00000e-18,
/GO

/com, ***********  Create The Model *************
/prep7


/com, Creating mass volume
BLOCK, 0, 0.5*mass_width, 0, 0.5*mass_width, -0.5*height, 0.5*height

/com, Creating inner spring volumes
BLOCK, 0.5*mass_width-inner_width, 0.5*mass_width, 0.5*mass_width,
0.5*mass_width+inner_length_y, -0.5*height, 0.5*height
BLOCK, 0.5*mass_width, 0.5*mass_width+inner_length_x,
0.5*mass_width-inner_width, 0.5*mass_width, -0.5*height, 0.5*height

/com, Creating centre beam volumes
BLOCK, 0, 0.5*mass_width, 0.5*mass_width+inner_length_y,
0.5*mass_width+inner_length_y+centre_width, -0.5*height, 0.5*height
BLOCK, 0.5*mass_width+inner_length_x,
0.5*mass_width+inner_length_x+centre_width, 0, 0.5*mass_width,
-0.5*height, 0.5*height

/com, Creating outer spring volumes
BLOCK, 0.5*mass_width+inner_length_x,
0.5*mass_width+inner_length_x+outer_width, 0.5*mass_width,
0.5*mass_width+outer_length_y, -0.5*height, 0.5*height
BLOCK, 0.5*mass_width, 0.5*mass_width+outer_length_x,
0.5*mass_width+inner_length_y, 0.5*mass_width+inner_length_y+outer_width,
-0.5*height, 0.5*height

/com, Using mirrored symmetry to create full model from one quarter
VSYMM, X, ALL, , , , 0, 0
VSYMM, Y, ALL, , , , 0, 0

/com, Gluing volumes
VSEL, ALL
VGLUE, ALL

/com, **************  Change View ***************
/VIEW, 1 ,1,1,1
VPLOT
/REPLOT

/com, ******  Apply Loads And Constraints *******

/com, Select areas to be constrained to zero displacement

VSEL, S, LOC, X, 0.5*mass_width+inner_length_x+0.5*outer_width,
```

```
0.5*mass_width+inner_length_x+0.5*outer_width, 0, 1
ASEL, R, LOC, Y, 0.5*mass_width+outer_length_y,
0.5*mass_width+outer_length_y, 0, 0
DA,ALL,ALL,0
VSEL, S, LOC, X, 0.5*mass_width+inner_length_x+0.5*outer_width,
0.5*mass_width+inner_length_x+0.5*outer_width, 0, 1
ASEL, R, LOC, Y, -0.5*mass_width-outer_length_y,
-0.5*mass_width-outer_length_y, 0, 0
DA,ALL,ALL,0
VSEL, S, LOC, X, -0.5*mass_width-inner_length_x-0.5*outer_width,
-0.5*mass_width-inner_length_x-0.5*outer_width, 0, 1
ASEL, R, LOC, Y, 0.5*mass_width+outer_length_y,
0.5*mass_width+outer_length_y, 0, 0
DA,ALL,ALL,0
VSEL, S, LOC, X, -0.5*mass_width-inner_length_x-0.5*outer_width,
-0.5*mass_width-inner_length_x-0.5*outer_width, 0, 1
ASEL, R, LOC, Y, -0.5*mass_width-outer_length_y,
-0.5*mass_width-outer_length_y, 0, 0
DA,ALL,ALL,0

VSEL, S, LOC, Y, 0.5*mass_width+inner_length_y+0.5*outer_width,
0.5*mass_width+inner_length_y+0.5*outer_width, 0, 1
ASEL, R, LOC, X, 0.5*mass_width+outer_length_x,
0.5*mass_width+outer_length_x, 0, 0
DA,ALL,ALL,0
VSEL, S, LOC, Y, 0.5*mass_width+inner_length_y+0.5*outer_width,
0.5*mass_width+inner_length_y+0.5*outer_width, 0, 1
ASEL, R, LOC, X, -0.5*mass_width-outer_length_x,
-0.5*mass_width-outer_length_x, 0, 0
DA,ALL,ALL,0
VSEL, S, LOC, Y, -0.5*mass_width-inner_length_y-0.5*outer_width,
-0.5*mass_width-inner_length_y-0.5*outer_width, 0, 1
ASEL, R, LOC, X, 0.5*mass_width+outer_length_x,
0.5*mass_width+outer_length_x, 0, 0
DA,ALL,ALL,0
VSEL, S, LOC, Y, -0.5*mass_width-inner_length_y-0.5*outer_width,
-0.5*mass_width-inner_length_y-0.5*outer_width, 0, 1
ASEL, R, LOC, X, -0.5*mass_width-outer_length_x,
-0.5*mass_width-outer_length_x, 0, 0
DA,ALL,ALL,0

ALLSEL, ALL


/com, ********  Create HP's prior to mesh *******
! Hard point at COM for applying displacement load.
LSEL, S, LOC, X,0
LSEL, R, LOC, Y,0
LSEL, R, LOC, Z,0
*GET, linethroughCOM, LINE, 0, NUM, MAX,
HPTCREATE,LINE,linethroughCOM,1000,COORD,0,0,0,
ALLSEL, ALL

/com, ****************************************
/com, ************* Modal analysis **************
/com, ****************************************
```

```
/com, *************  Mesh The Model *************
SMRTSIZE, 4, , 4, , , , , , , ,
VMESH,ALL
VIMP,ALL
ALLSEL, ALL
FINISH

/com, **************  Solution  *****************

/SOLU
/com, Set up for Modal analysis
ANTYPE,2
EQSLV,SPAR
MXPAND,4, , ,0
LUMPM,0
PSTRES,0
MODOPT,LANB,4,0,0, ,OFF, ,2

SOLVE
FINISH
/POST1
*GET,Mode1var,MODE,1,FREQ
*GET,Mode2var,MODE,2,FREQ
*GET,Mode3var,MODE,3,FREQ
*GET,Mode4var,MODE,4,FREQ

SV1 = Mode2var/Mode1var
SV2 = Mode3var/Mode2var

ObjtVar = (1/Mode4var)

FINISH
/com, ****************************************
/com, ************* Static analysis *************
/com, ****************************************


!/com, ************* Remesh The Model ************
/prep7
ALLSEL, ALL

!/com, Refining Mesh at level 1 around all vertical lines
LSEL, S,LOC, Z, 0
LSEL, U,LOC, Y, 0
LSEL, U,LOC, X, 0
EREF,ALL, , , , , ,1
ALLSEL, ALL
FINISH


/com, *************** Apply Loads ***************
! Apply displacement load on the mass.
/prep7
DK, 1000, UX, 10
DK, 1000, UY, 10
```

```
DK, 1000, UZ, 10
FINISH


/com, **************  Solution  ******************

/SOLU
ANTYPE,0
SOLVE
FINISH

/POST1
NSORT,S,INT,0,1
*GET,STRS,SORT,,Max
FINISH
```

Appendix B

ANSYS code for the triaxial single suspension beam design optimisation

```
! TriaxialCombinedOpt.txt
!
! This file controls the ANSYS optimisation process for establishing a
! structural design that has desirable modal frequencies in the x, y
! and z axes and does not exceed the maximum allowable stress intensity.
! The optimisationaims to maximise the unwanted fourth rotation modes
! so as to not intefere with the operation of the device.
!
! This file works in conjunction with TriaxialCombinedAnalysis.txt
! which builds the FEM and defines all the model variables and loads.
! Some of the device geometries have been given fixed values while
! others are able to bevaried by the optimisation process within their
! specified ranges.
!
! This file has been developed under ANSYS 8.1
!

! Enter the optimisation processor
/OPT

! Assign analysis file
OPANL,'TriaxialCombinedAnalysis','txt','.'

! Define the design variables and their limits
OPVAR,height,DV,3,5,
OPVAR,mass_width,DV,100,300,
OPVAR,inner_width,DV,1,5,
OPVAR,outer_width,DV,1,5,
OPVAR,inner_length_x,DV,100,300,
OPVAR,inn_length_y_inn_length_x_ratio,DV,1,1.2,
OPVAR,outer_inner_ratio,DV,0.5,1,

! Define the state varaiables of the system
```

```
OPVAR,Mode1var,SV,9000,11000,
OPVAR,SV1,SV,1.09,1.11
OPVAR,SV2,SV,1.09,1.11
OPVAR,STRS,SV,0,500

! Assign the optimisation objective function
OPVAR,Objtvar,OBJ,,,

! Set up the subproblem optimisation which is generally faster than
! first order optimisation
OPTYPE,SUBP
! Maximum of 100 iterations and stop after 100 infeasable iterations
! in a row.
OPSUBP, 100, 100

! Run optimization
OPEXE

FINISH
```

Appendix C

First Structure: Design Automation Results

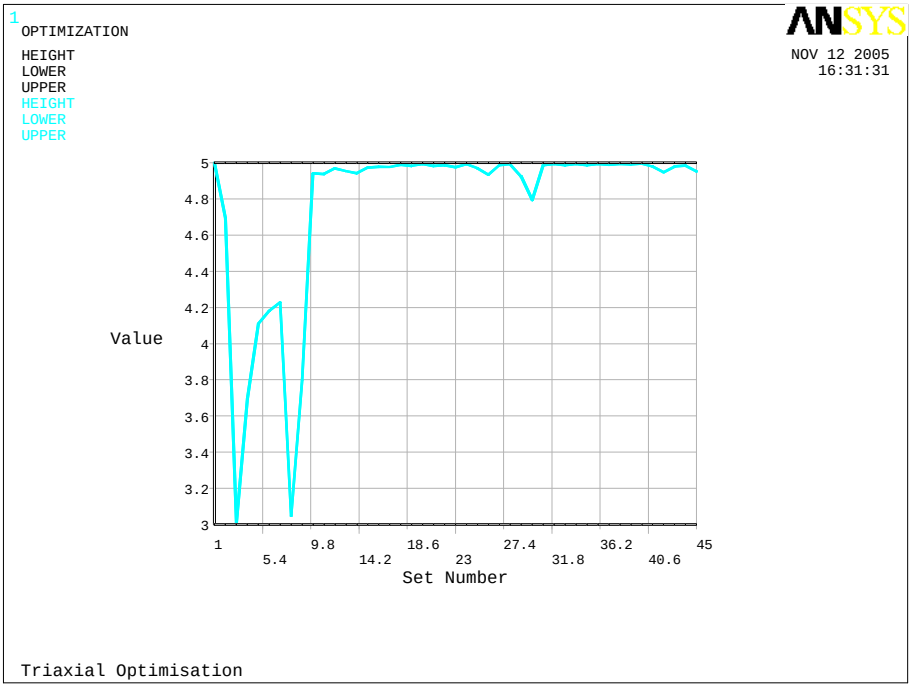

(a) HEIGHT.

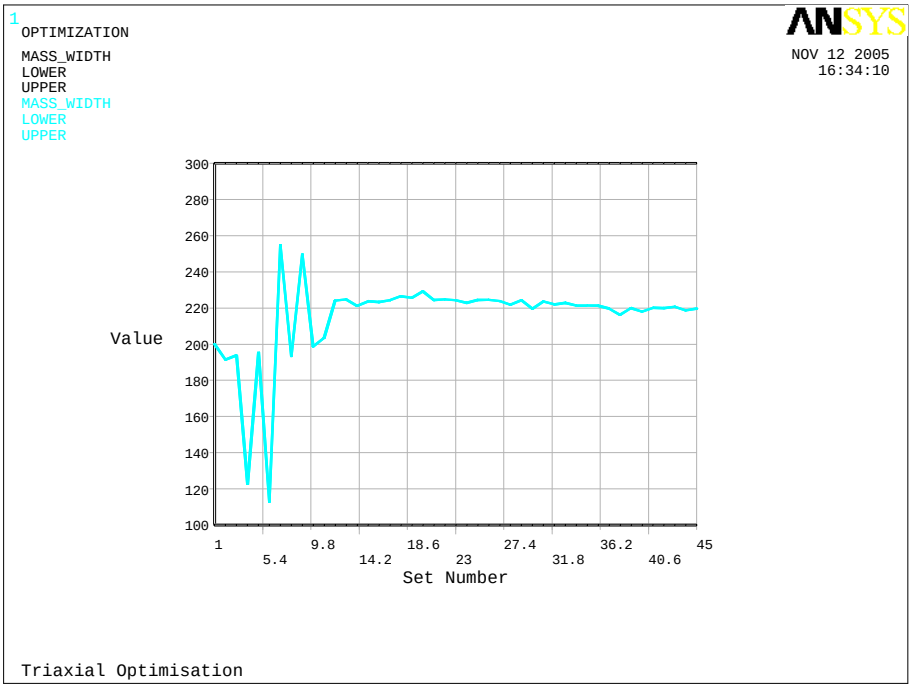

(b) MASS_WIDTH.

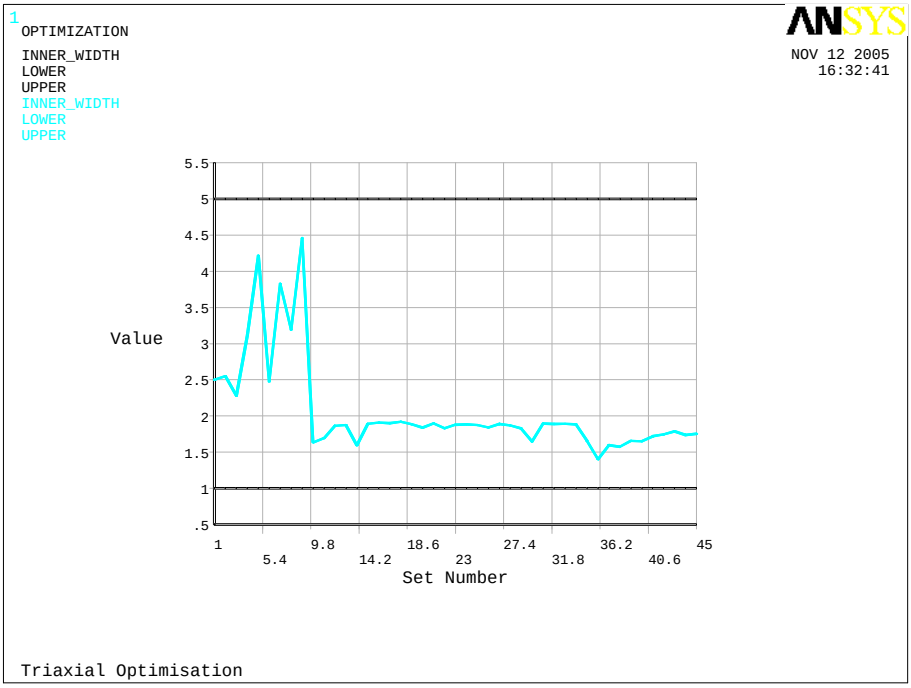

(c) INNER_WIDTH.

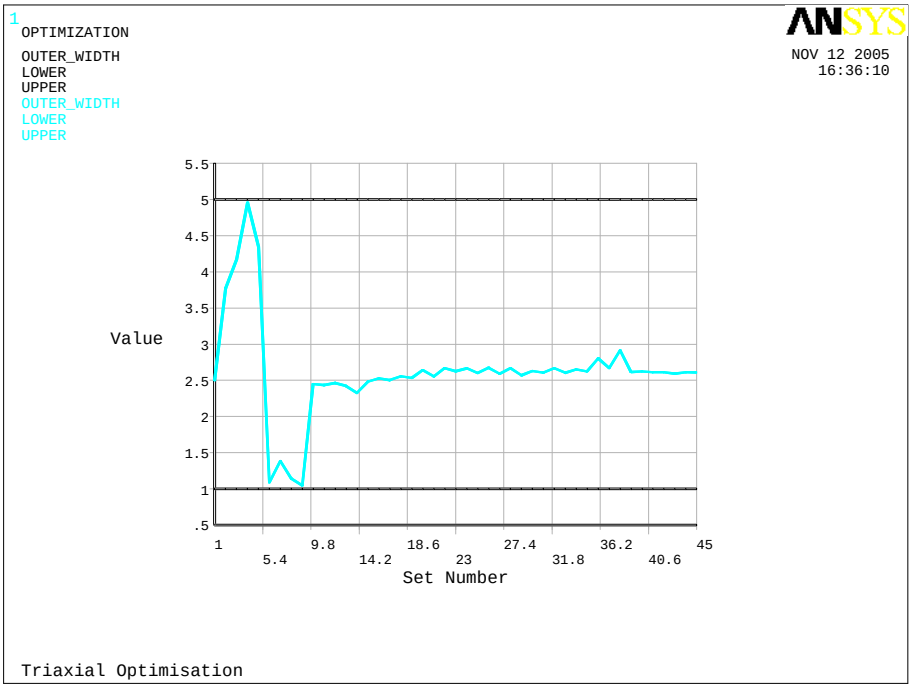

(d) OUTER_WIDTH.

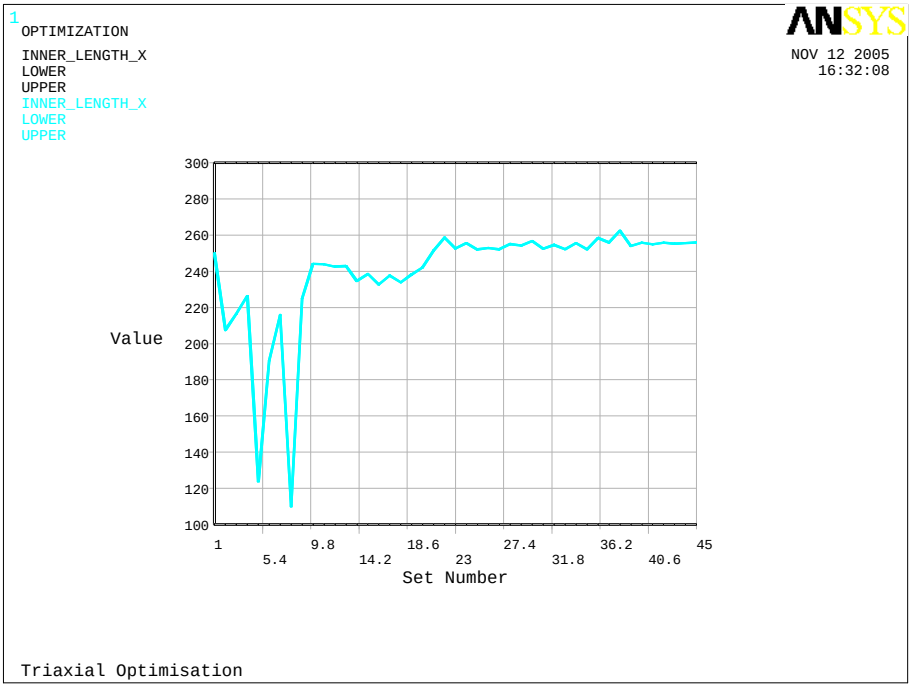

(e) INNER_LENGTH_X.

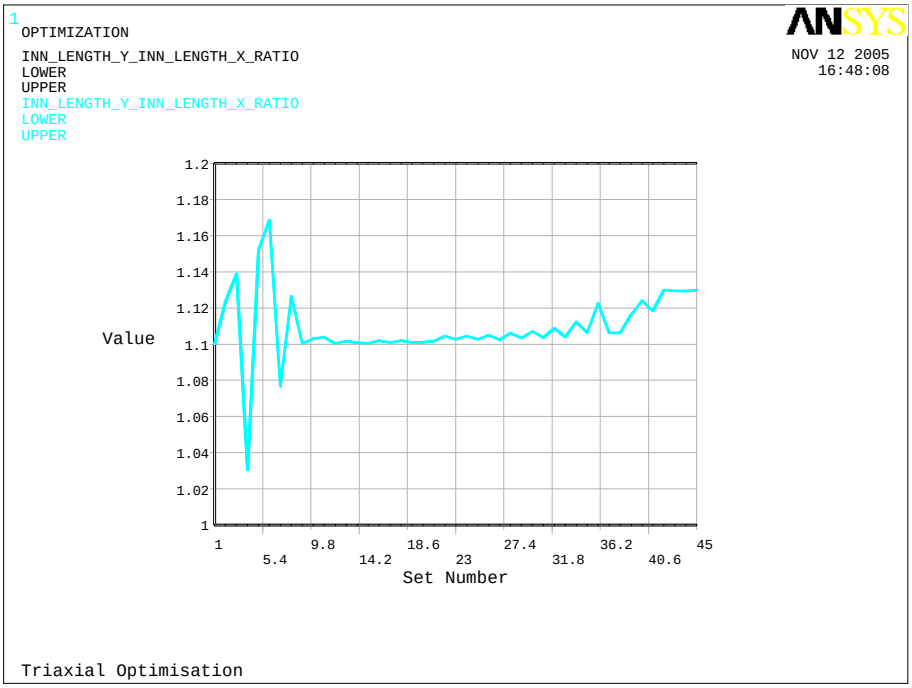

(f) INN_LENGTH_Y_INN_LENGTH_X_RATIO.

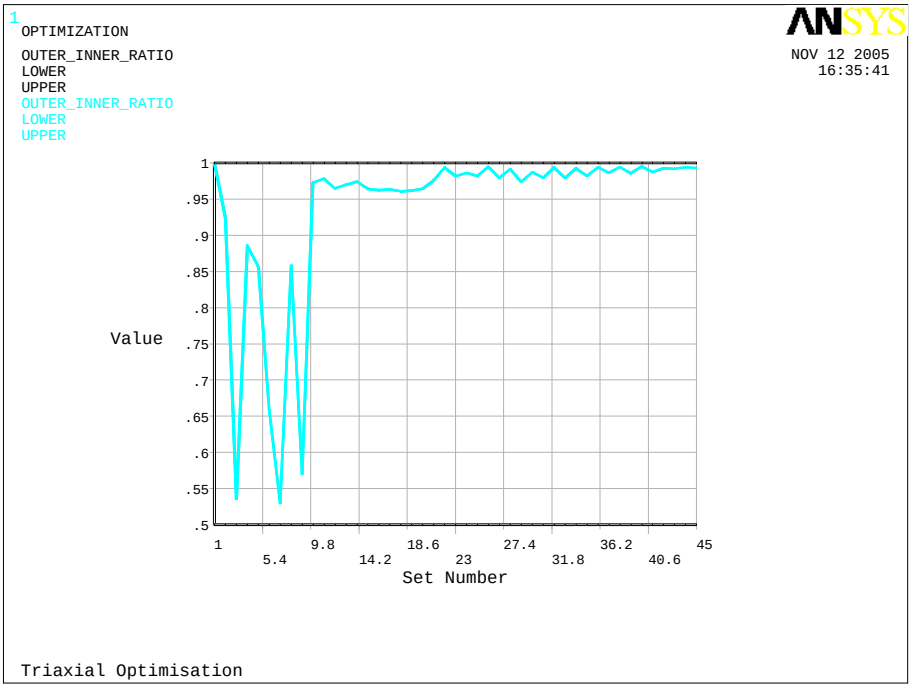

(g) OUTER_INNER_RATIO.

Figure C.1: First structure: Design automation design variables.

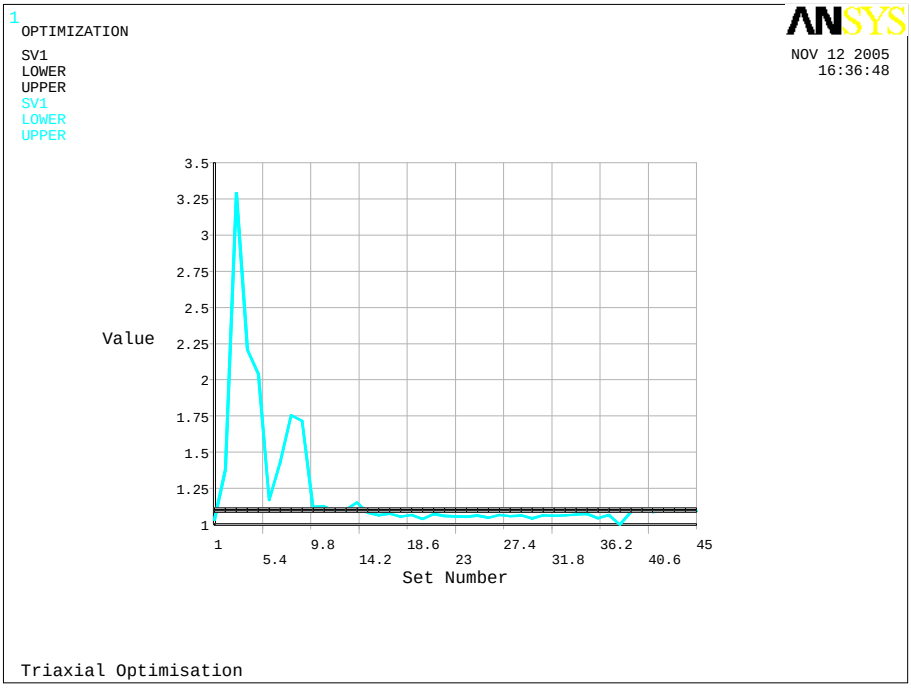
1
OPTIMIZATION
SV1
LOWER
UPPER
SV1
LOWER
UPPER
ANSYS
NOV 12 2005
16:36:48
Value
3.5
3.25
3
2.75
2.5
2.25
2
1.75
1.5
1.25
1
1
5.4
9.8
14.2
18.6
23
27.4
31.8
36.2
40.6
45
Set Number
Triaxial Optimisation

(a) SV1.

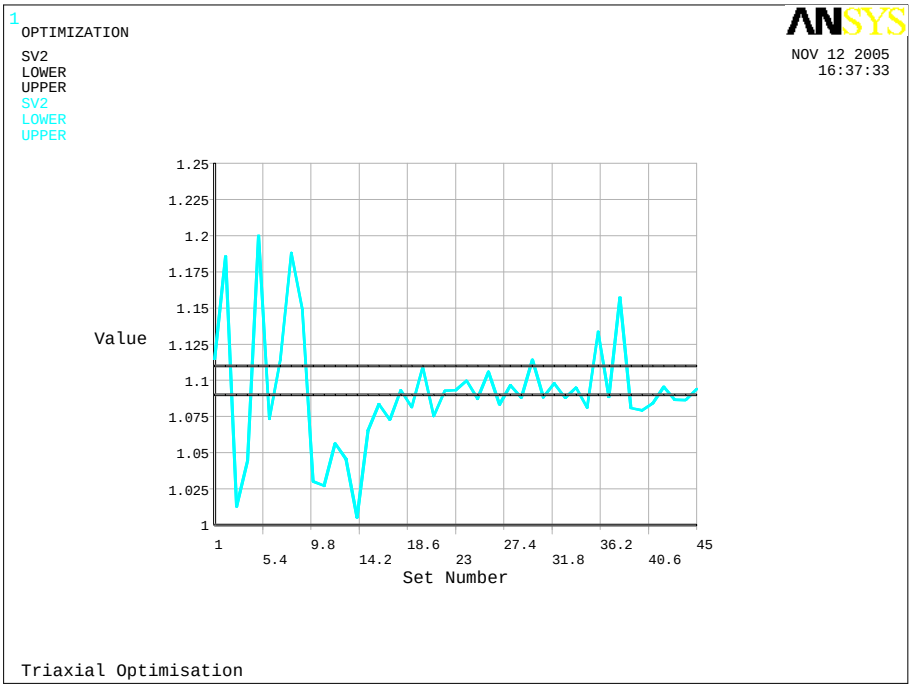
1
OPTIMIZATION
SV2
LOWER
UPPER
SV2
LOWER
UPPER
ANSYS
NOV 12 2005
16:37:33
Value
1.25
1.225
1.2
1.175
1.15
1.125
1.1
1.075
1.05
1.025
1
1
5.4
9.8
14.2
18.6
23
27.4
31.8
36.2
40.6
45
Set Number
Triaxial Optimisation

(b) SV2.

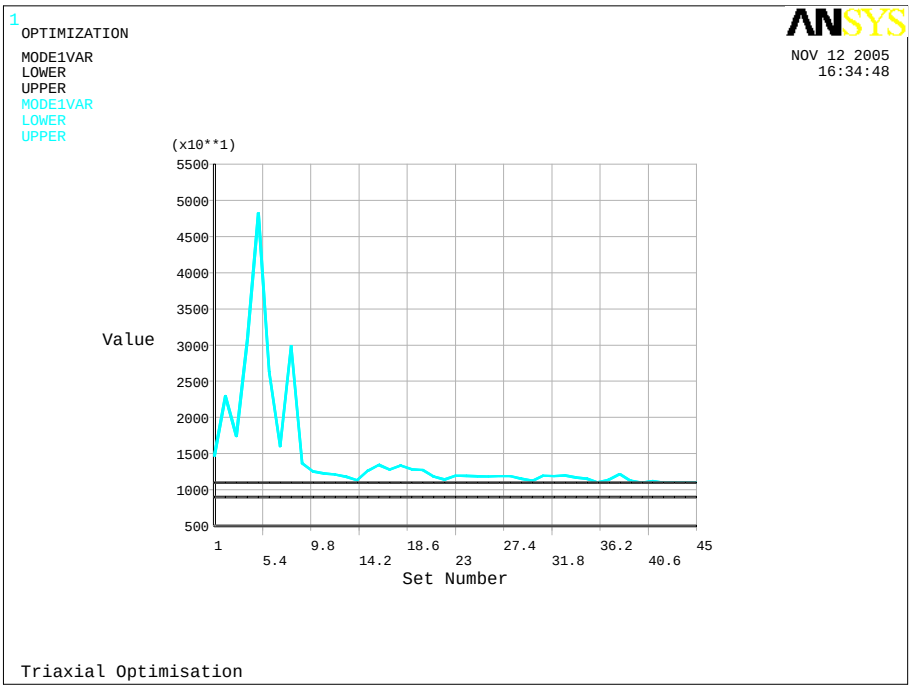

(c) MODE1VAR.

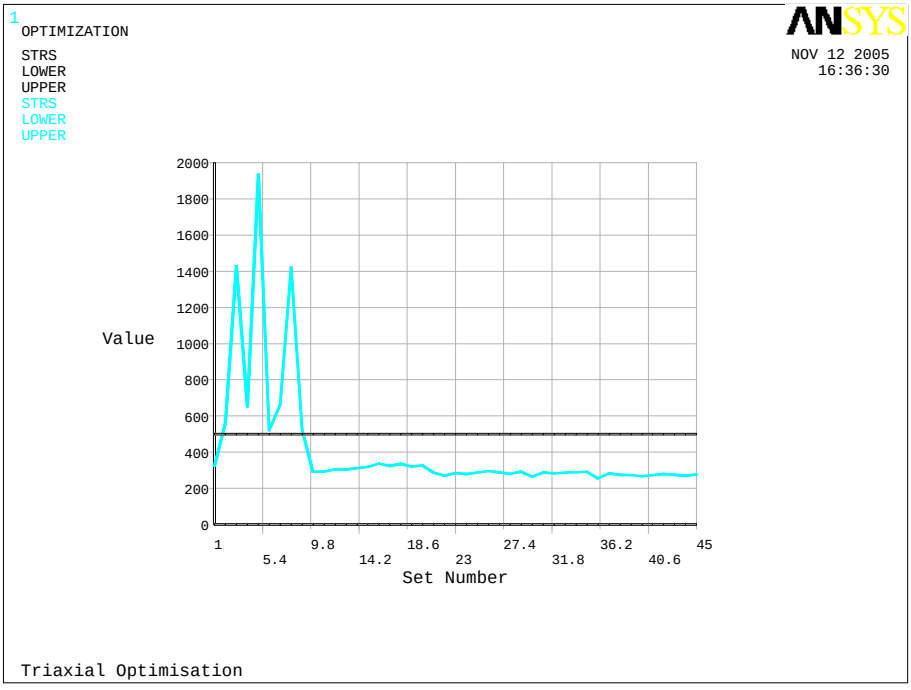

(d) STRS.

Figure C.2: First structure: Design automation state variables.

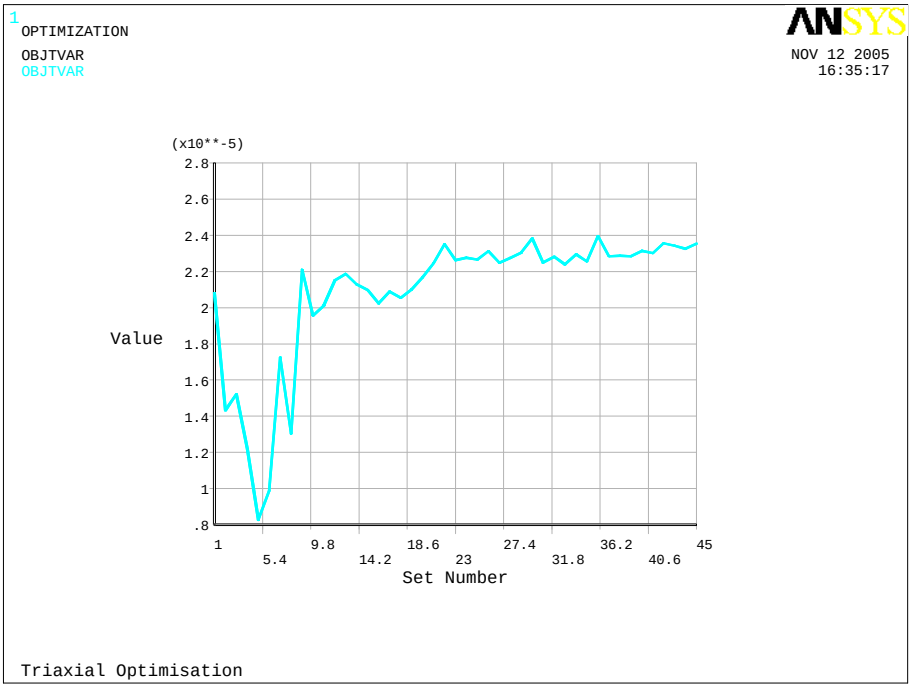

(a) OBJTVAR.

Figure C.3: First structure: Design automation objective variables.

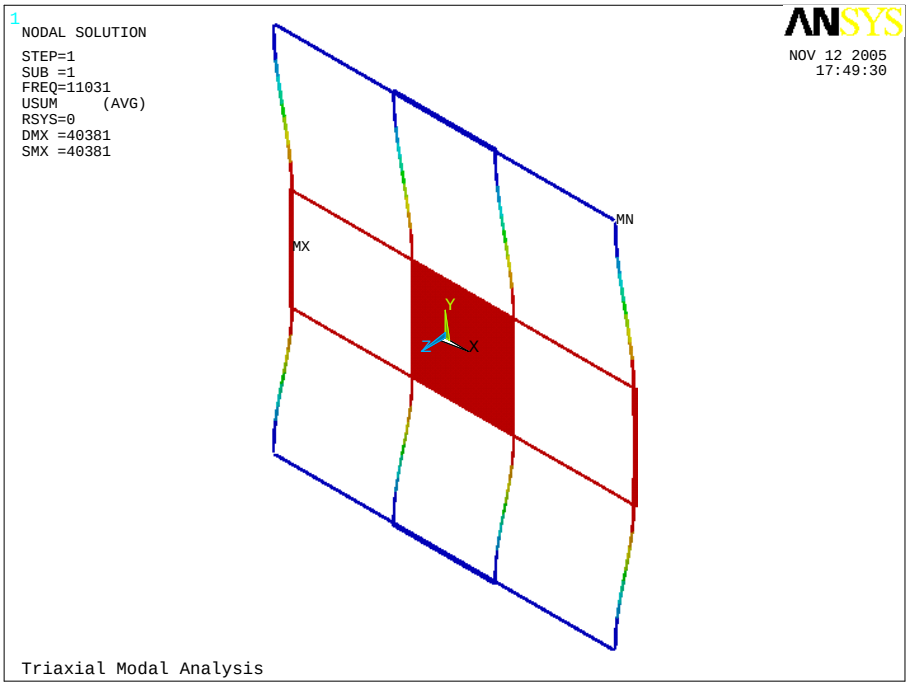

(a) x axis lateral, mode 1, 11031Hz.

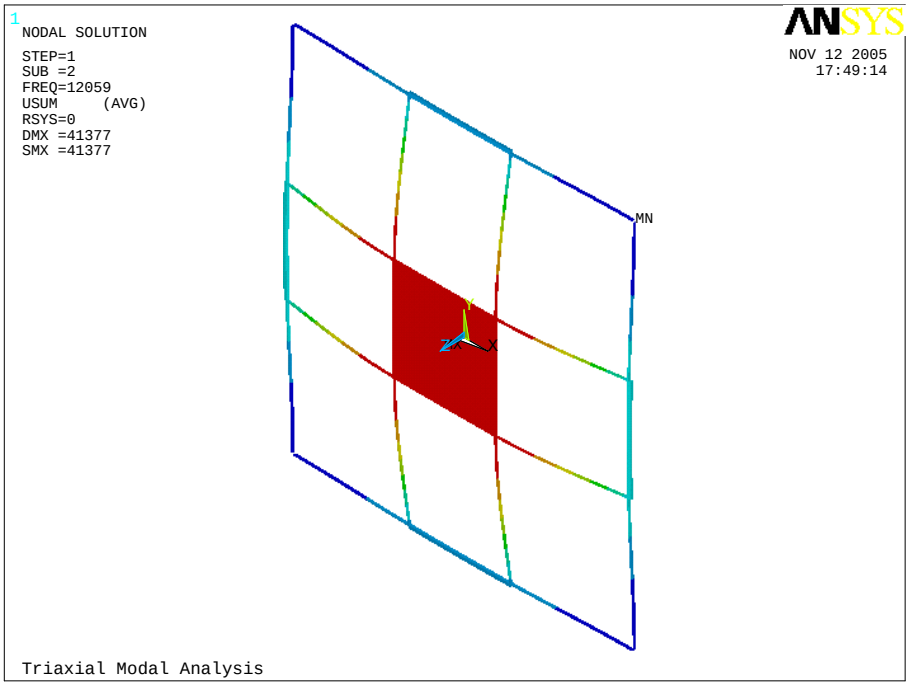

(b) z axis lateral, mode 2, 12059Hz.

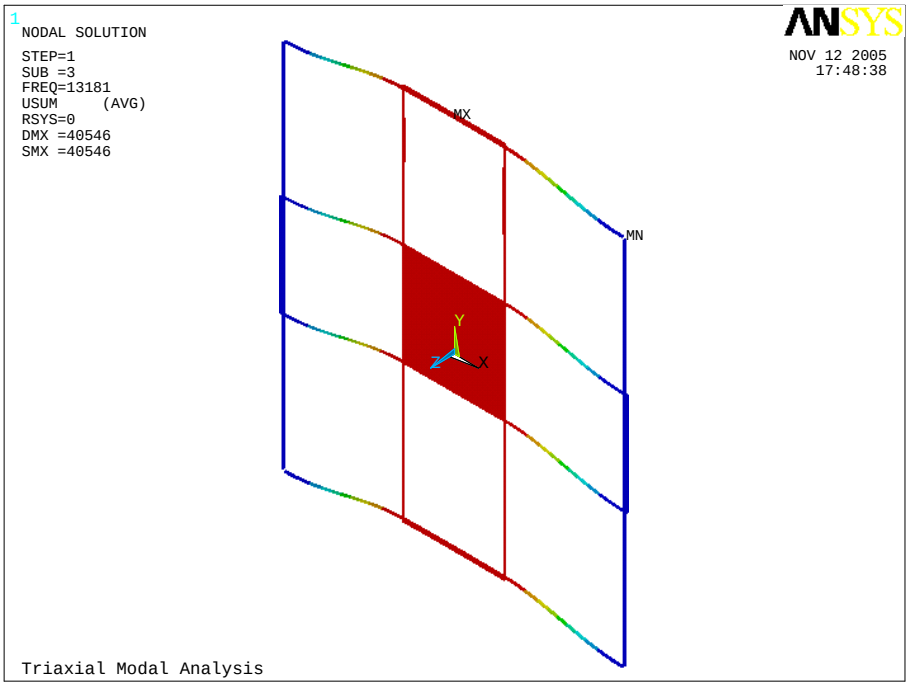

(c) y axis lateral, mode 3, 13181Hz.

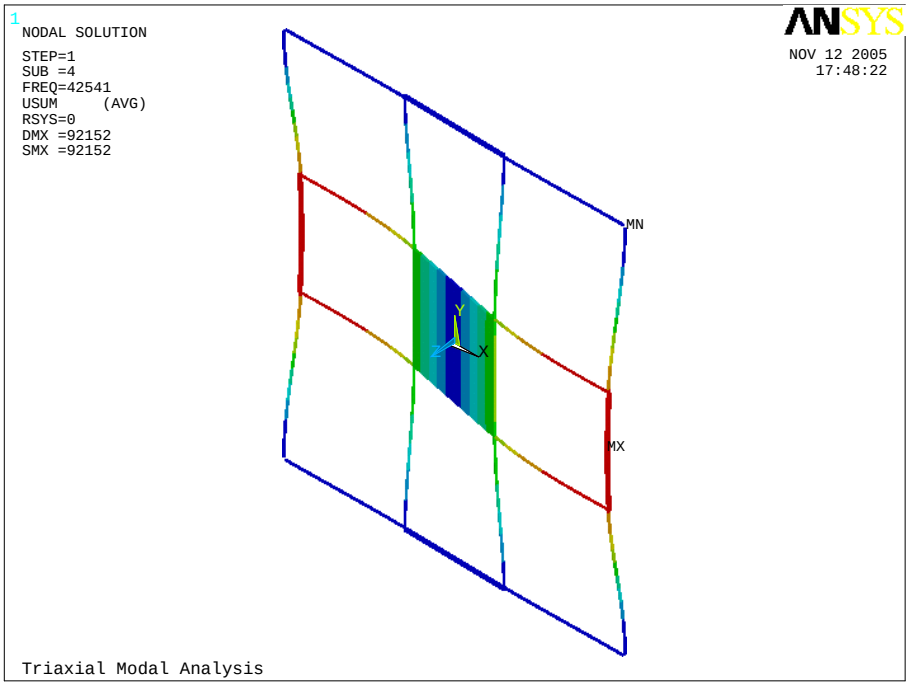

(d) y axis rotational, mode 4, 42541Hz.

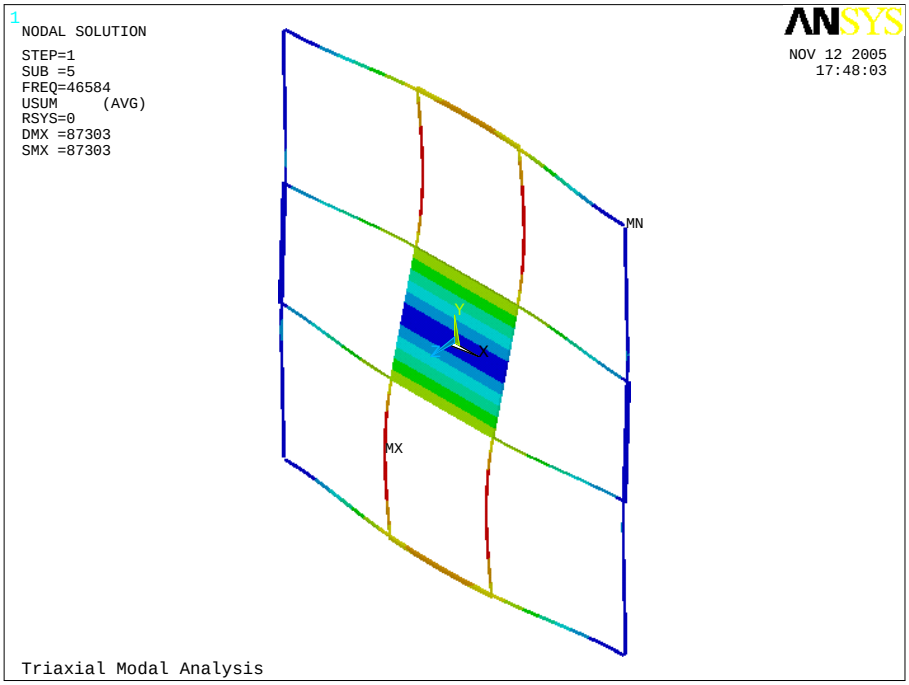

(e) x axis rotational, mode 5, 46584Hz.

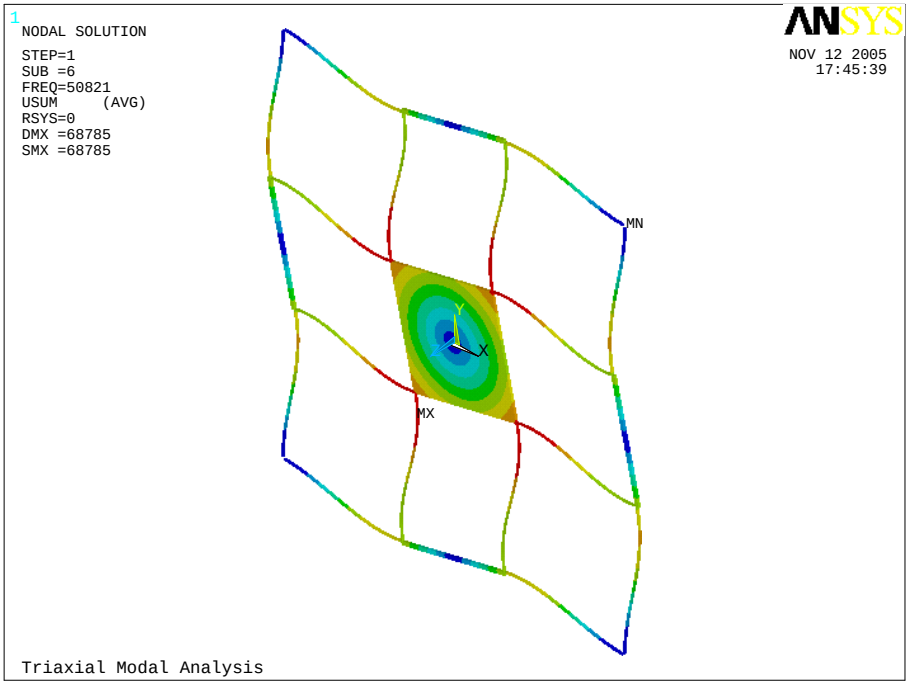

(f) z axis rotational, mode 6, 50821Hz.

Figure C.4: First six modal shapes and respective frequencies of the proposed device structure as found by ANSYS modal analysis.

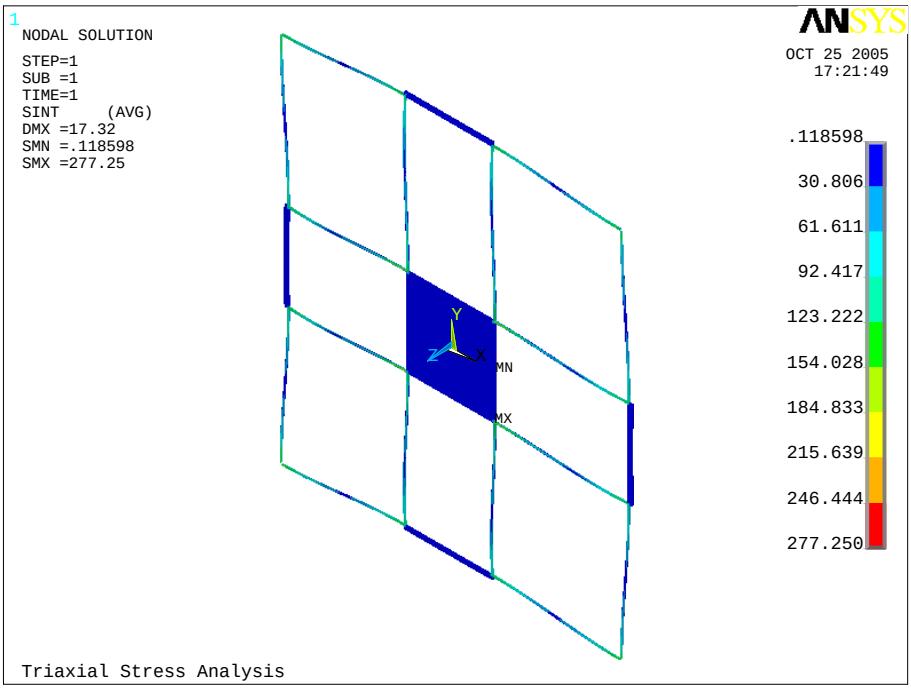

(a) Static analysis stress intensity.

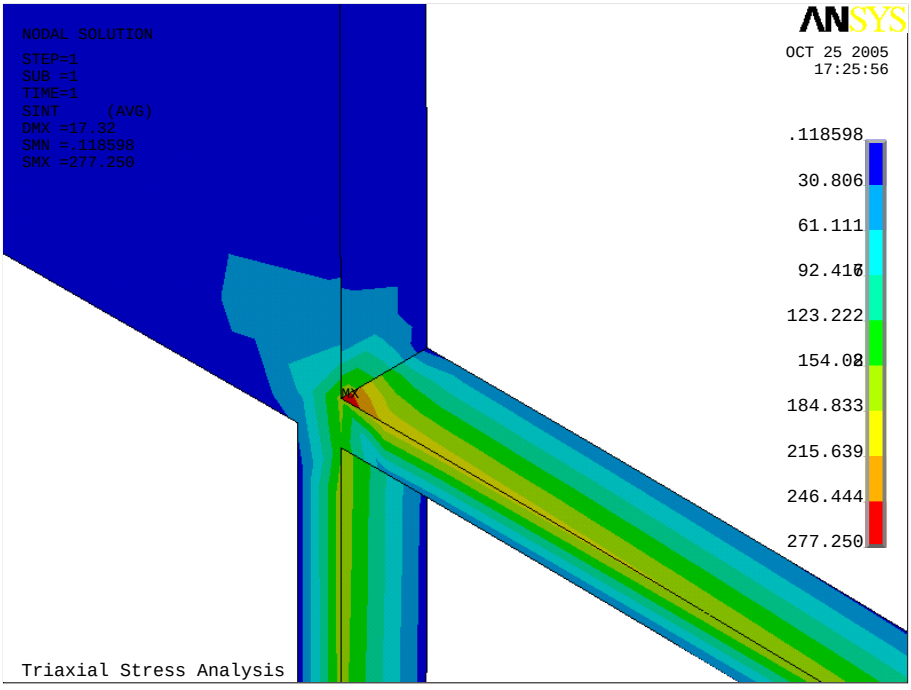

(b) Close up of area of maximum stress intensity MX.

Figure C.5: ANSYS Static analysis stress intensity.

Appendix D

ANSYS code for the triaxial double suspension beam design analysis

```
! TriCombinedDblAnalysis.txt
!
! This file builds the ANSYS FEM for the optimisation process. It is a
! triaxial vibrating mass supported by two rows of parallel flexural
! beam structures.
! This file works in conjunction with TriCombinedDblOpt.txt which
! controls the optimisation process.
!
! Some of the device geometries have been given fixed values while others
! are able to be varied by the optimisation process within their specified
! ranges.
!
! This file has been developed under ANSYS 8.1
!

/title, Triaxial Analysis Optimisation
!/filename, TriCombinedDblAnalsys.txt

/com, ***********  Define Constants  ************

/com, Defining - Units scaling factor constants
/prep7
youngs_unit   = 1e-6
force_unit    = 1e6
density_unit  = 1e-18
pressure_unit = 1e-6
velocity_unit = 1e6
acc_unit      = 1e6
stress_unit   = 1e-6
power_unit    = 1e12
conduct_unit  = 1e6
specheat_unit = 1e12
```

```
/com, Defining - Design geometric constants

! height always refers to the z axis dimension
! length refers to the longest of the x and y axis dimensions
! width refers to the smaller of the x and y axis dimensions

! mass refers to the vibrating mass element
height=5
mass_width=200

! inner_1 refers to the beams susspension beams connected to the mass
! the x and y subscript refers to the axis that their length runs along
inn_length_y_inn_length_x_ratio = 1.1
inner_width_1 = 2.5
inner_length_x_1 = 250
inner_length_y_1 = inn_length_y_inn_length_x_ratio*inner_length_x_1

! outer refers to the suspension beams that support the centre comb area
! the x and y subscript refers to the axis that their length runs along
outer_inner_ratio = 1 ! This cannot be more than 1

outer_width_1=2.5
outer_length_x_1=outer_inner_ratio*inner_length_x_1
outer_length_y_1=outer_inner_ratio*inner_length_y_1

! Centre (1) refers to the intermediate brace between the inner_1
!beams and the inner_2 beams.
centre_width_1 = 4*inner_width_1

! inner_2 refers to the beams susspension beams connected to centre_1
! the x and y subscript refers to the axis that their length runs along
inner_width_2 = 2.5
inner_length_x_2 = 100
inner_length_y_2 = 100

outer_width_2 = 2.5
k = 0.5 !This governs the length of the second outer beam elements it
!can be between 0 and 1
outer_length_x_2 = 0.5*inner_length_x_1
+ k*(0.5*inner_length_x_1+inner_length_x_2)
outer_length_y_2 = 0.5*inner_length_y_1
+ k*(0.5*inner_length_y_1+inner_length_y_2)


! Centre (2) refers to the area that the combs would be located
centre_width_2 = 4*inner_width_1


/com, ************  Define Element  *************
/prep7
ET,1,SOLID92

/com, ******  Define Material Properties  *******

/PREP7
!*
```

```
MAT,1,
! /INPUT,..\Material_Libraries\Si_blk_ln.SI_MPL
!
!ANSYS MEMS MATERIAL DATA BASE
!
!Silicon (Si), Bulk.
!Linear properties, temperture independent
!
!Reference: -CRC Materials Handbook
!  *Mechanics of Materials, 23(1996)
!  +Sensors & Actuators, Vol 20, #1&2,1989
!
!Notes:  -Coefficient of thermal expansion in units of: /K  At temp=300 K
!  *Young's Modulus in units of: MPa
!  -Solid Density in units of: Kg/um3
!  *Poisson's Ratio
!  -Specific heat in units of: pJ/Kg.C  At Temp=25 C.
!  +Thermal conductivity in units of: pW/um.K  At temp=300 K
!
/COM,ANSYS RELEASE  5.5.2                   14:36:43    07/22/1999
/NOP
/COM,Internal UNITS set at file creation time = SI   (uMKS)
TBDEL,ALL,_MATL
MPDEL,ALL,_MATL
MPTEMP,R5.0, 1, 1,  0.00000000    ,
MPDATA,R5.0, 1,EX  ,_MATL   , 1,  165.000000e3,
MPTEMP,R5.0, 1, 1,  0.00000000    ,
MPDATA,R5.0, 1,NUXY,_MATL   , 1,  0.22000000,
MPTEMP,R5.0, 1, 1,  0.00000000    ,
MPDATA,R5.0, 1,DENS,_MATL   , 1,  2330.00000e-18,
/GO

/com, ***********  Create The Model *************
/prep7

/com, Creating mass volume
BLOCK, 0, 0.5*mass_width, 0, 0.5*mass_width, -0.5*height, 0.5*height

/com, Creating first inner spring volumes
BLOCK, 0.5*mass_width-inner_width_1, 0.5*mass_width, 0.5*mass_width,
0.5*mass_width+inner_length_y_1, -0.5*height, 0.5*height
BLOCK, 0.5*mass_width, 0.5*mass_width+inner_length_x_1,
0.5*mass_width-inner_width_1, 0.5*mass_width, -0.5*height, 0.5*height

/com, Creating first centre beam volumes
BLOCK, 0, 0.5*mass_width, 0.5*mass_width+inner_length_y_1,
0.5*mass_width+inner_length_y_1+centre_width_1, -0.5*height, 0.5*height
BLOCK, 0.5*mass_width+inner_length_x_1,
0.5*mass_width+inner_length_x_1+centre_width_1,
0, 0.5*mass_width, -0.5*height, 0.5*height

/com, Creating first outer spring volumes
BLOCK, 0.5*mass_width+inner_length_x_1,
0.5*mass_width+inner_length_x_1+outer_width_1,
0.5*mass_width, 0.5*mass_width+outer_length_y_1, -0.5*height, 0.5*height
BLOCK, 0.5*mass_width, 0.5*mass_width+outer_length_x_1,
```

```
0.5*mass_width+inner_length_y_1,
0.5*mass_width+inner_length_y_1+outer_width_1, -0.5*height, 0.5*height

/com, Creating second inner spring volumes
BLOCK, 0.5*mass_width-inner_width_2, 0.5*mass_width,
0.5*mass_width+inner_length_y_1+centre_width_1,
0.5*mass_width+inner_length_y_1+centre_width_1+inner_length_y_2,
-0.5*height, 0.5*height
BLOCK, 0.5*mass_width+inner_length_x_1+centre_width_1,
0.5*mass_width+inner_length_x_1+centre_width_1+inner_length_x_2,
0.5*mass_width-inner_width_2, 0.5*mass_width, -0.5*height, 0.5*height

/com, Creating second centre beam volumes
BLOCK, 0, 0.5*mass_width,
0.5*mass_width+inner_length_y_1+centre_width_1+inner_length_y_2,
0.5*mass_width+inner_length_y_1+centre_width_1+inner_length_y_2+centre_width_2,
-0.5*height, 0.5*height
BLOCK, 0.5*mass_width+inner_length_x_1+centre_width_1+inner_length_x_2,
0.5*mass_width+inner_length_x_1+centre_width_1+inner_length_x_2+centre_width_2,
0, 0.5*mass_width, -0.5*height, 0.5*height

/com, Creating second outer spring volumes
BLOCK, 0.5*mass_width+inner_length_x_1+centre_width_1+inner_length_x_2,
0.5*mass_width+inner_length_x_1+centre_width_1+inner_length_x_2+outer_width_2,
0.5*mass_width, 0.5*mass_width+outer_length_y_2, -0.5*height, 0.5*height
BLOCK, 0.5*mass_width, 0.5*mass_width+outer_length_x_2,
0.5*mass_width+inner_length_y_1+centre_width_1+inner_length_y_2,
0.5*mass_width+inner_length_y_1+centre_width_1+inner_length_y_2+outer_width_2,
-0.5*height, 0.5*height


/com, Using mirrored symmetry to create full model from one quarter
VSYMM, X, ALL, , , , 0, 0
VSYMM, Y, ALL, , , , 0, 0

/com, Gluing volumes
VSEL, ALL
VGLUE, ALL

/com, **************  Change View ***************
/VIEW, 1 ,1,1,1
VPLOT
/REPLOT

/com, ******  Apply Loads And Constraints *******

/com, Select areas to be constrained to zero displacement

VSEL, S, LOC, X, 0.5*mass_width+inner_length_x_1+0.5*outer_width_1,
0.5*mass_width+inner_length_x_1+0.5*outer_width_1, 0, 1
ASEL, R, LOC, Y, 0.5*mass_width+outer_length_y_1,
0.5*mass_width+outer_length_y_1, 0, 0
DA,ALL,ALL,0
VSEL, S, LOC, X, 0.5*mass_width+inner_length_x_1+0.5*outer_width_1,
0.5*mass_width+inner_length_x_1+0.5*outer_width_1, 0, 1
ASEL, R, LOC, Y, -0.5*mass_width-outer_length_y_1,
```

```
-0.5*mass_width-outer_length_y_1, 0, 0
DA,ALL,ALL,0
VSEL, S, LOC, X, -0.5*mass_width-inner_length_x_1-0.5*outer_width_1,
-0.5*mass_width-inner_length_x_1-0.5*outer_width_1, 0, 1
ASEL, R, LOC, Y, 0.5*mass_width+outer_length_y_1,
0.5*mass_width+outer_length_y_1, 0, 0
DA,ALL,ALL,0
VSEL, S, LOC, X, -0.5*mass_width-inner_length_x_1-0.5*outer_width_1,
-0.5*mass_width-inner_length_x_1-0.5*outer_width_1, 0, 1
ASEL, R, LOC, Y, -0.5*mass_width-outer_length_y_1,
-0.5*mass_width-outer_length_y_1, 0, 0
DA,ALL,ALL,0

VSEL, S, LOC, Y, 0.5*mass_width+inner_length_y_1+0.5*outer_width_1,
0.5*mass_width+inner_length_y_1+0.5*outer_width_1, 0, 1
ASEL, R, LOC, X, 0.5*mass_width+outer_length_x_1,
0.5*mass_width+outer_length_x_1, 0, 0
DA,ALL,ALL,0
VSEL, S, LOC, Y, 0.5*mass_width+inner_length_y_1+0.5*outer_width_1,
0.5*mass_width+inner_length_y_1+0.5*outer_width_1, 0, 1
ASEL, R, LOC, X, -0.5*mass_width-outer_length_x_1,
-0.5*mass_width-outer_length_x_1, 0, 0
DA,ALL,ALL,0
VSEL, S, LOC, Y, -0.5*mass_width-inner_length_y_1-0.5*outer_width_1,
-0.5*mass_width-inner_length_y_1-0.5*outer_width_1, 0, 1
ASEL, R, LOC, X, 0.5*mass_width+outer_length_x_1,
0.5*mass_width+outer_length_x_1, 0, 0
DA,ALL,ALL,0
VSEL, S, LOC, Y, -0.5*mass_width-inner_length_y_1-0.5*outer_width_1,
-0.5*mass_width-inner_length_y_1-0.5*outer_width_1, 0, 1
ASEL, R, LOC, X, -0.5*mass_width-outer_length_x_1,
-0.5*mass_width-outer_length_x_1, 0, 0
DA,ALL,ALL,0

VSEL, S, LOC, X,
0.5*mass_width+inner_length_x_1+centre_width_1+inner_length_x_2+0.5*outer_width_2,
0.5*mass_width+inner_length_x_1+centre_width_1+inner_length_x_2+0.5*outer_width_2,
0, 1
ASEL, R, LOC, Y, 0.5*mass_width+outer_length_y_2, 0.5*mass_width+outer_length_y_2,
0, 0
DA,ALL,ALL,0
VSEL, S, LOC, X,
0.5*mass_width+inner_length_x_1+centre_width_1+inner_length_x_2+0.5*outer_width_2,
0.5*mass_width+inner_length_x_1+centre_width_1+inner_length_x_2+0.5*outer_width_2,
0, 1
ASEL, R, LOC, Y, -0.5*mass_width-outer_length_y_2, -0.5*mass_width-outer_length_y_2,
0, 0
DA,ALL,ALL,0
VSEL, S, LOC, X,
-0.5*mass_width-inner_length_x_1-centre_width_1-inner_length_x_2-0.5*outer_width_2,
-0.5*mass_width-inner_length_x_1-centre_width_1-inner_length_x_2-0.5*outer_width_2,
0, 1
ASEL, R, LOC, Y, 0.5*mass_width+outer_length_y_2, 0.5*mass_width+outer_length_y_2,
0, 0
DA,ALL,ALL,0
VSEL, S, LOC, X,
```

```
-0.5*mass_width-inner_length_x_1-centre_width_1-inner_length_x_2-0.5*outer_width_2,
-0.5*mass_width-inner_length_x_1-centre_width_1-inner_length_x_2-0.5*outer_width_2,
0, 1
ASEL, R, LOC, Y,
-0.5*mass_width-outer_length_y_2, -0.5*mass_width-outer_length_y_2, 0, 0
DA,ALL,ALL,0

VSEL, S, LOC, Y,
0.5*mass_width+inner_length_y_1+centre_width_1+inner_length_y_2+0.5*outer_width_2,
0.5*mass_width+inner_length_y_1+centre_width_1+inner_length_y_2+0.5*outer_width_2,
0, 1
ASEL, R, LOC, X,
0.5*mass_width+outer_length_x_2, 0.5*mass_width+outer_length_x_2, 0, 0
DA,ALL,ALL,0
VSEL, S, LOC, Y,
0.5*mass_width+inner_length_y_1+centre_width_1+inner_length_y_2+0.5*outer_width_2,
0.5*mass_width+inner_length_y_1+centre_width_1+inner_length_y_2+0.5*outer_width_2,
0, 1
ASEL, R, LOC, X,
-0.5*mass_width-outer_length_x_2, -0.5*mass_width-outer_length_x_2, 0, 0
DA,ALL,ALL,0
VSEL, S, LOC, Y,
-0.5*mass_width-inner_length_y_1-centre_width_1-inner_length_y_2-0.5*outer_width_2,
-0.5*mass_width-inner_length_y_1-centre_width_1-inner_length_y_2-0.5*outer_width_2,
0, 1
ASEL, R, LOC, X,
0.5*mass_width+outer_length_x_2, 0.5*mass_width+outer_length_x_2, 0, 0
DA,ALL,ALL,0
VSEL, S, LOC, Y,
-0.5*mass_width-inner_length_y_1-centre_width_1-inner_length_y_2-0.5*outer_width_2,
-0.5*mass_width-inner_length_y_1-centre_width_1-inner_length_y_2-0.5*outer_width_2,
0, 1
ASEL, R, LOC, X, -0.5*mass_width-outer_length_x_2, -0.5*mass_width-outer_length_x_2,
0, 0
DA,ALL,ALL,0

ALLSEL, ALL


/com, ********  Create HP's prior to mesh *******
! Hard point at COM for applying displacement load.
LSEL, S, LOC, X,0
LSEL, R, LOC, Y,0
LSEL, R, LOC, Z,0
*GET, linethroughCOM, LINE, 0, NUM, MAX,
HPTCREATE,LINE,linethroughCOM,1000,COORD,0,0,0,
ALLSEL, ALL

! Hard point at top edge of x comb for measuring twisting
KSEL, S, LOC, X,
0.5*mass_width+inner_length_x_1+centre_width_1+inner_length_x_2+centre_width_2
KSEL, R, LOC, Y, 0
KSEL, R, LOC, Z, 0.5*height
*GET, topedgecombx, KP, 0, NUM, MAX
ALLSEL, ALL
```

```
! Hard point at top edge of x comb for measuring twisting
KSEL, S, LOC, X,
0.5*mass_width+inner_length_x_1+centre_width_1+inner_length_x_2+centre_width_2
KSEL, R, LOC, Y, 0
KSEL, R, LOC, Z, -0.5*height
*GET, bottomedgecombx, KP, 0, NUM, MAX
ALLSEL, ALL

! Hard point at top edge of y comb for measuring twisting
KSEL, S, LOC, X, 0
KSEL, R, LOC, Y,
0.5*mass_width+inner_length_y_1+centre_width_1+inner_length_y_2+centre_width_2
KSEL, R, LOC, Z, 0.5*height
*GET, topedgecomby, KP, 0, NUM, MAX
ALLSEL, ALL

! Hard point at top edge of y comb for measuring twisting
KSEL, S, LOC, X, 0
KSEL, R, LOC, Y,
0.5*mass_width+inner_length_y_1+centre_width_1+inner_length_y_2+centre_width_2
KSEL, R, LOC, Z, -0.5*height
*GET, bottomedgecomby, KP, 0, NUM, MAX
ALLSEL, ALL

/com, ****************************************
/com, ************* Modal analysis **************
/com, ****************************************

/com, *************  Mesh The Model *************
SMRTSIZE, 10, , 4, , , , , , , ,
!MSHAPE,1,3D
!MSHKEY,0
!MOPT,TIMP,5
!MOPT,AORDER,ON
!MOPT,TETEXPND,2
VMESH,ALL
VIMP,ALL
!LSEL, S,LOC, Z, 0
!LSEL, U,LOC, Y, 0
!LSEL, U,LOC, X, 0
!EREF,ALL, , ,1,0,1,1
ALLSEL, ALL
VIMP,ALL
!SHPP,OFF
!VMESH,ALL
FINISH

/com, **************  Solution  *****************

/SOLU
/com, Set up for Modal analysis
ANTYPE,2
EQSLV,SPAR
MXPAND,4, , ,0
LUMPM,0
PSTRES,0
```

```
MODOPT,LANB,4,0,0, ,OFF, ,2

SOLVE
FINISH
/POST1
*GET,Mode1var,MODE,1,FREQ
*GET,Mode2var,MODE,2,FREQ
*GET,Mode3var,MODE,3,FREQ
*GET,Mode4var,MODE,4,FREQ

SV1 = Mode2var/Mode1var
SV2 = Mode3var/Mode2var

FINISH
/com, ****************************************
/com, ************* Static analysis *************
/com, ****************************************


!/com, ************* Remesh The Model ************
/prep7
ALLSEL, ALL

!/com, Rfining Mesh at level 1 around all vertical lines
LSEL, S,LOC, Z, 0
LSEL, U,LOC, Y, 0
LSEL, U,LOC, X, 0
EREF,ALL, , ,1,0,1,1
ALLSEL, ALL
VIMP,ALL
FINISH


/com, *************** Apply Loads ***************
! Apply displacement load on the mass.
/prep7
DK, 1000, UX, 10
DK, 1000, UY, 10
DK, 1000, UZ, 10
FINISH


/com, **************  Solution  *****************

/SOLU
ANTYPE,0
SOLVE
FINISH

/POST1
NSORT,S,INT,0,1
*GET,STRS,SORT,,Max
FINISH

*GET,TopXnode, KP, topedgecombx, ATTR, NODE
*GET,BottomXnode, KP, bottomedgecombx, ATTR, NODE
```

```
*GET,TopYnode, KP, topedgecomby, ATTR, NODE
*GET,BottomYnode, KP, bottomedgecomby, ATTR, NODE

*GET,TopUX,NODE,TopXnode,U,X
*GET,BottomUX,NODE,BottomXnode,U,X
*GET,TopUY,NODE,TopYnode,U,Y
*GET,BottomUY,NODE,BottomYnode,U,Y

ObjtVar = (TopUX-BottomUX)**2+(TopUY-BottomUY)**2
```

Appendix E

ANSYS code for the triaxial double suspension beam design optimisation

```
! TriCombinedDblOpt.txt
!
! This file controls the ANSYS optimisation process for establishing a
! structural design that has desirable modal frequencies in the x, y
! and z axes.
!
! This file works in conjunction with TriCombinedDblAnalysis.txt
! which builds the FEM and defines all the model variables and loads.
! Some of the device geometries have been given fixed values while
! others are able to bevaried by the optimisation process within their
! specified ranges.
!
! This file has been developed under ANSYS 8.1
!

! Enter the optimisation processor
/OPT

! Assign analysis file
OPANL,'TriCombinedDblAnalysis','txt','.'

! Define the design variables and their limits
OPVAR,mass_height,DV,1,5,
OPVAR,mass_width_x,DV,50,300,
OPVAR,inner_width_1,DV,1,5,
OPVAR,outer_width_1,DV,1,5,
OPVAR,inner_width_2,DV,1,5,
OPVAR,outer_width_2,DV,1,5,
OPVAR,inner_length_x_1,DV,50,300,
OPVAR,inn_length_y_inn_length_x_ratio,DV,1,1.2,
OPVAR,inner_length_x_2,DV,50,100,
OPVAR,inner_length_y_2,DV,50,100,
OPVAR,outer_inner_ratio,DV,0.5,1,
```

```
OPVAR,k,DV,0,1,

! Define the state varaiables of the system
OPVAR,Mode1var,SV,9000,11000,
OPVAR,SV1,SV,1.09,1.11
OPVAR,SV2,SV,1.09,1.11
OPVAR,STRS,SV,0,500

! Assign the optimisation objective function
OPVAR,Objtvar,OBJ,,,

! Set up the subproblem optimisation which is generally faster than
! first order optimisation
OPTYPE,SUBP

! Maximum of 100 iterations and stop after 100 infeasable iterations
! in a row.
OPSUBP, 100, 100

! Run optimization
OPEXE

FINISH
```

Appendix F

Second Structure: Design Automation Results

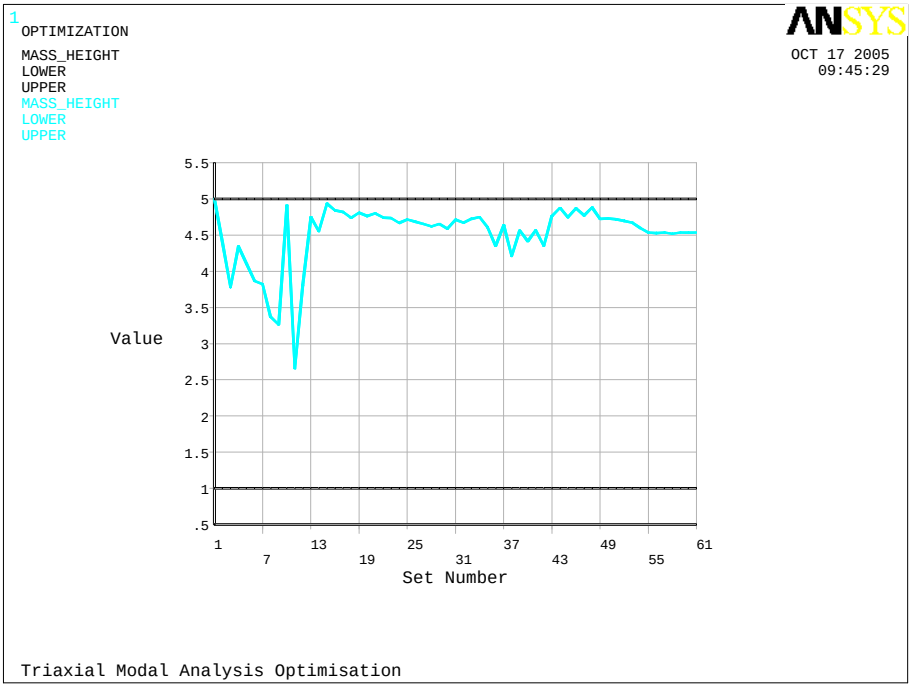

(a) HEIGHT.

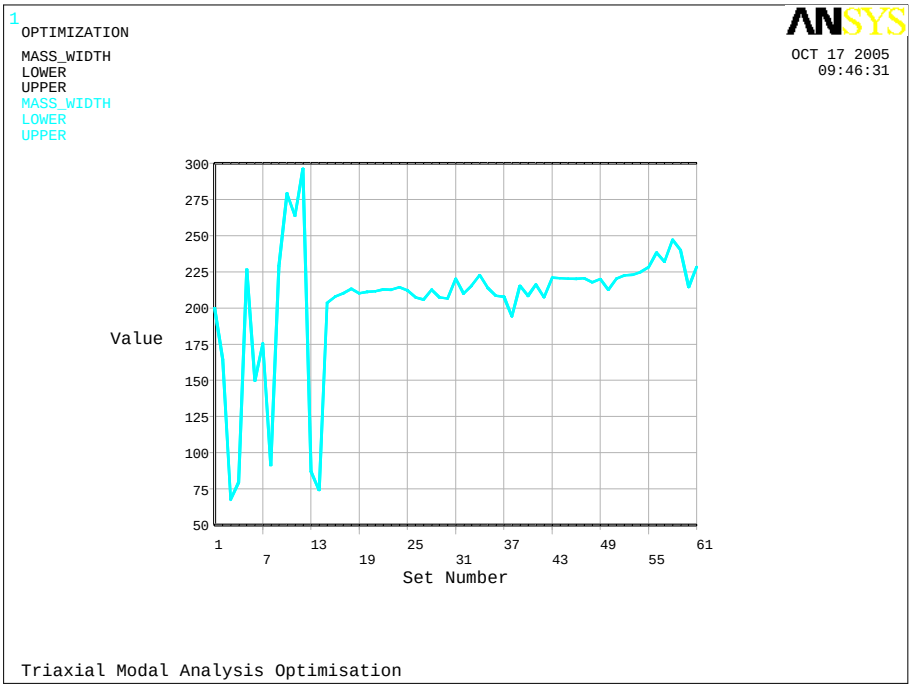

(b) MASS_WIDTH.

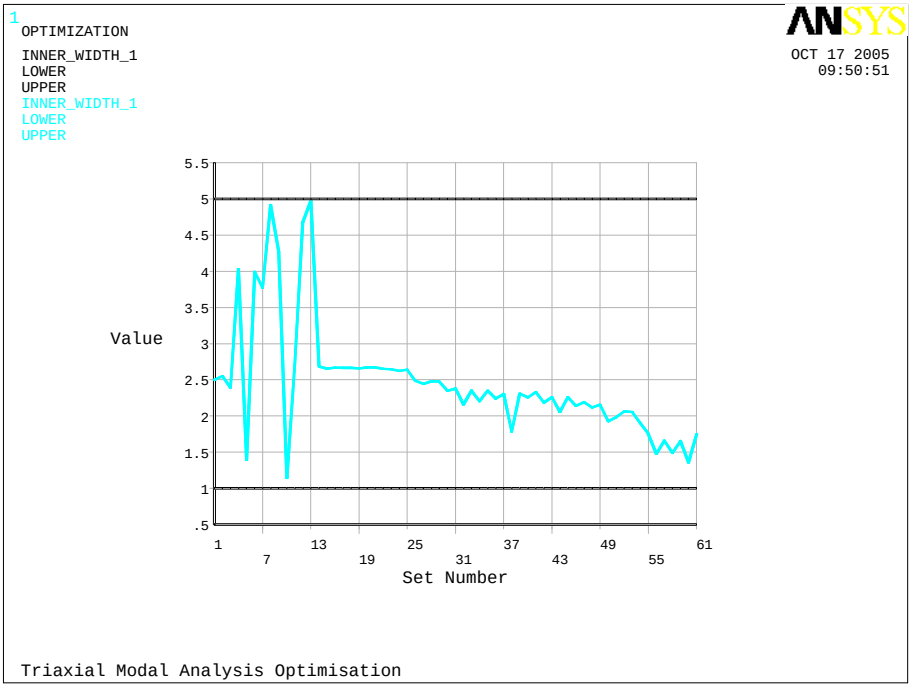

(c) INNER_WIDTH_1.

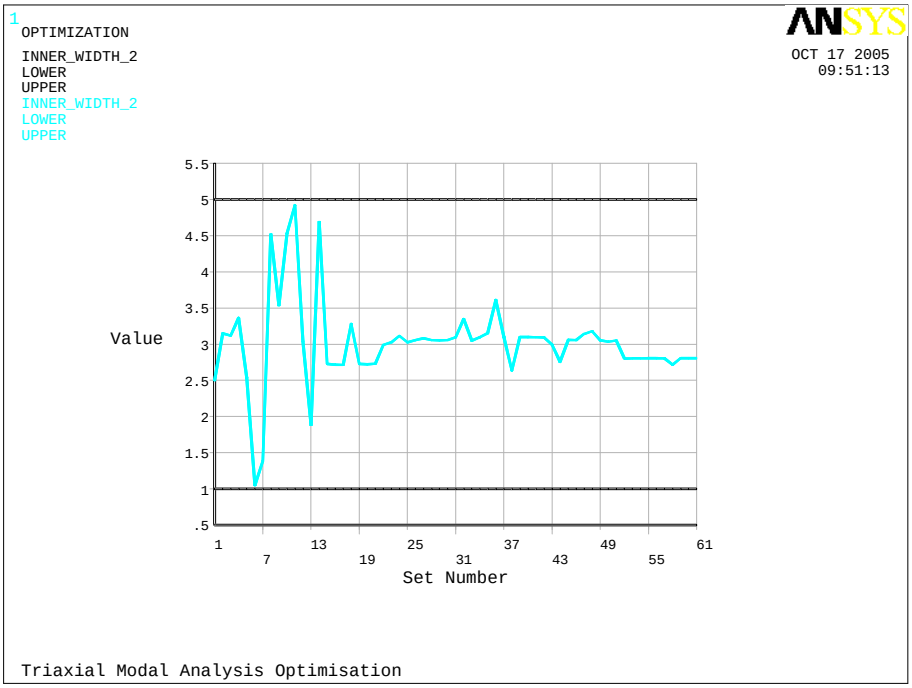

(d) INNER_WIDTH_2.

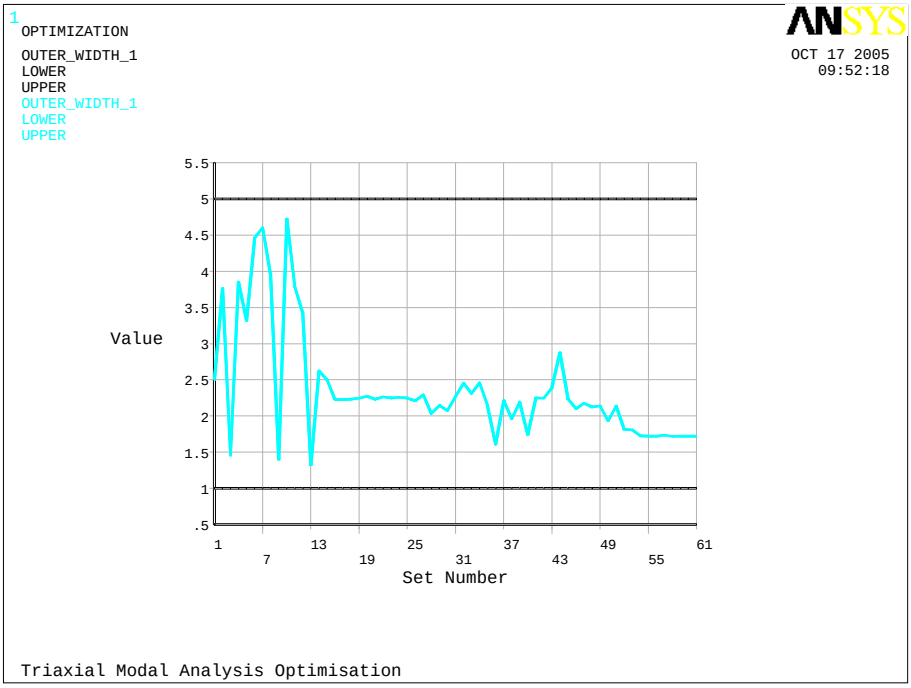

(e) OUTER_WIDTH_1.

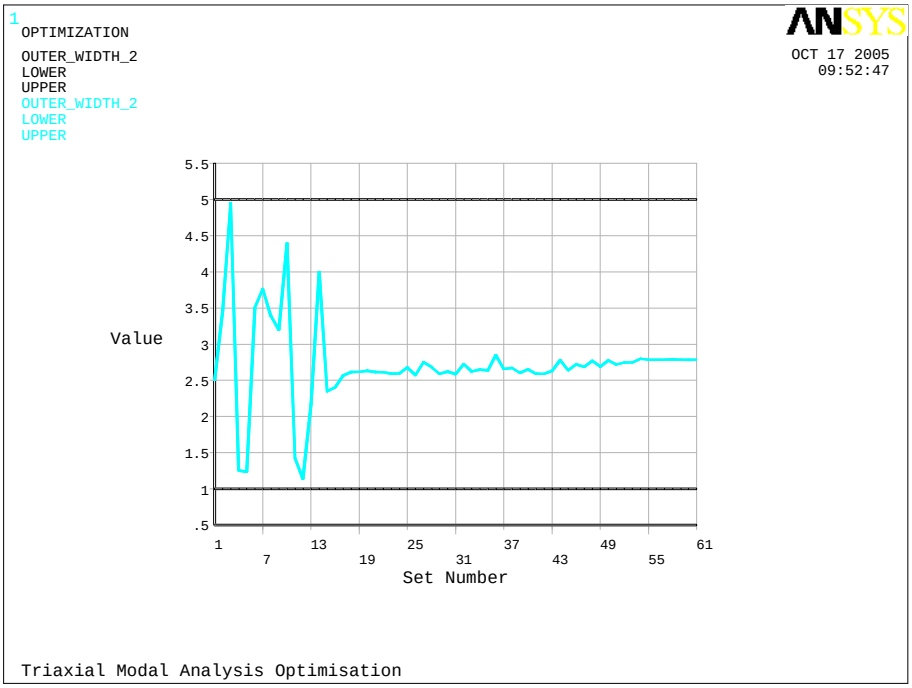

(f) OUTER_WIDTH_2.

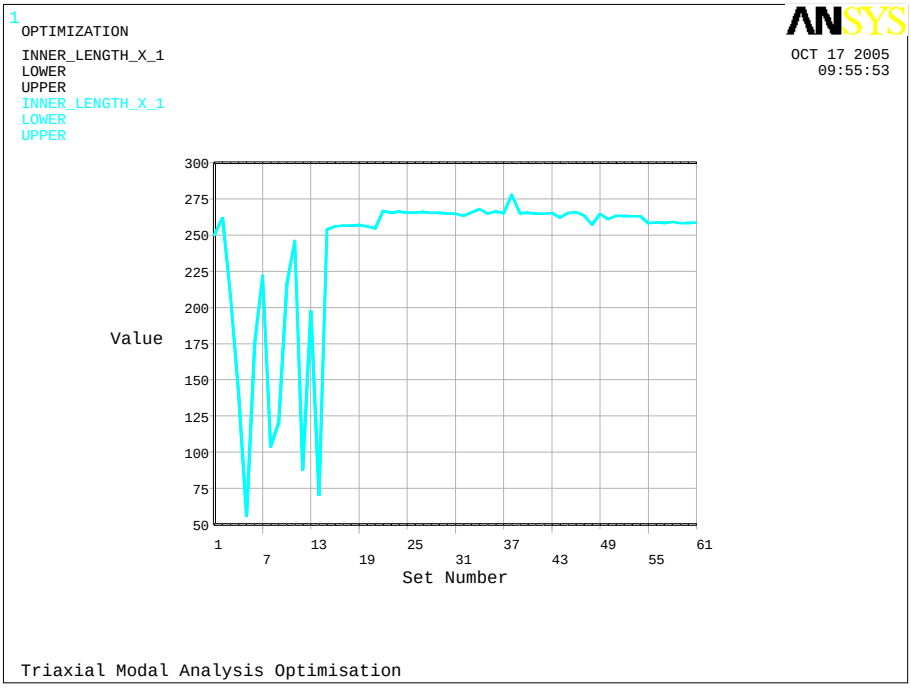

(g) INNER_LENGTH_X_1.

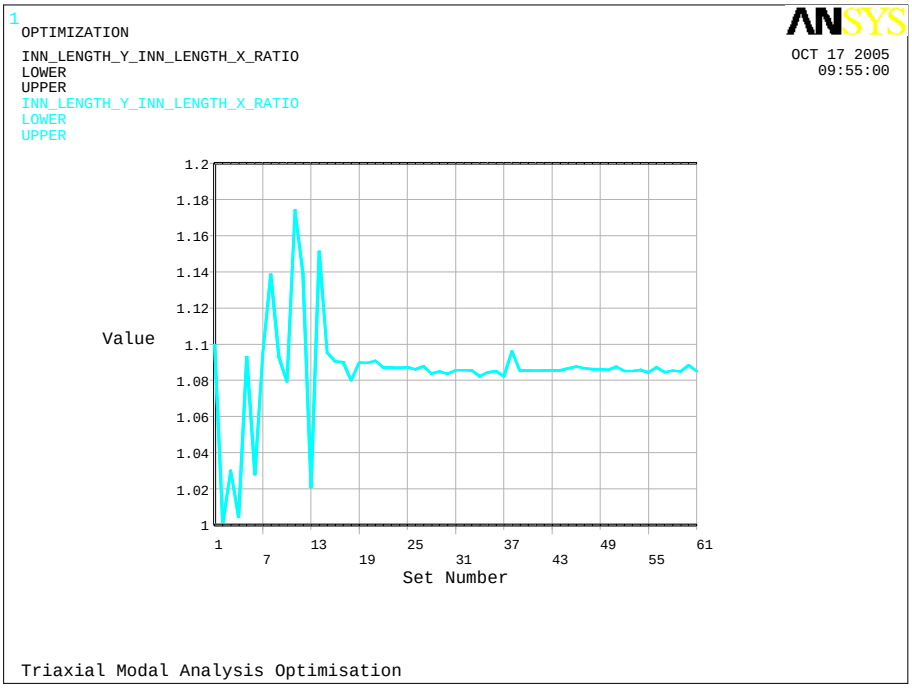

(h) INN_LENGTH_Y_INN_LENGTH_X_RATIO.

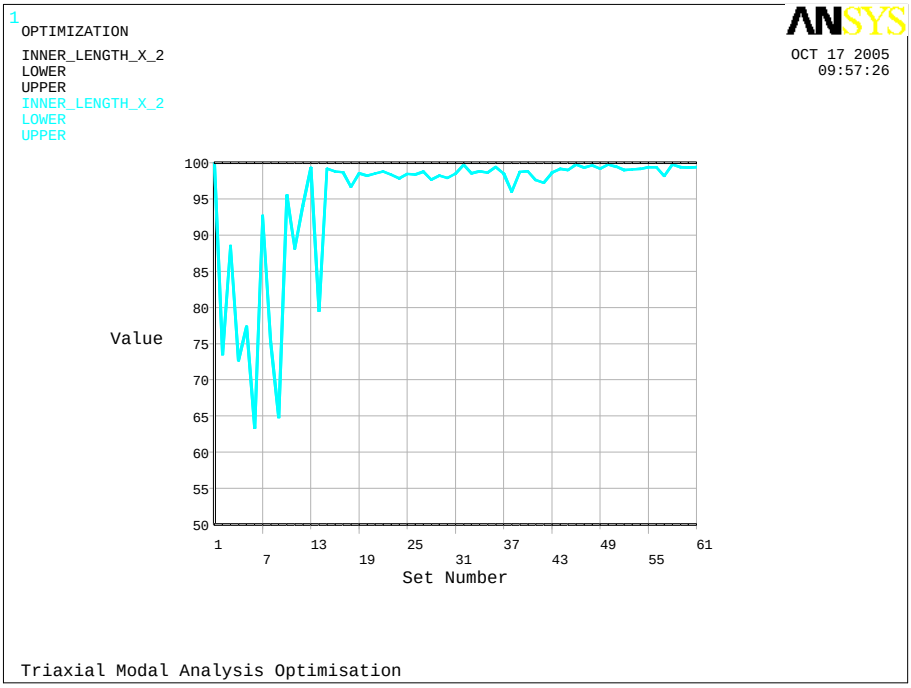

(i) INNER_LENGTH_X_2.

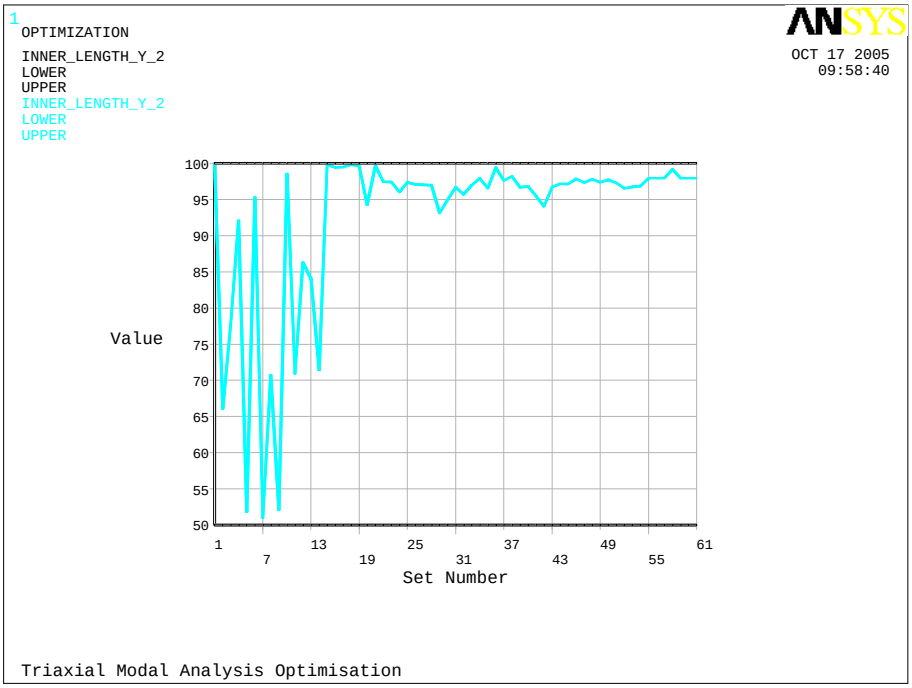

(j) INNER_LENGTH_Y_2.

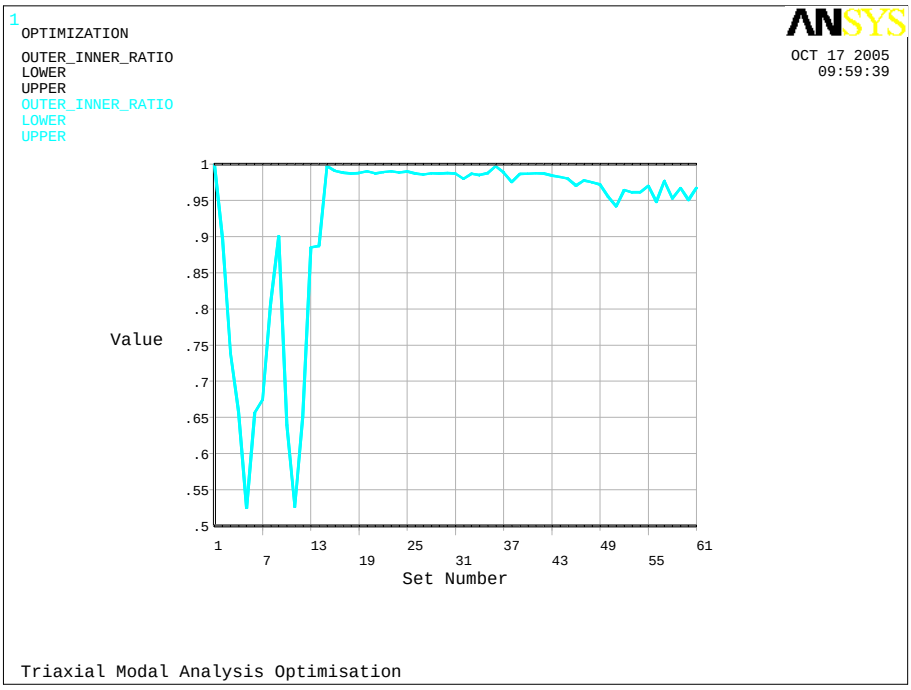

(k) OUTER_INNER_RATIO.

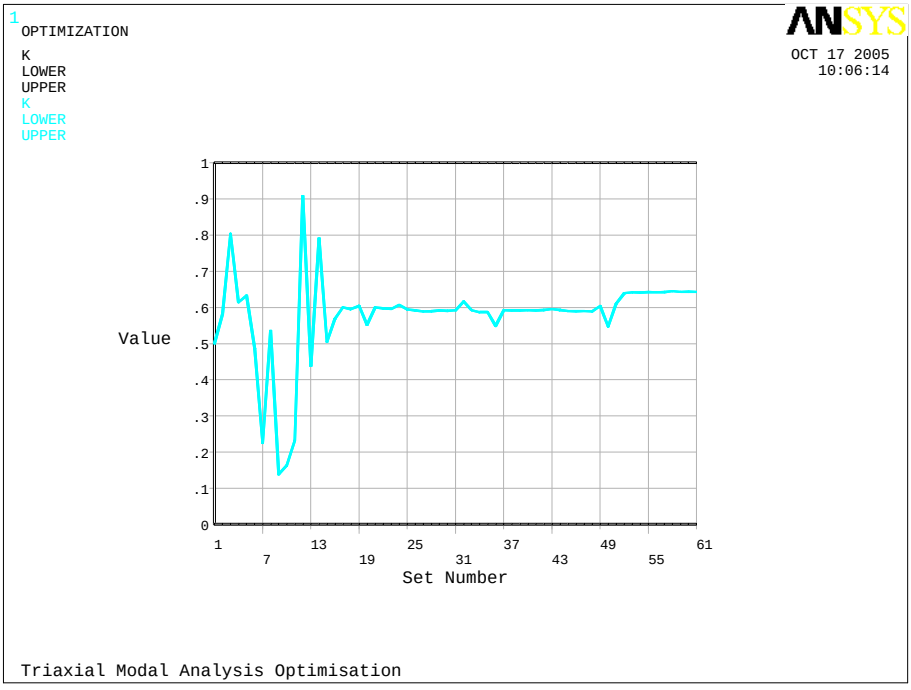

(l) K.

Figure F.1: Second structure: Design automation design variables.

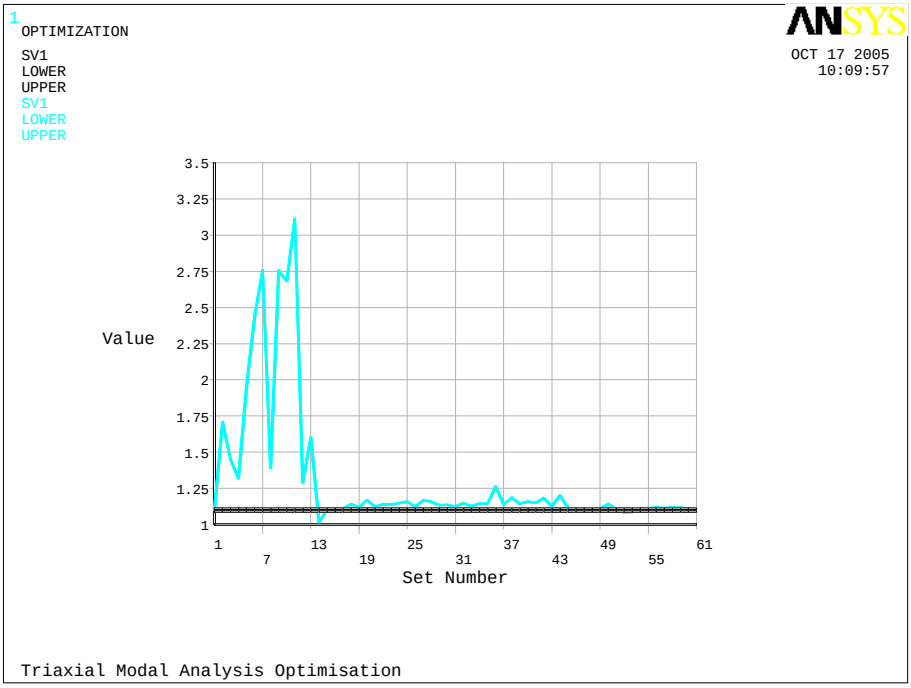
1
OPTIMIZATION
SV1
LOWER
UPPER
SV1
LOWER
UPPER
ANSYS
OCT 17 2005
10:09:57
Value
3.5
3.25
3
2.75
2.5
2.25
2
1.75
1.5
1.25
1
1
7
13
19
25
31
37
43
49
55
61
Set Number
Triaxial Modal Analysis Optimisation

(a) SV1.

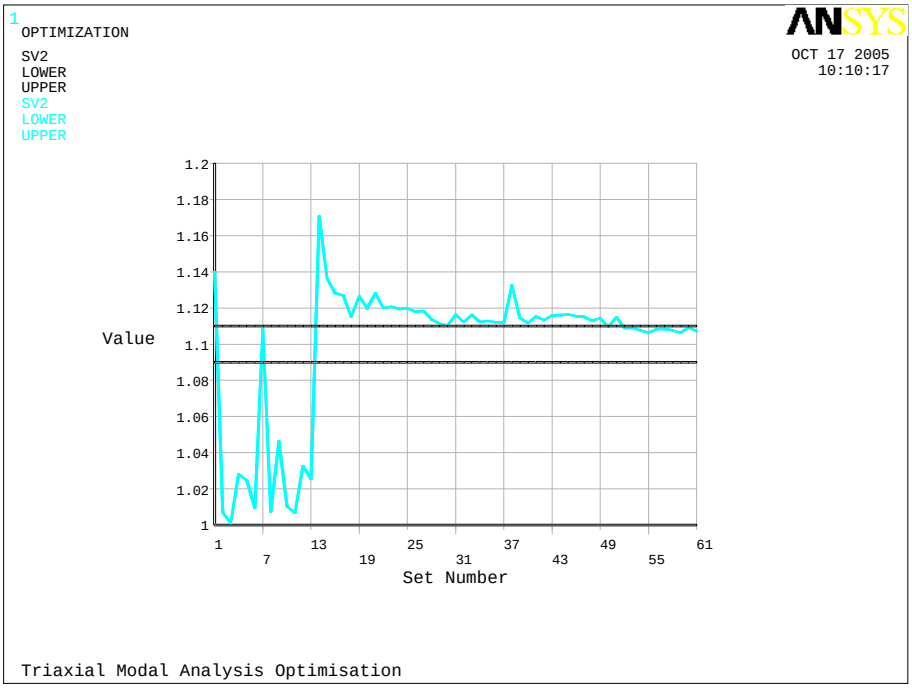
1
OPTIMIZATION
SV2
LOWER
UPPER
SV2
LOWER
UPPER
ANSYS
OCT 17 2005
10:10:17
Value
1.2
1.18
1.16
1.14
1.12
1.1
1.08
1.06
1.04
1.02
1
1
7
13
19
25
31
37
43
49
55
61
Set Number
Triaxial Modal Analysis Optimisation

(b) SV2.

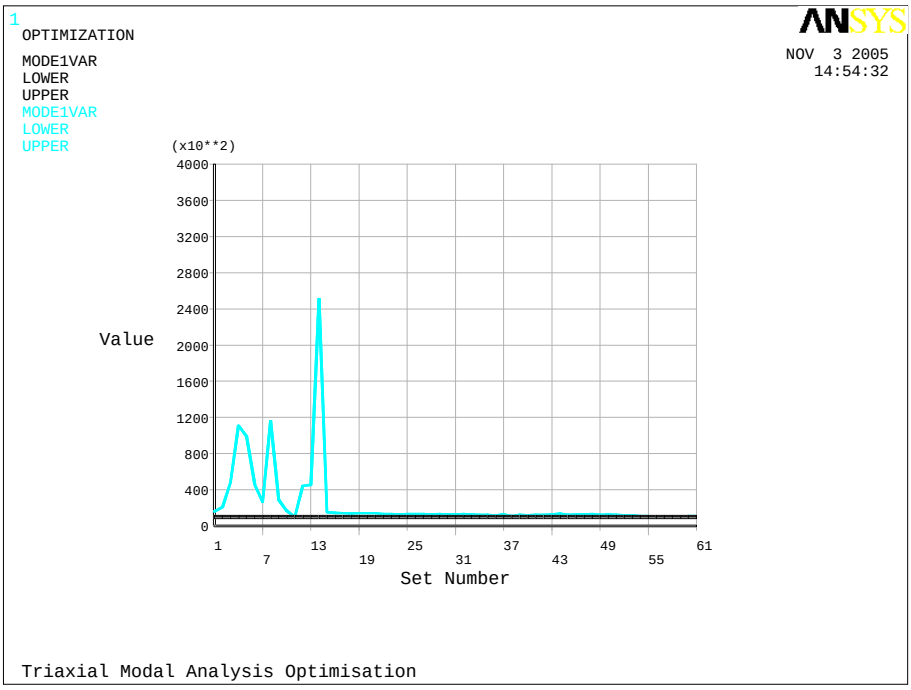

(c) MODE1VAR.

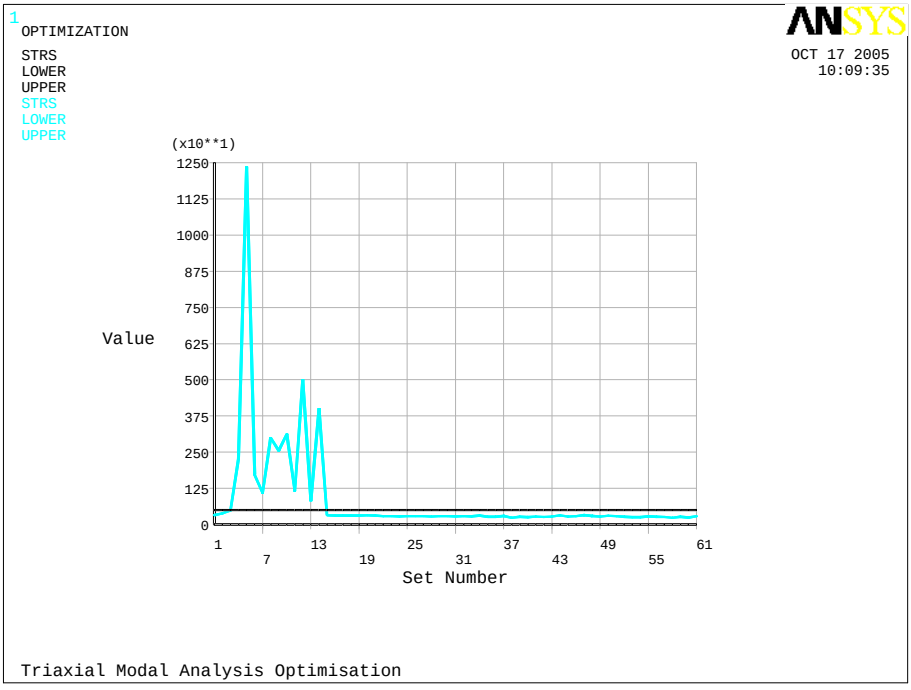

(d) STRS.

Figure F.2: Second structure: Design automation state variables.

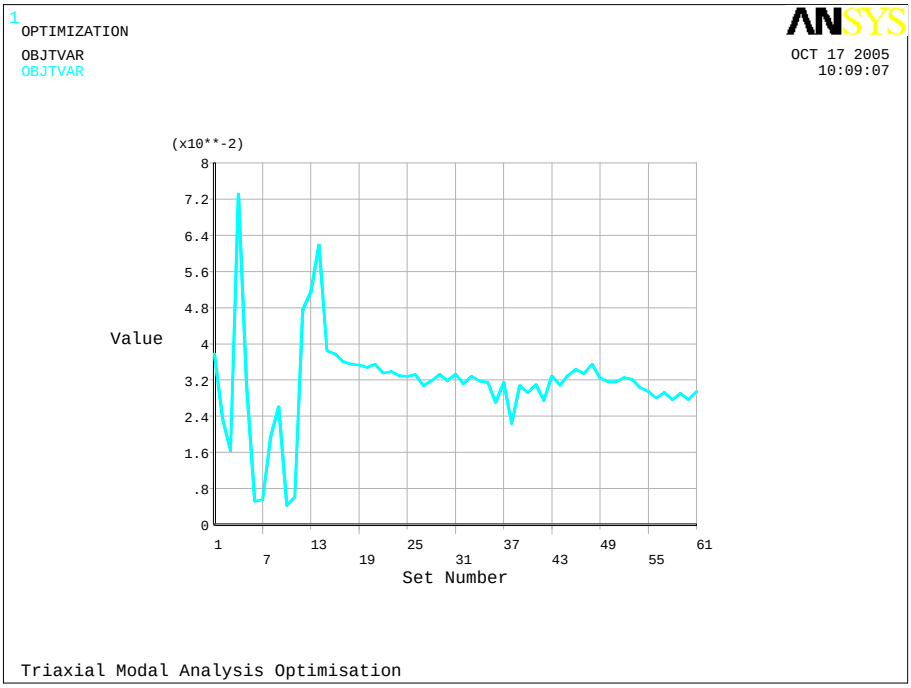

(a) OBJTVAR.

Figure F.3: Second structure: Design automation objective variables.

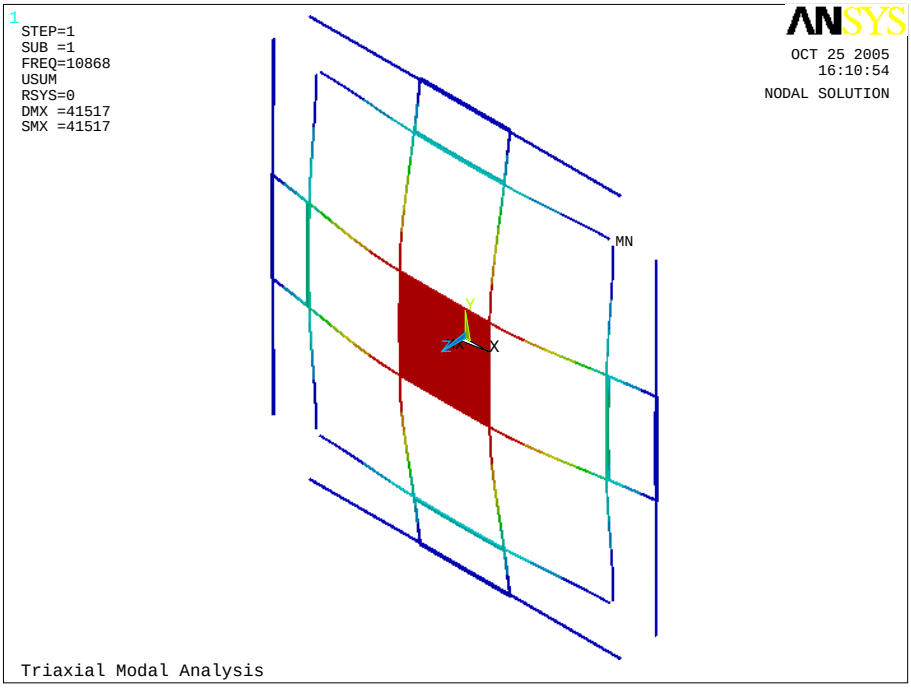

(a) x axis lateral, mode 1, 10868Hz.

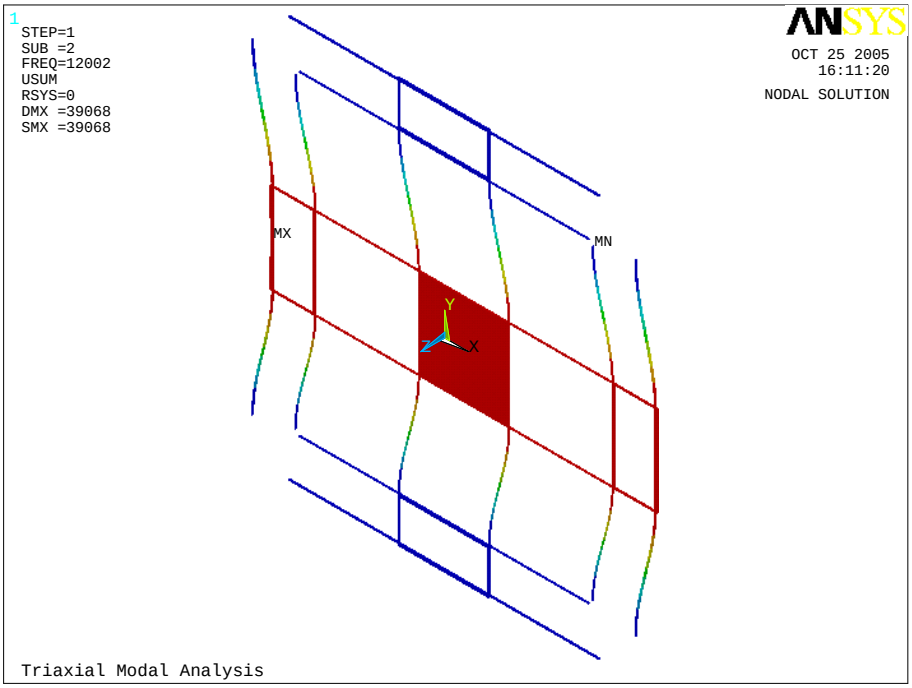

(b) z axis lateral, mode 2, 12002Hz.

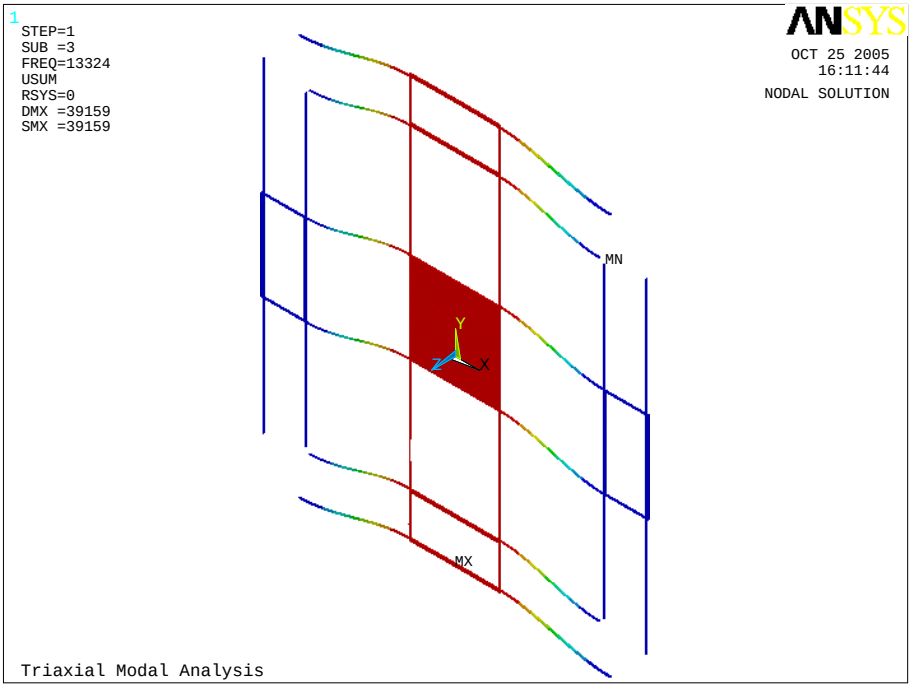

(c) y axis lateral, mode 3, 13324Hz.

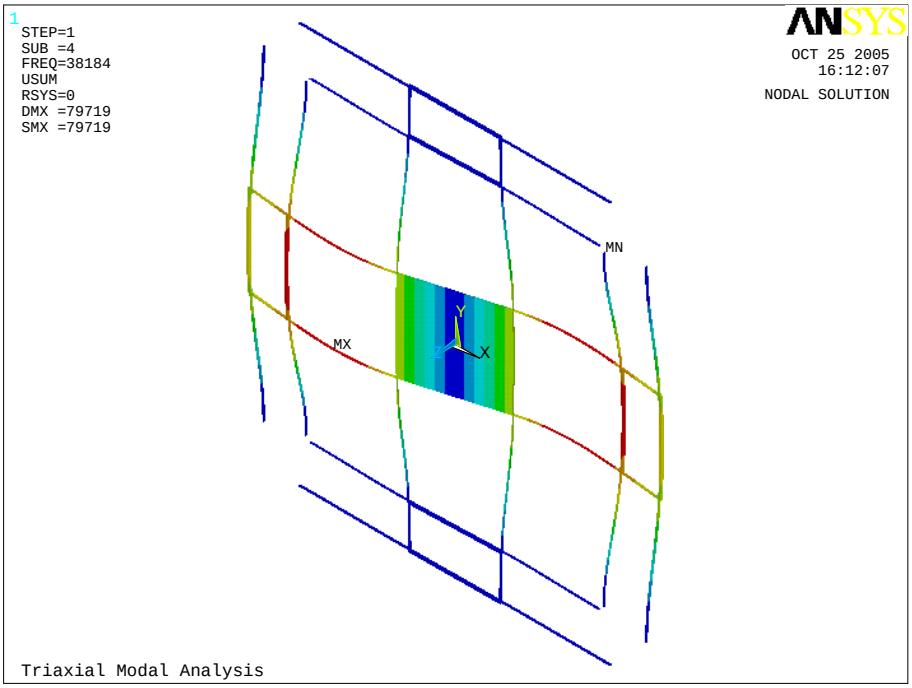

(d) y axis rotational, mode 4, 38184Hz.

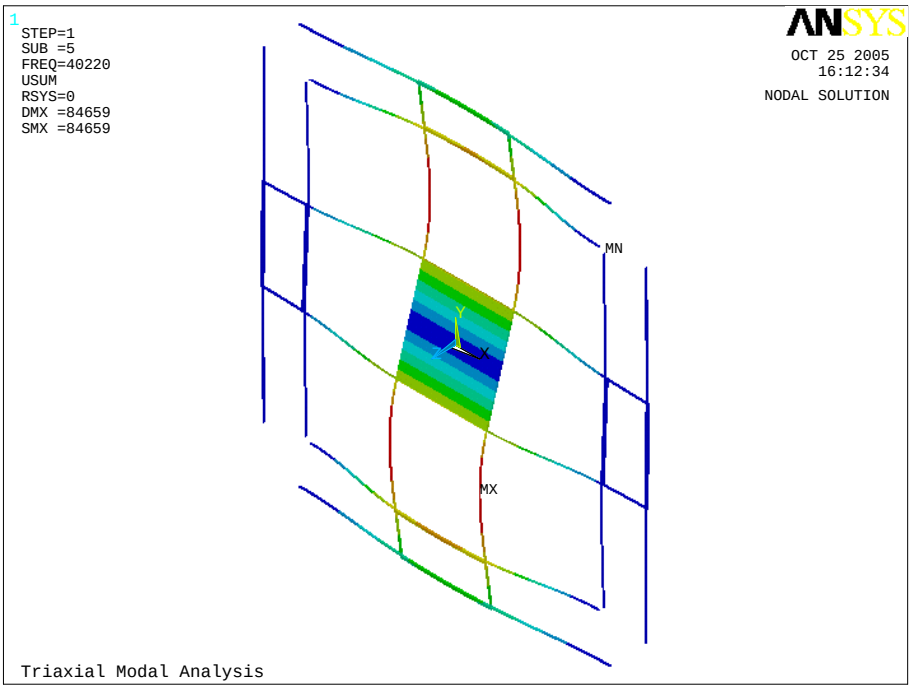

(e) x axis rotational, mode 5, 40220Hz.

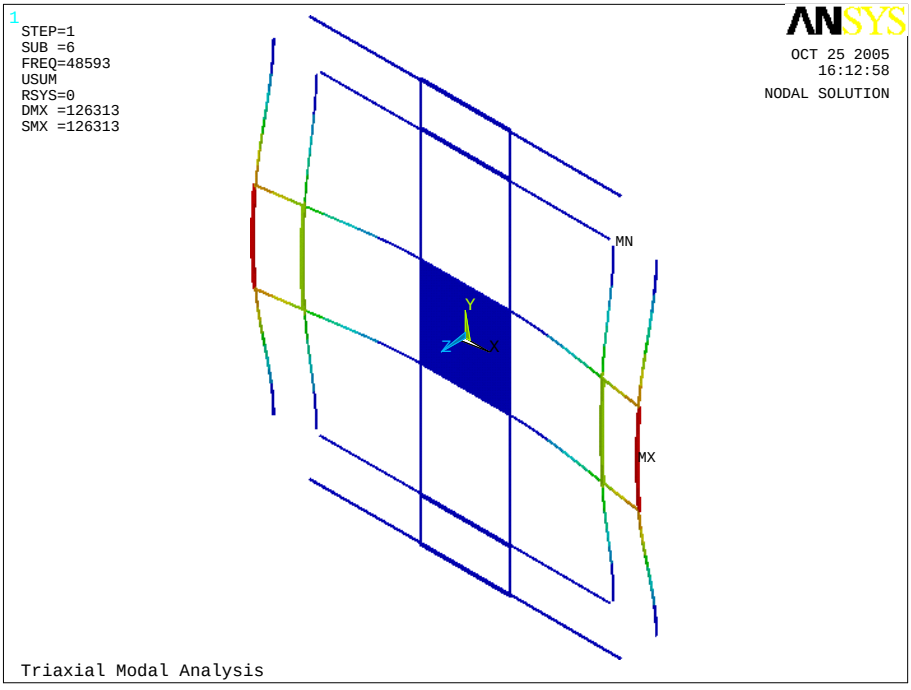

(f) z axis rotational, mode 6, 48593Hz.

Figure F.4: First six modal shapes and respective frequencies of the proposed device structure as found by ANSYS modal analysis.

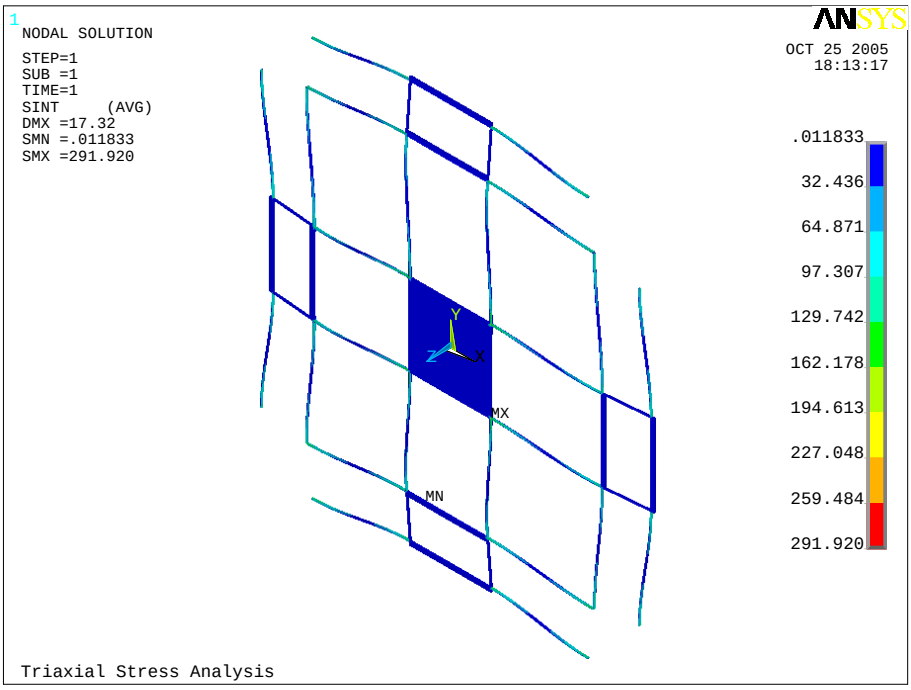

(a) Static analysis stress intensity.

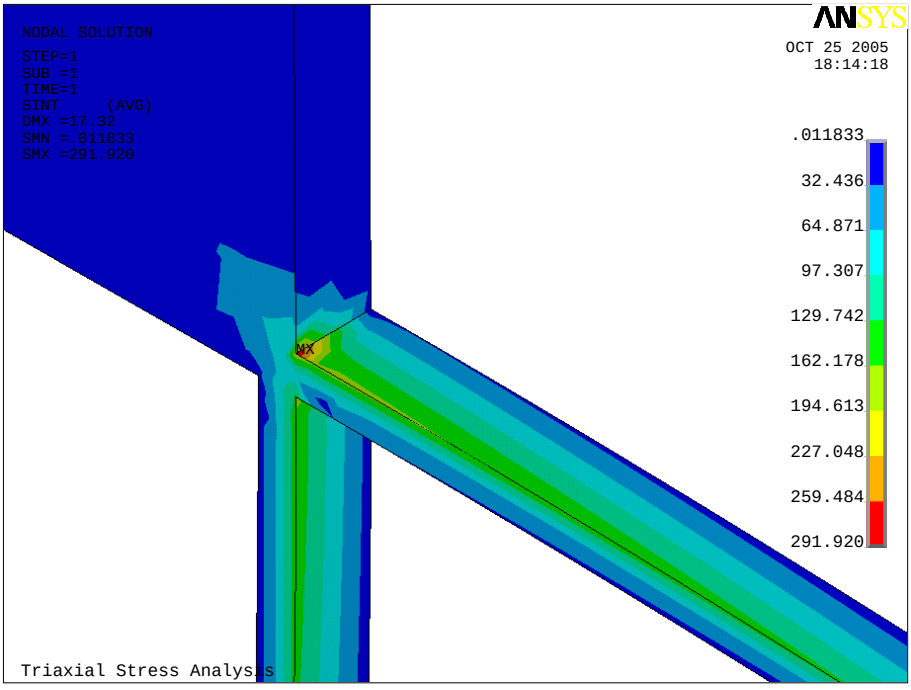

(b) Close up of area of maximum stress intensity MX.

Figure F.5: ANSYS Static analysis stress intensity.

Appendix G

Novel Phase Differential Angular Rate Sensor

G.1 Literature Review

The first reported angular rate sensor to use a phase detection scheme used a trident-type three pronged tuning fork configuration with the centre arm having two capacitive sensing element below it on either side of it's centreline [1]. When the arm traced an elliptical path due to the influence of Coriolis force, a phase difference representative of the input rotation, is induced in the sensor outputs. Phase detection has the advantage of removing the requirement of a constant drive amplitude, as will be shown in Section G.4.

The phase detection principle was also adopted by Yang [81] who developed a device consisting of a rectangular beam oscillated using electrostatic actuation. The electrostatic drive plate was offset to create unbalanced parasitic electrostatic forces and consequently a driving force that is slightly diagonal. This approach was suspected of causing non-linearity in the results. The likely cause of this is that the drive angle will alter as the beam starts to vibrate and the drive angle and gain factor are directly related.

In this paper we propose a symmetrical device structure with strategic positioning of the sensing elements that allows greater control over the driving force. The analysis section G.4 uncovers some novel device response curves that can be achieved with the proposed device.

G.2 Basic Structure

The proposed device structure includes all necessary physical parameters for a mathematical analysis of the phase detection scheme. For the purpose of this analysis it can be assumed that the device is driven

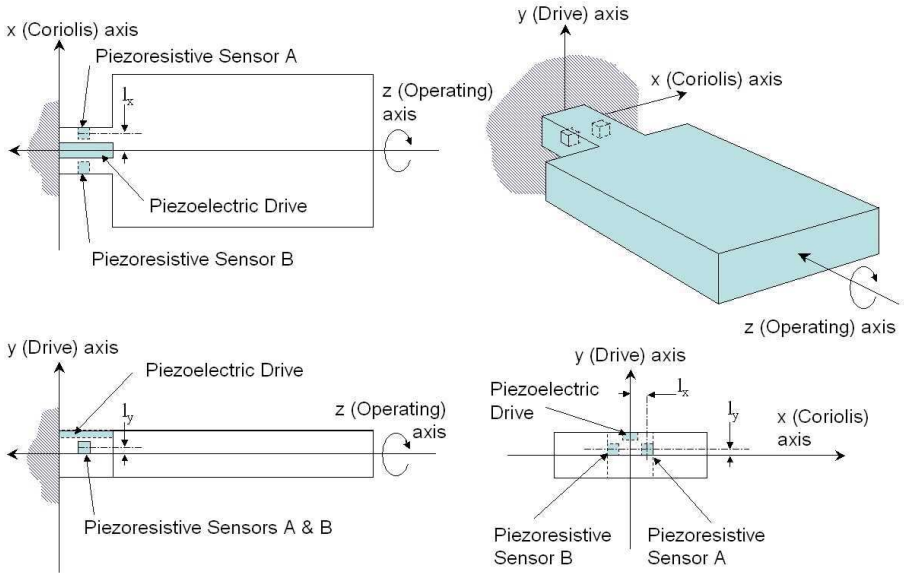

Figure G.1: Proposed device structure. Note that l_x and l_y describe the position of the piezoresistive sensor elements.

into oscillation using a piezoelectric drive element and the sensor elements are piezoresistive.

The current device shown in Figure G.1 is similar in structure to Yang [81] in that it consists of a rectangular cantilever beam mass. Unlike Yang [81] it is driven into vertical oscillation using piezoelectric actuators on the beam surface near its base, to ensure that the angle at which the driving force acts on the mass remains constant, with respect to the base of the device. The drive oscillation could also be achieved using electrostatic or electro-magnetic actuation, however the use of a piezoelectric drive allows the air gap around the mass to be increased, reducing any squeeze film damping effects between electrostatic actuator surfaces. The piezoresistive sensors are located on the beam slightly offset from the centreline in the y-axis, to acquire an evenly weighted ratio between drive and Coriolis vibration amplitudes. The usual trade-off of using piezoresistors is their temperature dependent output, however due to the amplitude independence of the phase differential scheme this trade-off is not applicable. Piezoresistive sensors have the advantages of being cheap, simple to fabricate and they do not require complex conditioning electronics as is required for capacitive sensing methods [35].

G.3 Operation

The beam mass is driven into oscillation vertically in the drive axis (y). When subject to a rotation around its operating axis (z), the mass begins oscillating in the Coriolis axis (x), due to Coriolis force acting on the mass. When the natural frequencies of the system in the x and y axes are not matched, the driving force and the Coriolis force make the mass trace an elliptical path. The piezoresistors are strategically located to sense both a component of the drive oscillation and opposite components of the

Coriolis oscillation. The opposing Coriolis components cause a phase differential in the two piezoresistor sensor signals that is representative of the input rotation.

The device resolution is limited by the resolution of the phase measurement method and the amount of noise on the signals. This dependency may be reduced by reducing the operating frequency so that the phase difference is easier to measure. The device resolution can also be improved by increasing the gain factor of the device through careful parameter optimisation, and by increasing the amplitude of the two sensor signals through optimum physical placement.

Although the output of the device is unaffected by variations in the drive axis amplitude, the drive amplitude must be large enough to create sufficient motion along the Coriolis axis. This can be achieved by driving the device at resonance. Typically, a phase-locked loop is used to adjust the input frequency until the drive axis output is out of phase with the input [41].

Since the system is driven very close to its resonance frequency, the drive amplitude is strongly dependent on the inherent damping in the system. To attain a sufficient drive amplitude this damping should be kept very low. Precise control of the drive-mode amplitude is not necessary.

The placement of the sensing elements and the other design parameters are investigated in the following analysis.

G.4 Analysis

Typically the effect of Coriolis force on the drive axis is negligible, therefore the respective equations describing the accelerations in the x and y axes for a non-zero mass are [41]

$$\ddot{x} + 2\zeta_x\omega_x\dot{x} + \omega_x^2 x - 2\Omega(t)\dot{y} = 0 \tag{G.1}$$

$$\ddot{y} + 2\zeta_y\omega_y\dot{y} + \omega_y^2 y = \frac{f_y(t)}{m} \tag{G.2}$$

where $f_y(t)$ is the driving force, m is the mass Ω is the input rotation, ζ_x and ζ_y are the damping ratios and ω_x and ω_y are the natural frequencies in their respective axes.

For this analysis $\Omega(t)$ is assumed to be steady state and can be replaced with Ω [81].

While this is valid for the following analysis, in general the bandwidth of this device will be similar to that of a device operating in open loop mode. The phase detection scheme relies on the mass having an elliptical path, therefore the motion in the Coriolis axis cannot be nulled to increase the bandwidth, as is the case with many devices that operate in closed loop mode. However, one technique to increase bandwidth is to cause a slight mismatch between the drive and Coriolis axis resonant modes, which is already a prerequisite for the design of phase detection devices (i.e. u_x cannot equal zero).

Taking the Laplace transform of Equations G.1 and G.2 where $X(s) = \mathcal{L}(x(t))$ and $Y(s) =$

$\mathcal{L}(y(t))$ and solving for $X(s)$ and $Y(s)$ gives

$$X(s) = \frac{2\Omega s F_y(s)}{m(s^2 + 2\zeta_y\omega_y s + \omega_y^2)(s^2 + 2\zeta_x\omega_x s + \omega_x^2)} \tag{G.3}$$

and

$$Y(s) = \frac{F_y(s)}{m(s^2 + 2\zeta_y\omega_y s + \omega_y^2)} \tag{G.4}$$

Piezoresistor sensors output a change in resistance due to stress

$$\frac{\Delta R}{R} = \sigma_l\pi_l + \sigma_t\pi_t \tag{G.5}$$

where σ_l and σ_t are the stress and π_l and π_t are the piezoresistance coefficients in the respective longitudinal and transverse directions with respect to the current flow [50].

The longitudinal and transverse stress on each sensor element can be expressed as [25]

$$\sigma_l = \frac{2E(X(s)l_x + Y(s)l_y)}{l_z^2},\ \sigma_t = -\frac{2E\nu(X(s)l_x + Y(s)l_y)}{l_z^2} \tag{G.6}$$

where ν is the Poisson's ratio, E the Young's modulus for the beam and l_{xA}, l_{yA}, l_{zA}, l_{xB}, l_{yB} and l_{zB} are the piezoresistor positions relative to the centre of the base of the beam. Subscripts A and B have been included as inequalities may arise between the two sensor locations due to fabrication limitations, this is investigated further with the sensitivity analysis in Section G.6. Combining Equation G.5 and Equation G.6 gives

$$\frac{\Delta R_A(s)}{R_A} = \frac{2E}{l_{zA}^2}\left(l_{xA}X(s) + l_{yA}Y(s)\right)(\pi_l - \pi_t\nu) \tag{G.7}$$

Note that, for a greater sensor signal amplitude, the distance from the base of the beam to the sensor element l_z should be minimised to increase the stress on it. Substituting Equation G.3 and Equation G.4 into Equation G.7 gives

$$\frac{\Delta R_A(s)}{R_A} = \frac{2EF_y(s)\left((s^2 + 2\zeta_x\omega_x s + \omega_x^2)l_{yA} + 2\Omega s l_{xA}\right)(\pi_l - \pi_t\nu)}{ml_{zA}^2(s^2 + 2\zeta_x\omega_x s + \omega_x^2)(s^2 + 2\zeta_y\omega_y s + \omega_y^2)}$$

Noting the change in sign of the Coriolis-axis term, sensor B becomes

$$\frac{\Delta R_B(s)}{R_B} = \frac{2EF_y(s)\left((s^2 + 2\zeta_x\omega_x s + \omega_x^2)l_{yB} - 2\Omega s l_{xB}\right)(\pi_l - \pi_t\nu)}{ml_{zB}^2(s^2 + 2\zeta_x\omega_x s + \omega_x^2)(s^2 + 2\zeta_y\omega_y s + \omega_y^2)}$$

Since both sensor elements are operating at similar frequencies within the sensor element bandwidth and are symmetrical in design, it is assumed that any inherent propagation delay will be small and affect both sensors equally, and is therefore neglected. Letting α be the length ratio between l_{xA} and

l_{yA}, β be the length ratio between l_{xB} and l_{yB}, u_x be the frequency ratio between ω and ω_x and λ be the frequency ratio, between Ω and ω_x

$$\alpha = \frac{l_{xA}}{l_{yA}},\ \beta = \frac{l_{xB}}{l_{yB}},\ u_x = \frac{\omega}{\omega_x},\ \lambda = \frac{\Omega}{\omega_x} \tag{G.8}$$

the phase difference between the two sensor signals $\Delta\phi$ becomes

$$\Delta\phi = artan\left(\frac{2u_x\lambda(u_x^2-1)(\alpha-\beta)}{(u_x^2-1)^2+4u_x^2\zeta_x^2+4\zeta_x u_x^2(\alpha+\beta)\lambda+4\alpha\beta u_x^2\lambda^2}\right)$$

Equation G.9 is used to investigate sensitivity to α and β in Section G.6, however in an ideal case the sensor elements will be located symmetrically therefore $\beta = -\alpha$

$$\Delta\phi = artan\left(\frac{4u_x\alpha\left(u_x^2-1\right)\lambda}{(u_x^2-1)^2+4\zeta_x^2u_x^2-4u_x^2\alpha^2\lambda^2}\right) \tag{G.9}$$

The driving force has dropped out of the equation, showing the benefit of phase detection scheme where control circuits to maintain constant driving amplitude are not required. The sensor element scaling constants have also dropped out indicating that any additional scale factor dependence such as temperature and inequalities in distances from the base of the beam l_{zA} and l_{zB}, will not affect the phase difference between the two signals.

The final expression for the Phase Scheme angular rate Sensor Equation G.9 is of the general form

$$\Delta\phi = artan\left(\frac{a\lambda}{b-c\lambda^2}\right) \tag{G.10}$$

where

$$a = 4u_x\alpha\left(u_x^2-1\right) \tag{G.11}$$

$$b = (u_x^2-1)^2+4\zeta^2u_x^2 \tag{G.12}$$

$$c = 4u_x^2\alpha^2 \tag{G.13}$$

Upon inspection the denominator in Equation G.10 becomes zero when $\lambda = \sqrt{\frac{b}{c}}$. This indicates that $\Delta\phi$ will always pass through the three points $\left(-\sqrt{\frac{b}{c}}, \frac{-\pi}{2}\right)$, $(0,0)$ and $\left(\sqrt{\frac{b}{c}}, \frac{+\pi}{2}\right)$ when $a > 0$ and $\left(-\sqrt{\frac{b}{c}}, \frac{+\pi}{2}\right)$, $(0,0)$ and $\left(\sqrt{\frac{b}{c}}, \frac{-\pi}{2}\right)$ when $a < 0$. Note that, only a can be negative (i.e. when $u_x < 1$). Substituting Equations G.12 and G.13 into $\pm\sqrt{\frac{b}{c}}$ gives $\lambda_{\pm\frac{\pi}{2}}$, the points where $\Delta\phi = \pm\frac{\pi}{2}$.

$$\lambda_{\pm\frac{\pi}{2}} = \frac{1}{2\alpha}\sqrt{\left(\frac{u_x^2-1}{u_x}\right)^2+4\zeta_x^2} \tag{G.14}$$

Equation G.10 can produce two general response shapes and a point of transition between the two as can be seen in Figure G.2. The first shape Figure G.2(a) resembles a regular arctan curve that has a relatively steep section around the origin and whose gradient decreases with increasing values of $|\lambda|$. The transition, Figure G.2(b) consists of a relatively straight line section that stretches between $\left(-\sqrt{\frac{b}{c}}, \frac{-\pi}{2}\right)$ and $\left(\sqrt{\frac{b}{c}}, \frac{\pi}{2}\right)$ when $a > 0$ and $\left(-\sqrt{\frac{b}{c}}, \frac{\pi}{2}\right)$ and $\left(\sqrt{\frac{b}{c}}, \frac{-\pi}{2}\right)$ when $a < 0$, before the gradient again decreases with increasing values of $|\lambda|$. The second response shape Figure G.2(c) resembles two arctan curves joined at the origin whose maximum gradient occurs at an offset in λ either side of zero.

The transition case occurs when $\frac{d^2\Delta\phi(\lambda)}{d\lambda^2}$ has a point of inflection at $\lambda = 0$, therefore solving for a, b and c gives

$$a = 0, b = 0, b = \frac{a^2}{3c} \tag{G.15}$$

Inspection of Equation G.12 shows that $b \geq 0$ however $b = 0$ would require the mass to be driven at resonance, destroying the elliptical nature of the movement of the mass. If the device is driven at the resonant frequency in the Coriolis axis ($\omega = \omega_x$) then u_x becomes zero and $\Delta\phi = 0$. This destroys the elliptical path because motion in the drive and Coriolis axes will be in phase and therefore along a straight line through the origin. If the drive frequency is adjusted further past the resonant frequency of the Coriolis axis, then the elliptical path is created in the opposite direction (eg. clockwise instead of anticlockwise).

Inspection of Equation G.11 also shows that $a = 0$ is nonsensical as it would require either (i) $\alpha = 0$ which would mean that the sensing element would be positioned to only pick up the driving vibration and no Coriolis motion, (ii) $u_x = 0$ meaning that mass is stationary and no driving oscillation is occurring, or (iii) $u_x = 1$, the previously mentioned resonance case. All three of these cases result in $\Delta\phi = 0$ or $\pm\pi$ for all λ as can be seen by inspecting Equation G.9.

Therefore the transition case occurs when

$$\frac{a}{\sqrt{bc}} = \pm\sqrt{3} \tag{G.16}$$

Substituting Equations G.11, G.12 and G.13 into Equation G.16 and simplifying gives the general expression

$$\frac{a}{\sqrt{bc}} = \frac{u_x^2 - 1}{2\zeta_x u_x} = \gamma \tag{G.17}$$

where γ is a variable that indicates what the general shape of the response will be.

Responses plotted across a range of γ values are shown in Figure G.3. The notable sections are shown individually in Figure G.2. These show that $|\gamma| < \sqrt{3}$ gives an offset from zero response $|\gamma| > \sqrt{3}$ gives a shape resembling a regular arctan shape and when $|\gamma| = \sqrt{3}$ the transition between the two occurs.

When $\gamma > 0$ the response has a positive gradient and when $\gamma < 0$ it has a negative gradient. The

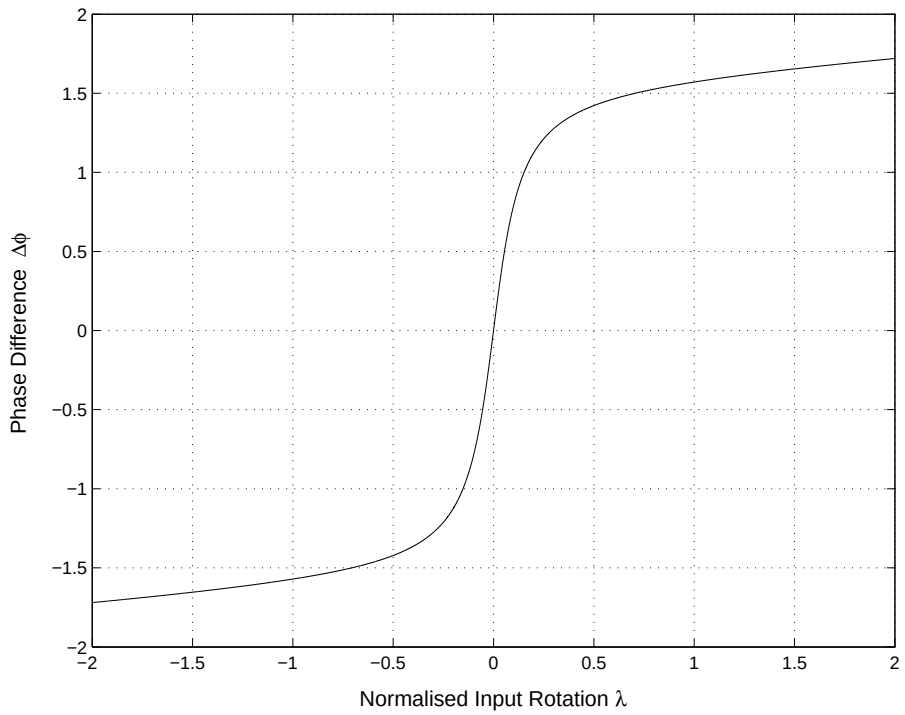

(a) $|\gamma| > \sqrt{3}$ Normal shape response: A high gain around the origin decreases as the value of $|\lambda|$ increases. (Only positive gradient case shown)

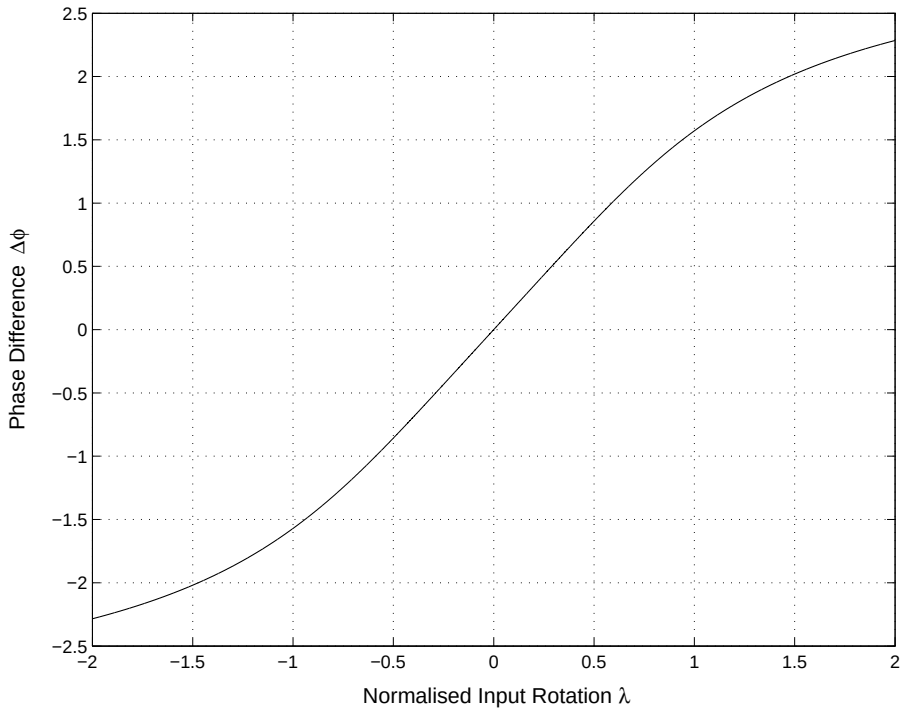

(b) $|\gamma| = \sqrt{3}$ Transition shape response: The transition between the offset and normal shapes (Only positive gradient case shown)

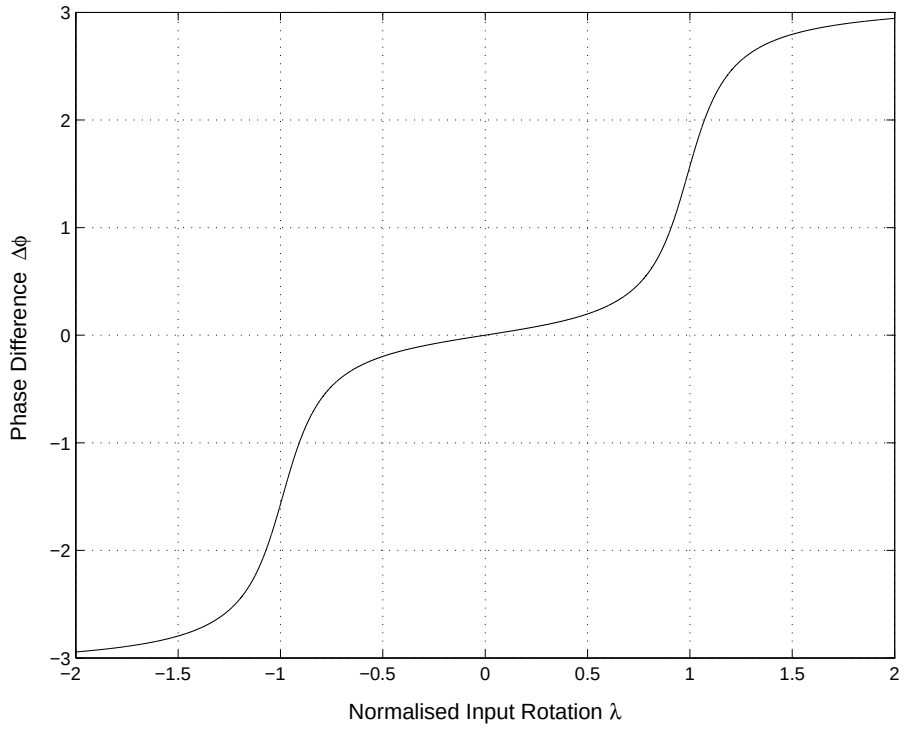

(c) $|\gamma| < \sqrt{3}$ Offset shape response: Response has a maximum gain, offset from the origin by λ_{Offset} in Equation G.21 (Only positive gradient case shown)

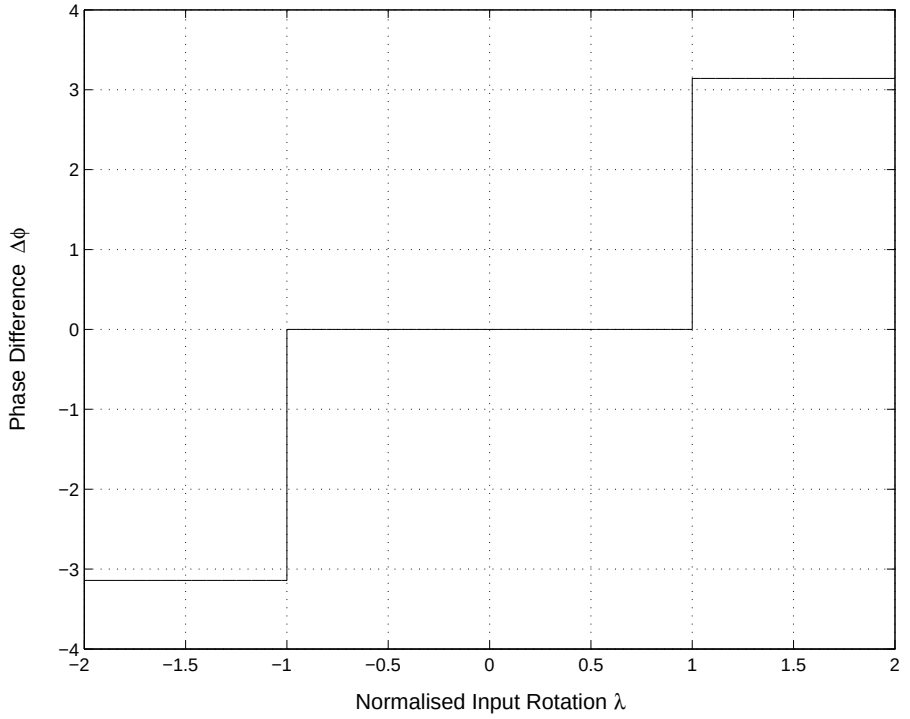

(d) $|\gamma| = 0$ Zero or $\pm\pi$ phase difference response. The sudden change is due to one of the sensor elements going through zero amplitude and then inverting its phase.

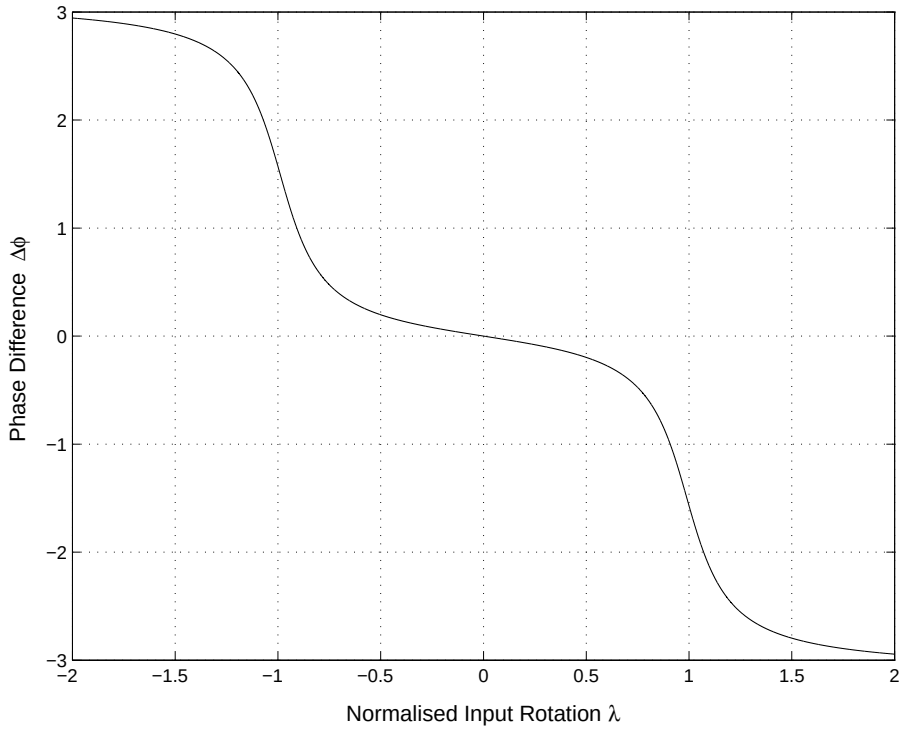

(e) $\gamma < 0$ The response has a negative gradient.

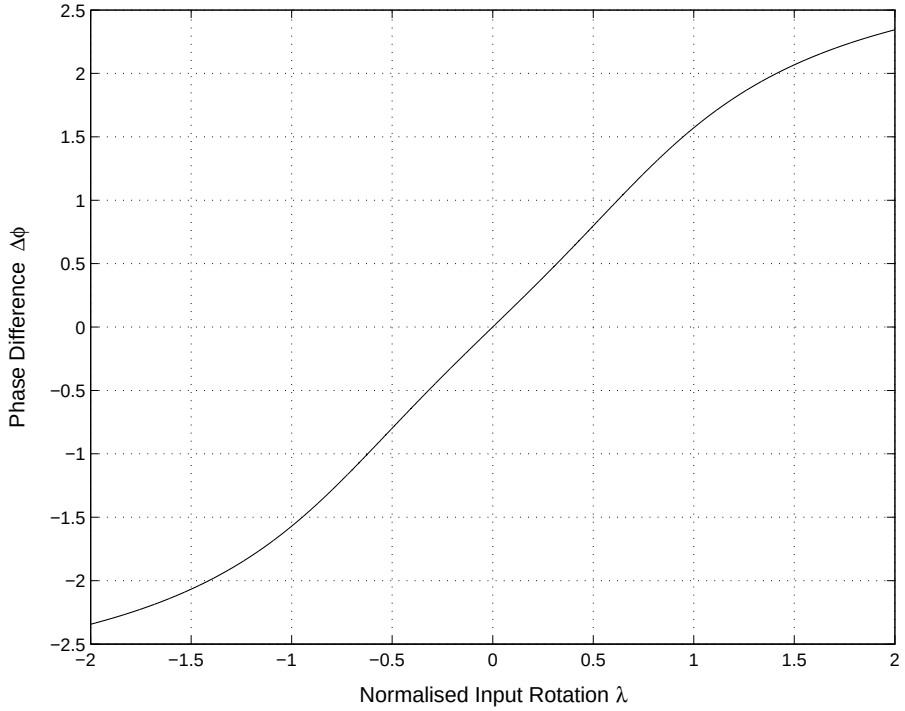

(f) $|\gamma| = 1.5375$ Optimal linear response: An optimally linear region in the range from -$\lambda_{\pm\frac{\pi}{2}}$ to $\lambda_{\pm\frac{\pi}{2}}$ with a gradient of approximately $\frac{2}{\pi\lambda_{OP}}$ (Only positive gradient case shown)

Figure G.2: Response Shape Determination

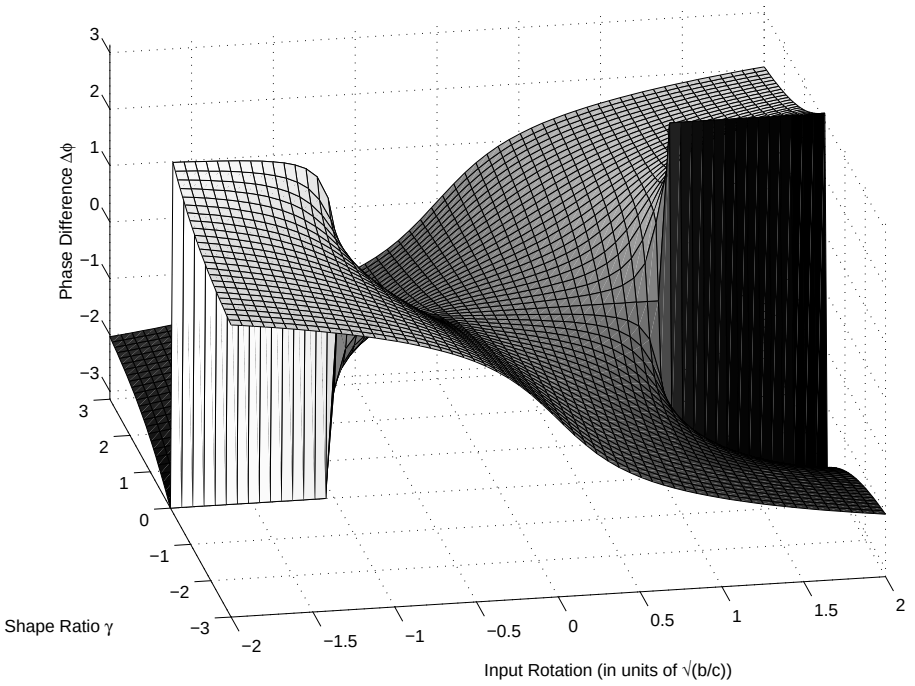

Figure G.3: Phase difference $\Delta\phi$ plotted across input angular rate range, for all values of γ. The γ parameter varies the response shape, with $|\gamma| < \sqrt{3}$ giving a response having maximum gradient for nonzero input rates. The gradient is positive for $\gamma > 0$ and negative for $\gamma < 0$.

seemingly discontinuous points when $\gamma = 0$ can be explained simply. When $|\lambda| = \sqrt{\frac{b}{c}}$, one of the sensing elements will have zero amplitude resulting in an undefined $\Delta\phi$. When $\gamma = 0$ and $|\Omega| > \sqrt{\frac{b}{c}}$ the sensing element signal is inverted, therefore $\Delta\phi = \pm\pi$.

Equation G.17 can be used as a design guideline to predict the response shape for given ζ_x and u_x values. It is interesting to note the shape of the response curve is independent of α indicating that the shape can be scaled in λ by varying α. By definition $u_x \geq 0$ and $0 \leq \zeta_x \leq 1$, therefore solving Equation G.17 for u_x gives

$$u_x = \gamma\zeta_x + \sqrt{\gamma^2\zeta_x^2 + 1} \tag{G.18}$$

The desired response shape, determined by the value of γ, can be achieved by adjusting u_x for any ζ_x value using Equation G.18 as a guide. This can physically be done by adjusting the driving frequency. For any value of ζ_x, there is always one value of u_x that will result in each response shape. Figure G.4 shows u_x plotted over ζ_x for various γ ratios. When $\zeta_x = 0$, $u_x = 1$ resulting again in the previously mentioned resonance case. If $u_x < 1$ then the response shape will have a negative gradient ($\gamma < 0$ in Figure G.3) and if $u_x > 1$ then the response has a positive gradient ($\gamma > 0$ in Figure G.3).

The shape can then be stretched or compressed in the λ axis to achieve the desired operating

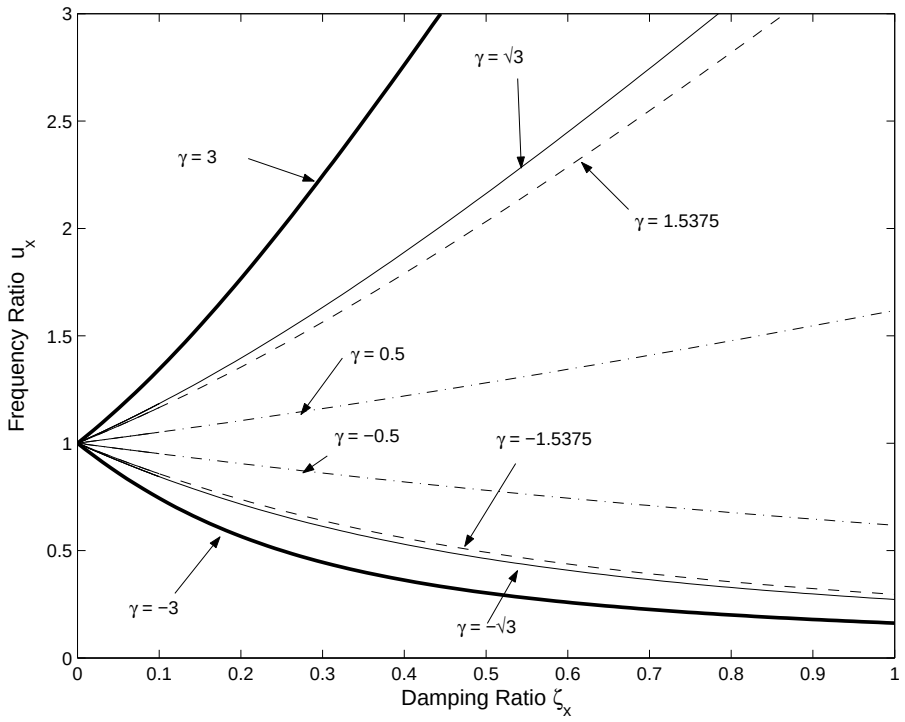

Figure G.4: Plot of u_x over ζ_x for various γ values.

range by adjusting the α parameter in Equation G.14, which can be more conveniently expressed as

$$\alpha = \frac{1}{2\lambda_{\pm\frac{\pi}{2}}}\sqrt{\left(\frac{u_x^2-1}{u_x}\right)^2 + 4\zeta_x^2} \tag{G.19}$$

Substituting u_x from Equation G.18 gives α in terms of $\lambda_{\pm\frac{\pi}{2}}$, ζ_x and γ

$$\alpha = \frac{\zeta_x}{\lambda_{\pm\frac{\pi}{2}}}\sqrt{\gamma^2+1} \tag{G.20}$$

Noting that γ is squared, α will be the same whether the response is positive ($\gamma > 0$) or negative ($\gamma < 0$).

It should be noted that there will be trade-offs and physical limitations on each parameter that will impose restrictions on the achievable shape and scale of the response. For example α is limited by the fabrication resolution, and ζ_x is limited by the operating environment. As such, these limitations make good starting points for design parameters.

G.4.1 Location of Response Curve Offset

The gradient of the response curve is proportional to the sensitivity of the device, and in turn its resolution. It was shown in Section G.4 that response shapes with maximum gradients around an offset in λ (λ_{Offset}) are achievable when $|\gamma| < \sqrt{3}$. The size of λ_{Offset} can be found knowing that the point of maximum gradient will be a point of inflection, therefore solving $\frac{d^2\Delta\phi(\lambda)}{d\lambda^2} = 0$ for λ and substituting in $a^2 = \gamma^2 bc$

from Equation G.17 gives

$$\lambda_{Offset} = \sqrt{\frac{\pm b\sqrt{4-\gamma^2}-b}{c}} \tag{G.21}$$

Equation G.21 has real solutions for $|\gamma| \leq \sqrt{3}$ as would be expected and $\lambda_{Offset} = \sqrt{\frac{b \mp \sqrt{4-\gamma^2}-b}{c}}$. For small values of γ Equation G.21 can be approximated to $\lambda = \sqrt{\frac{b}{c}}$, which is $\lambda_{\pm\frac{\pi}{2}}$ from Equation G.14.

In the opinion of the author, an angular rate sensor with offset operating point is novel and not described previously in the literature. Such a device could be used to give a steeper response gradient at angular rates within a range offset from zero, improving the output resolution in this range, and with shallower response gradient around zero. This variation in response gradient with angular rate is useful where the device rotates constantly and measures deviations from the constant rotation, or where measurements are expected within a narrow range of angular rates. One possible application for this may be on a vehicle, where higher rotation rates would need stabilisation system assistance, requiring a device with higher accuracy at higher rates.

A more interesting application is using an array configuration where multiple overlapping responses are used, each having a high resolution around their respective operating ranges, with sensor outputs combined to give a high resolution output over a wide input range. This type of configuration would be more efficient if all the masses in the array used common drive circuitry and possibly sensing circuitry. From Equation G.14, α influences the offset of the operating range. Therefore multiple responses curves with overlapping high sensitivity ranges can be achieved by incorporating multiple pairs of sensing elements, each with different α values, on a single vibrating mass. It may also be worth investigating if one mass could be used with a varying drive frequency to focus the operating point.

G.4.2 Optimising Response Linearity

The transition shape gives a relatively straight section between $\pm\sqrt{\frac{b}{c}}$ however it is not necessarily the straightest response achievable between these two points. Since γ governs the general shape of the response, it was hypothesised that there would be a corresponding value for γ that would give the straightest response over a range of interest of λ. Algebraic measures of the linearity were intractable, so this was verified using regression r^2 values as a measure of linearity and plotting the maximum achievable r^2 against the range of interest of λ in units of $\sqrt{\frac{b}{c}}$. This can be seen in Figure G.5(a). It shows that the r^2 values are very close to 1 for ranges of interest up to $\sqrt{\frac{b}{c}}$ before trailing off, indicating that an almost linear response ($r^2 = 0.99991$) can be achieved for ranges within $\pm\sqrt{\frac{b}{c}}$. The Figure G.5(b) shows the values of γ that will achieve the maximum r^2 values. For example $\gamma = 1.5375$ will maximise linearity over a range of $\pm\sqrt{\frac{b}{c}}$. This optimised shape is shown in Figure G.2(f). The bounds of the linearised region are given by $\lambda_{\pm\frac{\pi}{2}}$ in Equation G.14.

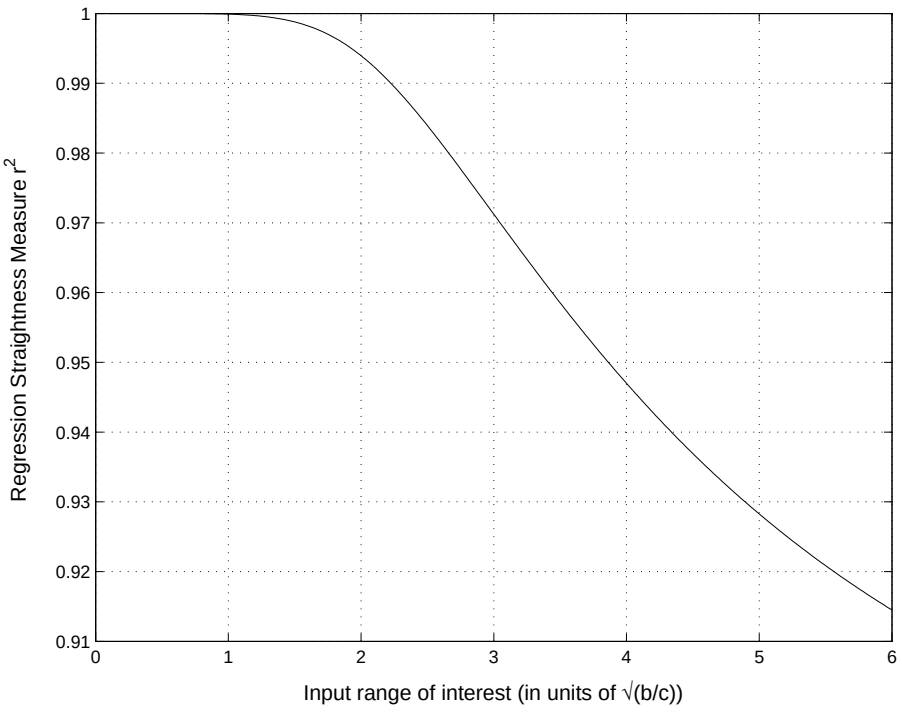

(a) Regression r^2 values for each multiple of $\sqrt{\frac{b}{c}}$.

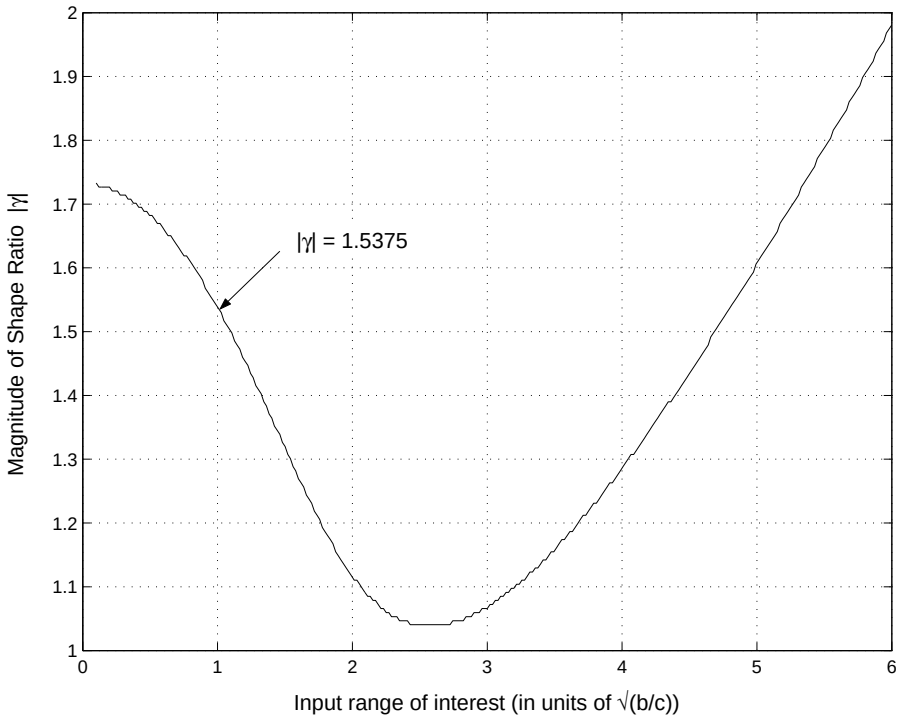

(b) Corresponding values of $|\gamma|$ for each multiple of $\sqrt{\frac{b}{c}}$.

Figure G.5: Optimising Response Linearity

It should be noted that a device does not necessarily require a linear response if the response is known. In some cases non-linearity may be an advantage. However if a linear response can be achieved it may save additional output-scaling signal-conditioning electronics. It should also be noted that the most linear response over a range of interest may not necessarily give the greatest gradient over the same range however a response with a greater gradient may still have acceptable linearity.

The next section gives a worked example that shows how the various derived equations can be used to choose parameter values to achieve the desired response shape.

G.5 Design Example

An angular rate sensor is required that gives a positive linear type response over $\pm 500°/s$ given that $\zeta_x = 0.05$ and $\omega_x = 1000Hz$

When $\gamma = \pm 1.5375$ in Equation G.17 the most linear response is achieve over the range $\pm\sqrt{\frac{b}{c}}$. Therefore from Equation G.18

$$u_x = +\sqrt{1.5375^2 \times 0.05^2 + 1} \pm 1.5375 \times 0.05 \tag{G.22}$$

$$u_x = 0.9261, 1.0798 \tag{G.23}$$

The response will have a positive gradient when $u_x > 1$, therefore

$$\omega = 1079.8Hz \tag{G.24}$$

Note that for a negative response $u_x = 0.9261$ would be used and treated the same way.

Given $\lambda = \frac{\Omega}{\omega_x}$,

$$\lambda_{\pm\frac{\pi}{2}} = \frac{\pm 500°/s \times \frac{\pi rad}{180°}}{1000Hz \times 2\pi rad} = 0.0014 \tag{G.25}$$

and using Equation G.20 $\alpha = \pm 66.0274$.

The design example response for $u_x = 1.0798$ can be seen in each plot in Figure G.6. The response is almost linear ($r^2 = 0.99991$) and it has phase differential of approximately $0.18°/°/s$ in the range of $\pm 500°$, as compared to Yang [81], which gave a phase change of $0.152°/°/s$ in the range of $\pm 120°$ with a driving frequency of 700.6Hz. This is a major improvement, due in part to using the phase differential between two sensor signals instead of the phase shift of a single sensor signal [81].

G.6 Sensitivity Analysis

Due to the large number of parameters in the model, an exhaustive algebraic exploration of model sensitivity is intractable, therefore numerical substitution will need to be used for each design case. A sensitivity analysis was carried out for the design example above using Equations G.9 and G.9, for $\beta = -\alpha_{de} \pm 20\%$, $\zeta_x = \zeta_{\pm} 20\%$ and $\omega_x = \omega_{xde} \pm 20\%$, where the subscript de indicates the design example values. The results are shown in Figure G.6. It can be seen that with a 20% parameter deviation in each case the deviation in output ranges from approximately 5% for ζ and 20% for ω_x. It should be noted that these results are valid for the design example and will vary for different parameter values.

When ω_x is varied, the frequency ratio u_x is assumed to be maintained by varying the driving frequency ω. This is a critical issue as the values of u_x to achieve the desired response are very precise. However a constant u_x can be achieved by monitoring the phase difference between the motion in the drive axis ($SensorA + SensorB$) and the Coriolis axis ($SensorA - SensorB$), which gives an indication of u_x and varying the drive frequency ω accordingly. This could be the basis of a self-calibration system for the device. Altering the driving frequency ω to maintain constant u_x, has no effect on the general shape of the response however it does affect its scale in the input axis linearly since $\lambda = \frac{\Omega}{\omega_x}$ in Equation G.14. This can be compensated for in the final scale factor of the output.

G.7 Discussion

A new phase differential angular rate sensor has been proposed. Analysis has shown it can be designed to give response shapes relatively linear for a given input range ($r^2 \approx 1$), give high sensitivity around zero or high sensitivity around input rates offset from zero. The not seen before, "offset from zero" case ($|\gamma| < \sqrt{3}$) may be exploited in an array configuration to give a device with high sensitivity over a wide range of input rotation rates. Sensitivity analysis of a design example has shown low sensitivity to variation in device parameters when the ratio between the driving frequency and the natural resonant frequency in the sense axis is maintained. As an alternative to amplitude detection for angular rate sensing, a phase differential scheme possess various other advantages. Phase differential is independent of driving amplitude, removing the need for complex amplitude control circuits. Any scale factor influence on the sensing element, such as temperature dependence does not affect the phase differential output.

As yet a prototype differential phase angular rate sensor has not been developed, but fabrication of a device is planned for future work. However, time domain Simulink simulations of the physical device operation yield the responses predicted by the mathematical model presented in G.9.

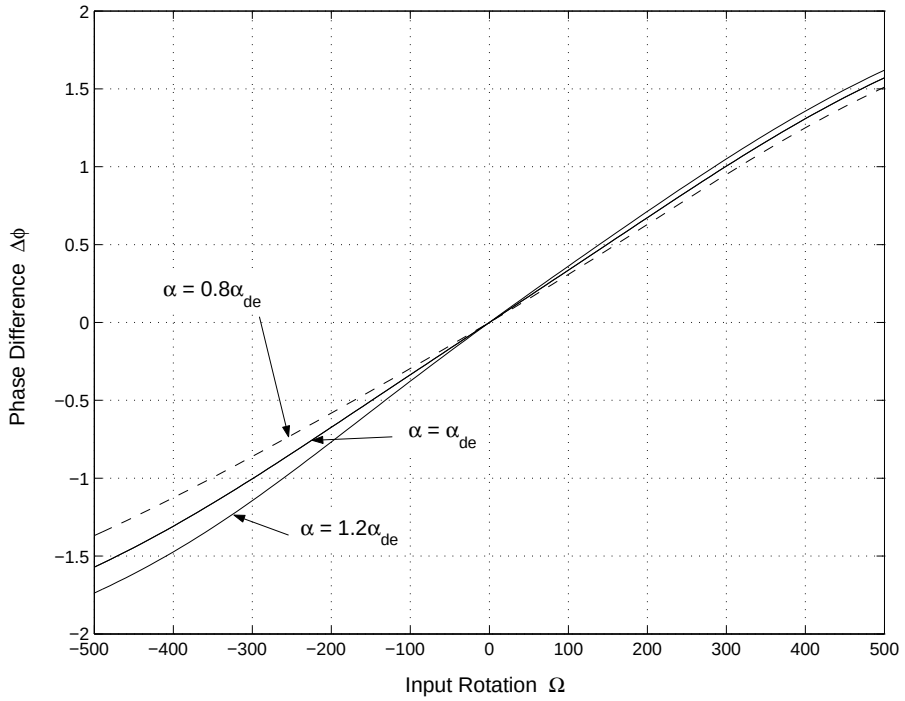

(a) Sensitivity to 20% variation in α shown either side of the design example responses for $u_x = 1.0798$.

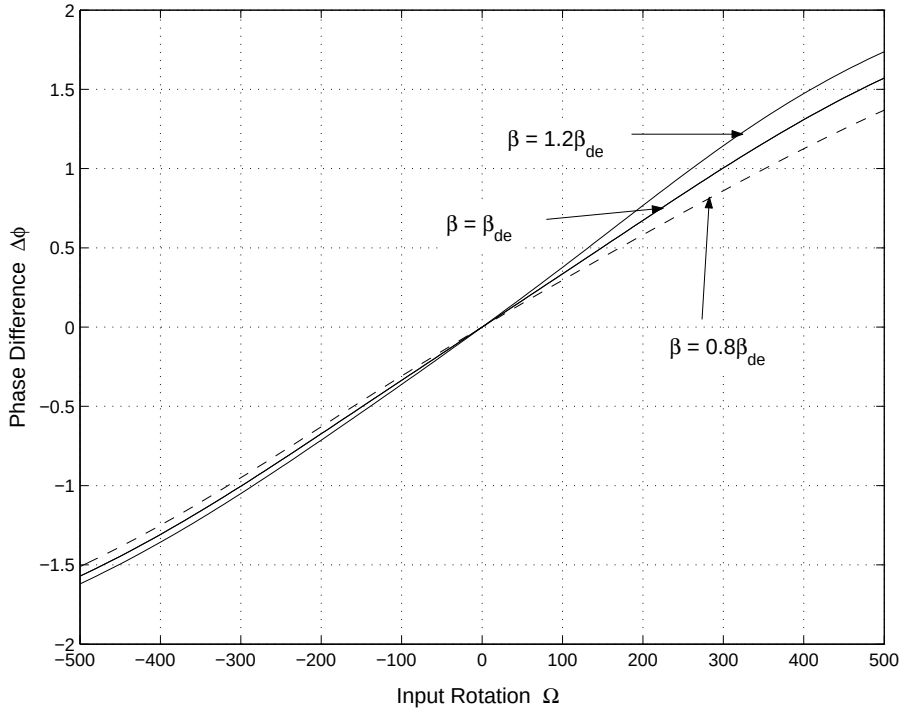

(b) Sensitivity to 20% variation in β shown either side of the design example responses for $u_x = 1.0798$

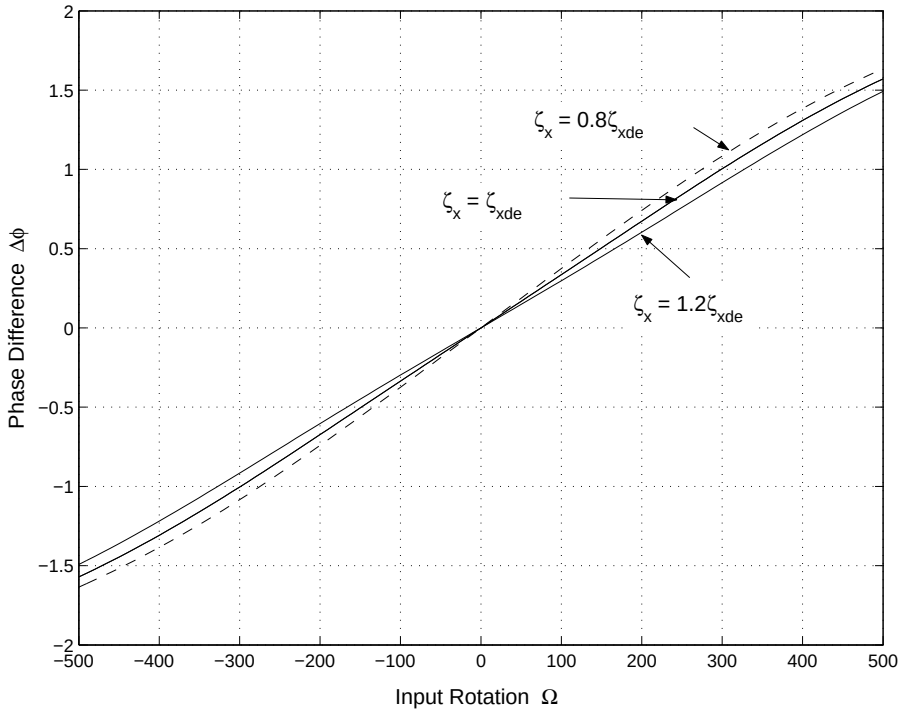

(c) Sensitivity to 20% variation in ζ_x shown either side of the design example responses for $u_x = 1.0798$

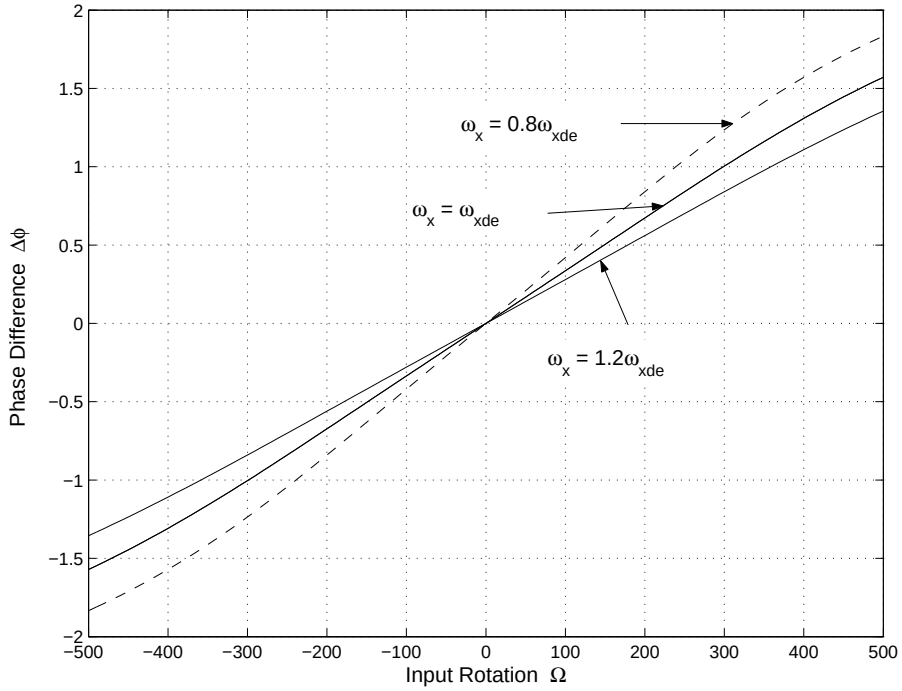

(d) Sensitivity to 20% variation in ω_x shown either side of the design example responses for $u_x = 1.0798$

Figure G.6: Sensitivity results for the design example.

Bibliography

[1] M. Abe, E. Shinohara, K. Hasegawa, S. Murata, and M. Esashi. Trident-type tuning fork silicon gyroscope by the phase difference detection. In *Micro Electro Mechanical Systems, 2000. MEMS 2000. The Thirteenth Annual International Conference on*, pages 508–513. Practical, 2000.

[2] C. Acar, S. Eler, and A. Shkel. Concept, implementation, and control of wide bandwidth mems gyroscopes. In *American Control Conference, 2001. Proceedings of the 2001*, volume 2, pages 1229–1234 vol.2. Practical, 2001.

[3] C. Acar and A. Shkel. Distributed-mass micromachined gyroscopes: demonstration of drive-mode bandwidth enhancement. In *Electronic Components and Technology, 2004. ECTC '04. Proceedings*, volume 1, pages 874–882 Vol.1, 2004.

[4] S. Adhikari and J. Woodhouse. Towards identification of a general model of damping. *Proceedings of SPIE - The International Society for Optical Engineering*, 4062 (I:377–383, 2000.

[5] S. E. Alper and T. Akin. A symmetric surface micromachined gyroscope with decoupled oscillation modes. *Sensors and Actuators A: Physical*, 97-98:347–358, 2002.

[6] F. Ayazi and K. Najafi. Design and fabrication of high-performance polysilicon vibrating ring gyroscope. In *Micro Electro Mechanical Systems, 1998. MEMS 98. Proceedings., The Eleventh Annual International Workshop on*, pages 621–626, 1998.

[7] F. Ayazi and K. Najafi. A harpss polysilicon vibrating ring gyroscope. *Microelectromechanical Systems, Journal of*, 10(2):169–179, 2001.

[8] N. Barbour and G. Schmidt. Inertial sensor technology trends. *Sensors Journal, IEEE*, 1(4):332–339, 2001.

[9] S. Beeby, G. Ensell, M. Kraft, and N. White. *MEMS Mechanical Sensors*. Microelectromechanical Sytems Series. Boston, MA : Artech House, 2004.

[10] B. Borovic, C. Hong, X. Zhang, A. Liu, and F. Lewis. Open vs. closed-loop control of the mems electrostatic comb drive. In *Intelligent Control, 2005. Proceedings of the 2005 IEEE International Symposium on, Mediterrean Conference on Control and Automation*, pages 982–988, 2005.

[11] R. Briggs. Stability of a two-degree-of-freedom gyro with external feedback. *Automatic Control, IEEE Transactions on*, 10(3):244–249, 1965.

[12] H. Cai, J. Wu, L. J, X. Zhang, Y. Wang, C. Lu, and A. Liu. Optical mems switch control and packaging. *Proceedings of the 5th Electronics Packaging Technology Conference (EPTC 2003)*, pages 291–293, 2003.

[13] D. Campos-Delgado and K. Zhou. Fault tolerant control of a gyroscope system. In *American Control Conference, 2001. Proceedings of the 2001*, volume 4, pages 2688–2693 vol.4, 2001.

[14] V. Chalam. *Adaptive Control Systems: Techniques and Applications*, volume 39 of *Electrical engineering and electronics*. Macrel Dekker, Inc., 1987.

[15] Y. Chingwen and K. Najafi. Bulk-silicon tunneling-based pressure sensors. *Technical Digest. Solid-State Sensor and Actuator Workshop*, pages 201–204, 1994.

[16] S. Cho, K. Najafi, and K. Wise. Internal stress compensation and scaling in ultrasensitive silicon pressure sensors. *IEEE Transactions on Electron Devices*, 39(4):836–842, 1992.

[17] U. Columbia. Photolithography basics. *Columbia Center for Integrated Science and Engineering. http://www.cise.columbia.edu/clean/process/Photolithography_Lessons.pdf Accessed 02/02/2005*, 2003.

[18] U. Columbia. Spin coat theory. *Columbia Center for Integrated Science and Engineering. http://www.cise.columbia.edu/clean/process/spintheory.pdf Accessed 01/02/2005*, 2003.

[19] B. Friedland and M. Hutton. Theory and error analysis of vibrating-member gyroscope. *Automatic Control, IEEE Transactions on*, 23(4):545–556, 1978.

[20] T. Gabrielson. Mechanical-thermal noise in micromachined acoustic and vibration sensors. *IEEE Transactions on Electron Devices*, 40(5):903–909, 1993.

[21] M. Gad-el Hak. *The MEMS Handbook*. CRC Press, 2002.

[22] B. Gallacher, J. Hedley, J. Burdess, A. Harris, A. Rickard, and D. King. Electrostatic correction of structural imperfections present in a microring gyroscope. *Microelectromechanical Systems, Journal of*, 14(2):221–234, 2005.

[23] B. Gogoi, C. C. Wang, and C. Mastrangelo. Force balanced micromachined pressure sensors, 2001.

[24] G. He and K. Najafi. A single-crystal silicon vibrating ring gyroscope, 2002.

[25] R. C. Hibbeler. *Statics and Mechanics of Materials*. Prentice-Hall, Eaglewood Cliffs, New Jersey, 1993.

[26] X. Jiang, J. Seeger, M. Kraft, and B. Boser. A monolithic surface micromachined z-axis gyroscope with digital output. In *VLSI Circuits, 2000. Digest of Technical Papers. 2000 Symposium on*, pages 16–19. Application, 2000.

[27] J. John, C. Jakob, T. Vinay, and L. Q. Phase differential angular rate sensor-concept and analysis. *Sensors Journal, IEEE*, 4(4):471–478, 2004.

[28] J. John and T. Vinay. Novel concept of a single mass adaptively controlled triaxial angular rate sensor. *Sensors Journal, IEEE*, Accepted for publication April, 2005.

[29] T. Kenny, W. Kaiser, H. Rockstad, J. Reynolds, J. Podosek, and E. Vote. Wide-bandwidth electromechanical actuators for tunneling displacement transducers. *Microelectromechanical Systems, Journal of*, 3(3):97–104, 1994.

[30] D. Keymeulen, W. Fink, M. Ferguson, C. Peay, B. Oks, R. Terrile, and K. Yee. Tuning of mems devices using evolutionary computation and open-loop frequency response. In *Aerospace, 2005 IEEE Conference*, pages 1–8, 2005.

[31] S. Kim, B. Lee, J. Lee, and K. Chun. A gyroscope array with linked-beam structure. In *Micro Electro Mechanical Systems, 2001. MEMS 2001. The 14th IEEE International Conference on*, pages 30–33, 2001.

[32] M. R. S. M. H. B. Koester David, Cowev Allen. Polymumps design handbook, 2003.

[33] B. Kooi, W. Oltuis, and P. Bergveld. Rate of turn sensing with a modified triaxial accelerometer. In *Eurosensors*, Kopenhagen, 2000.

[34] A. Kourepenis, J. Borenstein, J. Connelly, R. Elliott, P. Ward, and M. Weinberg. Performance of mems inertial sensors. In *Position Location and Navigation Symposium, IEEE 1998*, pages 1–8. Application Practical Experimental, 1998.

[35] M. Kraft. *Closed Loop Digital Accelerometer Employing Oversampling Conversion.* PhD thesis, Coventry University, School of Engineering, UK, 1997.

[36] M. Krstic, I. Kanellakopoulos, and P. Kokotovic. *Nonlinear and Adaptive Control Design.* Adaptive and Learning Systems for Signal Processing Communications, and Control. John Wiley and Sons Inc, 1995.

[37] R. L. Kubena, D. J. Vickers-Kirby, R. J. Joyce, F. P. Stratton, and D. T. Chang. A new tunneling-based sensor for inertial rotation rate measurements. *Sensors and Actuators A: Physical*, 83(1-3):109–117, 2000.

[38] M. B. Ladetto Quentin. Digital magnetic compass and gyroscope integration for pedestrian navigation. Technical report, AFaculte ENAC - Institut du Developpement Territorial, Geodetic Laboritory (TOPO), 2002.

[39] L. M. Landsberger, B. Nikpour, M. Kahrizi, A. Iftimie, and T. J. Hubbard. Concave corner compensation between vertical (010)-(001) planes anisotropically etched in si(100). *Sensors and Actuators A: Physical*, 66(1-3):299–307, 1998.

[40] J.-Y. Lee, S.-H. Jeon, H.-K. Jung, H.-K. Chang, and Y.-K. Kim. Vacuum packaged low noise gyroscope with sub mdeg/s//spl radic/hz resolution. In *Micro Electro Mechanical Systems, 2005. MEMS 2005. 18th IEEE International Conference on*, pages 359–362, 2005.

[41] R. Leland. Adaptive tuning for vibrational gyroscopes. In *Decision and Control, 2001. Proceedings of the 40th IEEE Conference on*, volume 4, pages 3447–3452 vol.4. Theoretical or Mathematical, 2001.

[42] R. Leland. Lyapunov based adaptive control of a mems gyroscope. *Proceedings of the 2002 American Control Conference (IEEE Cat. No.CH37301)*, pages 3765–3770 Volume 5, 2002.

[43] M. Lemkin and B. Boser. A three-axis micromachined accelerometer with a cmos position-sense interface and digital offset-trim electronics. *Solid-State Circuits, IEEE Journal of*, 34(4):456–468, 1999.

[44] Y. Liang, T. Zhao, Y. Xu, and S. Boh. A cmos fully-integrated low-voltage vibratory microgyroscope. In *Electrical and Electronic Technology, 2001. TENCON. Proceedings of IEEE Region 10 International Conference on*, volume 2, pages 825–828 vol.2. Practical, 2001.

[45] D. Lili and R. Leland. The adaptive control system of a mems gyroscope with time-varying rotation rate. *Proceedings of the 2005 American Control Conference (IEEE Cat. No. 05CH37668)*, pages 3592–3597 Volume 5, 2005.

[46] M. Long, J. Burdick, and E. Antonsson. Design of compensation structures for anisotropic etching. *1999 International Conference on Modeling and Simulation of Microsystems*, pages 124–127, 1999.

[47] H. Luinge. *Inertial Sensing of Human Movement.* Ph.d. thesis, Twente University Press P.O. Box 217, 7500 AE Enschede, the Netherlands, www.tup.utwente.nl, 2002.

[48] M. Lutz, W. Golderer, J. Gerstenmeier, J. Marek, B. Maihofer, S. Mahler, H. Munzel, and U. Bischof. A precision yaw rate sensor in silicon micromachining. In *Solid State Sensors and Actuators, Transducers '97 Chicago, International Conference on*, volume 2, pages 847–850 vol.2. Application, 1997.

[49] W. Macek and D. J. Davis. Rotation rate sensing with traveling-wave ring lasers. *Applied Physics Letters*, 2(3):67–68, 1963.

[50] M. J. Madau. *Fundamentals of Microfabrication : the science of miniturisation.* CRC Press LLC, second edition, 2002.

[51] R. M'Closkey, S. Gibson, and J. Hui. System identification of a mems gyroscope. *Transactions of the ASME. Journal of Dynamic Systems, Measurement and Control*, 123(2):201–210, 2001.

[52] Y. Mochida, M. Tamura, and K. Ohwada. A micromachined vibrating rate gyroscope with independent beams for the drive and detection modes. In *Micro Electro Mechanical Systems, 1999. MEMS '99. Twelfth IEEE International Conference on*, pages 618–623, 1999.

[53] H. Moritz. Optical single layer lift-off process. *Electron Devices, IEEE Transactions on*, 32(3):672–676, 1985.

[54] J. Newton, G. A rate gyroscope based on interaction of sonic waves. *Automatic Control, IEEE Transactions on*, 10(3):235–243, 1965.

[55] C. Painter and A. Shkel. Structural and thermal analysis of a mems angular gyroscope. *Proceedings of the SPIE - The International Society for Optical Engineering*, 4334:86–94, 2001.

[56] C. Painter and A. Shkel. Active structural error suppression in mems vibratory rate integrating gyroscopes. *IEEE Sensors Journal*, 3(5):595–606, 2003.

[57] W. Pan, P. Soussan, B. Nauwelaers, and H. A. Tilmans. A surface micromachined electrostatically tunable film bulk acoustic resonator. *Sensors and Actuators A: Physical*, In Press, Corrected Proof.

[58] A. Pantazi, M. Lantz, G. Cherubini, H. Pozidis, and E. Eleftheriou. A servomechanism for a micro-electromechanical-system-based scanning-probe data storage device. *Nanotechnology*, 15(10):S612–S621, 2004.

[59] K. Park, C. Lee, Y. Oh, and Y. Cho. Laterally oscillated and force-balanced micro vibratory rate gyroscope supported by fish hook shape springs. In *Micro Electro Mechanical Systems, 1997. MEMS '97, Proceedings, IEEE., Tenth Annual International Workshop on*, pages 494–499. Practical Experimental, 1997.

[60] S. Park. *Adaptive Control Strategies for MEMS Gyroscopes.* Phd thesis, University of California, Berkeley, 2000.

[61] S. Park, R. Horowitz, and T. Chin-Woo. Adaptive controller design of mems gyroscopes. *2001 IEEE Intelligent Transportation Systems. Proceedings (Cat. No.01TH8585)*, pages 496–501, 2001.

[62] P. Parks. Liapunov redesign of model reference adaptive control systems. *Automatic Control, IEEE Transactions on*, 11(3):362–367, 1966.

[63] B. Piekarski, D. DeVoe, M. Dubey, R. Kaul, and J. Conrad. Surface micromachined piezoelectric resonant beam filters. *Sensors and Actuators A: Physical*, 91(3):313–320, 2001.

[64] D. Piyabongkarn and R. Rajamani. The development of a mems gyroscope for absolute angle measurement. In *American Control Conference, 2002. Proceedings of the 2002*, volume 3, pages 1960–1965 vol.3. Theoretical or Mathematical, 2002.

[65] P. Qi Lin; Stern. Analysis of a correlation filter for thermal noise reduction in a mems gyroscope. In *System Theory, 2002. Proceedings of the Thirty-Fourth Southeastern Symposium on*, pages 197–203, 2002.

[66] P. Rai-Choudhury. *MEMS and MOEMS technology and applications.* SPIE Press monograph PM85. Bellingham, Wash. : SPIE Optical Engineering Press, 2000.

[67] S. Sastry. *Adaptive Control Stability, Convergence, and Robustness.* Prentice Hall Information and System Sciences Series. Prentice-Hall, 1989.

[68] A. Seshia, R. Howe, and S. Montague. An integrated microelectromechanical resonant output gyroscope. *Technical Digest. MEMS 2002 IEEE International Conference. Fifteenth IEEE International Conference on Micro Electro Mechanical Systems (Cat. No.02CH37266)*, pages 722–726, 2002.

[69] A. Sharma, F. Zaman, B. Amini, and F. Ayazi. A high-q in-plane soi tuning fork gyroscope. In *Sensors, 2004. Proceedings of IEEE*, pages 467–470 vol.1, 2004.

[70] A. Shkel, R. Horowitz, A. Seshia, S. Park, and R. Howe. Dynamics and control of micromachined gyroscopes. In *American Control Conference, 1999. Proceedings of the*, volume 3, pages 2119–2124 vol.3, 1999.

[71] A. Shkel, R. Howe, and R. Horowitz. Modeling and simulation of micromachined gyroscopes in the presence of imperfections. *1999 International Conference on Modeling and Simulation of Microsystems*, pages 605–608, 1999.

[72] T. Singh and T. Ytterdal. A single-ended to differential capacitive sensor interface circuit designed in cmos technology. In *Circuits and Systems, 2004. ISCAS '04. Proceedings of the 2004 International Symposium on*, volume 1, pages I–948–51 Vol.1, 2004.

[73] J. Song, Y. Ruan, and J. Zhai. Study on micro-mirror macro model and its dynamic behavior. *Optik - International Journal for Light and Electron Optics*, 115(11-12):569–573, 2004.

[74] T. Tang, R. Gutierrez, C. Stell, V. Vorperian, G. Arakaki, J. Rice, W. Li, I. Chakraborty, K. Shcheglov, J. Wilcox, and W. Kaiser. A packaged silicon mems vibratory gyroscope for microspacecraft. In *Micro Electro Mechanical Systems, 1997. MEMS '97, Proceedings, IEEE., Tenth Annual International Workshop on*, pages 500–505, 1997.

[75] S. P. Timoshenko and J. M. Gere. *Mechanics of Materials*. Chapman and Hall, 1987.

[76] G. Vincent, L. Quentin, and M. Bertrand. Two different approaches for augmented gps pedestrian navigation. Technical report, Geodetic Engineering Laboritory, Institute of Geomatics, Swiss Federal Institute of Technology, Lausanne, Switzerland, 2001.

[77] C.-h. Wang and X. Huang. Application of wavelet packet analysis in the de-noising of mems vibrating gyro. *PLANS 2004. Position Location and Navigation Symposium (IEEE Cat. No.04CH37556)*, pages 129–132, 2004.

[78] L. Wang, J. Dawson, J. Chen, P. Famouri, and A. Hornak. Stroke-length control of a mems device. *ISIE'2000. Proceedings of the 2000 IEEE International Symposium on Industrial Electronics (Cat. No.00TH8543)*, pages 535–539 Volume 2, 2000.

[79] Z. Wang, J. Tsaur, R. Maeda, and H. Kokawa. Deposition of pzt thin films by hybrid process comprising sol-gel method and laser ablation for microscanners. In *Applications of Ferroelectrics, 2004. ISAF-04. 2004 14th IEEE International Symposium on*, pages 169–172, 2004.

[80] G. Wu, Z. Xiao, Z. Li, and Y. Hao. Design and fabrication for inertial micro sensors. In M. Zhang and K. Tu, editors, *Solid-State and Integrated Circuit Technology, 1998. Proceedings. 1998 5th International Conference on*, pages 903–909. General or Review Practical Experimental, 1998.

[81] H. Yang, M. Bao, H. Yin, and S. Shen. A novel bulk micromachined gyroscope based on a rectangular beam-mass structure. *Sensors and Actuators A: Physical*, 96(2-3):145–151, 2002.

[82] J. Yang, H. Kahn, H. An-Qiang, S. Phillips, and A. Heuer. A new technique for producing large-area as-deposited zero-stress lpcvd polysilicon films: the multipoly process. *Journal of Microelectromechanical Systems*, 9(4):485–494, 2000.

[83] N. Yazdi, F. Ayazi, and K. Najafi. Micromachined inertial sensors. *Proceedings of the IEEE*, 86(8):1640–1659, 1998.

[84] Q. Zhang, L. Liu, and Z. Li. A new approach to convex corner compensation for anisotropic etching of (100) si in koh. *Sensors and Actuators A: Physical*, 56(3):251–254, 1996.

[85] X. Zhang, R. Ghodssi, K.-S. Chen, A. Ayon, and S. Spearing. Residual stress characterization of thick pecvd teos film for power mems applications. In *Technical digest. Solid-State Sensor and Actuator Workshop (TRF Cat. No.00TRF-0001)*, pages 316–319, 2000.